Pouya Sedighi

Application of advanced constitutive model for ground improvement

Dissertation

Eingereicht an der Fakultät für Bauingenieurwissenschaften
Technische Universität Graz

Begutachter:

Ao.Univ.-Prof. Dipl.-Ing. Dr.-techn. Helmut F. Schweiger, M.Sc

Institute for Soil Mechanics and Foundation Engineering
Graz University of Technology, Austria

Dr.-Ing. habil. Sascha Henke

BBI Geo- und Umwelttechnik Ingenieur-Gesellschaft mbH
Hamburg, Germany

Graz, February 2017

Acknowledgements

This thesis was not made possible without the great support, guidance and patience of my supervisor Ao.Univ.-Prof. Dipl.-Ing. Dr.techn. Helmut F. Schweiger, M.Sc., Head of the Computational Geotechnics Group of the institute for Soil mechanics and Foundation Engineering. I would like to thank him for providing a very pleasant research group and I enjoyed working in that nice scientific atmosphere.

I am also grateful to Dr.-Ing. habil. Sascha Henke for reviewing my thesis.

I am thankful to Keller Holding GmbH Germany and Keller Grunbau GmbH Austria for financing this research project. In addition, I am grateful to Prof. Wolfgang Jimmy Wehr and Dr. Vaclav Racansky for their valuable supports and providing me with the useful references and data.

Thanks are also due to Univ.-Prof. Dipl.-Ing. Dr.techn. Roman Marte, Head of the Institute for Soil Mechanics and Foundation Engineering, for making the research facilities of the institute available for me.

I really thank all my dear colleagues at the institute for their friendly helps, productive scientific viewpoints and for nice and pleasant working atmosphere. In Particular, I would like to thank Bert Schädlich, Laurentiu Floroiu, Patrick Pichler, Joshua Poganski, Georg Ausweger, Michael Havinga and Franz Tschuchnigg.

Last but not least, I would like to thank my wife Parwin for her great encouragements, love and support.

I would like to dedicate my dissertation to my lovely parents.

Graz, February 2017 Pouya Sedighi

Kurzfassung

Anwendung eines hochwertigen Materialmodells für Bodenverbesserung

Für die Verbesserung des mechanischen Verhaltens von weichen Böden haben sich Bodenverbesserungsverfahren wie z. B. das Düsenstrahlverfahren oder die tiefe Bodenvermörtelung bewährt. Eines der Schlüsselelemente der numerischen Analyse von Bodenverbesserungstechniken ist das Stoffmodell zur Beschreibung des mechanischen Verhaltens der Materialien. Einfache elastisch-perfekt plastische Bruchkriterien können wichtige Aspekte des mechanischen Verhaltens von Bodenverbesserungswerkstoffen nicht erfassen, wie die Zeitabhängigkeit von Festigkeit und Steifigkeit und Entfestigung wenn die maximale Druck- und Zugfestigkeit erreicht ist. Bodenverbesserungsmaßnahmen werden auch als erdbebenbeständige Elemente eingesetzt, da sie die seismische Reaktion natürlicher, weicher Bodenschichten unter Erdbebenbeanspruchungen verändern können.

In dieser Arbeit wird ein Materialmodell, das ursprünglich für die Beschreibung des Verhaltens von Spritzbeton entwickelt wurde, verwendet, um das Verhalten von unbewehrten, zementgebundenen Materialien sowohl bei statischer als auch bei dynamischer Belastung zu simulieren. Die Eignung des neuen Modells zur Simulation verschiedener Testresultate (z. B. uniaxialer Kompressionsversuch, Dreipunkt-Biegeversuch und Kriechversuch) zementgebundener Materialien wird bewertet. Die Ergebnisse zeigen, das wesentliche Aspekte des Materialverhaltens zementgebundener Materialien erfasst werden können. Die Anwendung des neuen Modells wird in der numerischen Simulation einer durch das Düsenstrahlverfahren hergestellten Sohle untersucht, die beim Aushub einer Baugrube als Auftriebssicherheit dient. Es konnte gezeigt werden, dass signifikant unterschiedliche Spannungsverteilungen im Vergleich zur Modellierung der Dichtsohle mit einem Mohr-Coulomb-Kriterium erhalten werden. Schließlich wird mit Hilfe der Finite-Elemente-Methode der Einfluss von Düsenstrahlsäulen (bzw. eines Rasters von „mixed-in-place“ Säulen) auf die Bodenreaktion von homogenem und geschichtetem Baugrund unter Erdebebenbeanspruchung untersucht. Die erhaltenen Ergebnisse zeigten, dass die Bodenverbesserungsmaßnahmen die seismischen Oberflächenbelastungen erhöhen bzw. verringern können, wenn die Eigenfrequenzen des natürlichen Baugrundes verändert werden. Diese Veränderungen spiegeln sich in der Folge auch in einer unterschiedlichen Klassifizierung des Baugrundes nach EC8 wider. Darüber hinaus konnte gezeigt werden, dass bei einem Erdbeben mögliche Risszonen in den spröden und unbewehrten Verbesserungselementen bestimmt werden können.

Abstract

Application of advanced constitutive model for ground improvement

Ground improvement methods such as jet grouting or deep soil mixing techniques have proven to be efficient for improving the mechanical behaviour of soft grounds. One of the key elements in numerical analysis of ground improvement techniques is the constitutive model employed for describing the mechanical behaviour of the materials. Conventional simple elastic-perfectly plastic failure criteria cannot capture the important aspects of the mechanical behaviour of ground improvement materials, like time dependency of strength and stiffness and softening when the maximum compression and tensile strength is reached. Therefore, having a proper constitutive model for a robust simulation is important. Ground improvement techniques are also used as earthquake resistant elements in the field of geotechnical earthquake engineering. This improvement may alter the seismic response of natural soft soil deposit subjected to strong motions.

In this thesis, a constitutive model originally developed for describing the behaviour of shotcrete material is used to simulate the behaviour of unreinforced cement-based materials in both static and dynamic loading. The ability of the new model to simulate various laboratory test results (such as uniaxial compressive, three point bending and creep tests) on cement-based materials is evaluated. The results prove the reliability of this model to capture the important aspects of cement-based materials. In further analyses, the application of the new model in numerical simulation of a jet-grout panel constructed at the bottom of a deep excavation against uplift pressure is investigated. It could be shown that significantly different stress distributions are obtained compared to modelling the panel with a Mohr-Coulomb criterion. Finally the influence of the jet-grout columns (and deep soil-mixing grid) on ground response of homogeneous and layered soil deposits subjected to strong motion are studied by means of the finite element method. The obtained results demonstrated that ground improvement can decrease but also may increase the surface seismic loads as the eigen frequencies of the natural deposit are changed. These changes are also reflected in varying the site classification according to EC8. In addition, it could be shown that possible crack zones in the brittle and unreinforced improving elements can be defined during an earthquake.

Table of contents

List of symbols

1 Introduction 1

1.1 Motivation 1

1.2 Outline of thesis 2

2 Constitutive model for cement-based materials 4

2.1 Introduction 4

2.2 A brief review on the shotcrete model 4

2.2.1 Model input parameters 4

2.2.2 Yield surface and strain hardening/softening 6

2.2.2.1 The model behaviour in compression 6

2.2.2.2 The model behaviour in tension 9

2.2.3 Time dependency of stiffness and strength 10

2.2.4 Creep 11

2.3 Performing dynamic calculations 12

2.4 Summary 12

3 Properties of cement-based material 13

3.1 Material properties 13

3.1.1 Density 13

3.1.2 Uniaxial compressive strength 14

3.1.3 Failure Strains 16

3.1.4 Tensile Strength 17

3.1.5 Modulus of elasticity 20

3.1.6 Shear strength parameters 23
3.1.7 Fracture energy 24
3.1.7.1 Tensile fracture energy 25
3.1.7.2 Compression fracture energy 27
3.1.8 Poisson's ratio 29
3.2 Parameter calibration of new constitutive model 29
3.2.1 Time dependency of strength and stiffness 30
3.2.2 Stress-strain curves 31
3.2.3 Calibration of softening parameters 32
3.2.3.1 Compression softening 32
3.2.3.2 Tension softening 35
3.2.4 Creep test 37
3.3 Dynamic properties of cement-based material 39
3.4 Summary 47

4 Numerical modelling of deep excavation 48
4.1 Jet-grout slab under uplift pressure 48
4.1.1 Introduction 48
4.1.2 Material properties 49
4.1.3 Connection of slab to the diaphragm wall 51
4.1.4 Results 52
4.1.4.1 Horizontal and straight slab 52
4.1.4.2 Arched slab (Influence of slab geometry) 73
4.2 Deep excavation supported by row of deep soil mixing columns 76
4.2.1 Introduction 76
4.2.2 Model description and material parameter 76

4.2.3 Results 78

4.3 Summary and conclusion 81

5 Methods of performing ground response analysis 82

5.1 Site response analysis 82

5.2 Earthquake motion characterization 83

5.3 Dynamic soil behaviour 84

5.4 Cyclic stress-strain behaviour of soils 85

5.4.1 Equivalent linear representation 85

5.4.1.1 Shear modulus degradation curves 87

5.4.1.2 Damping ratio 88

5.4.2 Cyclic non-linear models 88

5.4.3 Advanced constitutive models 89

5.5 One-Dimensional Ground response analysis 89

5.5.1 Linear method 90

5.5.2 Equivalent linear method 94

5.5.3 Non-linear approach 96

5.6 2D and 3D analysis 96

5.7 Calculation of ground response 96

5.8 Amplification ratio 97

5.9 Response to earthquake 99

5.9.1 Response spectrum 99

5.9.2 Design spectrum 101

5.10 Dynamic Finite element analysis with Plaxis 103

5.10.1 Time integration algorithm 104

5.10.2 Time steps 104

5.10.3 Minimum element size 105

5.10.4 Energy dissipation 106

5.10.4.1 Material damping 106

5.10.4.2 Numerical damping 107

5.10.4.3 Boundary conditions 107

5.11 Summary and further study 111

6 Preliminary dynamic analyses 112

6.1 Behaviour of jet-grout columns under earthquake loading 112

6.1.1 Model description 112

6.1.2 Influence of damping ratio of the columns 115

6.1.3 Influence of the stiffness and fracture energy 115

6.1.4 Influence of the main domain width 116

6.2 Evaluation of shotcrete model in dynamic analysis 118

6.3 Summary and conclusion 121

7 Ground response of an improved soil deposits 122

7.1 Introduction 122

7.2 Homogeneous soil layer 123

7.2.1 Model description 123

7.2.2 Input motion 124

7.2.3 Model description 125

7.2.4 Material parameters of the soil 126

7.2.5 Verification of the Free-Field boundary condition for the 2D analysis 128

7.2.6 Results 131

7.3 Layered soil deposits 137

7.3.1 Ground conditions 137

7.3.2 Finite element model 138

7.3.3 Material parameters of the soil layers 140

7.3.4 Material properties of the columns 142

7.3.5 Results and discussion 143

7.4 Influence of a different earthquakes 149

7.4.1 Unimproved soil 150

7.4.1.1 Material parameters of the soil layers 150

7.4.2 Improved soil deposit 155

7.5 Influence of overlapping jet-grouting columns against single columns 158

7.5.1 Results 160

7.6 Influence of Lattice-shaped improvement on ground response of a layered soil 163

7.6.1 Introduction 163

7.6.2 Model description: 164

7.6.3 Input motion 165

7.6.4 Material parameter of the soil 166

7.6.5 Material parameters of the soil improvement 169

7.6.6 Results 170

7.7 Summary and conclusion 177

8 Evaluation of influence of concrete slab above stiff columns 179

8.1.1 Introduction 179

8.1.2 Influence of unsupported slab 179

8.1.2.1 Damping ratio of slab 179

8.1.2.2 Slab stiffness 180

8.1.2.3 Slab geometry 181

8.1.3 Supported slab 183

8.1.3.1 Geometry of the models 183

8.1.3.2 Material parameters of the columns and slab 184

8.1.3.3 Results 184

8.2 Effect of presence of surface Structure on soil amplification ratio 187

8.3 Summary 191

9 Conclusion and further research 192

9.1 Conclusion 192

9.2 Further research 194

10 Bibliography 195

List of symbols

This section lists the used symbols in alphabetical. The symbols are explained in the text additionally when they first time are introduced. The units and abbreviations are not included in this list and will be defined in the thesis.

Small letters

$\ddot{u}_g$	base acceleration
$\ddot{u}$	acceleration
$\dot{u}$	velocity
a	increase of failure strain with increase of mean effective stress
a_0	mean value of displacement in the Furrier series
a_g	design ground acceleration on type A ground according to EC8
a_{gR}	reference ground acceleration on type A ground
a_n	amplitude of the harmonic load
c/c	centre-to-centre distance of soil improvement elements
c'	effective cohesion
c_s	damping of SDOF structure
c_u	undrained shear strength of the soil
d	diameter of improvement element / diameter of embedded pile
d_{eq}	equivalent plate thickness
d_{max}	maximum aggregate size
e	void ratio
f	frequency
f_1	first eigen frequency of the soil column
f_2	second eigen frequency of the soil column
$f_{c,1}$	uniaxial compressive strength of cured sample for 1 day
f_c	uniaxial compressive strength of cured sample e.g 28 days ($f_{c,28}$)
f_{c0n}	normalized initially mobilised strength
f_{cf}	failure strength (compression)
f_{cfn}	normalized failure strength (compression)
f_{ck}	characteristic compressive strength
$f_{ct,sp}$	tensile strength from Brazilian test
f_{cun}	normalized residual strength (compression)
f_{cy}	uniaxial compression yield stress
f_m , f_n	target frequencies for calculation of Rayleigh damping coefficients
$f_{m,d}$	design value of uniaxial compressive strength $f_{m,d}$
f_{max}	maximum frequency of interest
f_p	predominant frequency of the earthquake signal
f_t	uniaxial tensile strength of cured sample for e.g 28 days ($f_{t,28}$)
$f_{t,y}$	tensile yield stress
f_{tu}	tensile residual strength

f_{tun}	ratio of residual vs. peak tensile strength
h_i	thickness of the sublayers
k_s	stiffness of SDOF system
l_e	average element size of the FE model
l_{node}	distance between two neighbouring nodes of a finite element
m	number of additional dynamic time steps / Power index that controls the stress dependency of stiffness
m_s	mass of the SDOF structure
n	number of dynamic sub steps
n_{GP}	number of gauss points per element
$p´$	mean effective stress
p_{ref}	atmospheric pressure
q	behaviour factor of structure according to EC8
q_u	uniaxial compressive strength
t	time
t_0^{cr}	start time of creep loading
t_{50}^{cr}	time for 50% of creep strains
t_{50}^{shr}	time for 50% of shrinkage strains
$t_{hydr.}$	time for full hydration
u	displacement (horizontal)
u^{ff}	normal displacement related to free-field domain
u^{m}	normal displacement related to main domain
u_{max}	maximum horizontal displacement at ground level
u_s	displacement of the SDOF system
u_{s0}	peak deformation (displacement) of SDOF system
v^{ff}	normal displacement related to free-field domain
v^{m}	normal displacement related to main domain
v	tangential displacement
v_i	shear wave velocity of the sublayers
w	*unit weight*
w_{slab}	load acting on the jet-grout slab
x, y, z	Cartesian coordinates
Δt	dynamic time step
$\Delta t_{critical}$	critical time step

Capital letters

A	cross section area
$A(f)$	amplification function
A_{el}	size of the finite element
A_r	replacement ratio
$A(t)$	pseudo-acceleration
A^{SI}	area of one soil improvement element
A^{soil}	area of the unimproved soil in on soil improvement block

A_{total}	area of the soil improvement block
B	largest dimension of the finite element
C	damping matrix
C_1	relaxation coefficient in the Plaxis formulation of Rayleigh damping
C_2	relaxation coefficient in the Plaxis formulation of Rayleigh damping
D	damping ratio
D^{SI}	damping ratio of the soil improvement elements
D^{Soil}	damping ratio of the unimproved soil
D_e	linear elastic stiffness matrix
$D_{equivalent}$	equivalent damping ratio for one soil improvement cell
D_i	damping ratio of the improvement material
D_{min}	minimum (small strain) damping ratio of cement-based material
E	elastic Young's modulus
E^{SI}	Young's modulus of soil improvement element in one soil improvement block
E^{soil}	Young's modulus of unimproved soil one soil improvement block
E_0	small strain Young's modulus
E_1	Young's modulus of 1day cured sample
E_{28}	Young's modulus of cured sample at $t_{hydr.}$
E_{50}	secant modulus of elasticity in a stress–strain curve at half of the unconfined compressive strength
$E_{50\%}$	tangent modulus corresponding to half of the uniaxial compressive strength
$E_{50,ref}$	deviatoric hardening modulus in hardening soil model at reference pressure
EA	axial stiffness
E_{cm}	Young's modulus of jet-grouted sand and clay soils
$E_{equivalent}$	equivalent Young's modulus for one soil improvement cell
EI	bending stiffness
$E_{oed,ref}$	reference stiffness for primary oedometer test
E_{t50}	tangent modulus at 50% of uniaxial compressive strength
$E_{ur,ref}$	Stiffness for unloading/reloading at reference pressure
F	frequency factor / load vector in dynamic equation of motion
F_N	normal force
F_s	equivalent static force acting on SDOF system
F_y	yield stress of steel
G	shear modulus
G^*	complex shear modulus
G_0	maximum shear modulus
G_c	compressive Fracture Energy of cured sample at t_{hydr} (e.g. $G_{c,28}$)
G_f	specific fracture energy or fracture energy in tension
G_{fc}	fracture energy in compression
G_{ft}	tensile fracture energy
G_{max}	maximum shear modulus
G_r	ratio of the shear modulus of the improvement cell to the soil

G_{sec}	secant shear modulus
G_t	tensile Fracture Energy of cured sample at t_{hydr} (e.g. $G_{t,28}$)
G_{tan}	tangent shear modulus
H	soil deposit depth
H_c	normalised hardening/softening parameter in compression
H_{cf}	normalised softening parameter in compression correspond to failure
H_{cu}	normalised softening parameter in compression correspond to residual level
H_t	normalised softening parameter in
I^{SI}	moment of inertia of the improvement element
I^{soil}	moment of inertia of unimproved soil
ISF	interface stiffness factor of embedded piles
K	global stiffness matrix
K_0	earth pressure coefficient at rest
L	spacing
L_{eq}	required equivalent length to provides the necessary regularization to avoid mesh dependent numerical results
M	global mass matrix / earthquake magnitude
N	bearing capacity of the tension pile
N_{SPT}	standard Penetration Test blow-count
PI	plasticity index
PSA	pseudo spectral acceleration
PSV	pseudo spectral velocity
$P_{t\text{-}allowable}$	maximum allowable tension load for uncased length of micro piles
Q	shear force
R_{inter}	interface reduction factor
S	soil factor according to Eurocode 8
S_a	spectral acceleration
S_d	spectral displacement
S_e	elastic response spectrum according to Eurocode 8
$S_{el.}$	surface area of the element
S_{stiff}	the parameter governing stiffness evolution with time
$S_{strength}$	the parameter governing strength evolution with time
S_u	undrained shear strength
S_v	spectral velocity
T	vibration period of a linear SDOF system according to Eurocode 8
T_1	first eigen period of the soil column
T_2	second eigen period of the soil column
T_B	corner periods of elastic response spectrum EC8
T_C	corner periods of elastic response spectrum EC8
T_D	corner periods of elastic response spectrum EC8
T_n	natural period of SDOF system
T_s	fundamental period of the soil column
$T_{bot,max}$	Skin resistance at pile bottom
$T_{top,max}$	Skin resistance at pile top
V_b	equivalent shear force acting on SDOF system

$V_{i,equiv}$	equivalent shear wave velocity of a layered soil
V_p	compressional wave velocity corresponding to the seismic shear strain level
V_s	velocity of the shear waves (SH waves)
V_{s0}	shear wave velocity at small strains
$V_{s0,30}$	average value of shear waves velocity, at small strains, in the upper 30m of the soil column
W	maximum strain energy in one hysteresis loop
ΔW	dissipated energy in one hysteresis loop

Small Greek letters

α_R	Rayleigh coefficient
α	Newmark coefficient
β	Newmark coefficient
β_E	factor for the correlation of Young's modulus and strength of jet grouting material
β_R	Rayleigh coefficient
δt	duration of the dynamic (seismic) input record
γ	shear strain
γ_0	amplitude of the harmonic shear strain
γ_c	shear strain amplitude in one hysteresis loop or cyclic shear strain
γ_{eff}	effective shear strain
γ_{equiv}	equivalent unit weight for one soil improvement cell
γ_H	numerical dissipation parameter
γ_I	importance factor of structures in EC8
γ_{col}	unit weight of the the columns
γ_{EP}	bulk unit weight of the embedded pile
γ_{sat}	bulk unit weight of soil b ground water table
γ_{soil}	unit weight of the soil
γ_{unsat}	bulk unit weight of soil above ground water table
ε_{30}	strain at 30% of the failure stress
ε_{70}	strain at 70% of the failure stress
$\varepsilon_1^{\,p}$	major principal plastic strain in the formulation of shotcrete model
$\varepsilon_3^{\,p}$	minor principal plastic strain in the formulation of shotcrete model
ε^{cr}	creep strain
$\varepsilon_\infty^{\,shr}$	final shrinkage strain
$\varepsilon_{cf}^{\,p}$	plastic failure strain in uniaxial compression
ε_{cp}	total peak strain
$\varepsilon_{cp}^{\,e}$	elastic strains
$\varepsilon_{cp}^{\,p}$	plastic peak strain in uniaxial compression
$\varepsilon_{cu}^{\,p}$	plastic residual strain in uniaxial compression
$\varepsilon_{tu}^{\,p}$	plastic ultimate strain in uniaxial tension
λ_{min}	minimum wavelength

v	Poisson's ratio
v_{ur}	Poisson's ratio for unloading/reloading
ξ	damping ratio
ξ_m, ξ_n	target damping ratio for calculation of Rayleigh Dumping coefficient
η	soil viscosity
η_d	damping correction factor of structures in EC8
ρ	density of material
ρ_s	soil density
ρ_d	dry density of material
σ	stress
σ_1, σ_2, σ_3	major, intermediate and minor principle stresses
σ_{30}	stress at 30% of the failure stress
σ_{70}	stress at 70% of the failure stress
σ_t	bending tensile strength
σ_c	confining pressure / compressive stress
σ_n	reflected normal stresses at the boundary
σ_n^0	normal static stresses at the boundary of the main domain
σ_n^m	reflected normal stresses at the free-field boundary condition
σ_t	tensile strength
$\sigma_{T,B}$	Brazilian tensile strength
σ'_{xx}	horizontal effective stress
σ_{zx}	shear stress in x-z plane
τ	shear stress
τ_c	shear stress amplitude in one hysteresis loop
τ^0	tangential static stresses at the boundary of the main domain
φ	friction angle of soil or cement-based material
φ'	effective friction angle of soil
φ^{cr}	ratio between creep and elastic strains
φ_k^{cr}	non-linear creep effect
φ_{max}	maximum friction angle of shotcrete
ω	frequency of a harmonic load
ω_n	natural frequency / angular frequency
ω_s	natural circular frequency of the SDOF system
ψ	dilatancy angle
ϕ_{max}	maximum aggregate size
ϕ_n	phase angle

1 Introduction

1.1 Motivation

Ground improvement methods such as jet grouting or deep soil mixing techniques have proven to be efficient for improving the mechanical behaviour of soft grounds. Jet grouting and deep soil mixing are widely used as an attractive method in the field of ground improvement to increase bearing capacity, shear strength and reduce settlements of soft soils. These methods can be implemented as single columns, or by overlapping columns a block, slab, wall, grid or any other desired shape of improvement can be constructed (Figure 1). Some of the main applications of these ground improvement methods can be summarized as sealing the bottom of deep excavations (against uplift pressure), improving the foundation of road embankments, settlement control (e.g. foundation of wind turbines), underpinning and liquefaction mitigation.

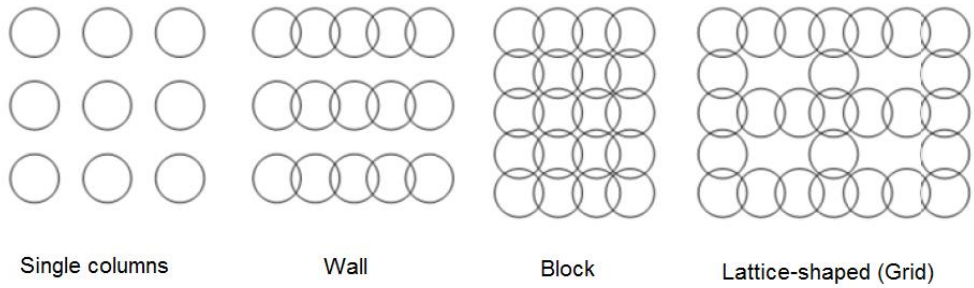

Fig. 1: Various improvement types with deep soil mixing (after Topolnicki 2004)

Although the design of ground improvement techniques is essentially based on empirical rules, numerical methods are frequently employed not only to assess the deformation behaviour of these elements, but also to evaluate the stress distribution in the treated soils. One of the key elements in numerical analysis is the constitutive model employed for describing the mechanical behaviour of the materials. Simple elastic-perfectly plastic failure criteria are often applied in practice for modelling the behaviour of improvement elements (in numerical analysis volume elements or structural elements like plates and embedded piles with linear elastic or elastic-perfectly plastic material model are often used). However, these criteria cannot capture the important aspects of the mechanical behaviour of ground improvement materials, like time dependency of strength and stiffness, also when the maximum compression and tensile strength is

reached. In addition, it should be emphasized that in general, jet grouting or deep soil mixing materials are not reinforced and considered as brittle materials. Therefore, either significant engineering judgement is required to interpret the results, or the parameters of the model have to be changed manually during the numerical analysis to take into account e.g. the development of cracks or evolution of stiffness/ strength with time. In order to design these types of ground improvement methods in a safe and economical manner, a robust constitutive models is required, which is able to take into account the various aspects of the mechanical behaviour of aforementioned materials.

As mentioned earlier, soil improvement techniques are primarily employed in order to improve bearing capacity or reduce settlements of foundations on soft soils under static loading. However, ground improvement techniques such as soil-cement mixing or jet grout columns can be used as earthquake resistant elements in the field of geotechnical earthquake engineering. This improvement may alter the seismic response of natural soft soil deposit subjected to strong motions. On the other hand, the site classifications (ground type) can be also changed due to improvement and consequently has an influence on the maximum design acceleration of surface structures, which is generally not discussed and taken into account in the design codes such as Eurocode 8 (EC8). Furthermore, as these cement-based columns/grids are not generally reinforced, crack occurrence during an earthquake is one of the other important points, which must be taken into account. Defining the possible crack zones, also the orientation of the crack can provide useful information for an optimum design.

1.2 Outline of thesis

The focus of this research is first to introduce the recently developed user defined constitutive model for Plaxis software, the so-called “Shotcrete model” and its capability to capture the most important aspects of cement-based materials. Second, it is attempted to present the application of this model to solve various problems in the field of geotechnical engineering. Therefore, simple examples together with some case studies in both static and dynamic conditions are modelled using Plaxis 2D and 3D codes. In addition, a part of this thesis focuses on ground response analysis of improved soil deposits by means of stiff elements.

Chapter 2 presents the new advanced constitutive model applied for the purpose of this thesis. First of all, a short description about the history of developing constitutive models for concrete or cement-based materials are given and then input parameters and some features of the new model so-called shotcrete model are briefly discussed.

Chapter 3 presents an overview of properties of cement-based materials, which is used for ground improvement e.g. jet-grouting and cement-treated soils. In addition, dynamic properties of these materials are discussed. Finally using some available laboratory tests data, the capability of the new constitutive model for simulating the behaviour of cement-based materials is validated. Calibration of the model is demonstrated by back-calculation of experimental results.

Chapter 4 presents the results of numerical analyses of a deep excavation where a jet-grout slab was executed at the bottom of a deep excavation to resist against uplift pressure. The influence of the various modelling assumption and input parameters are discussed. Finally, another case study in which deep soil mixing columns are installed in rows (in interaction with a sheet pile wall) to support the excavation is investigated, to show the ability of the model to define the locations and orientation of tension cracks.

Chapter 5 gives a brief introduction about the history and the method of performing ground response analysis. The cyclic loading of soil and the way of modelling dynamic soil behaviour for ground response analysis are discussed. Some expressions, which are used for the purpose of this thesis, will also be explained in this chapter. At the end of this chapter, some important points and considerations that must be taken into account when performing a numerical dynamic analysis will be discussed.

Chapter 6 presents some primary dynamic analyses in which the influence of the various input parameters of the shotcrete model on crack patterns inside jet grout columns (used as earthquake resistant elements), are investigated. In addition, some shortcomings of the new constitutive model in dynamic analysis are discussed via a simple model.

Chapter 7 presents the results of numerical dynamic analyses by means of the finite element method where the effect of jet-grouting columns on ground response of improved homogeneous and layered soil deposits is discussed. The influence of improvement width, depth and geometry on ground response is investigated. Application of a lattice-shaped improvement on ground response is also presented by using a case study. In addition, it is attempted to define the possible crack zones in the improvement elements.

Chapter 8 gives the outcomes of some additional calculations are performed to verify the ground response in a condition where a concrete slab is present above the deep soil mixed (DSM) columns.

Chapter 9 gives a summary of performed work and the main findings of this thesis that is followed by the recommendations for further research. Finally, the references are listed in chapter 10.

2 Constitutive model for cement-based materials

2.1 Introduction

In order to model the mechanical behaviour of cement-based materials, some researchers have developed models based on the concepts of modelling structured soils (e.g. Gens & Nova 1993). These models are usually extensions of Cam-Clay type models (e.g. Horpibulsuk et al. 2010) or modifications of it. For instance, Arroyo et al. (2012) employed the Clay and Sand Model (CASM) developed by Yu (1998). Although this approach has proven to be successful, it is not well suited to model concrete-like materials such as jet grout and deep soil mixing because these materials behave like weak concrete where modelling of tension softening becomes important. On the other hand, some complex input parameters required for these models are hard to define properly for practical use. For this reason strength criteria based on the simple and conventional Mohr-Coulomb failure criterion with tension cut-off are preferred, and occasionally developed to include viscous effects (e.g. Kudella et al. 2003), or empirical formulations (e.g. Fang et al. 1994b) have been proposed in the past.

The constitutive model applied in this thesis to model the mechanical behaviour of ground improvement material is the same as presented in detail by Schädlich & Schweiger (2014a) for modelling the time dependent behaviour of shotcrete. Shotcrete exhibits plastic behaviour before reaching the maximum strength and material strength reduces after peak strength has been reached. A similar behaviour can be observed in other cement-based materials in the field of geotechnical engineering and ground improvement methods like jet grouting and deep soil mixing. In this chapter, a brief description of the aforementioned constitutive model is presented based on the publication from Schädlich & Schweiger (2014a) and an internal report from Schädlich and Schweiger (2014b).

2.2 A brief review on the shotcrete model

2.2.1 Model input parameters

The complete list of input parameters of the model is listed in Table 1. It should be noted that all of these parameters have to be determined for each individual project but many of them can be taken from standards and guidelines. One of the advantages of this model is that certain parameters can be switched on or off according to the particular problem being studied. This feature will be discussed

in the following, because some features of the model will not be used in the numerical calculations of this thesis.

Tab. 1: Input parameters of the model (Schädlich & Schwiger 2014b)

Parameter	Description	Unit
E_{28*}	Young's modulus of cured sample at $t_{hydr.}$	stress
ν	Poisson's ratio	--
$f_{c,28}$	Uniaxial compressive strength of cured sample at t_{hydr}	stress
$f_{t,28}$	Uniaxial tensile strength of cured shotcrete at t_{hydr}	stress
ψ	Dilatancy angle	°
φ_{max}	Maximum friction angle	°
E_1/E_{28}	Time dependency of elastic stiffness	--
$f_{c,1}/f_{c,28}$	Time dependency of strength	--
f_{c0n}	Normalized initially mobilised strength	--
f_{cfn}	Normalized failure strength (compression)	--
f_{cun}	Normalized residual strength (compression)	--
ε_{cp}^{p}	Uniaxial plastic failure strain at 1h, 8h, 24h	--
$G_{c,28}$	Compressive Fracture Energy of cured sample at t_{hydr}	force/length
f_{tun}	Ratio of residual vs. peak tensile strength	--
$G_{t,28}$	Tensile Fracture Energy of cured sample at t_{hydr}	force/length
a	Increase of ε_{cp} with increase of p'	
φ^{cr}	Ratio between creep and elastic strains	--
t_{50}^{cr}	Time for 50% of creep strains	time
$\varepsilon_{\infty}^{shr}$	Final shrinkage strain	--
t_{50}^{shr}	Time for 50% of shrinkage strains	time
$t_{hydr.}$	Time for full hydration (**usually 28 days**)	time

*28days is normally considered for concrete/shotcrete materials, but this value can vary according to a desired curing time e.g. 90, 120, 200days.

2.2.2 Yield surface and strain hardening/softening

The calculation of plastic strains is according to strain/hardening softening elastoplasticity. A Mohr-Coulomb yield surface F_c in deviatoric loading and the Rankine yield surface F_t in the tensile zone are utilized (Figure 2). It must be mentioned that compression has negative notation in the formulation of this model.

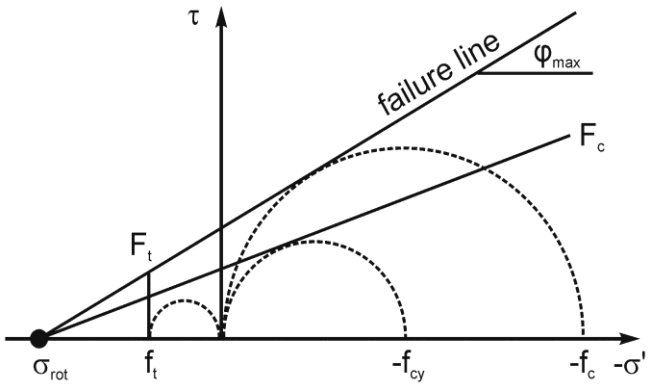

Fig. 2: Yield surface and failure envelope (Schädlich & Schweiger 2014b)

2.2.2.1 The model behaviour in compression

A quadratic hardening behaviour up to the maximum compressive strength is assumed, followed by a bi-linear softening until residual level is reached (Figure 3). The change in ductility is represented by a time dependent plastic strains ε_{cp}^{p} at t=1h, 8h and 24h which is assumed to be constant beyond 24h. Due to time dependency of the material parameters a normalised hardening/softening parameter $H_c = \varepsilon_3^p / \varepsilon_{cp}^p$ is used, where ε_3^p = minor principal plastic strain and ε_{cp}^p = plastic peak strain in uniaxial compression. The stress-strain behaviour in compression is divided into four parts. In part I, according to a quadratic function the uniaxial yield stress f_{cy} is mobilised with H_c as follows:

$$f_{cy,I} = f_c \cdot \left(f_{c0n} + (1 - f_{c0n}) \cdot \left(2H_c - H_c^2 \right) \right) \tag{1}$$

where f_{c0n} is the ratio of f_{cy} / f_c.

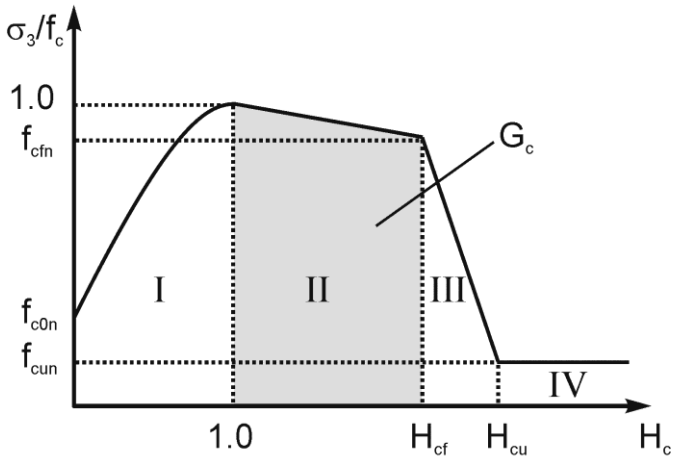

Fig. 3: Normalized stress-strain curve in compression (Schädlich & Schweiger 2014b)

In hardening, the yield surface F_c rotates about the anchor point σ_{rot} on the isotropic axis until reaching the failure line. $H_c = 1$ shows full mobilization of f_c, after which bilinear softening takes place, until $H_{cf} = \varepsilon_{cf}^p / \varepsilon_{cp}^p$ where the failure strength $f_{cf} = f_{cfn} \cdot f_c$ is reached. In compression softening it is assumed that the reduction of strength is due to destruction of inter particle bonds and therefore softening can be modelled by means of cohesion softening and a parallel shift of the failure envelope.

$$f_{cy,II} = f_c \cdot \left(1 + \left(f_{cfn} - 1\right) \cdot \left(\frac{H_c - 1}{H_{cf} - 1}\right)\right) \tag{2}$$

ε_{cf}^p is calculated using the fracture energy in compression, G_c, and the characteristic length of the finite element, L_{eq}:

$$\varepsilon_{cf}^p = \varepsilon_{cp}^p - \frac{2 \cdot G_c}{\left(1 + f_{cfn}\right) \cdot f_c \cdot L_{eq}} \tag{3}$$

L_{eq} is related to the size of the finite element, A_{el}, and the number of gauss points per element, n_{GP} (Pölling 2000) which provides the necessary regularization to avoid mesh dependent numerical results.

$$L_{eq} = 2\sqrt{\frac{A_{el}}{\sqrt{3}\cdot n_{GP}}} \tag{4}$$

The plastic ultimate strain ε_{cu}^{p} in part III is calculated as follow:

$$\varepsilon_{cu}^{p} = \varepsilon_{cf}^{p} - \frac{2 f_c \cdot \left(f_{cfn} - f_{cun}\right)}{E} \tag{5}$$

Residual strength level $f_{cun} = f_{cu} / f_c$ and E = elastic Young's modulus. The yield stress f_{cy} follows as

$$f_{cy,III} = f_c \cdot \left(f_{cfn} + \left(f_{cun} - f_{cfn}\right) \cdot \left(\frac{H_c - H_{cf}}{H_{cu} - H_{cf}} \right) \right) \tag{6}$$

where $H_{cu} = \varepsilon_{cu}^{p} / \varepsilon_{cp}^{p}$. No softening occurs in part IV of the stress strain curve, when:

$$f_{cy,IV} = f_c \cdot f_{cun} \tag{7}$$

To account for an increase of ductility with increasing confining pressure (i.e. the total peak strain $\varepsilon_{cp} = \varepsilon_{cp}^{p} + \varepsilon_{cp}^{e}$ increases with confining pressure), an input parameter "*a*" is introduced.

$$\varepsilon_{cp} = \varepsilon_{cp,UC} \cdot \left(1 + a \cdot \frac{\sigma_1}{-f_c} \right) \tag{8}$$

Please note that in the notation of the model, σ_1 is the confining pressure in a triaxial compression test.

2.2.2.2 The model behaviour in tension

The model behaviour in tension is linear elastic until the tensile strength f_t is reached. Linear strain softening follows, governed by the normalized tension softening parameter $H_t = \varepsilon_1^p / \varepsilon_{tu}^p$ where ε_1^p = major principal plastic strain and ε_{tu}^p = plastic ultimate strain in uniaxial tension (Figure 4).

$$f_{ty} = f_t \cdot \left(1 + \left(f_{tu,n} - 1\right) \cdot H_t\right) \tag{9}$$

ε_{tu}^p is derived from the fracture energy in tension G_t, and the characteristic length of the finite element L_{eq}, Similar to compression softening L_{eq} is calculated from the size of the finite element A_{el}, and the number of stress points per element, n_{GP}.

$$\varepsilon_{tu}^p = \frac{2 \cdot G_t}{\left(1 + f_{tun}\right) \cdot f_t \cdot L_{eq}} \tag{10}$$

When the residual strength $f_{tu} = f_{tun} \cdot f_t$ is reached, no further softening occurs.

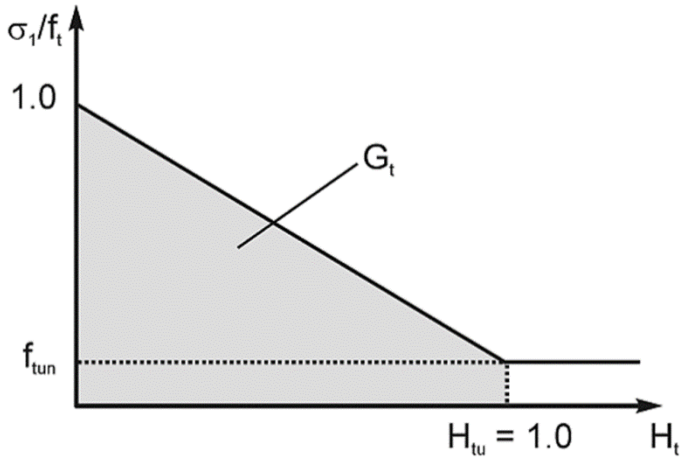

Fig. 4: Normalized stress-strain curve in tension (Schädlich & Schweiger 2014b)

H_t equal to zero means the value of the tensile stress is below or equal to F_t, $0<H_t<1$ describe the softening zone and $H_t>1$ indicates the residual level. By plotting the H_t values between zero and one, it is possible to show the crack locations.

2.2.3 Time dependency of stiffness and strength

The Stiffness strength of cement-based material increases with time due to the hydration of cement paste. In this model, the development of Young's modulus with time follows the recommendation of CEB-FIP model code (1990) as shown in Figure 5.

$$E(t) = E_{28}.e^{S_{stiff}\cdot(1-\sqrt{t_{hydr}/t})} \tag{11}$$

Where S_{stiff} governs the evolution of stiffness with time as

$$S_{stiff} = -\frac{\ln(E_1/E_{28})}{\sqrt{t_{hydr}}-1} \tag{12}$$

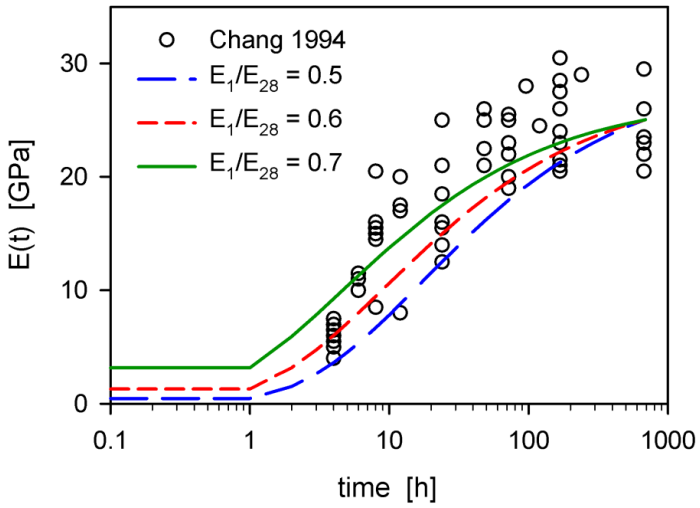

Fig. 5: Increase of Young's modulus with time (Schädlich & Schweiger 2014b)

A similar approach is used for the evolution of strength of cement-based materials with time. Figure 6 compares the evolution of f_c according to the shotcrete early strength classes (J1, J2 and J3) of EN 14487-1 (2006) with the CEB-FIP model code (1990) Formulation for concrete with $f_{c,28}$=25 MPa. More detail about the increase of shotcrete strength with time can be found in Schädlich & Schweiger (2014a). The parameter $S_{strength}$ governs the evolution of strength with time.

$$f_c(t) = f_{c,28}.e^{S_{strength}\cdot(1-\sqrt{t_{hydr}/t})} \tag{13}$$

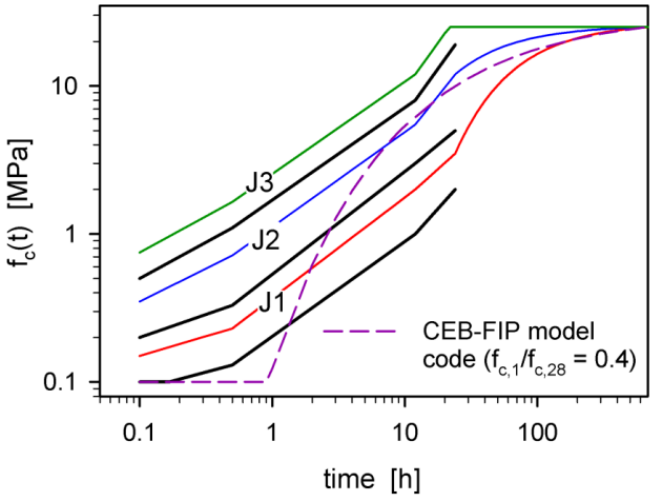

Fig. 6: Increase of strength with time (Schädlich & Schweiger 2014b)

When the ratio of E_1/E_{28} and f_1/f_{28} is equal to one, then time dependency of stiffness and strength is not considered and the value of Young's modulus and uniaxial compressive strength is equal to the input parameters for specified curing time.

2.2.4 Creep

In this model using a viscoelastic approach, creep strains ε^{cr} increase linearly with stress σ and are related to elastic strains via the creep factor φ^{cr}.

$$\varepsilon^{cr}(t) = \frac{\phi^{cr}\cdot\sigma}{D_e}\cdot\frac{t-t_0^{cr}}{t+t_{50}^{cr}} \tag{14}$$

Where D_e, is the linear elastic stiffness matrix and σ is stress. The development of creep with time is governed by the start of loading at time (t_0^{cr}) and the parameter (t_{50}^{cr}) indicates that 50% of the creep strains have developed. Non-linear creep effect is also considered in the model for shotcrete utilization higher than 45% of uniaxial compressive strength (fc). In this regard, the φ^{cr} is replaced by $\varphi_k^{cr} = \varphi^{cr}.e^{1.5(\sigma_3/f_c-0.45)}$ (Schädlich & Schweiger 2014a).

2.3 Performing dynamic calculations

It has to be mentioned that this constitutive model has not been intended to be used in dynamic analyses and therefore only the initiation of cracks can be reliably assessed but not the behaviour thereafter because a multiple sequence of crack opening/closing is not correctly modelled.

2.4 Summary

With the new shotcrete model most important features of shotcrete, concrete or other type of cement-based materials can be captured including time dependency of stiffness and strength, strain hardening/softening in compression and tension in addition to creep. On the other hand, this model can provide a continuum model for studying the behaviour of ground improvement techniques in the FE-method, which may be previously modelled using structural elements like plate or embedded piles that apply an elastic or elastic-perfectly plastic material model. One of the shortcomings of this model is that only the initiation of cracks can be reliably assessed in dynamic analysis.

3 Properties of cement-based material

In this chapter, first the most important parameters of cement-based materials (especially jet-grouting materials) are discussed. These parameters like stiffness, uniaxial compressive strength, tensile strength, failure strains and fracture energy in compression and tension, are to some extent uncertain and affect the numerical results. Then the capability of the proposed model to simulate the behaviour of cement-based materials in addition to parameters calibration based on laboratory test data are presented. In order to have a comprehensive view on the various aspects of the behaviour of cement-based materials, the dynamic properties of various treated soils are discussed as well.

The methods of implementation and installation process of different soil improvement techniques are beyond the scope of this study and the emphasis is only on the features and material behaviour. It is acknowledged that the installation process may have an influence on the material behaviour e.g. in jet grouting, when single, double or triple method of execution is used.

3.1 Material properties

The mechanical behaviour of jet-grouting, deep soil mixing and other type of cement-treated soils have been studied and published by many researchers (e.g. Bell & Burke 1992, Croce et al. 2014, Fang et al. 1994a, Nikbakhtan & Ahangari 2010, Nikbakhtan et al. 2010, van der Stoel 2001, Kudella et al. 2003, Kitzume & Terashi 2013, Porbaha 1998). Some important parameters of these materials will be discussed herein and an overview is provided about the practical range of these parameters which will be utilized in numerical analyses later in this thesis:

3.1.1 Density

In practice, when using single and triple-fluid systems it can be assumed that the jet-grouted material has a unit weight roughly equal to untreated soil while with the double-fluid system, slightly lower unit weights are obtained (see Figure 7) because of the bubbles of compressed air entrapped in the final jet grout matrix (Croce et al. 2014). However, it depends on soil conditions and can be changed and improved by newer technologies.

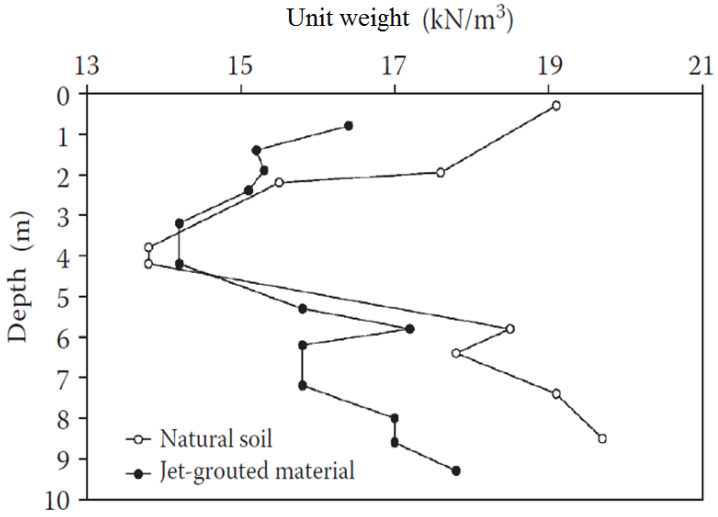

Fig. 7: Unit weight of the natural soil and jet-grouted material for single fluid jet grouting (Croce et al. 2014)

3.1.2 Uniaxial compressive strength

The uniaxial compression test is one of the most common tests for describing the quality of concrete and cement-based materials. The uniaxial compressive strength (q_u) of jet grouting is strongly related to the dry unit weight (γ_d), and this relation depends on natural soil type (Figure 8). It is accepted and experimental data prove that the increase in both dry unit weight and uniaxial compressive strength is related to the increase in depth of sampling (Croce & Flora 1998). Generally, higher values of compressive strength for jet grouting in coarse-grained soils with high cement contents has been reported while in fine grained soils, even for high cement content lower strength has been obtained.

In addition, the uniaxial compressive strength q_u depends on the execution methods (e.g. single, double or triple fluid systems) and cement–water ratio. This is also confirmed by the experimental results reported by van der Stoel (2001). Figure 9 shows the influence of cement-water ratio on the uniaxial compressive strength of single-fluid jet grouted sandy soils. It can be seen that by increasing the water content the compressive strength is decreasing. One another important factor is curing time that has to be taken in to account.

Defining specific values for uniaxial compressive strength of jet grouting materials is difficult, but according to literature, typical average values for fine grain soils (Peat, clay and silt) are in a range of 1-10MPa and for coarse grain soils, a range between 5 to 30 MPa is proposed (van der Stoel 2011, Bell 1992, Nikbakhtan et al. 2010).

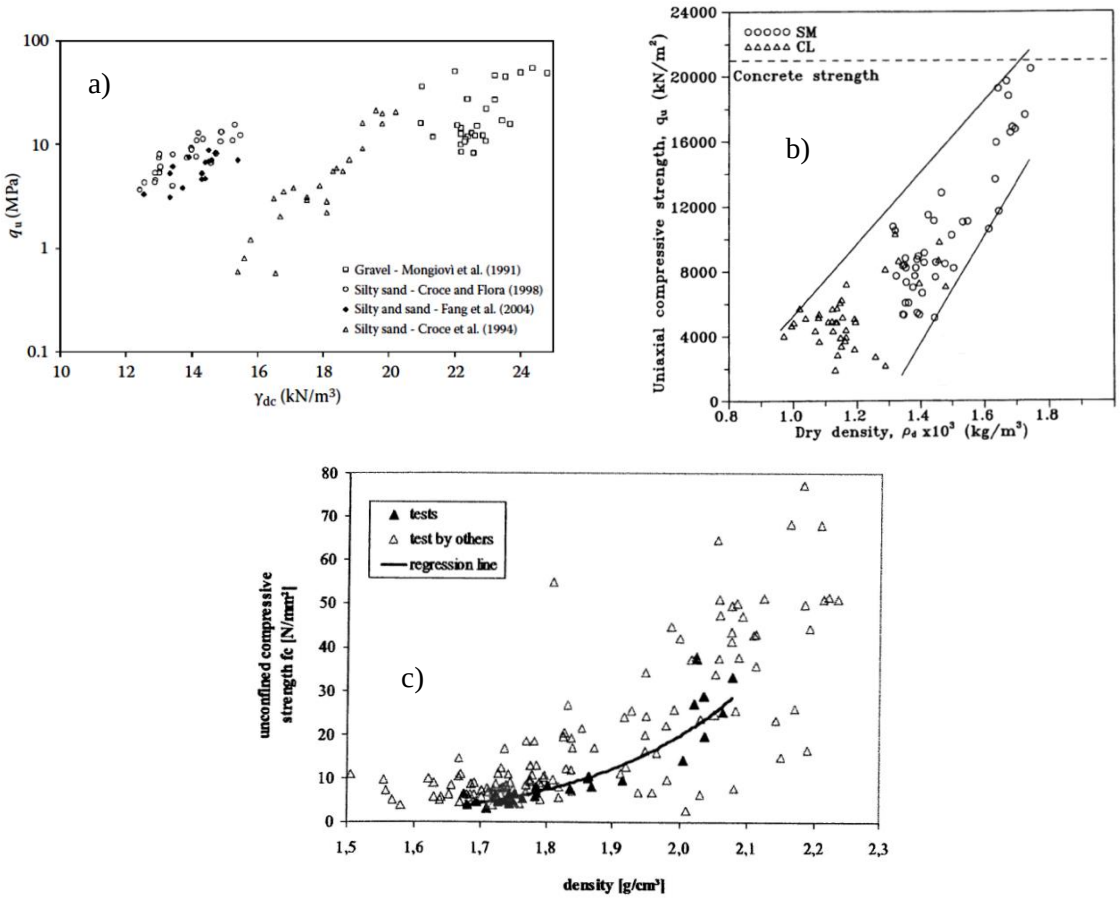

Fig. 8: Relation of uniaxial compressive strength of jet-grouting material with dry density; a) Croce et al. 2014; b) after Fang et al. 1994b; c) Kudella et al. (2003)

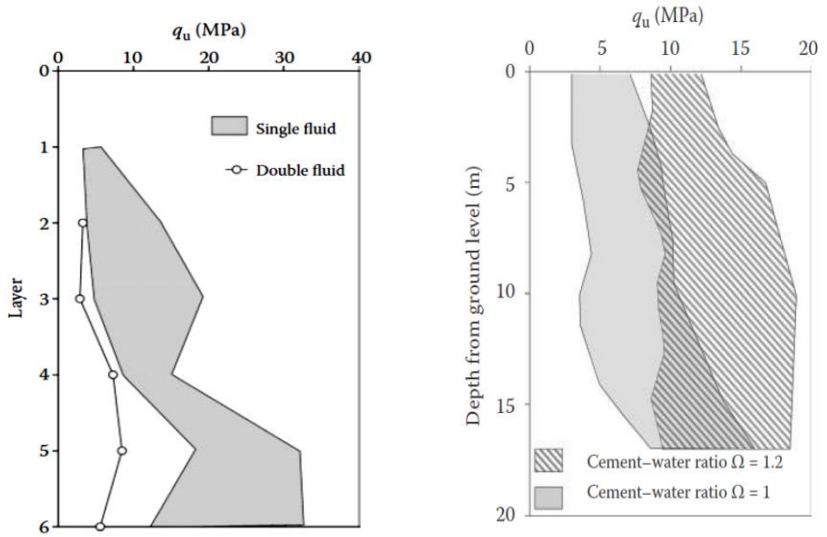

Fig. 9: a) Influence of single and double fluid jet grouting on unconfined compression strength (Croce et al. 2014); b) effect of water to cement ratio on the uniaxial compressive strength (Croce et al. 2014)

3.1.3 Failure Strains

Figure 10 depicts that the failure strain increases with increasing dry density. However, it is significantly higher in presence of confining pressure. For dense jet-grouted materials, the stress-strain behaviour has an axial failure strain 0.2-0.3% like concrete. The value of the failure strain can also be influenced by presence of micro cracks in the samples.

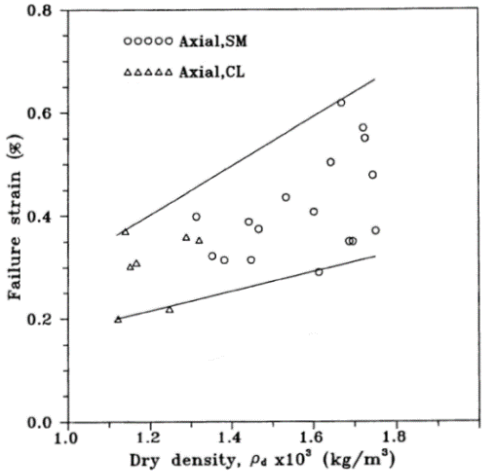

Fig. 10: Failure strain vs jet grout density (after Fang et al. 1994a)

Figure 11 shows the failure strain of stabilized marine clay with both lime and cement. It can be seen that the failure strain of the cement-treated samples is in the range of 1-4%, which is much smaller compared to the typical range of non-treated clayey soils.

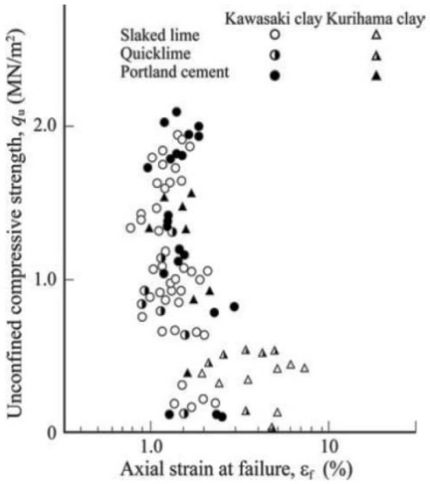

Fig. 11: Failure strain of stabilized soil (Terashi et al. 1990)

3.1.4 Tensile Strength

In order to define the tensile strength of cement-based materials usually three types of laboratory are used:

- Direct tension test
- Split tension test (Brazilian test and indirect tension test)
- Bending test (usually three/four point bending test)

The value of tensile strength is influenced by the test procedure. For example in simple direct tension test always, a large scatter in the results is reported.

Brazilian test generally overestimate the direct tensile strength of concrete, but for mortar, usually underestimation was observed (Neville 1997). Van der Stoel (2001) via Brazilian test reported the tensile strength ($f_{ct,sp}$) for sandy and clayey jet grouting samples, and suggested an empirical formula in terms of uniaxial compressive strength (Figures 12 and 13).

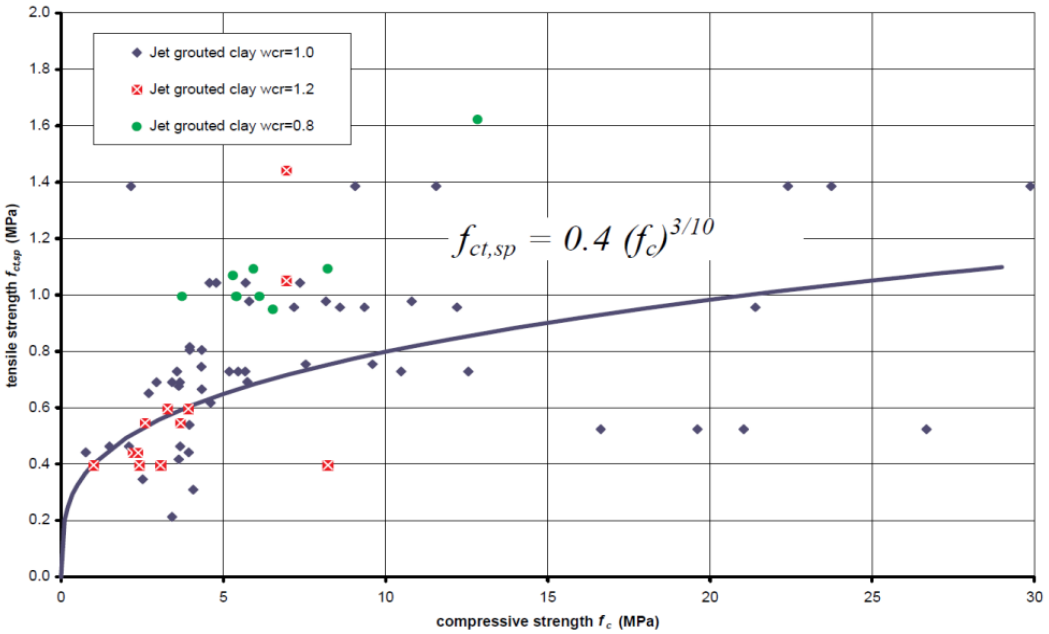

Fig. 12: Tensile strength vs uniaxial compressive strength for clayey jet grouting samples (van der Stoel 2001)

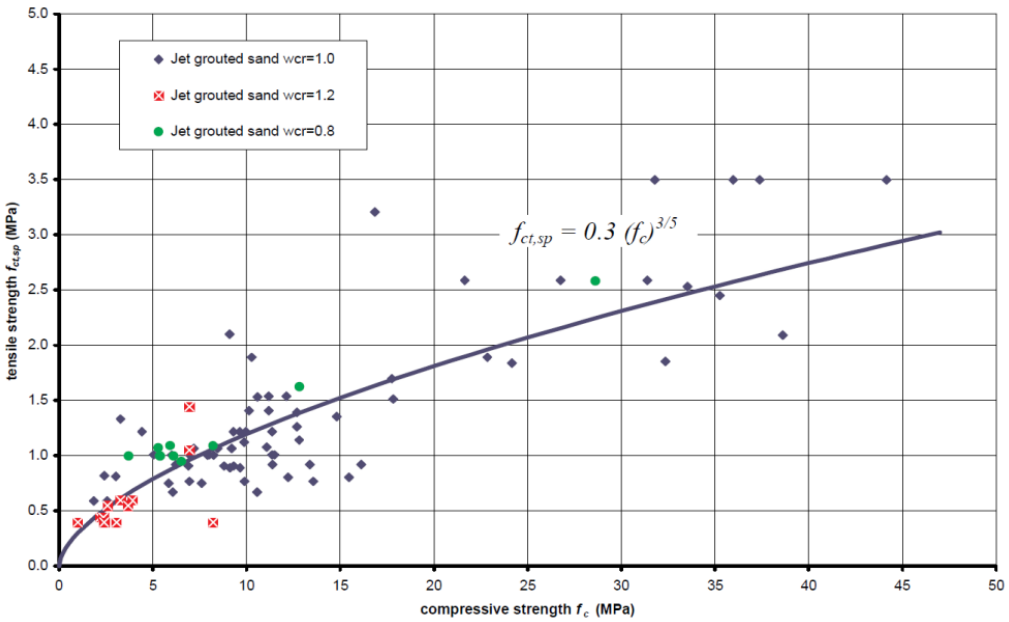

Fig. 13: Tensile strength vs uniaxial compressive strength for sandy jet grouting samples (van der Stoel 2001)

Fang et al. (1994b) has published the Brazilian test data against dry density, which indicates an increase in tensile strength with increasing in dry density. In addition, the value of tensile strength for sandy soilcrete is higher compared to clayey soilcrete (Figure 14).

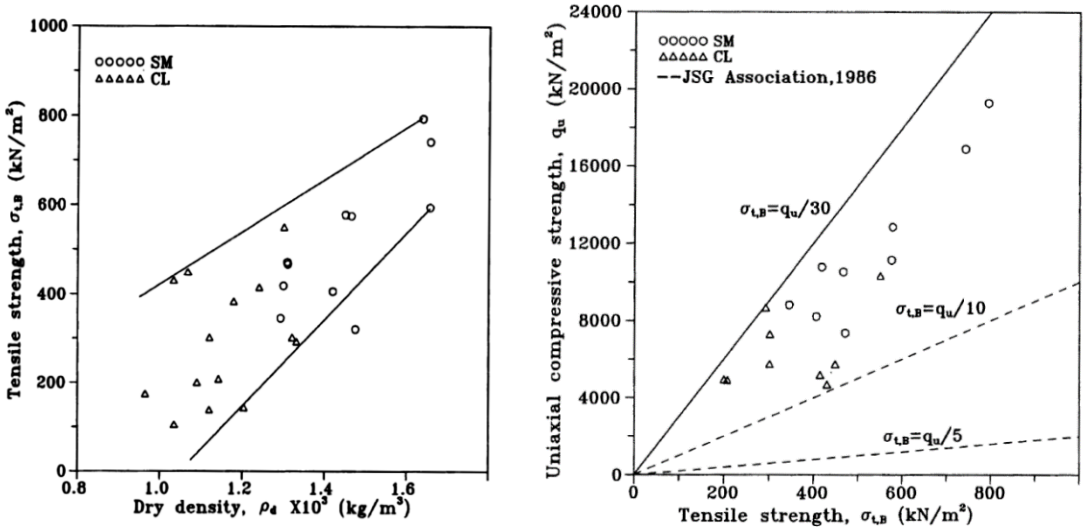

Fig. 14: Relation between tensile strength and dry density and uniaxial compressive strength (Fang et al. 1994a)

Tariq & Maki (2015) presented the results of splitting tension test and three point bending test on the cement-treated sand samples and compared the them with the suggested tensile strength value for the concrete (Figure 15). As it can be seen in Figure 16 the values of bending test are smaller, compared to splitting test.

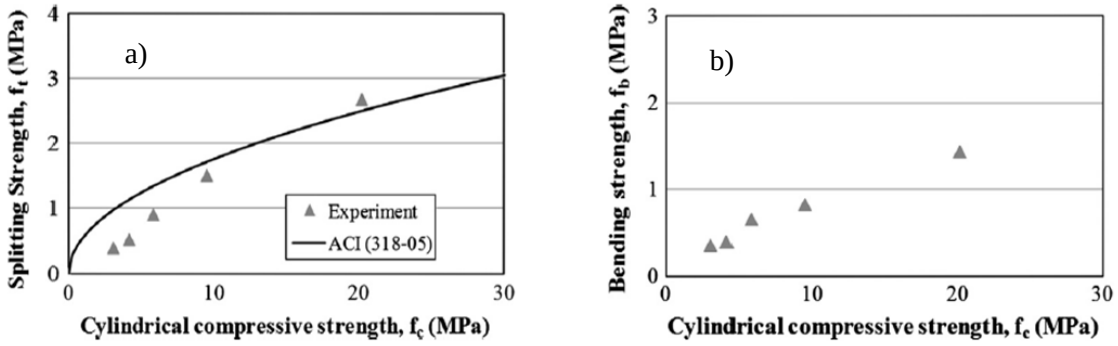

Fig. 15: Variation of tensile strength with compressive strength a) Splitting test; b) Bending test, (Tariq & Maki 2015)

For clayey materials stabilized with lime or cement, different behaviour was obtained by researchers. Kitzume & Terashi (2013) reported that the splitting tensile strength (σ_t) has almost a linear relation with unconfined compressive strength (q_u) irrespective to binder type, but its ratio becomes lower with increasing q_u (Figure 16a). Figure 16(b) shows that the bending tensile strength (σ_b) is in range of 0.1 to 0.6 of the unconfined compressive.

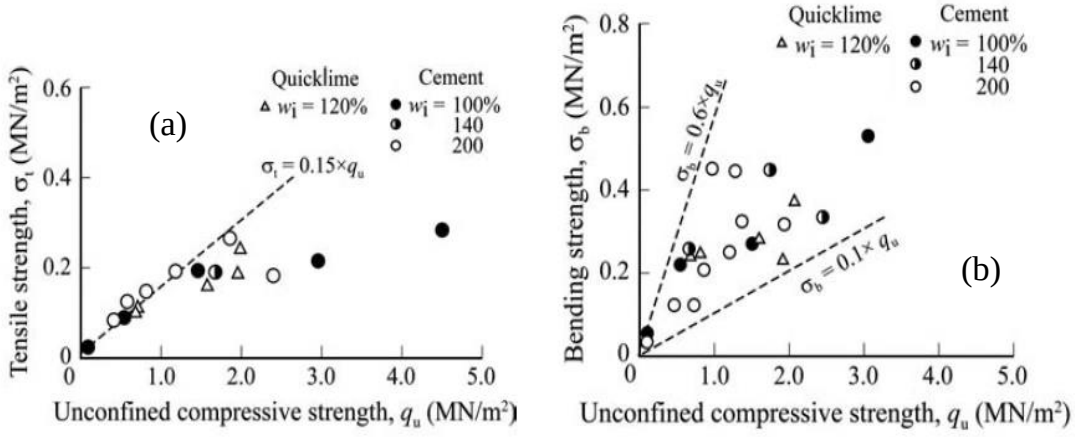

Fig. 16: Tensile strength against unconfined compressive strength; a) split tension test, b) bending test (Kitzume & Terashi 2013)

According to DIN 4093:2012-08 the tensile strength can be estimated to 10% of the design value of uniaxial compressive strength $f_{m,d}$ (Figure 17).

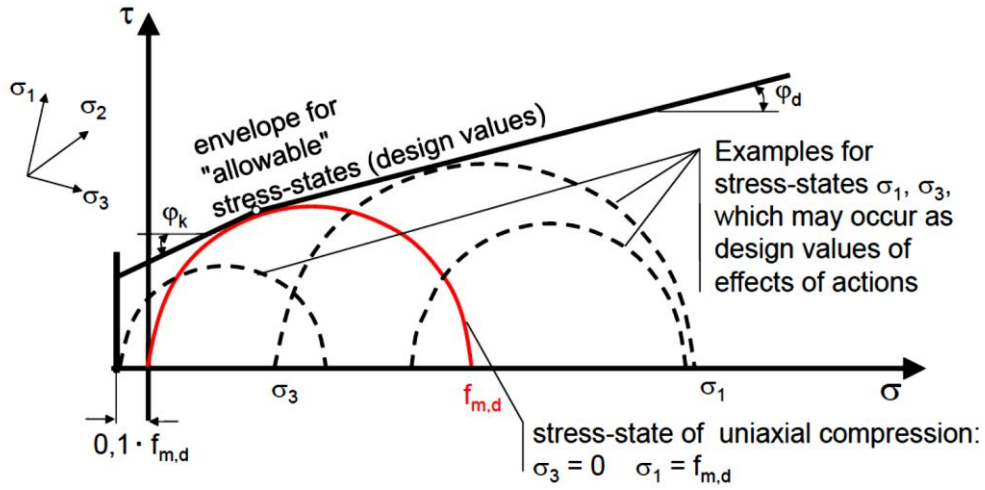

Fig. 17: Acceptable zone of tensile strength for jet grout material (DIN 4093:2012-08)

3.1.5 Modulus of elasticity

The Young's modulus of jet-grouting materials can be obtained via uniaxial or triaxial compressive test in laboratory. Different relation between stiffness and uniaxial compressive has been reported. van der Stoel (2001) attempted to provide the relation between compressive strength and Young's modulus (E_{cm}) of jet-grouted sand and clay soils (Figures 18 and 19). The Secant or Young's modulus is defined as:

$$E_{cm} = \frac{\sigma_{70} - \sigma_{30}}{\varepsilon_{70} - \varepsilon_{30}} \tag{15}$$

where σ and ε are the stress and strain at either 30% or 70% of the failure stress during testing of the sample respectively

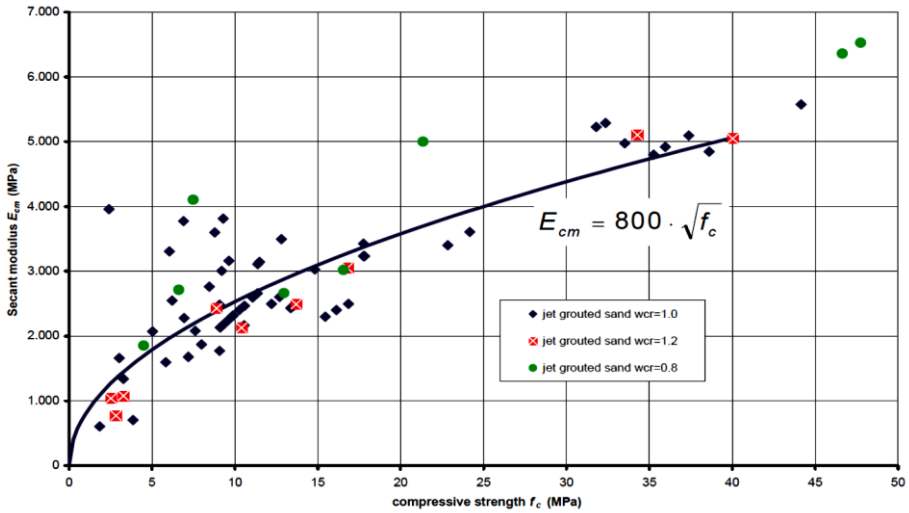

Fig. 18: Young's modulus E_{cm} vs. compressive strength f_c for jet-grouted Sand layers (van der Stoel 2001)

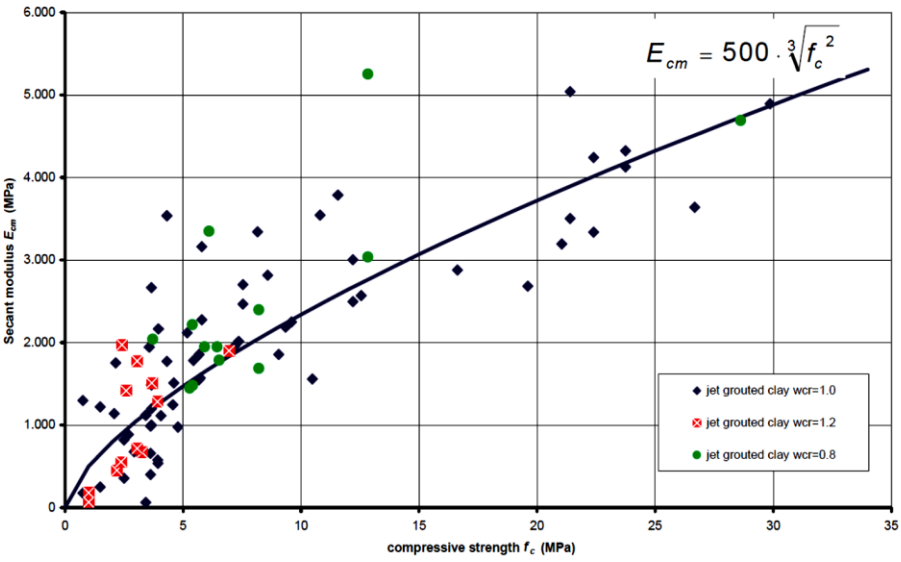

Fig. 19: Young's modulus E_{cm} vs. compressive strength f_c for jet grouted clay layers (van der Stoel 2001)

Figure 20 present the variation of E_{t50} (tangent modulus at 50% of q_u) with dry density and the relation between uniaxial compressive strength of the jet grouting materials in sand and clay and compared it with the suggestion of Jumbo-jet Special Grout (JSG) association of Japan.

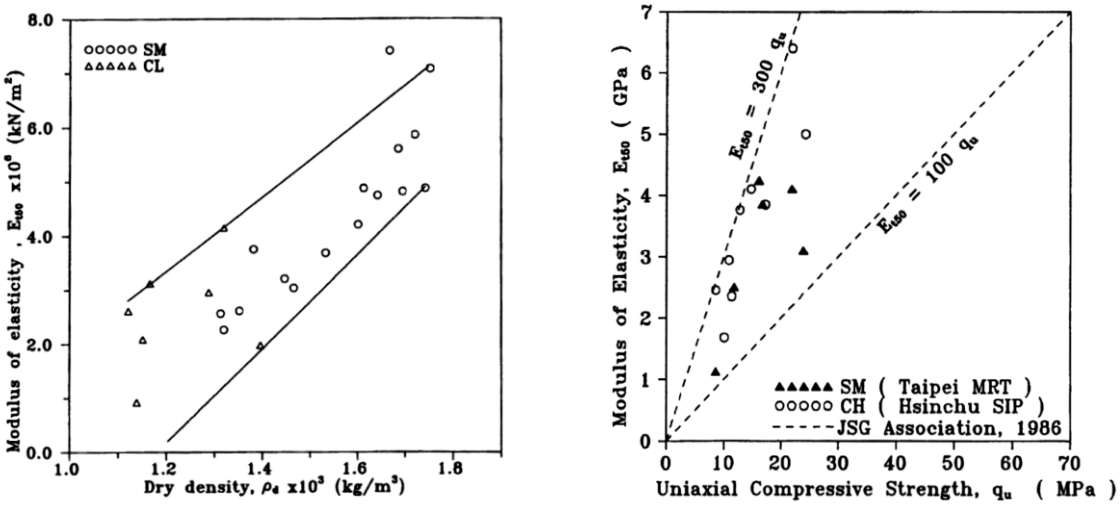

Fig. 20: Relation of modulus of elasticity with dry density and uniaxial compressive strength: Fang et al. 1994b (left); Fang et al. 1994a (right)

Figure 21 presents the results of laboratory cement stabilized clay and sandy silts from Niina et al. (1981) which was reported by Kitzume & Terashi (2013). A linear relation of E_{50} (E_{50} is the secant modulus of elasticity in a stress–strain curve at half of the unconfined compressive strength, q_u) with the q_u is observed.

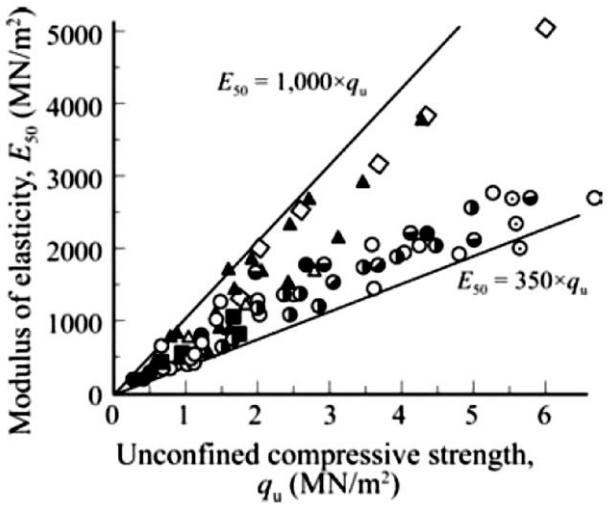

Fig. 21: Modulus of elasticity of cement-stabilized soils (Niina et al. 1981)

Figure 22 presents the correlation of Young's modulus and strength using a simple linear relation ($E_{50}=\beta_E * q_u$) which is collected by Croce et al. (2014).

Reference	*Definition of E*	*Soil type*	β_E
Mongiovì et al. (1991)	Tangent unspecified	Gravel	280–1000
Lunardi (1992)	Secant at 40% q_u	Gravel and sand	500–1200
Nanni et al. (2004)	Tangent unspecified	Gravel and sand	440–1000
Croce et al. (1994)	Tangent unspecified	Sandy gravel	210–670
Croce and Flora (1998)	Secant at ε_a = 0.01%	Silty sand	220–700
Nanni et al. (2004)	Tangent unspecified	Silty sand	330–830
Fang et al. (2004)	Tangent at 50% of the failure stress	Silty sand	300–750
Fang et al. (2004)	Tangent at 50% of the failure stress	Silty sand, silty clay	100–300
Lunardi (1992)	Secant at 40% q_u	Silt and clay	200–500

Fig. 22: Relationship between Young moduli and uniaxial compressive strength of jet-grouted material (Croce et. al 2004)

It must be emphasised that defining the relation between unconfined compressive strength and stiffness depend on many factors such as curing time and the ratio of water to cement and the quality of the sample. Since this value is uncertain and may change in a wide range, for designing purposes it is recommended to verify the influence of various stiffness values on the calculation results. For example, Borchert et al. (2013) examined the deflection of a jet-grout slab under uplift pressure and also the maximum shear stresses at the connection of diaphragm wall and slab by variation of slab stiffness in the range of 5-20GPa.

3.1.6 Shear strength parameters

In practice, the shear strength of jet grout materials can be expressed with Mohr-Coulomb criterion or with the simple Tresca criterion ($\tau=c=q_u/2$). The results of many triaxial tests on jet-grouted samples published by Croce & Flora (1998), Fang et al. (2004), Bzowka (2009) exhibit a linear trend in the *t-s* plane ($t=(\sigma_1-\sigma_3)/2$, $s=(\sigma_1+\sigma_3)/2$) at their analysed stress levels (0.5-10 MPa) which suggest that the assumption of a linear failure envelope can be suitable in practice. The friction angle and the cohesion of jet grouting materials can be easily obtained via triaxial test for design purposes. Figure 23 shows the Mohr-coulomb failure parameters resulted from a number of case studies.

Reference	Soil type	φ_T (°)	c_T (MPa)
Bzòwka (2009)	Sandy	58.2	2.3
Croce and Flora (1998)	Silty sand	26.1	3.2
Mongiovì et al. (1991)	Gravel	52.0	2.1
Mongiovì et al. (1991)	Gravel	42.0	0.3
Mitchell and Katti (1981)	Clay	39.5	0.58
Yahiro et al. (1982)	Sand and clay	28.5	0.4–1.0
Miki (1982)	Various	20–30	0.7–1.0
Yu (1994)	Clay–silty sand	40.6	1.1
Fang et al. (1994a)	Silty sand	35	4.2
Fang et al. (1994b)	Clay–silty sand	40–44	4.2
Fang and Chung (1997)	Clay and silty sand	38.6	0.8
Fang et al. (2004)	Silt and sand	38.7	0.7
Nikbakhtan and Osanloo (2009)	Clay and sand	42–49	0.4–0.8
	Clay and sand	25	0.77

Fig. 23: Mohr-coulomb parameters from different case studies (Croce et al. 2014)

Defining a specific range for the cohesion and friction angle of jet-grouted samples in various soils is difficult. There is a large scatter in the published results, which can be attributed to irregularities in grout and the testing methods, sample condition and natural soil properties. It is also conservative to use the friction angle of a jet-grouted sandy soil equal to the friction angle of the natural soil. This can be explained by the fact that jetting method used the compressed air which can entrapped as gas-filled voids in the final matrix and once the cement bridges are broken, the cemented granular skeleton is in a critical density. There is no dilatancy and therefore not more than the critical friction angle of the sandy aggregates (e.g. Kudella et. al 2003 and Borchert et al. 2013).

3.1.7 Fracture energy

One important material parameter in the softening part of the stress-strain curves of concrete or cement-based materials is fracture energy in both compression and tension. The post peak behaviour of concrete material and specially the fracture energy (in some references it is called specific fracture energy) determination in tension has been extensively studied (e.g. Petersson 1980, Barros & Figueiras 1999, Karihaloo et al. 2003, Chen & Liu 2004, Cifuentes et al. 2013). The values of fracture energy in tension have been reported mostly for concrete material based on the results of the three point bending test (or simple direct tension test), but for jet grouting materials not much data is available and therefore further investigations are required. The fracture energy of concrete and cement treated soils are discussed herein in two sections.

3.1.7.1 Tensile fracture energy

The mechanical interaction of the aggregates with the cement-based matrix essentially governs the fracture energy and strain softening (Wittmann 2002). Figure 24 indicates the influence of maximum aggregate size on the fracture energy. The lowest fracture energy is measured on pure hardened cement paste and the highest value is observed in dam concrete. The influence of maximum aggregate size (ϕ_{max}) on fracture energy between them can be described by a power function from Trunk & Wittmann 1998 as follows.

$$G_f = a\phi_{\max}^{n} \tag{16}$$

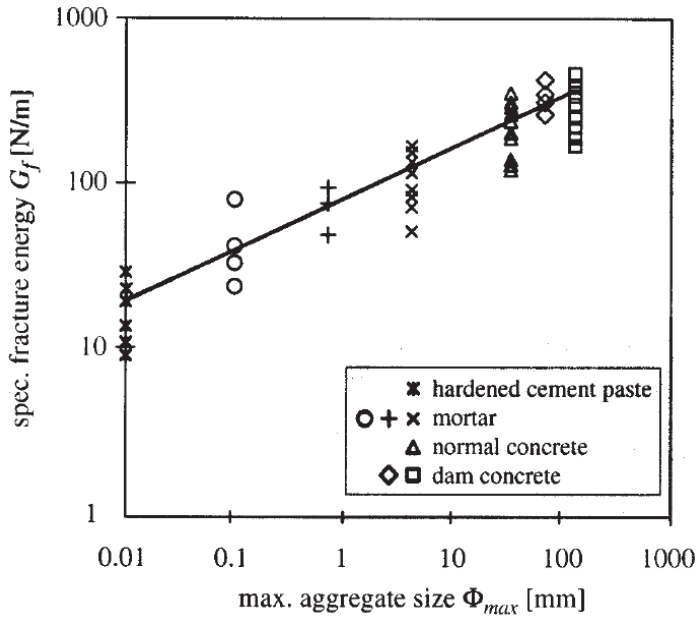

Fig. 24: Specific fracture energy of cement-based materials as function of maximum aggregate size (Wittmann, 2002)

According to the Japan concrete institute (JCI 2003), this parameter can be estimated in terms of maximum aggregate size (d_{max}) and characteristic compressive strength (f_{ck}) as follows:

$$G_f = 10(d_{\max})^{1/3} f_{ck}^{1/3} \tag{17}$$

Figure 25 denotes the relation between fracture energy, compressive strength and the aggregate size of concrete according to JCI (2003).

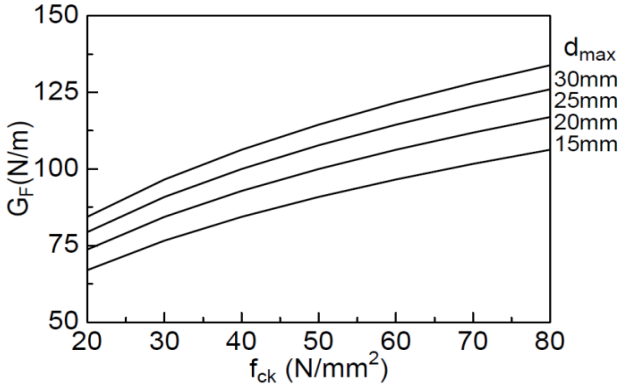

Fig. 25: Relation of fracture energy with compressive strength and aggregate size (JCI 2003)

Generally, in literature this value revealed to be in the rage of 75 N/m to 250N/m for normal and high strength concrete.

Tariq & Maki (2015) found out that the tensile fracture energy is very small even for high strength cement-treated sand compared with concrete material because of the absence of coarse particles (Figure 26). A similar result was obtained by Namikawa & Koseki (2006) on cement-treated sands.

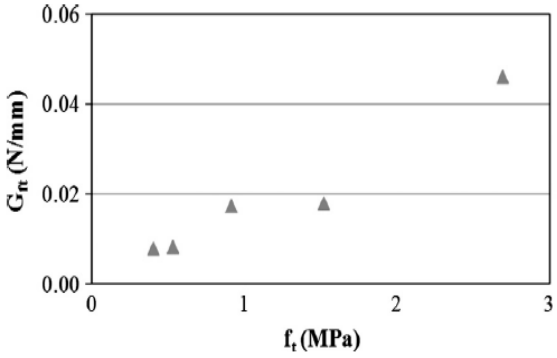

Fig. 26: Variation of fracture energy with splitting tensile strength (Tariq & Maki 2015)

3.1.7.2 Compression fracture energy

Tariq & Maki (2015) denoted the energy absorbed per unit area within fracture zone length as compression fracture energy as it seen in Figure 27.

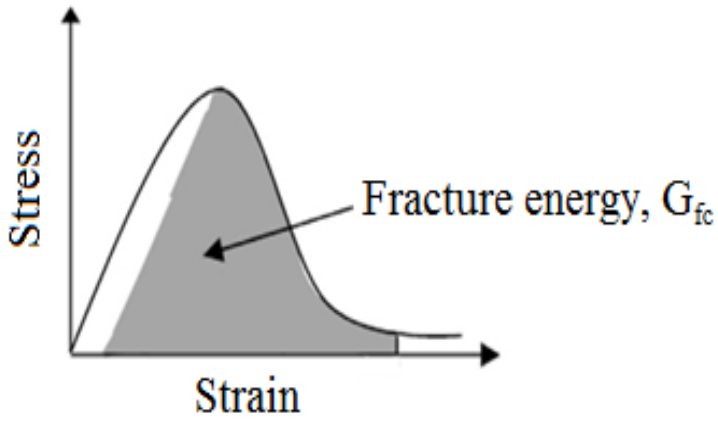

Fig. 27: Schematic representation of uniaxial compressive test and fracture energy concept

Nakamura & Higai (2001) defined the relation between the uniaxial compressive strength f_c and compression fracture energy (G_{fc}) of concrete as follows:

$$G_{fc} = 8.8\sqrt{f_c} \tag{18}$$

Based on laboratory test results Tariq & Maki (2015) showed that the compressive fracture energy increases with the compressive strength via a non-linear relation (Figure 28). They proposed an equation to estimate the compressive fracture energy as follows:

$$G_{fc} = 3\sqrt{f_c} \tag{19}$$

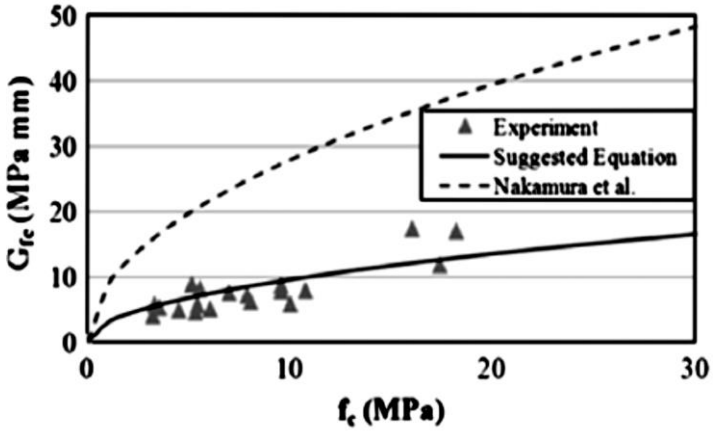

Fig. 28: Variation of fracture energy in compression with the compressive strength (Tariq & Maki 2015)

Tariq & Maki 2015 also investigated the relation between compressive and tensile fracture energy of cement-treated sand and revealed that fracture energy in compression has a linear relation with tensile fracture energy (Figure. 29).

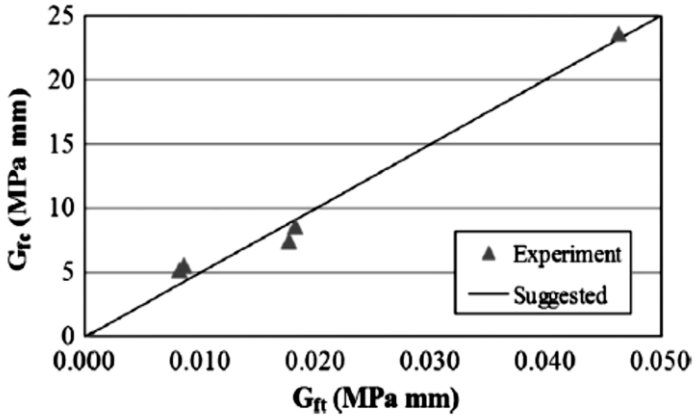

Fig. 29: Relation between the compressive fracture energy and the tensile fracture energy (Tariq & Maki 2015)

There are still no accurate data available for the fracture energy in tension or compression of jet grouting, deep soil mixing and other type of cement-based material. Therefore, for calculations purposes it is reasonable to evaluate the influence of various fracture energy values. However choosing smaller values gives results that are more conservative.

3.1.8 Poisson's ratio

Poisson's ratio of cement-based materials obtained by laboratory tests generally shows a range between 0.15 and 0.3 (Fang et al. 1994b, Kitzume & Terashi 2013). Figure 30 indicates the variation of Poisson ratio of jet-grouted sand and clay, which are close to concrete material.

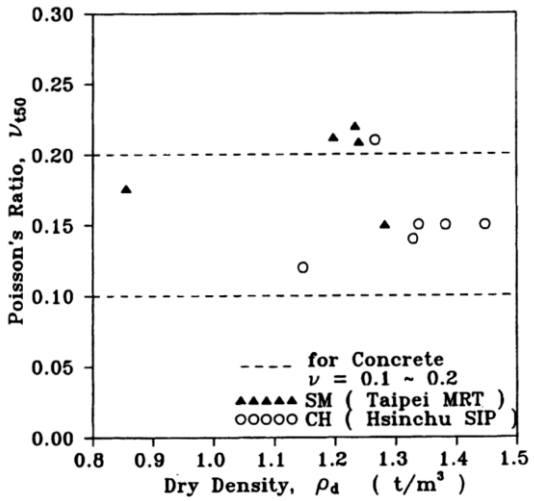

Fig. 30: Poisson's ratio vs dry density (Fang et al. 1994b)

3.2 Parameter calibration of new constitutive model

In this section, the capability of the constitutive model described in chapter two, to capture the behaviour of cement-based materials is investigated. With the exception of "φ_{max}" and "a" (see table 1) all required parameters can be derived from uniaxial compression test, three point bending test (or direct tension test) and creep and shrinkage test. The simulations include the development of stiffness and strength with time, stress-strain curves of cement-based materials e.g., jet grouting or cement-mixed soils both in uniaxial compressive strength test (UCS) and triaxial consolidated drained test. In addition, simulation of a three point bending test on a cement-treated sand sample and a creep test of jet grout material are presented.

It should be noted that there are still not sufficient laboratory data available on jet-grouted materials in particular with respect to curing time, triaxial testing and three point bending testing in order to arrive at a very accurate set of parameters for such materials.

3.2.1 Time dependency of strength and stiffness

As described in chapter two, time dependent evolution of strength and stiffness can be considered for any desired curing time in this model. Generally, for concrete and jet grouting material 28 days will be considered. The input Parameters E_1/E_{28} and F_1/F_{28} can be calibrated with available experimental data. Figures 31 and 32 show the evolution of stiffness and strength with time for jet-grout materials. The result of the model was compared with the empirical equations proposed by Coulter & Martin (2006). A large difference is seen between the results of the model and the experiments. The strength gain depends on the hydration process of cement paste. It seems that the hydration has small contribution to the strength of jet-grout samples in the period less than 10 hours, and maybe the cement gel is still discontinuous. However, for the parameter calibration of the model the strength/stiffness less than 1 day is not considered.

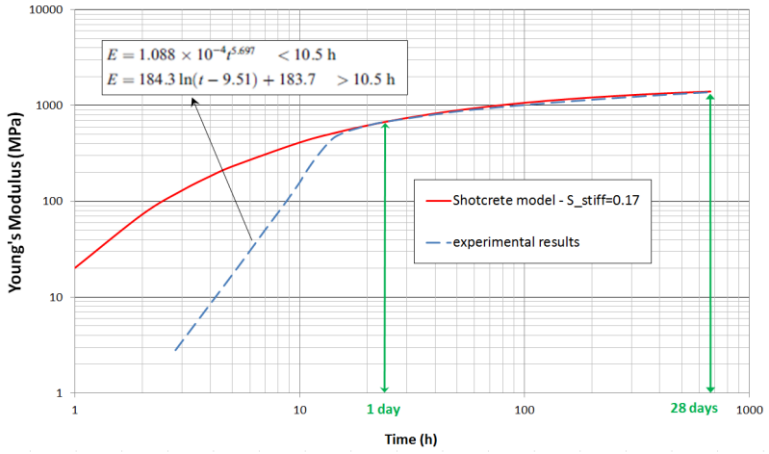

Fig. 31: Time dependency of stiffness of the jet grout material

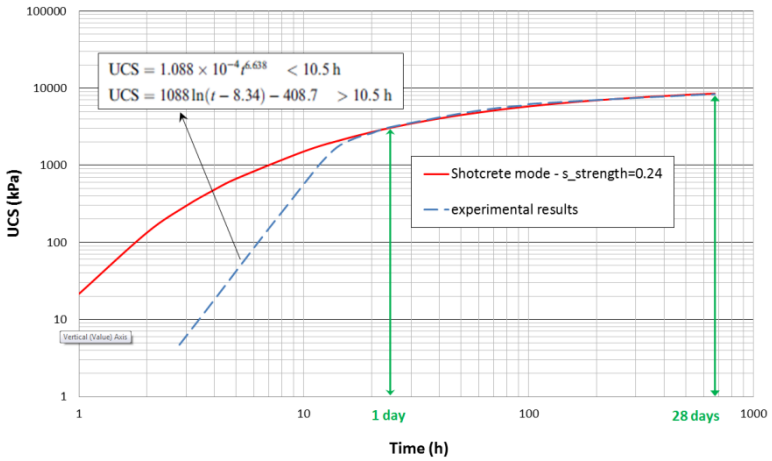

Fig. 32: Time dependency of strength of the jet grout material

3.2.2 Stress-strain curves

In order to calibrate the parameters E, f_c, ε_{cp}, $f_{c.0n}$, E_1/E_{28}, f_1/f_{28} and the parameter "φ_{max}" and "a", results of both uniaxial and triaxial tests on cured samples are required. Results of simulations prove that the uniaxial and the triaxial tests can be modelled reasonably well with this model. The match is not perfect, but generally, good agreement with experimental data could be achieved (Figures 33 and 34).

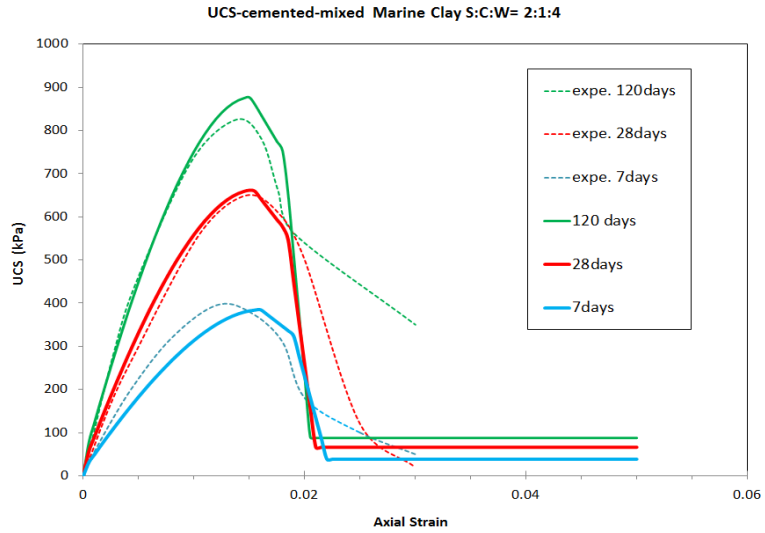

Fig. 33: Uniaxial compression test of cement mixed clay-different curing time (experiments from Xiao & Lee 2009)

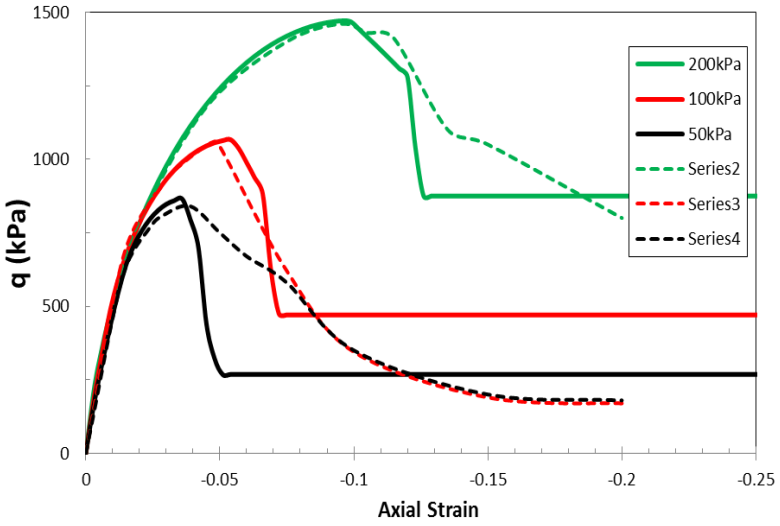

Fig. 34: Triaxial CD test on 28 days cured samples of cement mixed clay (experiments from Xiao & Lee 2009)

In addition, Figure 35 shows the results of simulations of uniaxial compressive tests of 50days cured jet-grouting samples (from the project of Bahnhof Wien Mitte). It must be pointed out that the simulations have been done on stress point level (i.e. in the Plaxis soil test tool) where an arbitrary value of the l_{eq} (which is not a correct representation for the numerical calculations of the post peak behaviour) is required for running the analysis, therefore the softening behaviour cannot be accounted for correctly. Only the general ability of the model to capture the softening behaviour can be presented. The calibration using stress point level is only valid when the compression softening is not considered in the analyses. The details of the calibration of softening parameters will be discussed later.

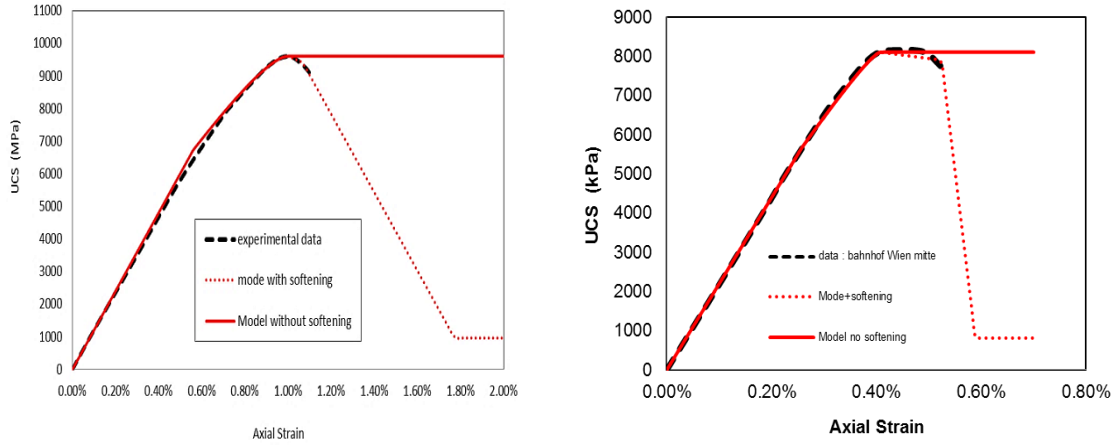

Fig. 35: UCS test on jet grout samples (experiments from Bahnhof Wien Mitte)

3.2.3 Calibration of softening parameters

3.2.3.1 Compression softening

In order to calibrate compression softening parameters i.e. G_c, $f_{c,fn}$, $f_{c,un}$ (see Table 1) 3D simulation of uniaxial compressive test with the real sample size is required. Figure 36 presents the numerical results of a uniaxial compressive strength test on a cylindrical sample of jet grouting reported by Borchert et al. (2013). The height of the sample was 22cm and in numerical calculations, a stiff plate was used on top of the samples. The input parameters for the simulation are summarized in Table 2. Two different sample heights were used to show the size effect on the results. As it can be observed that, a sample with longer height shows a different behaviour. This behaviour (i.e. size effect) is known in numerical analysis of brittle materials and has been investigated by researches

(e.g. by Karihaloo 2003). Figure 37 shows the failure zone and deformation of the samples.

Tab. 2: Model Input parameters

Jet grouting	Unit	Value
E_{28}	[kN/m^2]	15e6
ν	[-]	0.2
ψ	[°]	0
$f_{c,28}$	[kN/m^2]	8000
E_1/E_{28}	[-]	1
f_1/f_{28}	[-]	1
f_{con}	[-]	0.7
f_{cfn}	[-]	0.75
f_{cun}	[-]	0.1
ε_{cp}^{p}	[-]	-0.0005
G_{c28}	kN/m	0.4

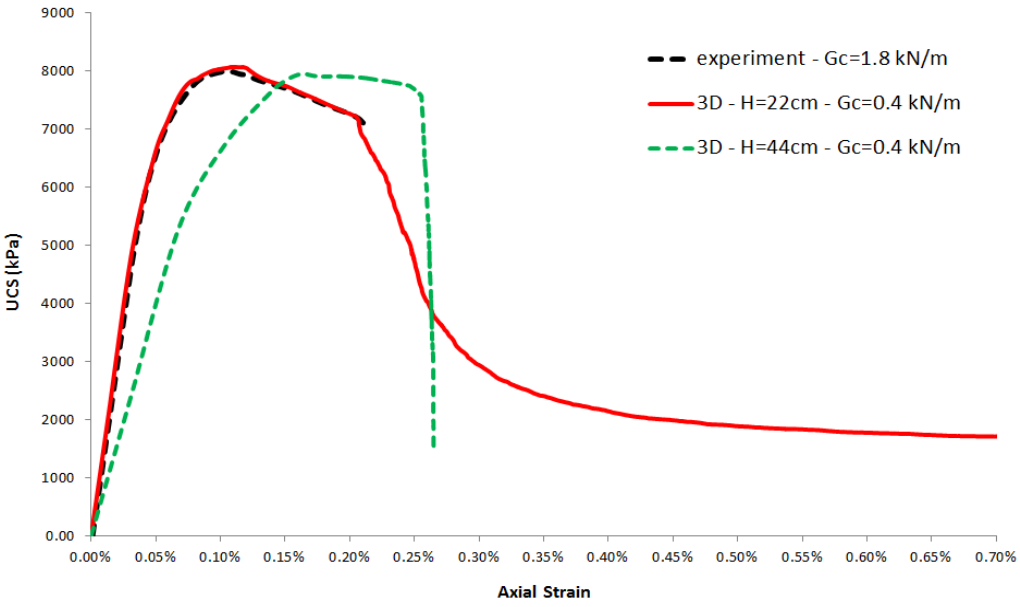

Fig. 36: Stress-strain curves obtained from numerical simulation

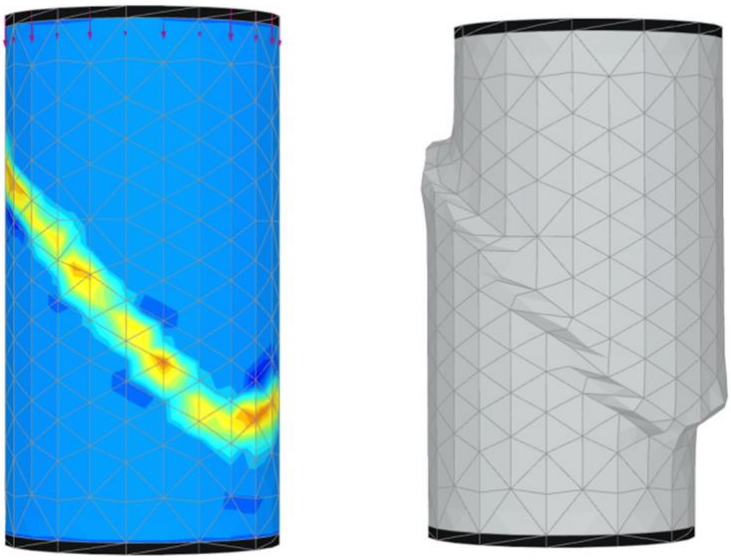

Fig. 37: Failure zone and sample deformation - Simulation of uniaxial compressive test of a jet-grouting sample

Figure 38 shows another simulation of a uniaxial test, based on the results of Kudella et al. (2003) in which the height of the sample was 101.2mm. Simulation and experimental data agree very well when G_c is taken as 0.45 kN/m.

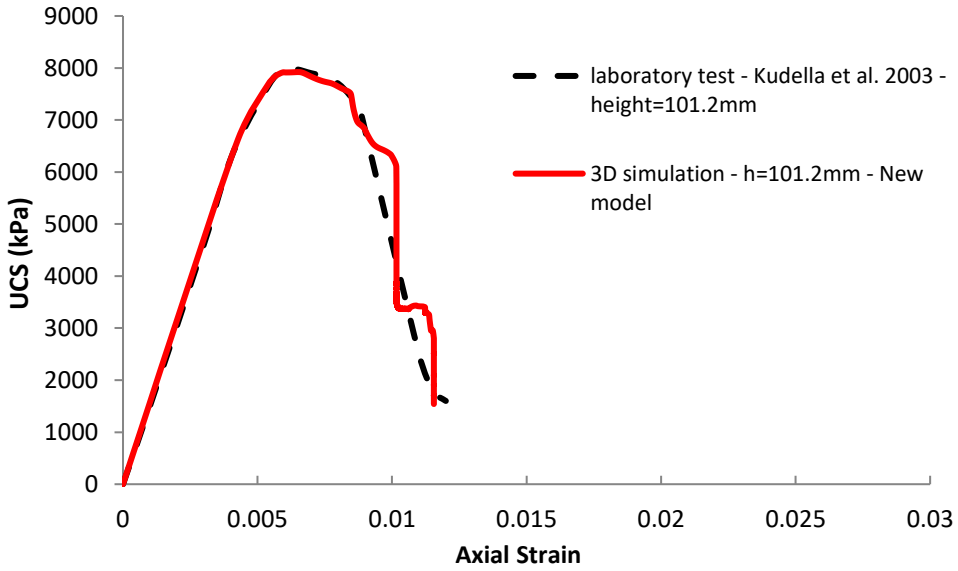

Fig. 38: Comparison of the stress-strain curves of experimental data with the numerical simulation of uniaxial compressive test

3.2.3.2 Tension softening

First, the effect of parameter G_t on the result of numerical calculations is shown qualitatively in Figure 39. A simple direct tension test on stress point level was used to present the influence of G_t on stress-strain curves. It is obvious that by increasing G_t the materials become more ductile and the softening becomes less severe. This parameter has an important role in numerical analyses where the tension softening has to be taken in to account and it can affect crack patterns.

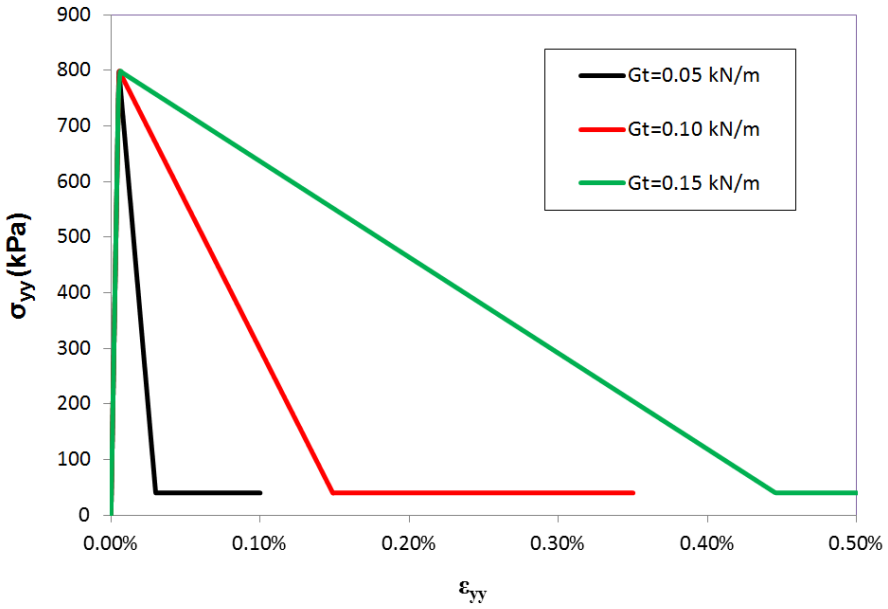

Fig. 39: Schematic stress-strain curves respect to tension softening

In order to calibrate the tension softening parameters i.e. G_t and $f_{tu,n}$, 2D simulation of three point bending test with the real sample size (height and length) has been proved to be sufficient (Schädlich & Schweiger 2014b, Witasse 2016).

Here, test results presented by Namikawa & Koseki (2006) are back analysed with the shotcrete model. They implemented three point bending tests on notched beams of cement-treated sand. Beam dimension and the FE model is shown in Figure 40. The set of material parameters, which have been adopted for this indirect tension test are summarized in Table 3. The input parameters of hardening and compression softening have no influence in tension test. It must be noted that the tensile strength of the material was reported to 380 kPa via direct tension test, which is different to the bending tensile strength and gives an incorrect estimation of the maximum tensile strength in a bending test. Therefore, a value of 300kPa is considered as the bending tensile strength in the current

analysis. In the numerical analysis, a prescribed displacement is used on top of the notched beam to apply the load.

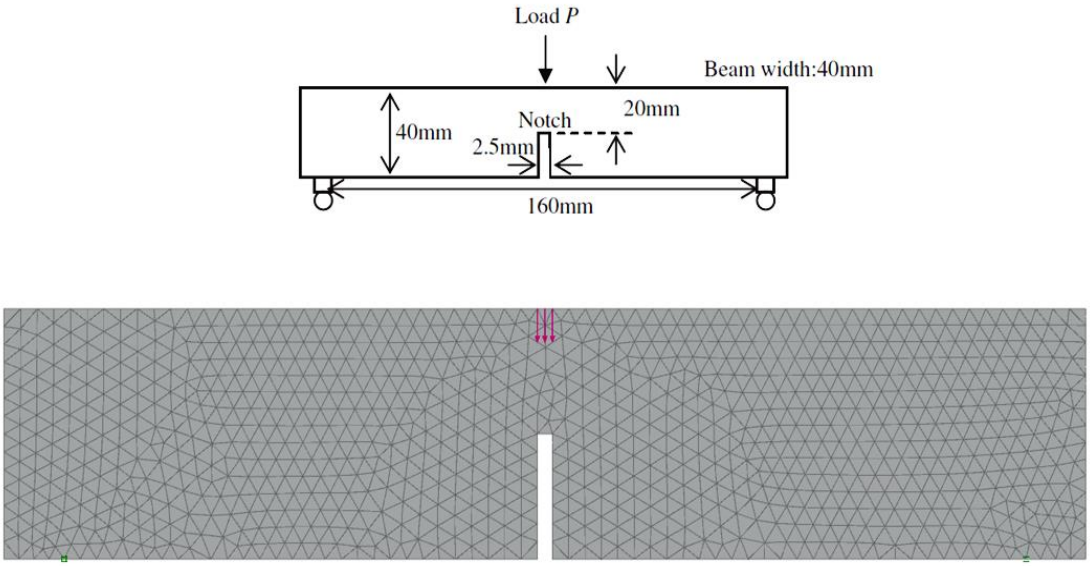

Fig. 40: Notched beam dimension and adopted FE-mesh

Tab. 3: Adopted material parameters

Jet grouting	Unit	Value
E_{28}	[kN/m^2]	3e6
ν	[-]	0.167
ψ	[°]	0
f_t	[kN/m^2]	300
E_1/E_{28}	[-]	1
f_1/f_{28}	[-]	1
f_{tun}	[-]	0
G_t	[kN/m]	0.009

The computed load-deflection curve is presented in Figure 41. The observation point is at the bottom of the beam and at the edge of the notch. In comparison with the experimental data from Namikawa & Koseki (2006), it can be concluded that there is a good match between numerical and experimental values. Figure 42 presents the contour plot of the normalised tension softening parameter (H_t) where the beam deflection was about 1.1mm. A localisation of the shear deformation above the notch is also observed.

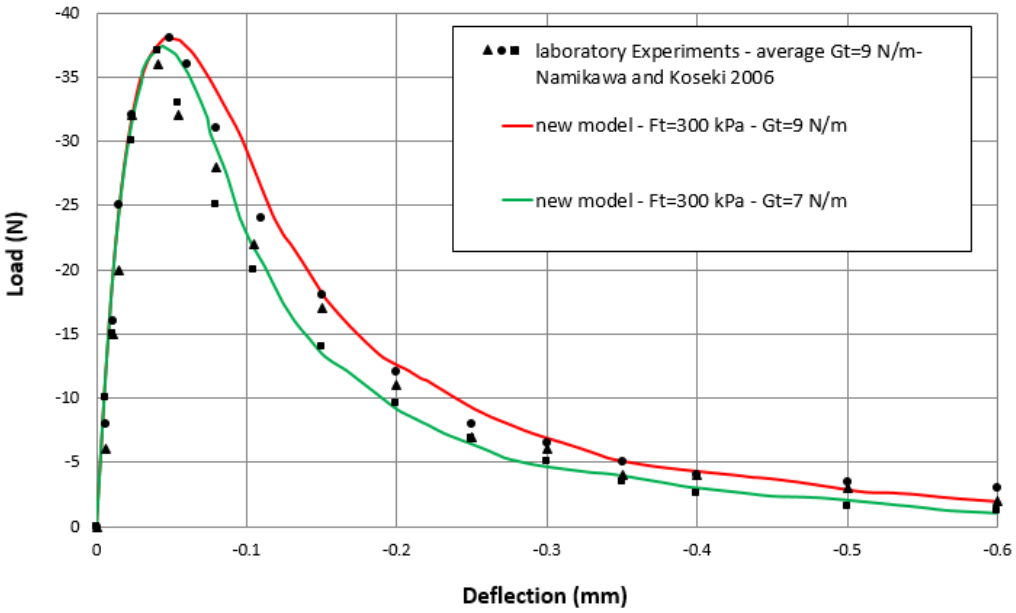

Fig. 41: Comparison of load deflection curve from experimental data and back calculations.

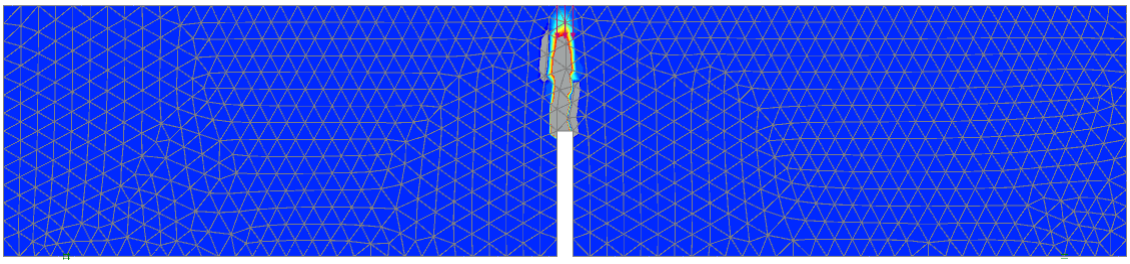

Fig. 42: Crack locations in the beam at 1.1mm deflection.

3.2.4 Creep test

Results of creep tests on jet-grouting samples published by Kudella et al. (2003) were used to check if the model is able to simulate the creep test. Two type of creep tests including uniaxial and triaxial test are simulated. The material parameter used in the shotcrete model is presented in Table 4.

The important parameter that can be calibrated with creep tests is the creep number (or creep factor φ^{cr}). The value of the creep number has been chosen according to the results of laboratory tests done by Kudella et al. (2003).

Tab. 4: Adopted parameters for creep test simulation.

Jet grouting	Unit	Value
E_{99}	[kN/m^2]	1.1 E6
ν	[--]	0.2
$f_{c,99}$	[kN/m^2]	4500
E_1/E_{99}	[-]	0.1
f_1/f_{99}	[-]	0.05
$f_{c,0n}$	[-]	0.3
ε_{cp}^{p} *1h*	[-]	-0.06
ε_{cp}^{p} *8h*	[-]	-0.03
ε_{cp}^{p} *24h*	[-]	-0.002
φ	[°]	30
φ^{cr}	[-]	0.5-2.5
$t_{50\%}{}^{cr}$	day	10
t_{hyd}	day	99

Uniaxial creep test:

The sample had an age of 67 days when the test started. The test lasted about 607 hours (26days). The creep pressure was 1.032, 2.064 and 3.095 MPa. In the simulations, the sample was cured for 67 days and then loading steps started systematically. Figure 43 presents back calculations using different values of φ^{cr}.

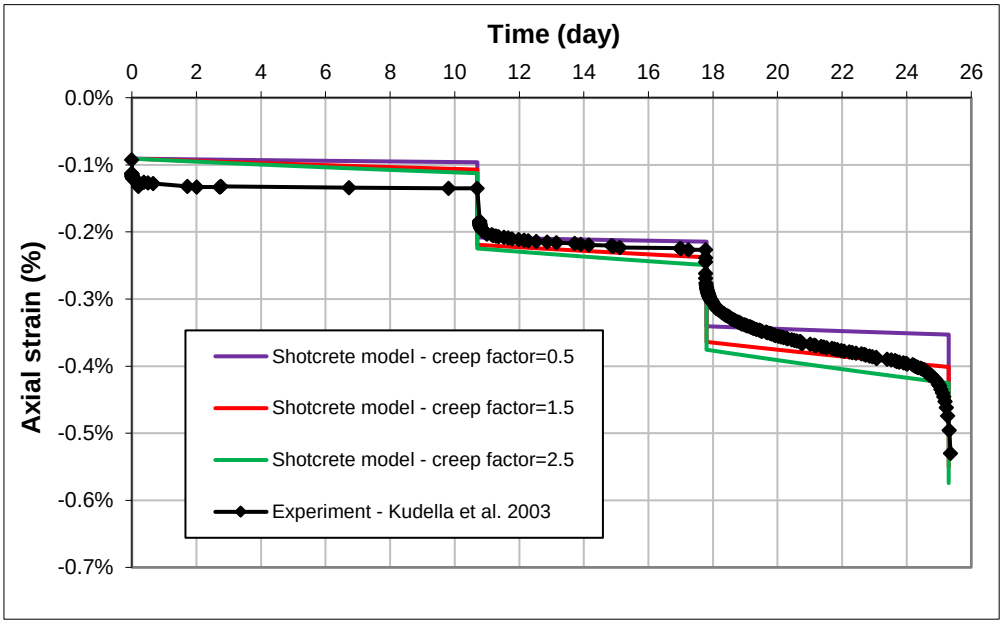

Fig. 43: Comparison of uniaxial creep test with back calculations

Triaxial creep test:

The sample had an age of 45 days when the test started. The test lasted about 54 days (1298 hours). Cell pressure is about 1MPa and creep pressures of 1.780-2.780-3.780-4.780 MPa were applied to the sample. Figure 44 shows the result of back calculations with various φ^{cr} and comparison with experimental data. The match with the experiment is not perfect but it is similar to the results of back-calculations published by Kudella et.al (2003).

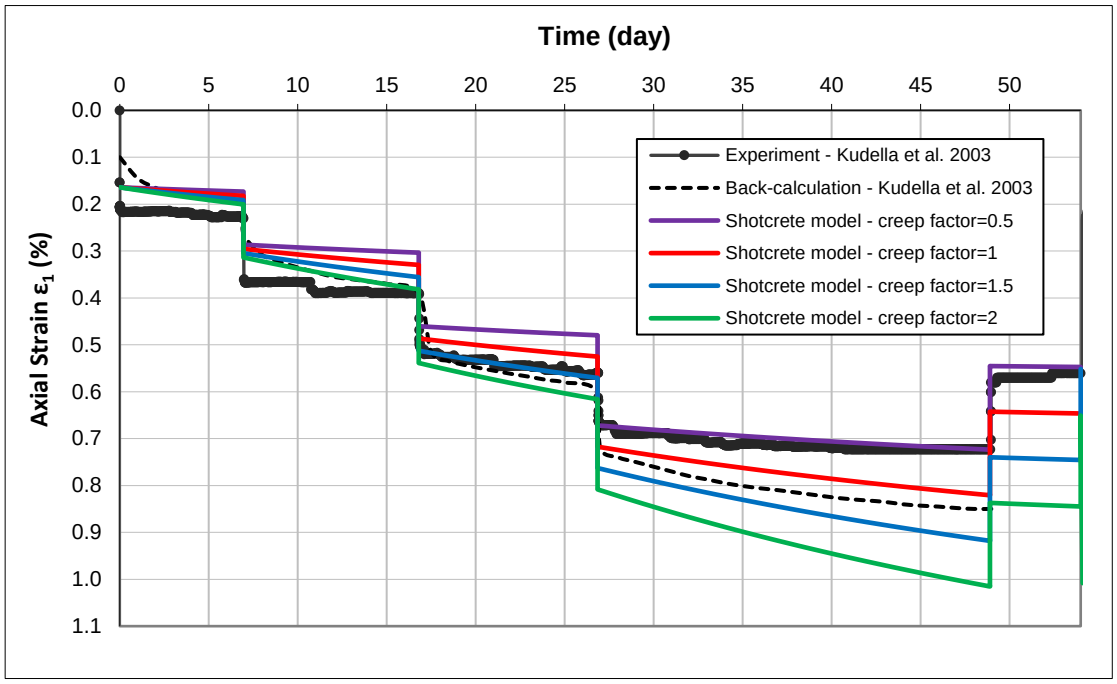

Fig. 44: Comparison of triaxial creep test with back calculations

3.3 Dynamic properties of cement-based material

In order to provide additional information about the behaviour of ground improvement methods like jet-grouting, deep soil mixing or cement/lime-treated soils, it is attempted to look into the dynamic properties of treated soils. Dynamic behaviour of cement-based material is investigated in the laboratory using resonant column or cyclic triaxial test. On the other hand, a cross-hole test is more frequently applied for in-situ measurements. There is still little information available about the dynamic properties of jet grouting material, but there are some publications about the dynamic behaviour of cement stabilized soil and cement/chemical grouting materials (Axtell & Stark 2008, Delfosse-Ribay et al. 2004, Pantazopoulos et al. 2012, Tsai & Ni 2011, Maher et al. 1994).

Figure 45 shows a comparison between the small strain Young's modulus (E_0) and the tangent modulus corresponding to half of the uniaxial compressive strength ($E_{50\%}$) resulted from uniaxial compression test. The small strain stiffness E_0 is somewhat higher than $E_{50\%}$, with the tendency as $E_{50\%}$ increases the ratio $E_0/E_{50\%}$ is reducing. (Croce et al. 2014).

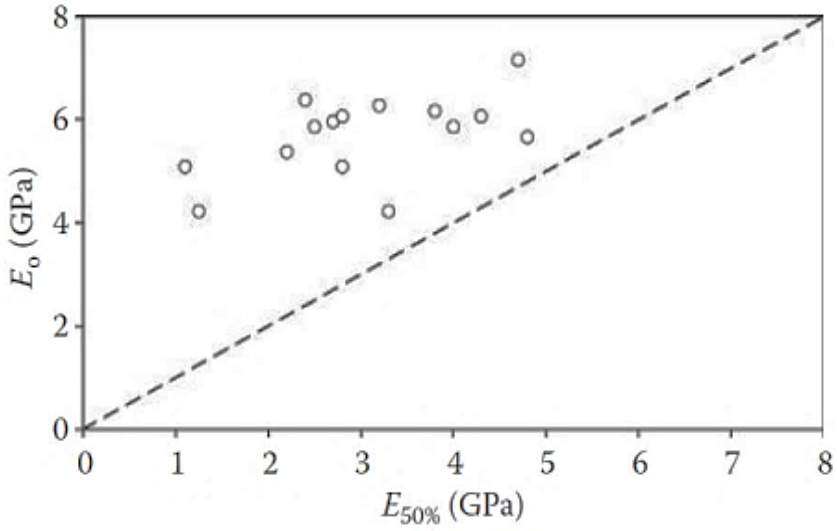

Fig. 45: Large strain Young modulus E_{50} versus small strain Young's modulus E_0 of jet grouting material

In Figure 46, a Cross-hole test results are shown. The tests were carried out in the borehole drilled in a cylindrical jet-grouted shaft which was performed in a soil deposit composed of sandy layer and clayey silt. The measured values of compressive wave velocities are much more scattered than the measured values of shear wave velocities which prove that the latter are more suitable to quantify the effects of improvement (Croce et al. 2014). Shear wave velocity is used to calculate the small strain shear modulus $G_0=\rho V_s^2$. As it can be seen in Figure 46, there is a large difference between laboratory results and in-situ test for shear wave velocity.

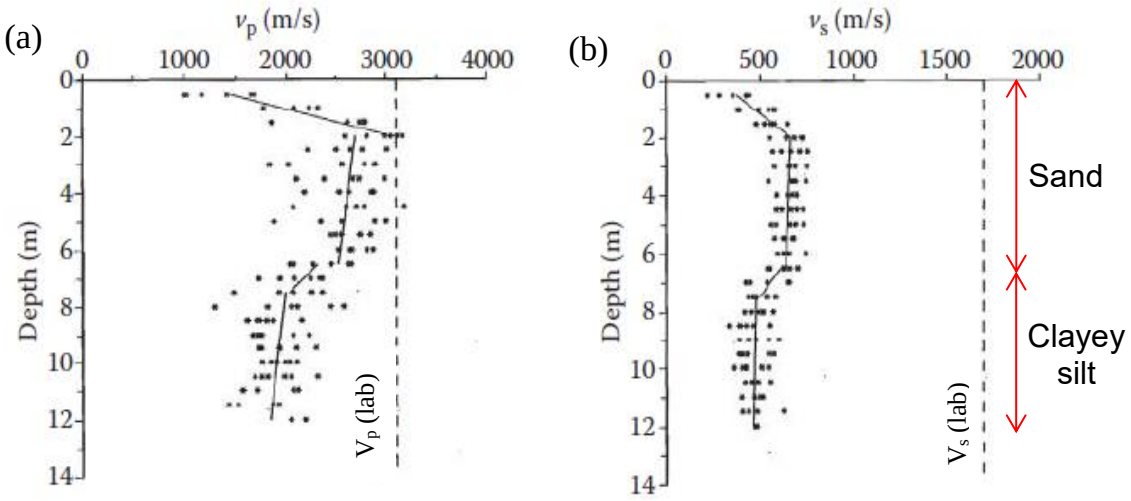

Fig. 46: Cross-hole tests in a cylindrical jet-grouted shell: (a) compressive waves; (b) shear waves (Croce et al. 1994)

Axtell & Stark (2008), investigated the dynamic behaviour of jet grouting material (JG) and deep soil mixing (SM) in a soil deposit consisting of 5m clay, 5m loose to medium sand and 10m dense coarse to gravelly layer. The maximum value of E_0 for jet grouting and deep soil mixing, considered as "small-strain" is approximately twice of the "large-strain" stiffness. The shear modulus of a soil is considerably increased by jet grouting or cement mixing methods. The shear modulus measured in the laboratory is significantly larger than the in-situ shear modulus from cross-hole tests. Three possible reasons were reported by Axtell & Stark (2008); first, proper cores could be tested in laboratory. Second, usually there is more curing time for laboratory tests compare to in-situ test and the third error appear due to the installation of the access tube and the implementation of cross-hole test (Figure 47). The data termed as "Laboratory" refers to those measured with resonant column test and the data labelled by "In-Situ (Low)" or "In-Situ (High)" represent the range of shear modulus calculated from in-situ shear wave velocity determined by cross-hole testing at the same depth as the core samples tested in the laboratory. The shear modulus reduction curves from resonant column test are shown in Figure 48. Beside all these data, the authors did not report any information about the damping ratio.

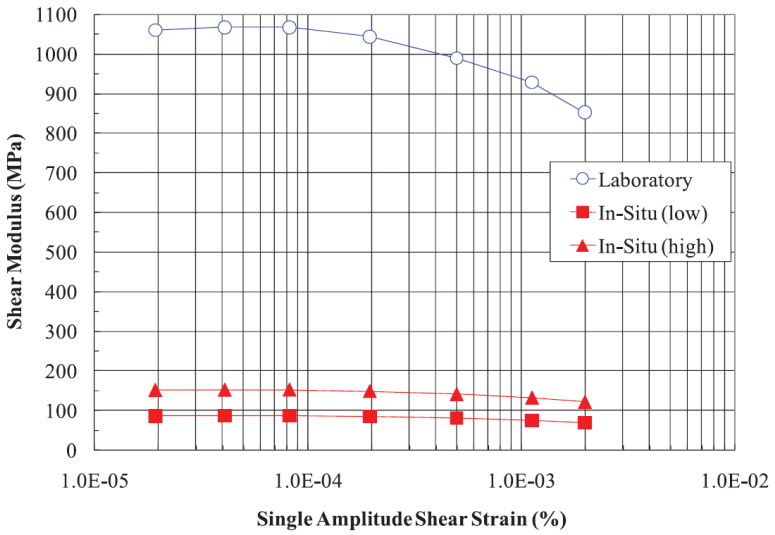

Fig. 47: Laboratory and In-Situ measured shear modulus (Axtel & Stark 2008)

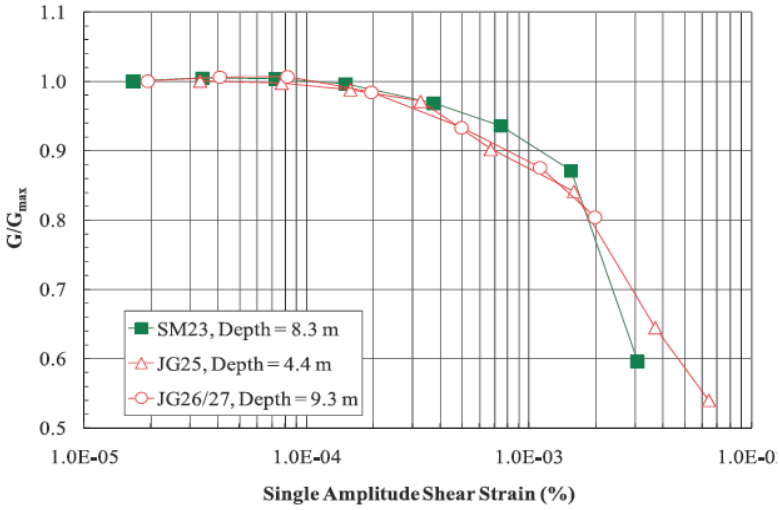

Fig. 48: Normalized shear modulus measured by resonant column tests (Axtel & Stark 2008)

Figure 49a, shows the relationship between the equivalent shear modulus, $G_{e.}$ and the shear strain from dynamic triaxial tests on the stabilized Toyoura sands (Kitazume & Terashi 2013). The soil was stabilized with cement-based special binder content, α. The uniaxial compressive strengths of the treated soils were 800, 1,100 and 1,400 kN/m^2 for α of 250, 300 and 350 kg/m^3 respectively. Equivalent shear modulus increases with increase in confining pressure. Figure 49b also shows the effect of the confining pressure on the small strain shear modulus. The G_0 increases with the confining pressure, while the binder content

does not result in large effect on the G_0 value. The damping ratio of the stabilized sand is plotted in Figure 50 against the shear strain, γ. The damping ratio increases with the increase of shear strain but is not influenced significantly by the confining pressure, σ_c (Kitazume & Terashi 2013).

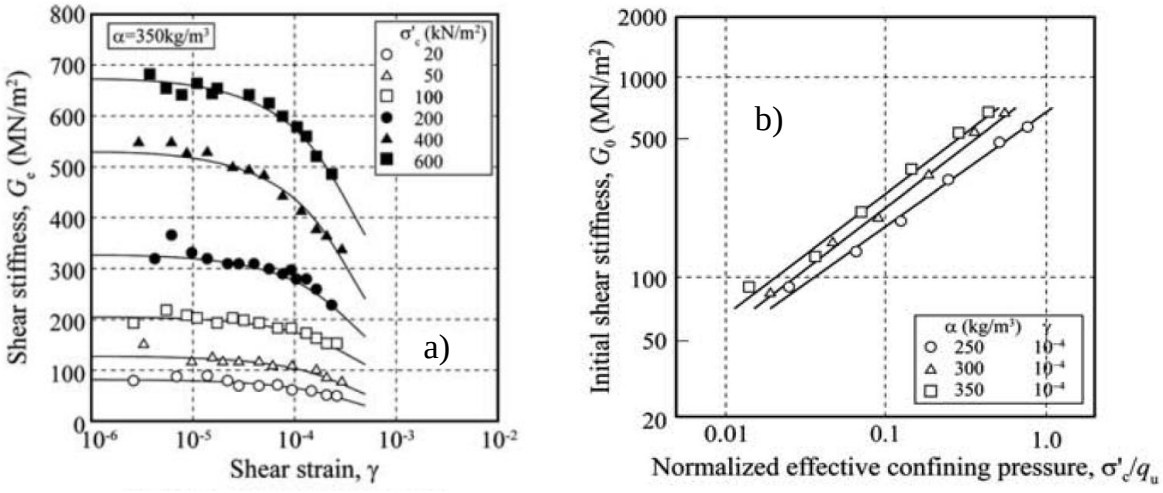

Fig. 49: a) Relationship of equivalent shear modulus with shear strain; b) effect of confining pressure on small strain shear modulus (Kitazume & Terashi 2013)

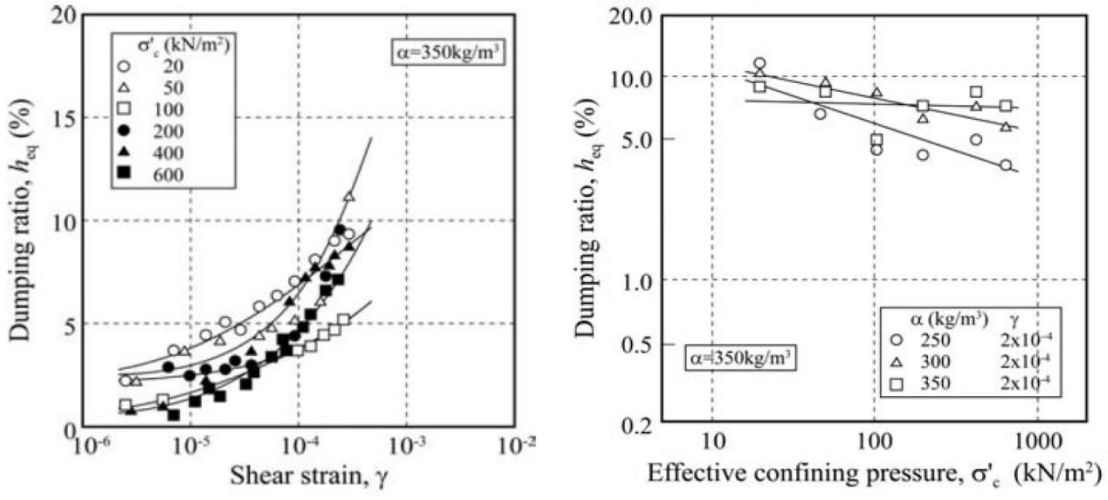

Fig. 50: Damping ratio of cement stabilized soil (Kitazume & Terashi 2013)

Pantazopoulos et al. (2012) used torsional resonant column tests to investigate micro fine and ordinary cement grouted sands. Shear modulus and damping ratio

values were obtained. The effect of confining pressure, cement type, grout water-to-cement (W/C) ratio and sand gradation were investigated. The shear modulus of the grouted sands increased with increasing confining pressure and decreasing W/C ratio, while the damping ratio increased with decreasing confining pressure, increasing shear strain and increasing W/C ratio (Figure 51). Authors also reported that shear wave velocity values of the grouted sand may range from 700 to 1300 m/s.

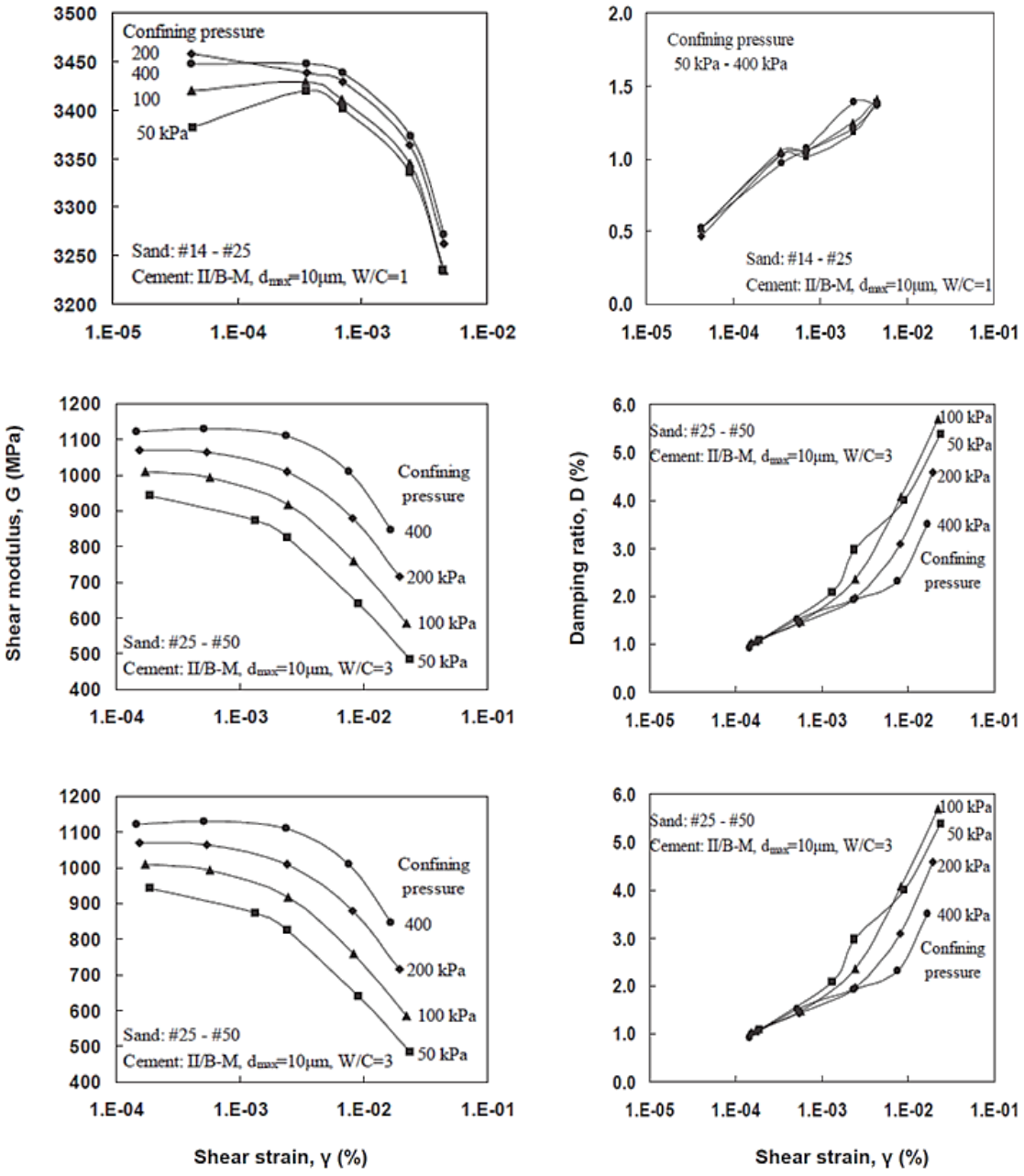

Fig. 51: Dynamic properties of Grouted sand (After Pantazopoulos et al. 2012)

Delfosse-Ribay et al. (2004), published values for the shear modulus and damping ratio of three different grouted sands using resonant column tests and cyclic triaxial tests. The behaviour of pure Fontainebleau sand is compared with the behaviour of Fontainebleau sand grouted with a silicate grout, a micro-fine cement grout and a mineral grout. The results of their study showed that grouted sand has higher shear modulus especially at small strains. On the other hand, when shear strain increases, the shear modulus decreases while the damping ratio increases (Figure 52). They reported that the confining pressure increases the shear modulus and has a greater effect on the cement-grouted sand whereas it has no significant effect on the damping ratio regardless of the type of material.

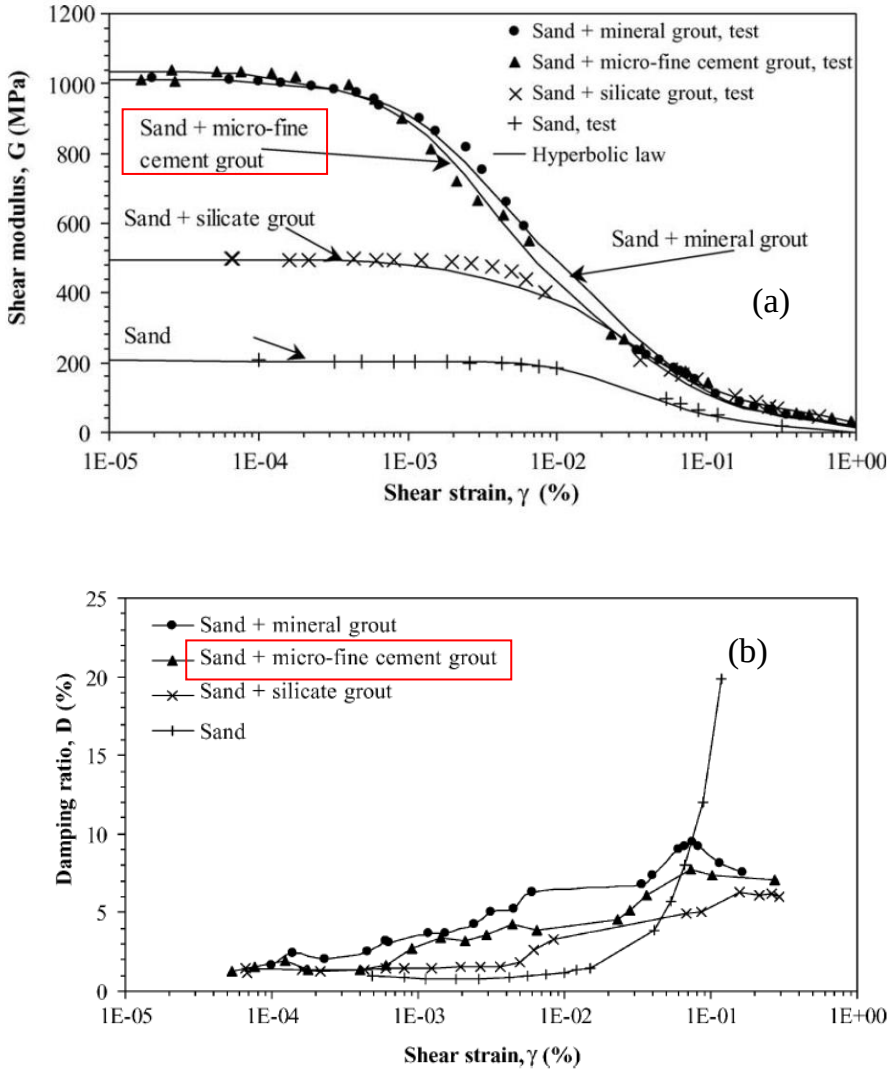

Fig. 52: a) Variation of shear modulus with strain from resonant column test and cyclic triaxial test; b) Variation of damping ratio with shear strain from resonant column test and cyclic triaxial test (Delfosse-Ribay et. al. 2004)

Cement mixing can be an appropriate method for stabilization of clayey soil. However, the dynamic characteristics of cement-treated clay have not yet been much investigated. Tsai & Ni (2011) tried to study the effect of some factors on the small strain shear modulus (G_{max}) and small strain-damping ratio (D_{min}). The tested soil was grey silty clay with very little sand, and it can be classified as low plastic clay (CL). The cement-mixed samples were prepared with the water to cement ratio of 0.5 and cured for 7 days. Some parametric studies were performed in low amplitude resonant column tests. The variable parameters of cement-stabilized soil are cement content and confining pressure. The shear modulus decreases markedly with an increase in shearing strain amplitude, and the damping ratio increases with increasing shearing strain amplitude (Figure 53). Maximum shear modulus increases with the increase in cement content and is less influenced by the confining pressure. D_{min} decrease by increasing the cement content and slightly decrease with confining pressure because the material becomes stiffer due to confinement (Figure 54).

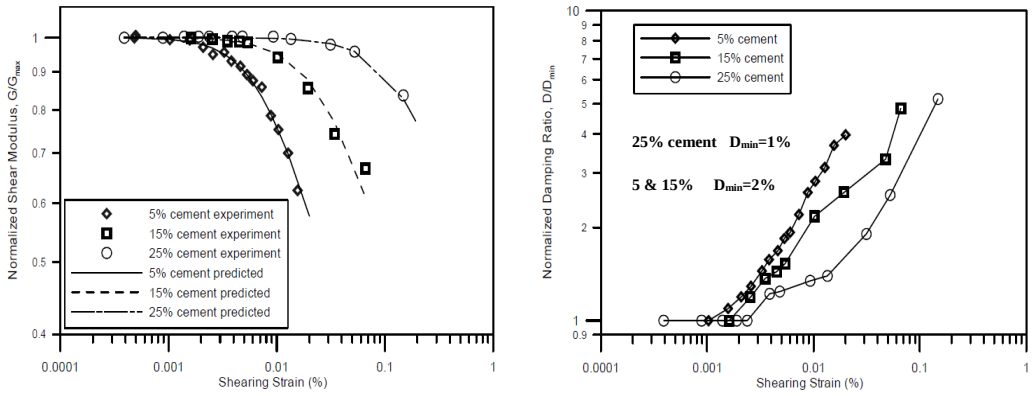

Fig. 53: Influence of cement content on: G/G_{max} versus shear strain curve -and D/D_{min} versus shear strains (Tsai & Ni 2011)

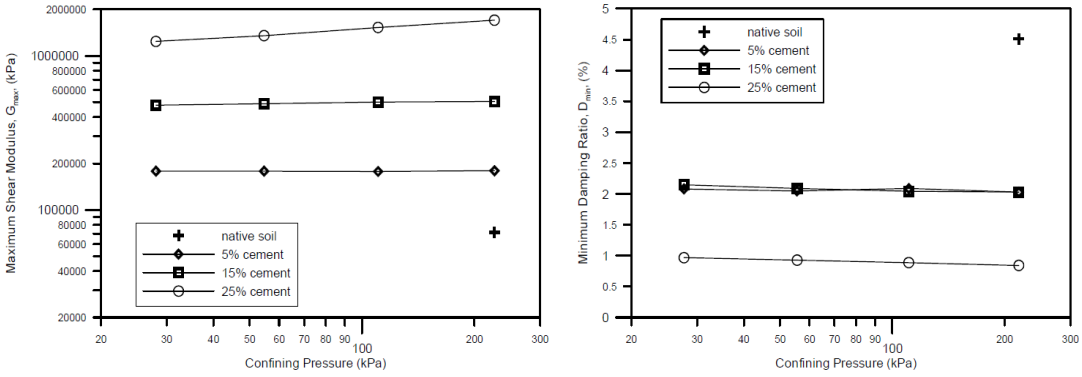

Fig. 54: Influence of cement content on: G/G_{max} and D/D_{min} versus shear strains (Tsai & Ni 2011)

3.4 Summary

The most important material properties of cement-based materials in addition to their dynamic properties were discussed according to the available data mainly for various cement-treated soils and jet-grouting materials. The calibration of the input parameters of the new constitutive model was also investigated. The input parameters could be simply calibrated via back-calculation of the laboratory test results such as the uniaxial compression, triaxial test, three point bending test and creep test. The parameters related to time dependency of stiffness and strength can be calibrated from the results of uniaxial compressive tests on different age samples. To calibrate the compression softening parameters, a 3D simulation of a uniaxial compressive test with its real sample size is required and for the post peak behaviour in tension, a 2D simulation of a three-point bending test is sufficient. Creep number can be calibrated using a uniaxial or triaxial creep test.

4 Numerical modelling of deep excavation

4.1 Jet-grout slab under uplift pressure

4.1.1 Introduction

The problem considered is a deep excavation with a jet grout slab constructed below excavation level which is modelled by Plaxis 2D (Brinkgreve et al. 2014). The slab is subjected to uplift pressure and thus additional tension piles are required (Figure 55). The emphasis is to prove the applicability of the model described in Chapter 2 to practical geotechnical engineering by solving a, slightly simplified, problem of a deep excavation involving a jet grout slab and tension piles. The main purpose of this study is to show that the newly developed constitutive model can be applied to solve this kind of problems, providing a better insight into the behaviour of jet grout panels under uplift pressure as compared to analyses where the jet grout material is modelled as elastic-perfectly plastic material without the presence of tension softening. The influence of various modelling assumptions such as the fracture energy, the thickness and the shape of the slab on the results has been examined and the potential of the model for optimizing the design is shown.

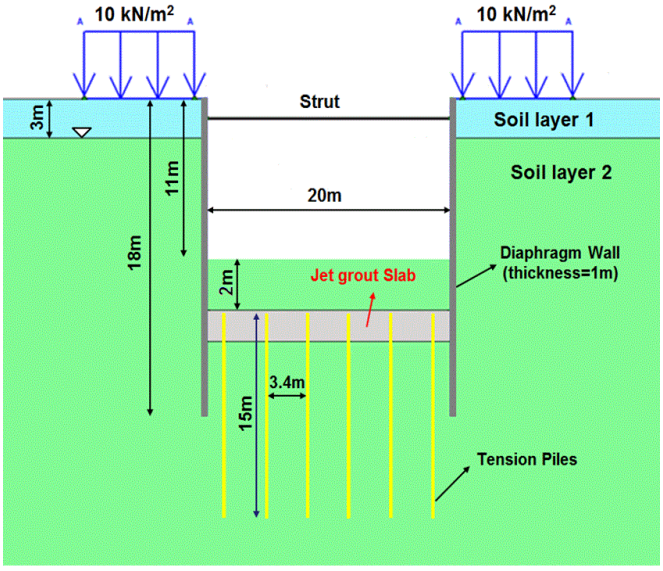

Fig. 55: Layout of example

For the tension-softening region, the consequences of different assumptions are highlighted. Emphasis is placed on the development of crack patterns. Although this usually does not have a severe impact on the global safety of the structure, but to provide additional information for designing the required thickness of the

jet-grout slab it is worthwhile to consider these effects in the numerical analysis. During excavation and due to slab rotation a failure zone may occur at the contact of wall and top of the slab and therefore a plastic hinge is created. Therefore, the ability of the model to take into account compression softening is also discussed. The time dependent development of strength and stiffness of the jet grout slab is not considered in this study because generally the slab is stressed only after curing.

In the further analyses, first it is tried to investigate at what level of excavation the horizontal slab in absence of tension piles reaches failure. Then the behaviour of the horizontal slab with tension piles and the influence of the slab parameters are studied. Finally, the behaviour of a different slab geometry (curved slab) will be checked.

4.1.2 Material properties

Material parameters of soil layers are presented in Table 5 and 6. For soil layers 1 and 2, a simple Mohr-Coulomb failure criterion and the Hardening Soil Model are employed respectively. The reason for choosing Hardening Soil Model for the soil layer 2, is that it takes into account the difference in stiffness between primary loading and unloading/reloading, which is important in this particular case, because a constant stiffness would overestimate the heave of the excavation base, leading to higher bending moments in the slab and consequently the developments of predicted crack patterns would be unrealistic.

Tab. 5: Soil properties for Mohr-Coulomb soil model (layer 1).

parameter	γ_{unsat} (kN/m^3)	E (kN/m^2)	ν (-)	c' (kN/m^2)	φ' (°)	R_{inter}
value	17	20E3	0.33	0.1	30	0.7

Tab. 6: Soil properties for Hardening Soil model (layer 2).

parameter	γ_{unsat} (kN/m^3)	γ_{sat} (kN/m^3)	$E_{50,ref}$ (kN/m^2)	$E_{oed,ref}$ (kN/m^2)	$E_{ur,ref}$ (kN/m^2)	m (-)	ν_{ur} (-)	c' (kN/m^2)	φ' (°)	R_{inter} (-)
value	18	21	20	20	60	0.5	0.2	0.1	32.5	0.7

The diaphragm wall, strut and tension piles are assumed as an elastic material. The related material parameters of structural elements can be found in Tables 7 and 8. The material parameters of the tension piles and the method of modelling of the tension piles will be discussed later. Analysis steps follow the usual procedure, i.e. initial stresses, walls wished-in-place, installation of structural elements (i.e. slab, strut and tension piles), groundwater lowering and excavation in steps.

Tab. 7: Material properties of diaphragm walls.

Diaphragm wall (Plate element)	
Material type	Elastic
EA_1 (kN/m)	25E6
EA_2 (kN/m)	25E6
EI (kN/m^2/m)	2.08E6
d_{eq} (m)	1
w (kN/m/m)	5

Tab. 8: Material properties of strut.

Strut (node to node anchor)	
Material type	Elastic
EA (kN)	2E6
L spacing (m)	3

The material properties of jet grouting are extracted from experimental data. Softening parameters in compression and tension in order to apply in numerical analysis have to be calibrated based on the real sample size simulation. Compression softening parameters (i.e. G_c, f_{cfn}, f_{cun}) of the jet grouting material has been obtained from 3D simulation of uniaxial compressive strength test data on jet grouting cylindrical sample with the height of 22cm (see Figure 36). The maximum tensile strength considered as 10 percent of uniaxial compressive strength. The value of Parameter “a” (see Table 1 and Equation 8) is proposed for shotcrete/concrete material in range of 16-20 (Schädlich & Schweiger 2014b) and for this brittle material, it is assumed to be roughly 10, which is also a conservative value. The value of the friction angle of the slab is set to 32.5, which is equal to soil friction angle. Various parameter for the stiffness and tensile fracture energy are considered. The relevant parameters used for the analysis are listed in Table 9.

Tab. 9: Material properties of jet-grout slab.

Name	Unit	Value
E_{28}	[kN/m^2]	5E6 & 10E6
ν	[-]	0.2
ψ	[°]	0
$f_{c,28}$	[kN/m^2]	8000
$f_{t,28}$	[kN/m^2]	800
f_{c0n}	[-]	0.7
f_{cfn}	[-]	0.75
f_{cun}	[-]	0.1
ε_{cp}^{p}	[-]	-0.05%
G_c	[-]	0.5
f_{tun}	[-]	0
$G_{t,28}$	[kN/m]	0.01 and 0.05
φ_{max}	[°]	32.5
a	[-]	10

4.1.3 Connection of slab to the diaphragm wall

A consideration is given to the behaviour of the slab in the vicinity of the diaphragm wall supporting the deep excavation. Generally, when a slab with jet grout technology is constructed, high pressures are involved and it can be expected that any residuals of slurry cake, resulting from the construction of diaphragm wall, will be cleaned off and therefore the strength of the "interface" slab/wall will be relatively high and no distinct interface is created. To account for that in the numerical analysis no interface is placed between wall and slab but a small cluster is introduced where the tensile strength is reduced to 250kPa. Schweiger et al. (2014) showed that this assumption has an influence on the crack development near the wall but the overall behaviour of the remaining slab is not affected significantly (Figure 56 and 57). They performed a study with a slab thickness of 1m (which is not realistic from a practical point of view) but it was chosen to look at extreme conditions. Keeping in mind that a numerical procedure involving tension softening is in general sensitive and therefore one should not put too much of interpretation on the exact position of individual cracks.

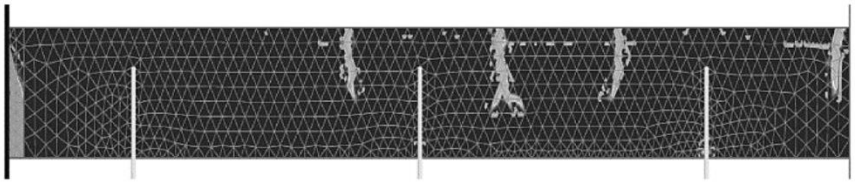

Fig. 56: Crack pattern for reduced tensile strength (i.e. 250kPa) near the wall (Schweiger et al. 2014)

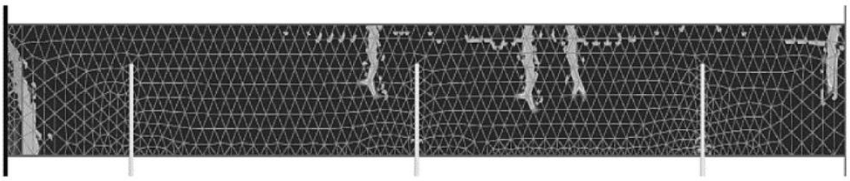

Fig. 57: Crack pattern for full tensile strength (i.e. 800kPa) near the wall (Schweiger et al. 2014)

4.1.4 Results

4.1.4.1 Horizontal and straight slab

In this section, the performance of a slab with 1.5m thickness, which is realistic from a practical point of view under uplift pressure, is examined. The tensile strength in the cluster near the wall has been reduced to 250 kPa. First, it is attempted to find out at what level of excavation the slab without tension piles reaches failure. Two analyses with the shotcrete model and the Mohr-Coulomb criterion for slab behaviour have been performed. The slab's parameters have been chosen for extreme cases (i.e. high stiffness and low fracture energy). Stiffness is 10GPa and the fracture energy in tension and compression is equal to 0.01 kN/m and 0.4 kN/m respectively. Results revealed that in the analysis using the shotcrete model for the slab, calculation failed after 11m excavation. Figure 58 shows the plastic points and tension cut-off point's history at failure. More detail about the failure mechanism will be discussed in the following.

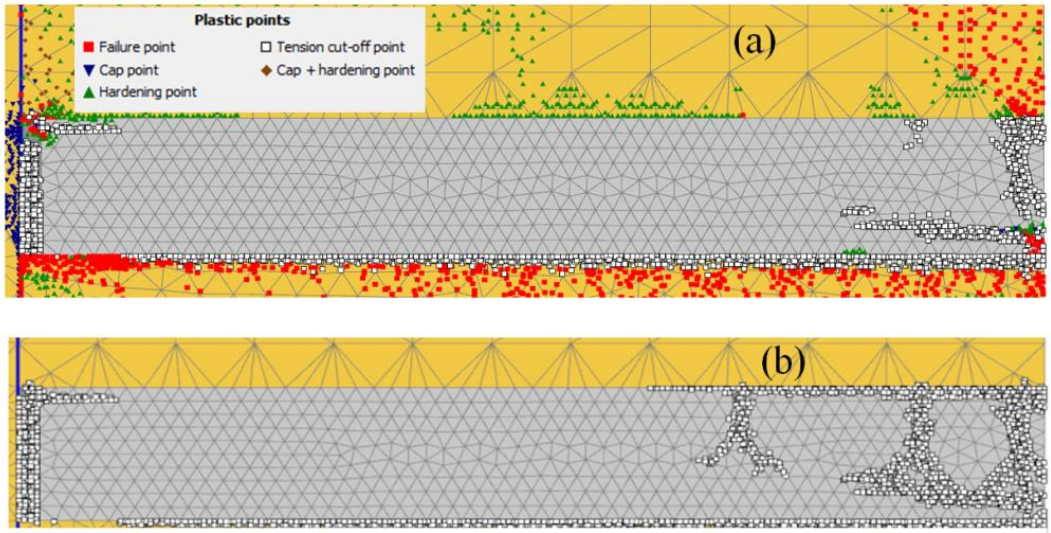

Fig. 58: a) Plastic points at failure; b) Plastic point history-tension cut-off at 11m excavation

The crack pattern can be shown by plotting the variable H_t (tension softening parameter) between 0-1, where $H_t>1$ means that the residual level has been reached. Cracks can be seen in the middle of the slab and also near the diaphragm wall (Figure 59).

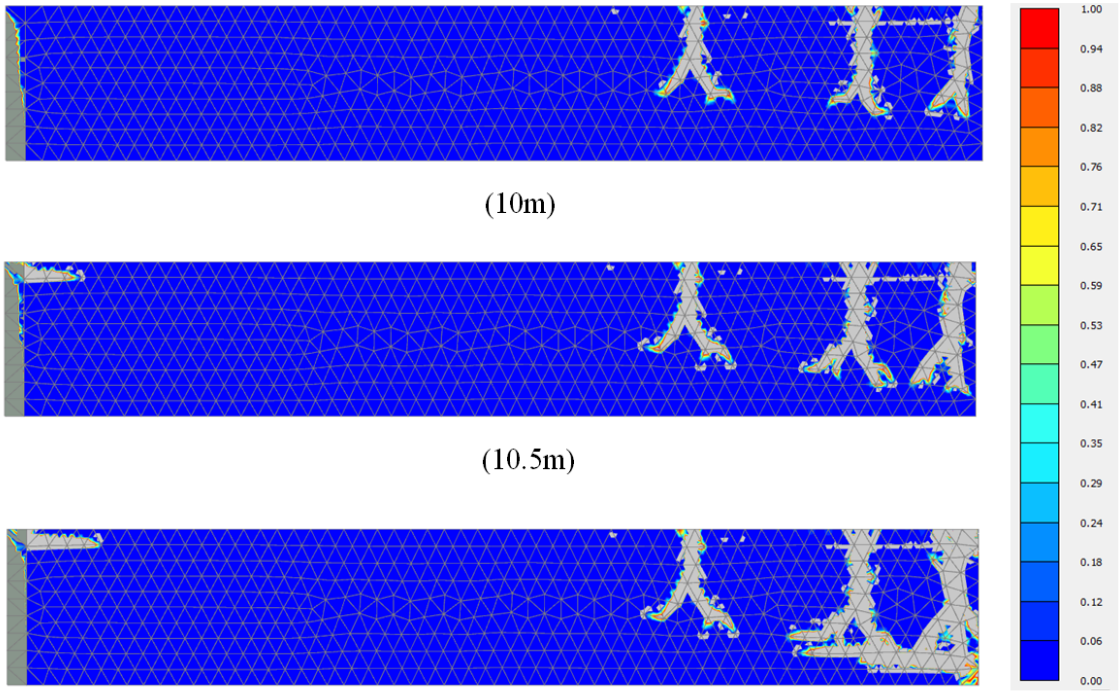

Fig. 59: Crack locations in slab without tension piles at different excavation level ($0<H_t<1$)

Figure 60 presents the contour plot of the principle stresses σ_3 in the slab where only tensile stresses are shown between 0-800kPa. Crack locations can be seen at different excavation levels between 10m-11m. In the crack locations σ_3 is equal to zero. By plotting σ_1 in the slab (in range 0-8 MPa), it can be observed that the slab reaches failure at 11m excavation due to compression softening near the mid-span at the bottom (Figure 61c). Stresses reduced to residual level and finally the cracks develop all over the cross section (Figure 59c). A small zone near the wall on the top can be also seen in the Figure 61 where the stresses highly exceed the jet grouting uniaxial compressive strength. In this area (in some stress points), the compression capacity increased due to the confining effect (increase in σ_3 and σ_2). Principle stresses directions σ_1 and σ_3 in the slab at level 10m are shown in Figure 62. It must be noted that the same result was observed in the analysis where compression softening was switched off and the slab failed at 11m excavation when the stresses reach the peak compressive strength in the mid-span.

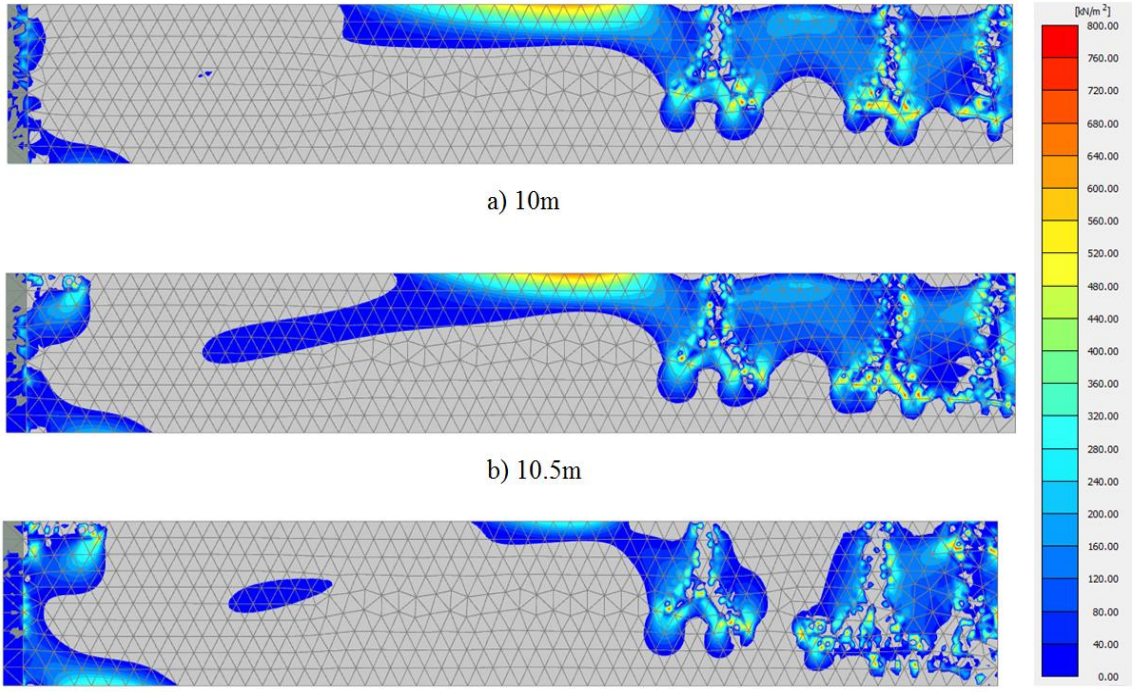

Fig. 60: Contour plot of principal stress σ_3 (0-800 kPa) at different excavation levels

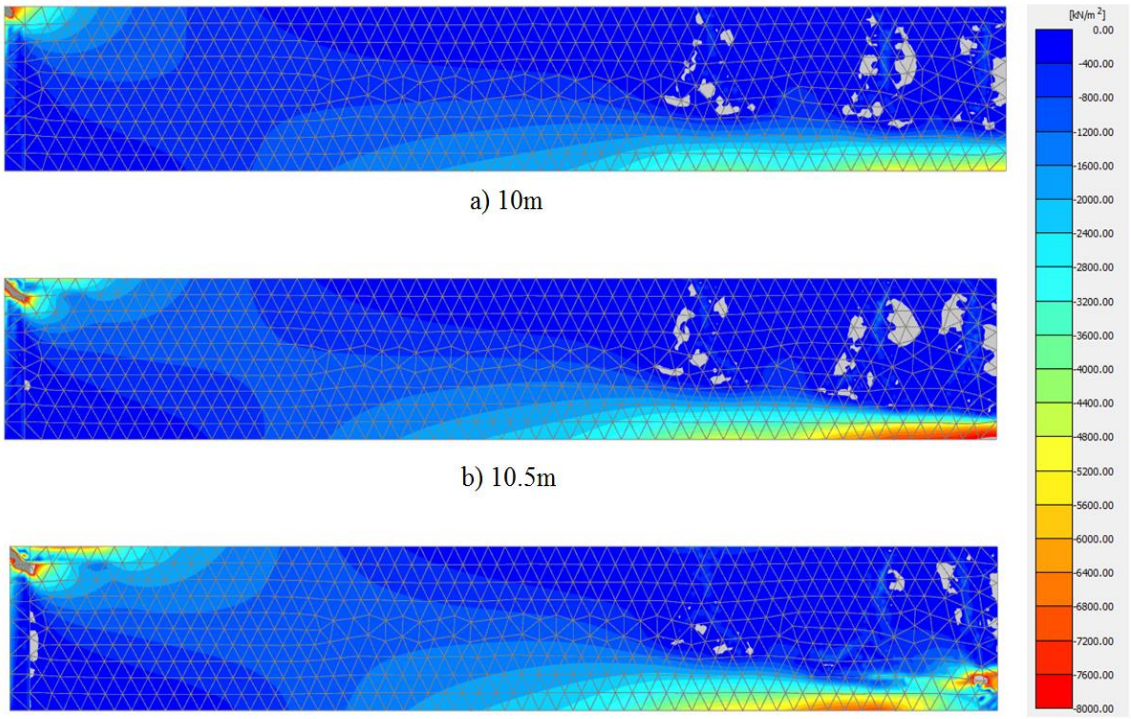

a) 10m

b) 10.5m

c) 11m

Fig. 61: Contour plot of principal stress σ_1 (-8000 - 0 kPa)

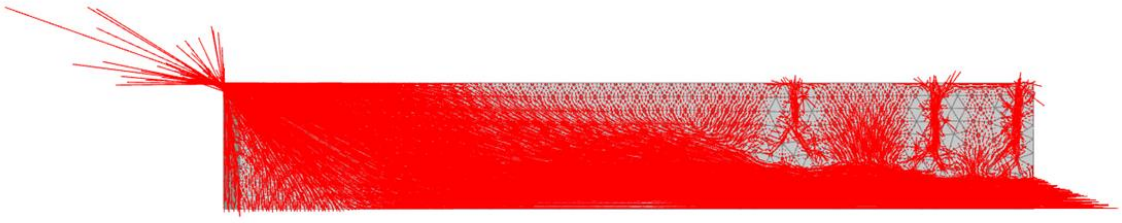

Principle stress direction σ_1

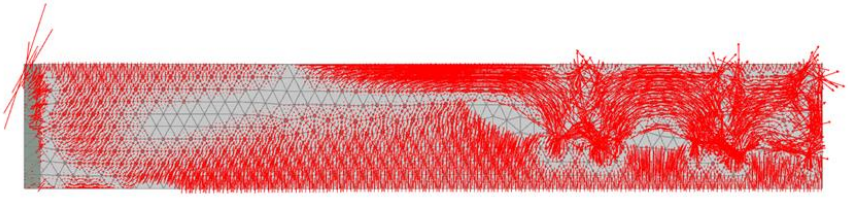

Principle stress direction σ_3

Fig. 62: Principle stress direction σ_1 and σ_3 in slab at level 10m excavation

By plotting the H_c (compression hardening/softening parameter) in range of [0,1] it is possible to show in which area stress points exceed the peak compressive strength (Figure 63). Where $0<H_c<1$ denotes hardening behaviour, $H_c=1$ corresponds to the peak compressive strength and $H_c>1$ means softening behaviour (see Figure 3). It must be noted that the total peak strain in compression increases due to increase in ε_{cp}^{p} which is governed by the mean stress p' (see Equation 8). Therefore, the value of H_c corresponding to the residual level can be different for each stress point.

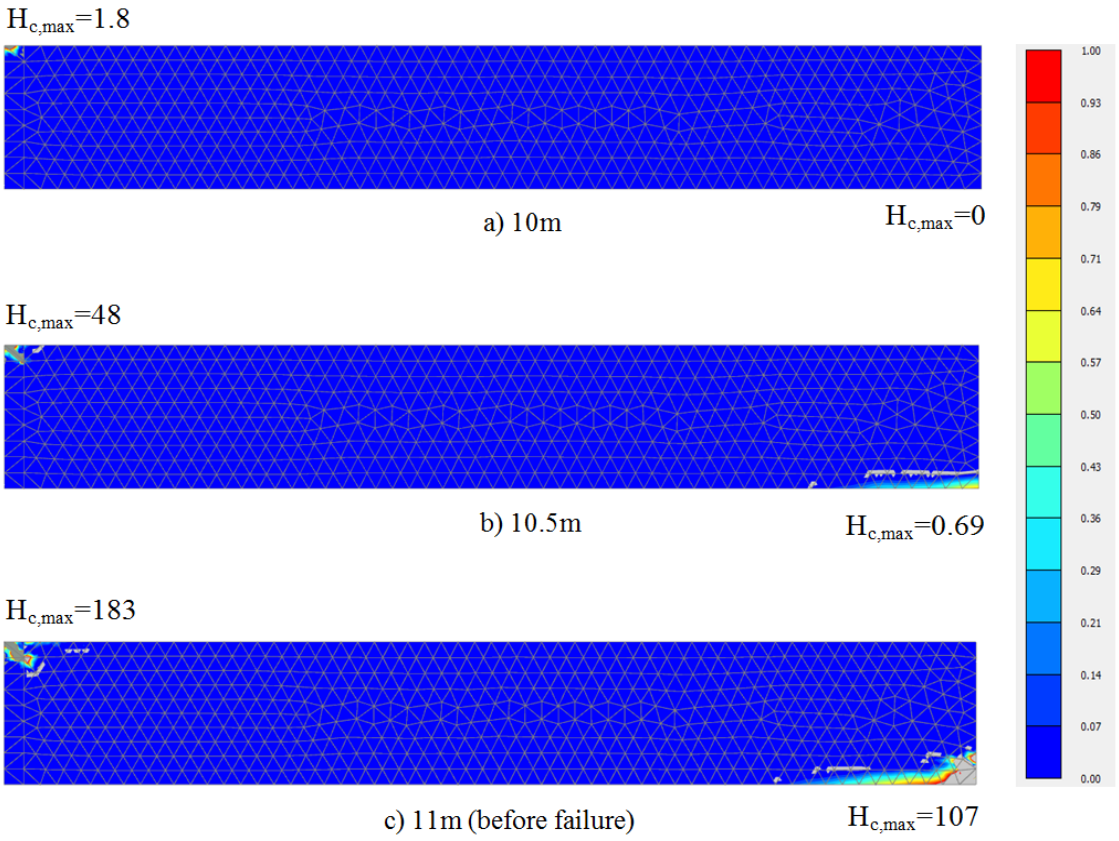

Fig. 63: Plot of compression Hardening/softening parameter Hc (0<Hc<1)

Figure 64 depicts the wall deflection of different excavation levels. It is observed that due to slab deformation and creation of tensile cracks the diaphragm wall is pushed back gradually until the failure state is reached of 11m excavation.

The shear forces in the wall are also increased slightly during excavation up to failure (Figure 65). These forces can be compared with the normal forces from the slab which will be calculated in the following.

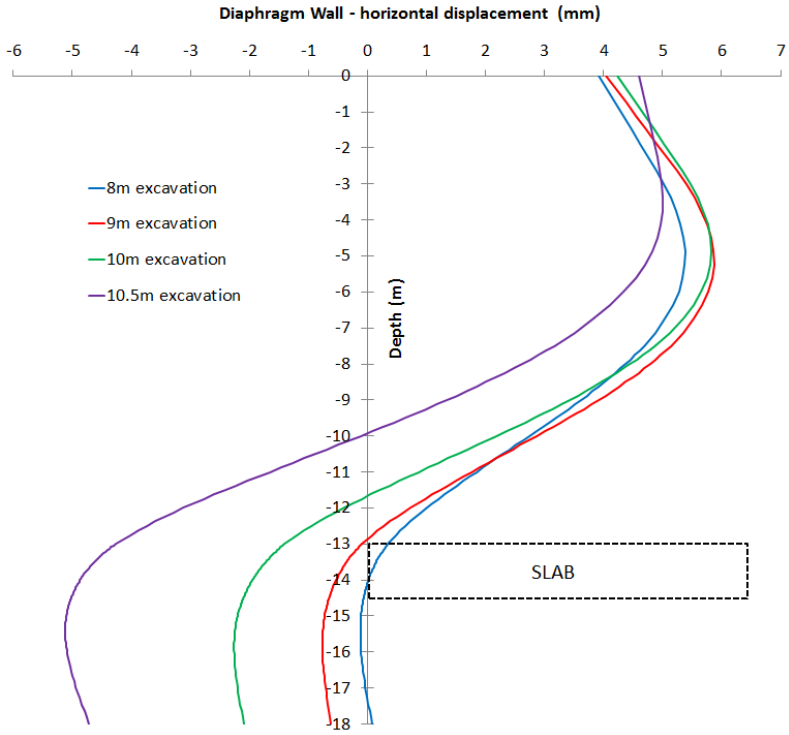

Fig. 64: Horizontal displacement of diaphragm wall

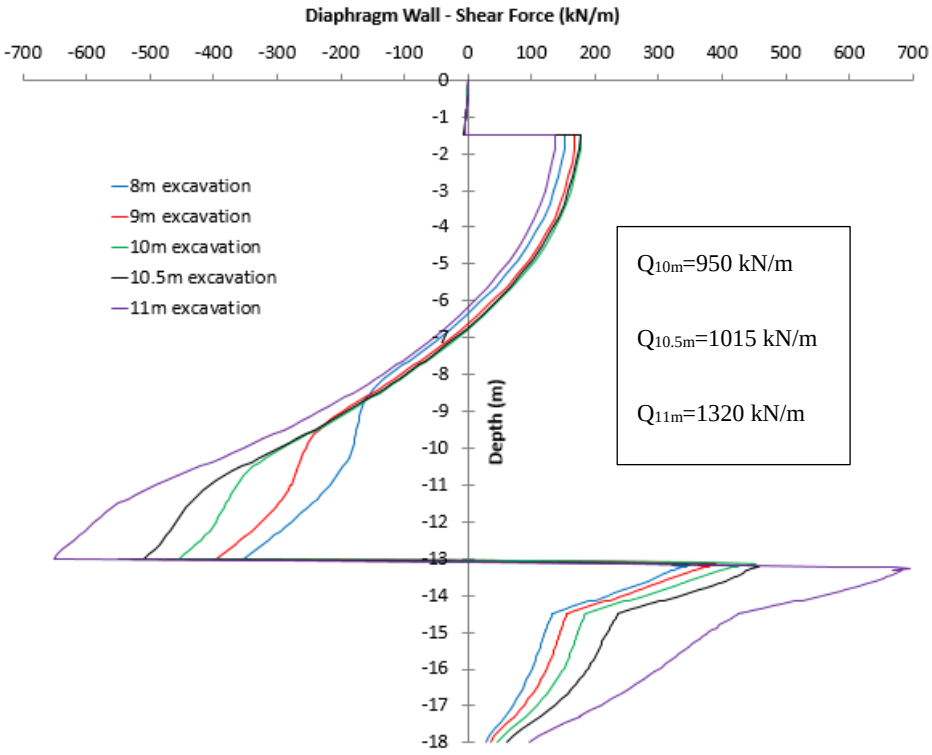

Fig. 65: Shear forces (Q) of diaphragm wall

A simple analytical calculation can be compared with numerical results. The goal is to verify the normal forces in slab near the wall and at the mid-span. When a concrete slab is laterally restrained by a stiff boundary, due to its deflection an internal arching mechanism or Compressive Membrane Action (CMA) is induced. The arching effect enhances the load capacity of the slab and occurs in concrete due to the significant difference in tensile and compressive strengths. The weak strength in tension causes cracking due to the loads and shifts the neutral axis towards the compression part (Taylor et al. 2002). In this case, according to Rankin's model, three hinges at the support and mid-span can be considered (Figure 66).

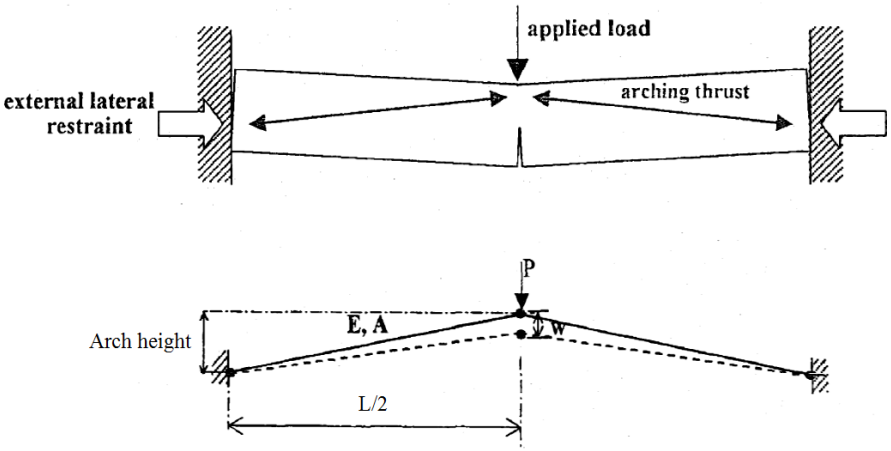

Fig. 66: Arching action in laterally restrained slab - Equivalent rigidly restrained arch (Taylor et al. 2002)

A simple static calculation has been done to estimate the forces in the slab (Figure 67). Plastic hinges are assumed to be formed roughly 5cm below the slab top surface (at support) and 10 cm above the slab bottom at mid-span.

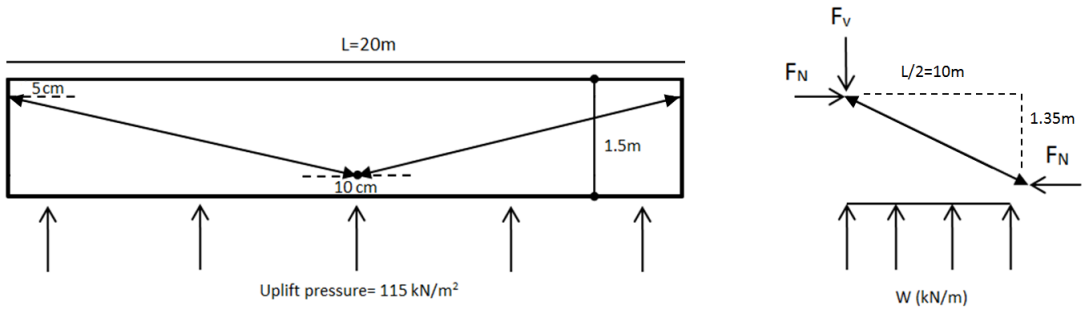

Fig. 67: Analytical calculation model and its assumptions

At level 11m (where failure occurs in numerical analysis), the acting load on the slab can be summarized as:

W_{slab}= uplift force – soil weight (2m soil above) – slab weight = 47.75 (kN/m/m)

then the normal force is equal to:

$F_N \times 1.35 = w_{slab} \times L^2/8 \rightarrow F_N = 1770$ kN/m

If the same procedure is assumed for other levels:

Level 10.5: $F_N = 1390$ kN/m

Level 10m: $F_N = 1065$ kN/m

Figure 68 presents the approximate value of normal forces inside the slab. In level 10m two cross section, one close to the wall and the other at the mid-span show the normal forces inside the slab which are in a good agreement with the analytical solution. Due to the deformation and development of the cracks, compressive forces inside the slab increase and these high forces push the diaphragm wall back (Figure 64). At excavation level 10.5m, softening occurs in a small area on the top of the slab near the wall and consequently the stresses distribution changes in this area (see Figures 61b and 63b) but the system is still in equilibrium. A cross section close to the wall cannot show the correct normal force which is expected to be equal with the force at the mid-span. If a cross section were chosen at a small distance from the wall (for example10cm), the forces inside the slab are roughly equal. However, it must be mentioned that this excavation level is also close the failure behaviour. At excavation level 11m, softening happens at the mid-span and failure occurs. Due to the failure, forces are not in equilibrium at this level.

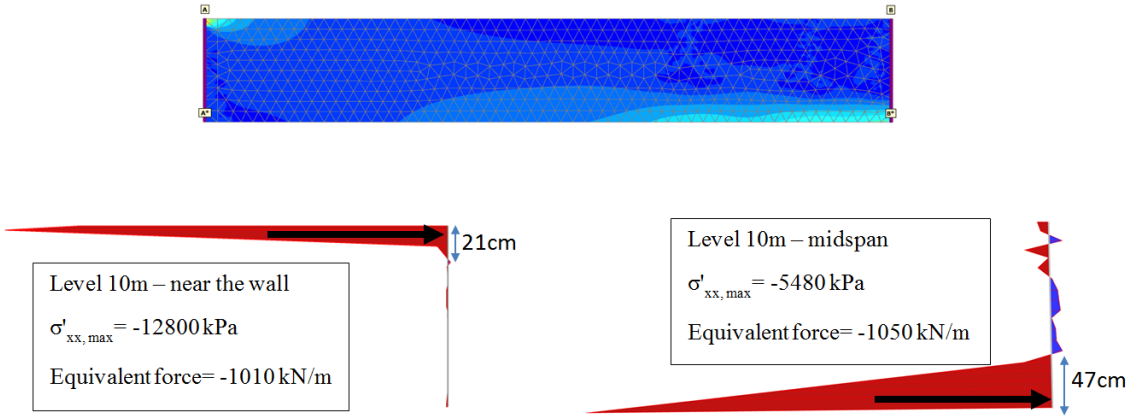

(a) Excavation level: 10m

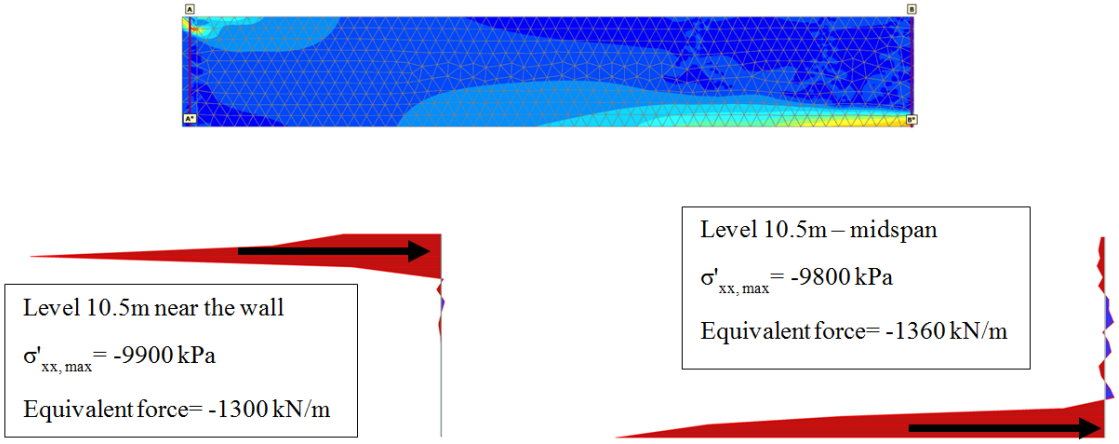

(b) Excavation level: 10.5m excavation

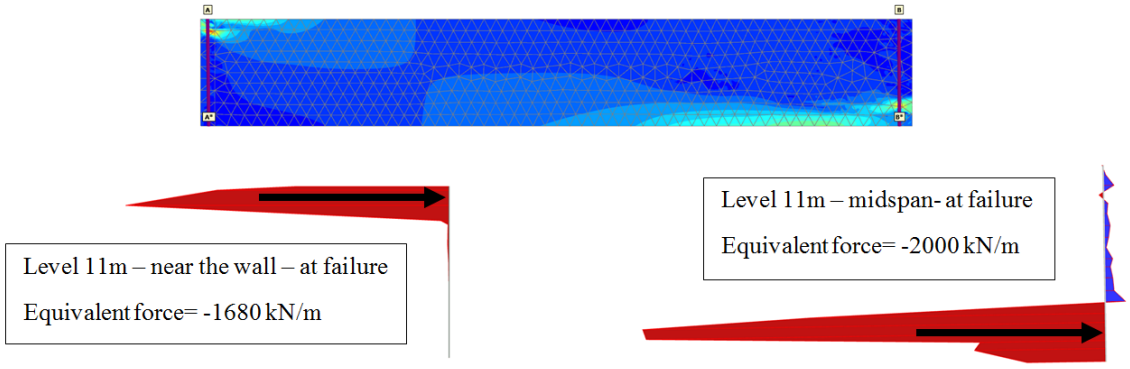

(c) Excavation level: 1m excavation - failure

Fig. 68: Normal forces in the slab at the middle and near the wall: a) 10m excavation; b) 10.5m excavation; c) 11m excavation

Calculations using the Mohr-Coulomb criterion with 10GPa stiffness for the slab failed at level 12m without tension piles. Figure 69 shows the plastic points at 11m and 12m excavation level. These results can be compared with the calculation using the shotcrete model where failure occurred at 11m excavation.

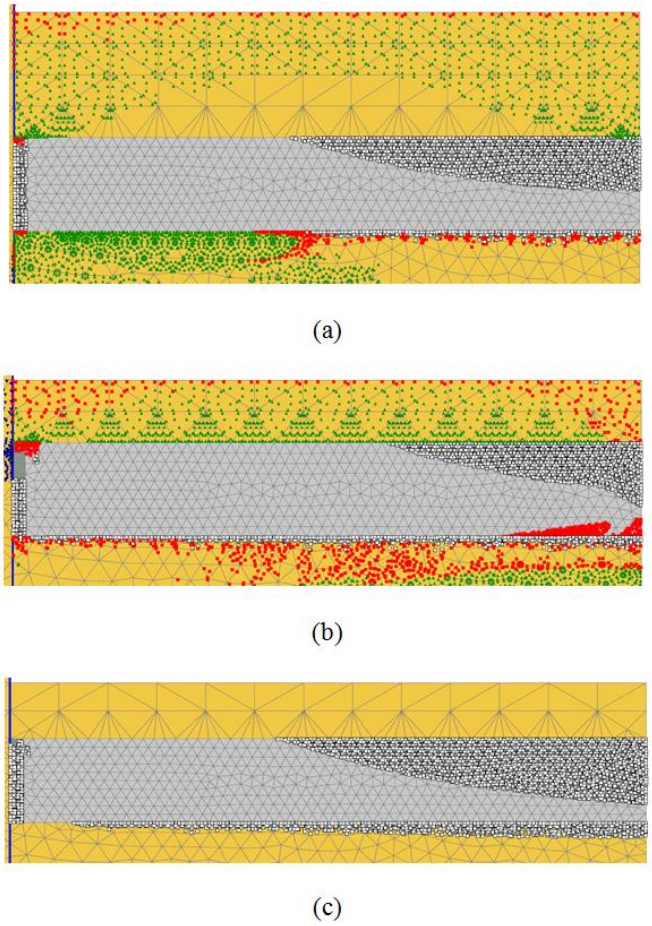

Fig. 69: Plastic points at different excavation levels: a) 11m; b) 12m; c) Plastic points history-tension cut-off- at 11m excavation

The calculation failed because the compressive stresses at the bottom in the mid-span reach the maximum compressive strength (Figure 70) while in a calculation with the shotcrete model failure occurred earlier in 11m excavation due to crack propagation and increase in compressive stresses at the mid-span. It is important to realize that with the Mohr-coulomb criterion tensile stresses are limited but cannot be reduced to residual level.

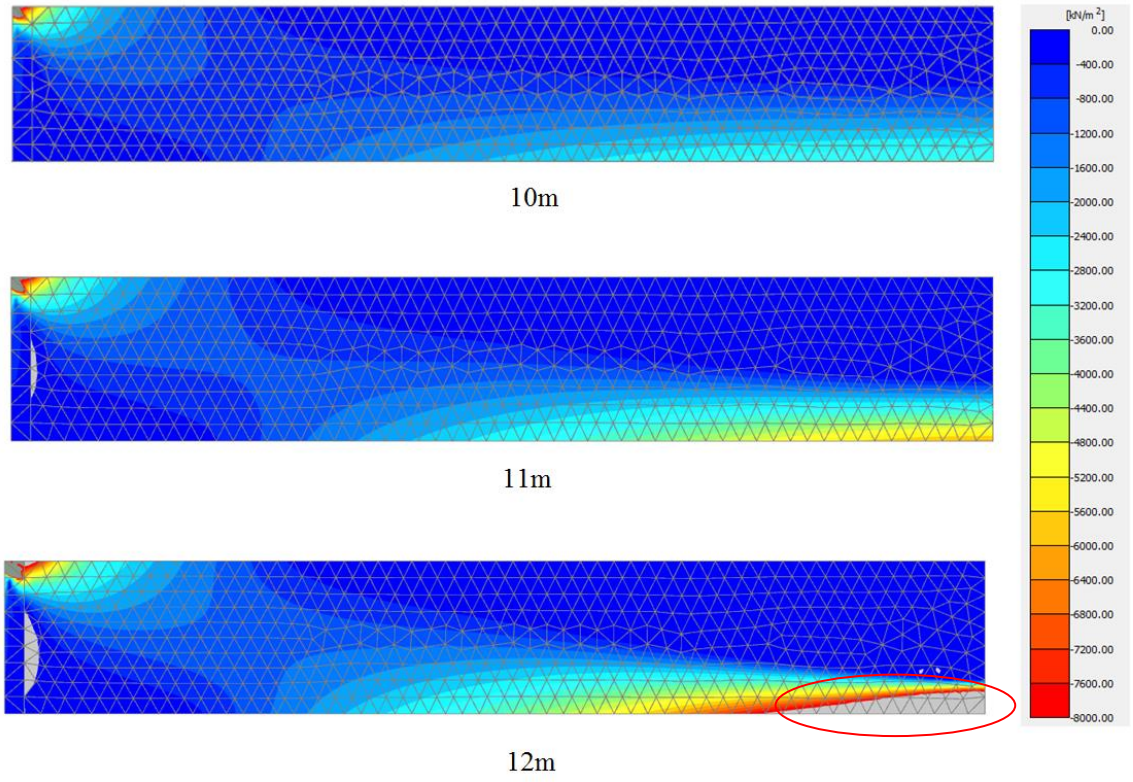

Fig. 70: Contour plot of principal stress σ_1 (-8000 – 0 kPa)

Different slab deformation without cracks development compared to the shotcrete model is also reflected in diaphragm wall deflections (Figure 71)

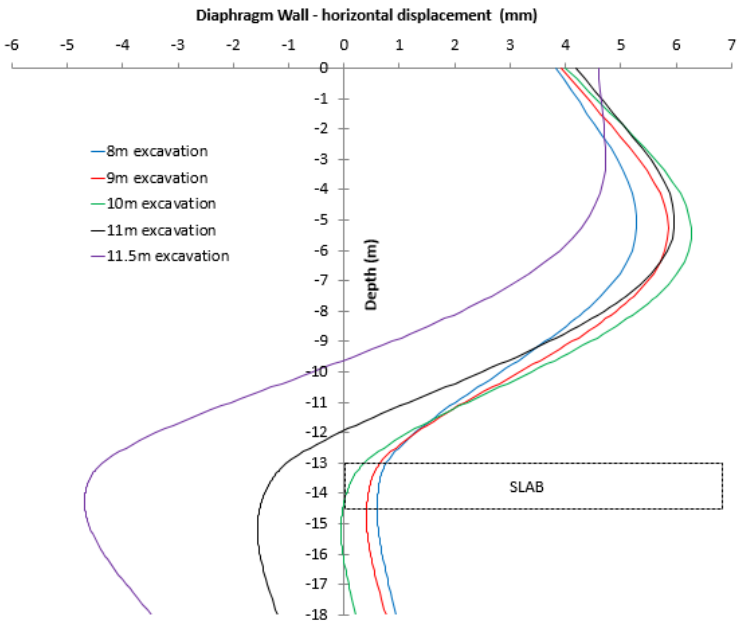

Fig. 71: Horizontal deflection of diaphragm wall - jet grout slab is modelled with Mohr-Coulomb criterion

As it was shown in the previous part, the uplift pressure caused failure in the slab and thus additional tension piles are required. These piles can be modelled using the embedded-pile rows feature. The important point here is the way of connecting the piles to the slab (which is a volume element) and therefore two different methods are examined as shown in Figure 72. One is using a Geogrid element that is only a tensile element with axial stiffness. It is placed within about 2/3 of the slab thickness (which is assumed to be fixed inside the slab i.e. no relative displacement between slab and piles) and the embedded pile is connected to it at the bottom. The other method is using a soft plate (low stiffness) at the bottom of the slab and connecting the embedded pile to this soft plate. Comparison of these two approaches will be shown in the following.

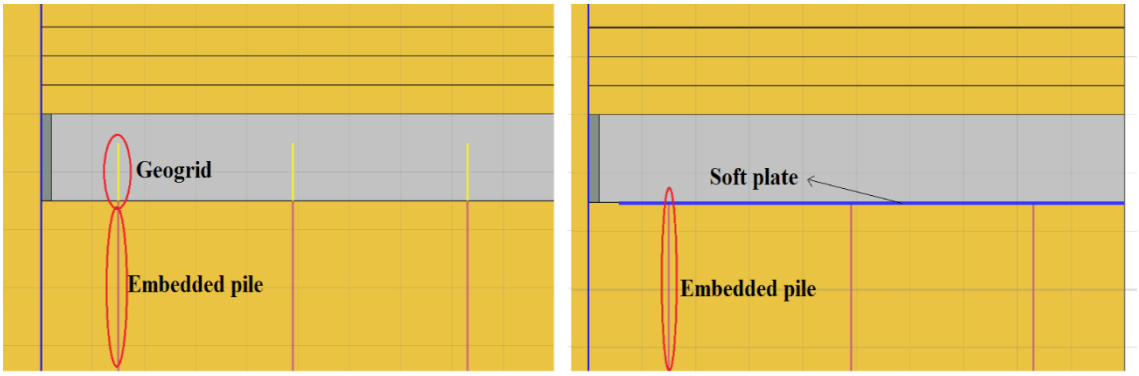

Fig. 72: Two different methods for modelling the tension piles

Appropriate choice of input parameters of the embedded pile especially the interface stiffness factor (ISF) is an issue and requires experience. The interface stiffness factor can be overruled by the user, because the default values are extracted for only a limited number of cases (Sluis et al. 2013). However, in this study the default values of the Plaxis are accepted because the emphasis is on the slab behaviour. The input parameters of the embedded piles and also the geogrids are presented in Tables 10 and 11. Usually, in tensile loading the contribution of the grout to the pile's stiffness can be ignored and only the bar's stiffness is considered i.e. $EA_{pile}=E_{steel}.A_{steel}$ and therefore the stiffness of the embedded pile can be calculated accordingly (Bruce et al. 2005). The GEWI steel bar diameter is 50mm ($E_{GEWI}=206*10^6$ kPa) and the micro piles diameter was considered equal to 170mm.

Tab. 10: Material parameters of embedded pile

Parameter		value	unit
Young's modulus	E	18e6	kN/m^2
Bulk unit weight	γ_{EP}	3	kN/m^3
diameter	d	0.17	m
spacing	L	3	m
Skin resistance at pile top	$T_{top,max}$	60	kN/m
Skin resistance at pile bottom	$T_{bot,max}$	60	kN/m
Interface stiffness factor	ISF	Default= 0.29	

Tab. 11: Material parameters of the tension piles - Geogrids

Tension Piles (geogrid element)	
Material type	Elastic
EA_1 (kN/m)	126.9E3
EA_2 (kN/m)	126.9E3

In these analyses, the stiffness of the jet grout slab is 10GPa and the tensile fracture energy in 0.01kN/m. Results of the crack patterns, pile displacements and pile forces at 11m excavation showed good consistency in both methods (Figures 73, 74 and 75). However the soft plate stiffness must be defined carefully so that it has no effect on the slab behaviour, too low stiffness make it inefficient and using higher values may change the crack pattern and slab deformation. Therefore, for further calculations the system of Geogrid-embedded pile will be used.

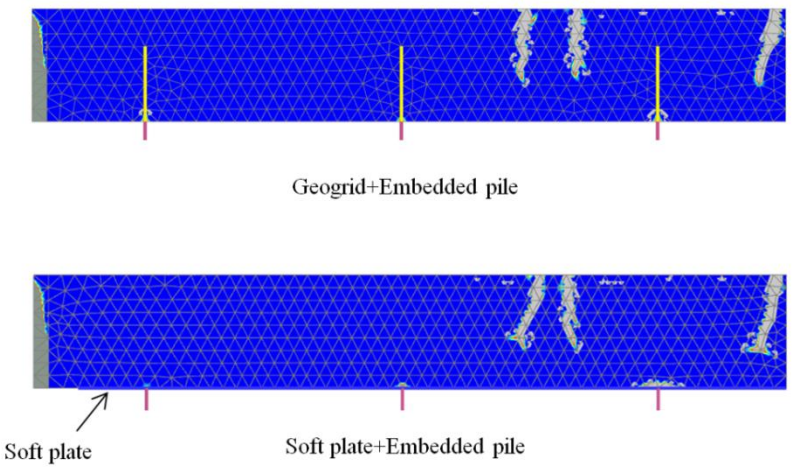

Fig. 73: Crack locations in slab with different pile modelling.

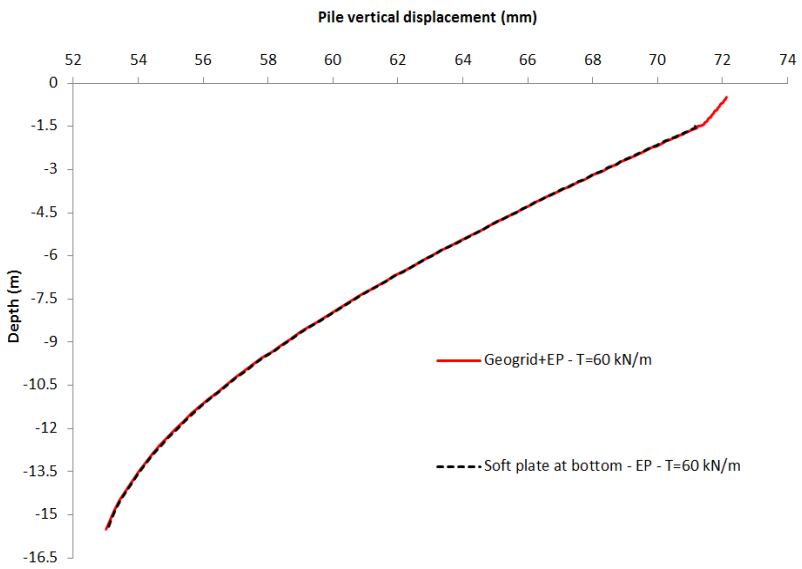

Fig. 74: Vertical pile displacement of the central pile near mid-span

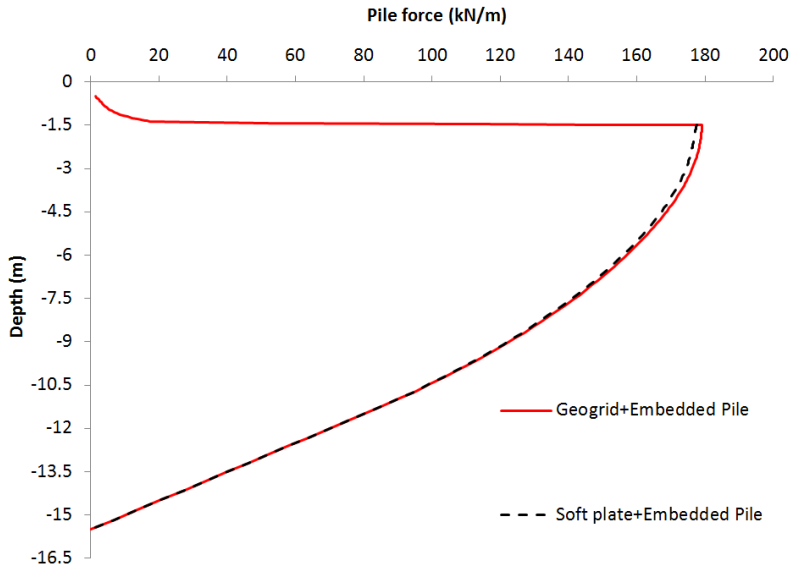

Fig. 75: Axial force in the central pile near mid-span

In the following analyses, the behaviour of the slab is investigated using various parameters and different constitutive models. In order to compare the results obtained from the shotcrete model some analyses with the Mohr-Coulomb strength criterion without considering softening in the tensile regime for the slab have been performed. It must be emphasized that all the results belong to the end of excavation level 11m, which is still a stable excavation level.

The effect of varying stiffness (5 and 10 GPa) for the slab is investigated. Two values of fracture energy equal to 0.01kN/m and 0.05kN/m have been considered. For the compression softening only one value of fracture energy

G_c=0.4kN/m is utilized. Although the value seems to be very small but it is a conservative value and helps to check whether the compression softening in the upper corner near the wall occurs and affects the global stability of the system.

Figures 76 and 77 depict the obtained crack patterns in the slab with different stiffness and fracture energy. As it can be seen in the slab with 10GPa stiffness and minimum value of G_t, three cracks develop in the middle and close to the wall, by increasing the fracture energy to 0.05kN/m, one crack developed just in the central part of the slab and near the wall. In the analysis with 5GPa stiffness for the jet grouting material and fracture energy equal to 0.01kN/m cracks developed in the 1/3 of upper middle part and near the wall but by increasing the fracture energy to 0.05 no cracks propagated in the central part but just near the diaphragm wall.

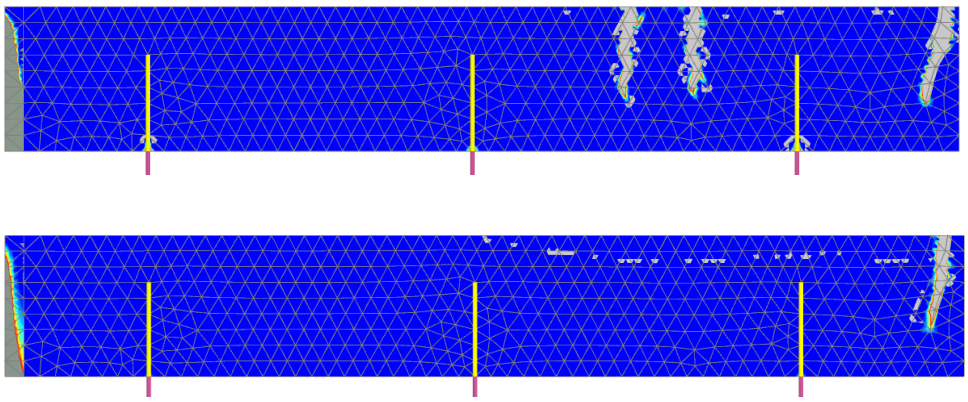

Fig. 76: Crack location in slab with 10GPa Stiffness: a) G_t=0.01 kN/m; b) G_t=0.05 kN/m

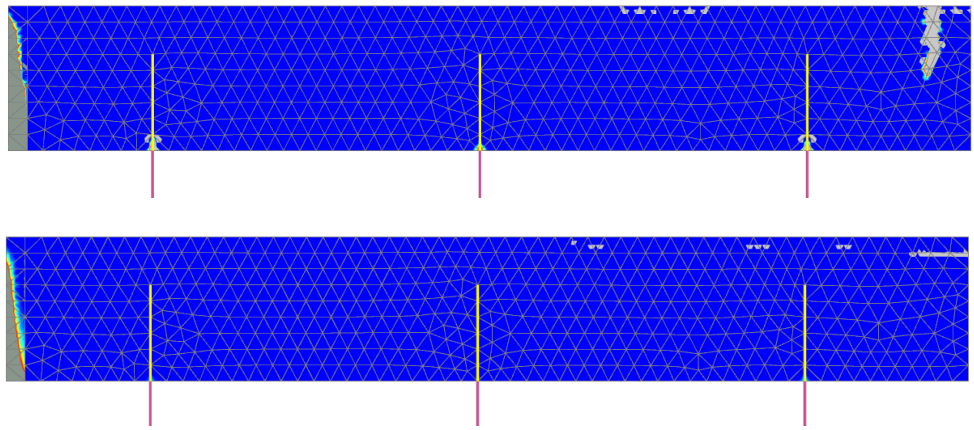

Fig. 77: Crack location in slab with 5GPa Stiffness. a) G_t=0.01 kN/m; b) G_t=0.05 kN/m

Figure 78-79 present the contour plot of σ_3 where only tensile strength (0-800kPa) has been shown. With the stiffness of 10GPa and G_t=0.01kN/m, cracks developed in the middle part of the slab with depth of 2/3 of the slab thickness, but when G_t=0.05kN/m, although the maximum tensile stress is reached towards the centre in the upper third of the slab, cracks do not develop deeper because softening is less severe. For the analysis employing a Mohr-Coulomb criterion for the slab with 10GPa stiffness, it is obvious that stresses in the slab are significantly different. In other calculations with 5GPa stiffness (see Figure 79), it is observed that by increasing the fracture energy to 0.05kN/m, although the maximum tensile strength is reached in the upper part of the slab, no cracks developed. The results of the Mohr-coulomb analysis show a small zone in the top of the slab where the tension cut-off limit is reached. This behaviour of the slab is also reflected in Figure 80 where normal stresses are plotted in a cross section of the slab where a crack exists. With the shotcrete model, the normal stress in the crack is zero but with the Mohr-Coulomb criterion, the stress is 800kPa. The depth of tensile stresses and cracks is much deeper and consequently the compressive stresses are higher with the new model. In the analysis with the Mohr-Coulomb model and 5GPa stiffness, tensile stresses reached the peak only near the top surface.

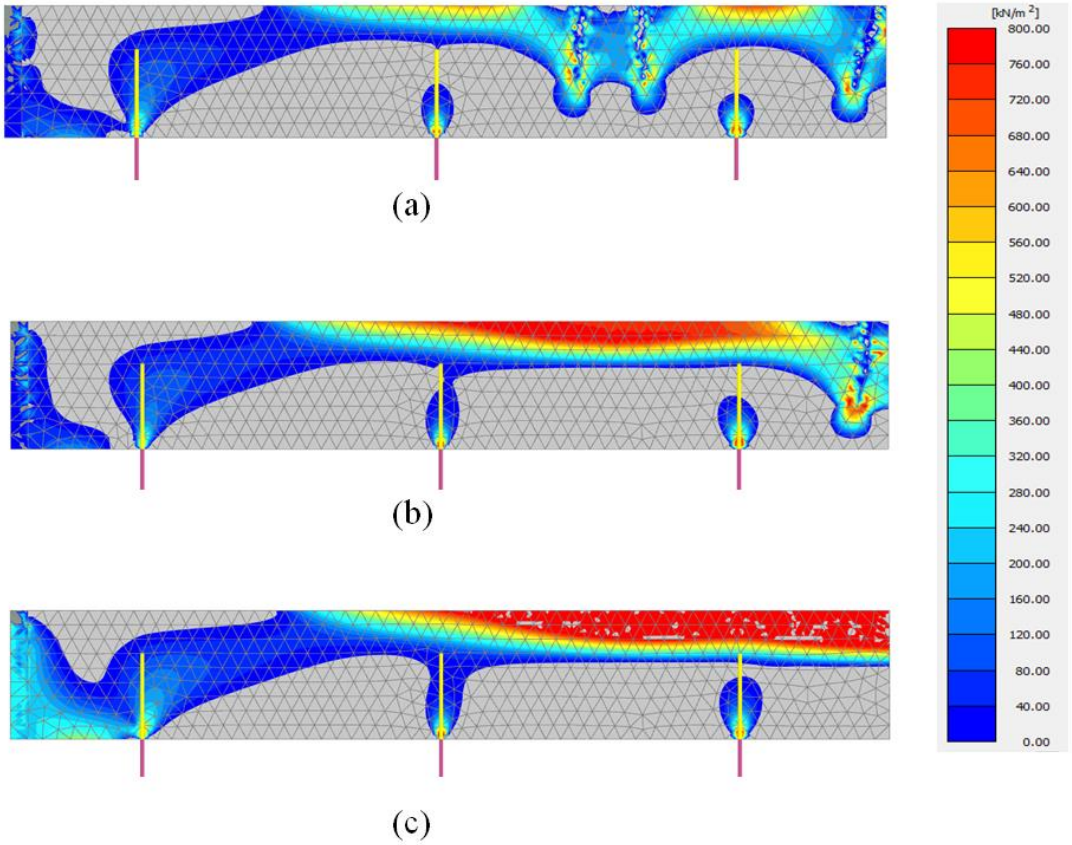

Fig. 78: Contour plot of principle stresses σ_3 in slab with 10GPa Stiffness: a) G_t=0.01 kN/m; b) G_t=0.05; kN/m c) MC

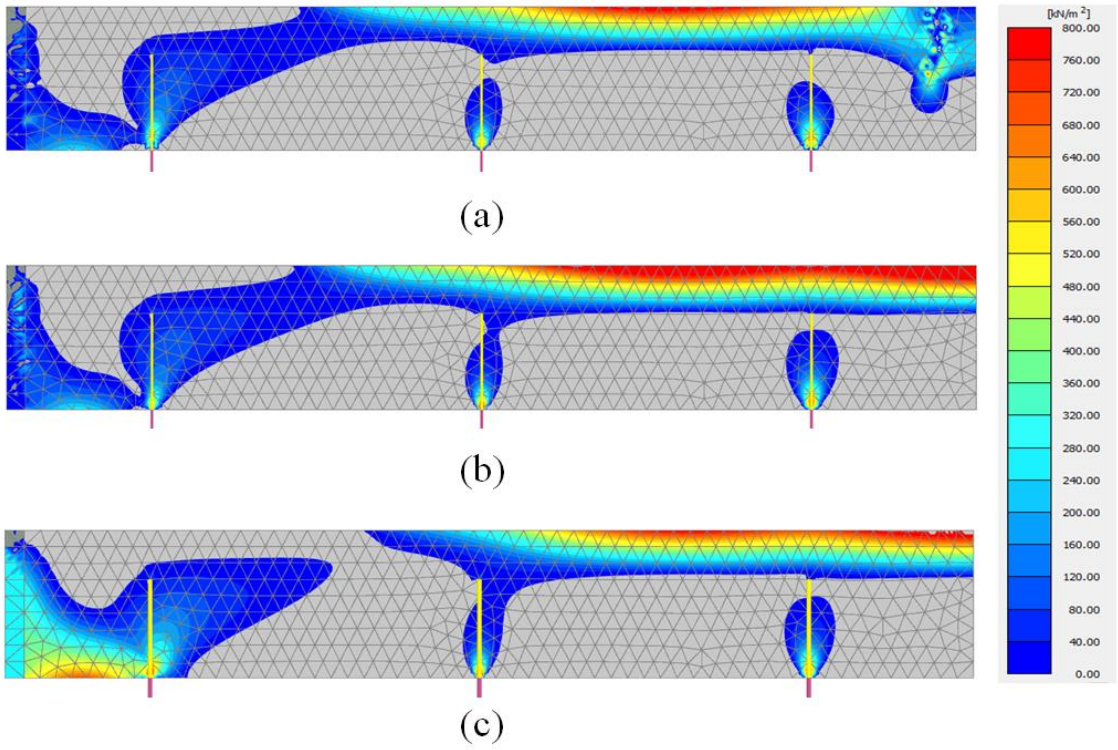

Fig. 79: Contour plot of principle stresses σ_3 in slab with 5GPa Stiffness: a) G_t=0.01 kN/m; b) G_t=0.05 kN/m; c) MC

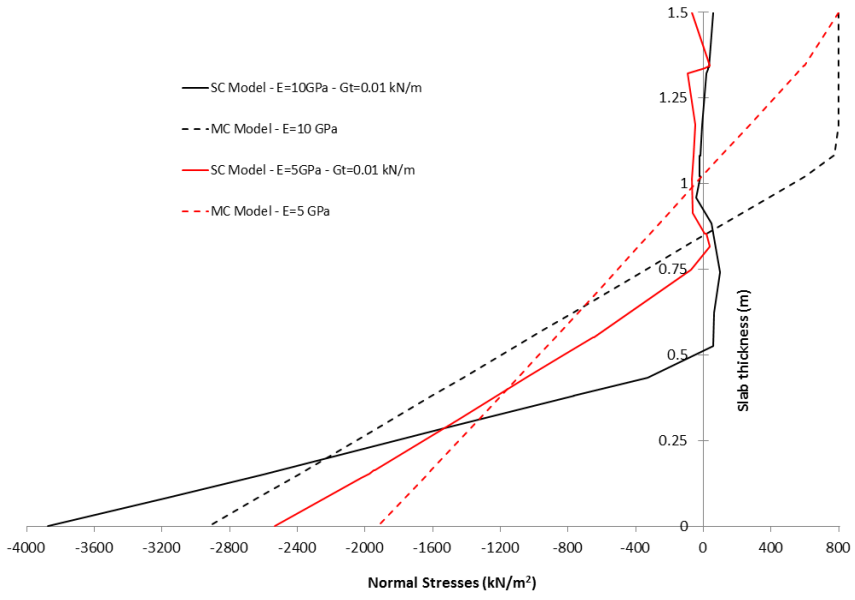

Fig. 80: Comparison of normal stresses across the slab

The same conclusion can be evoked from Figure 81 where bending moments are shown. It is evident that the bending capacity of the slab applying the Mohr-Coulomb criterion and 10GPa stiffness is significantly higher compared to the slab employing the new shotcrete model with 10GPa stiffness. However, the

bending moments of the slab (in the middle of the slab) where employing Mohr-Coulomb criterion with 5GPa stiffness is roughly similar to the analysis with the shotcrete model applying the same stiffness.

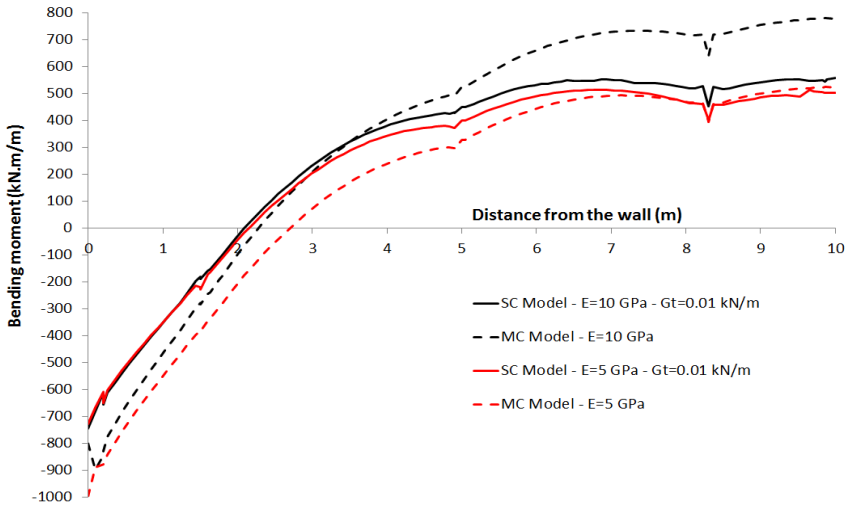

Fig. 81: Comparison of bending moments in slab

The horizontal stresses (σ'_{xx}) distribution of the top and bottom of the slab in calculations using the shotcrete model with 10GPa stiffness has been examined. It can be seen in Figure 82 that of the top where the cracks develop, the horizontal stresses are near zero and with the Mohr-coulomb criterion are equal to the tension cut-off limit. But, moving towards the wall the compressive stresses increase and in an area at the edge of the slab close to the wall these stresses highly exceed the uniaxial compressive strength of the jet grouting material (i.e. 8000kPa). This is caused by the confining effect in this small zone which is shown for instance in Figure 83, by depicting σ'_{xx}, σ'_1, σ'_3. Figure 84 depicts the horizontal stresses at the bottom of the slab where due to cracks compressive stresses have been increased. For the analysis using G_t=0.01kN/m cracks developed in two different locations in the middle part of the slab therefore two peaks of horizontal stresses are seen in its diagram. When G_t is 0.05kN/m only one crack can penetrates in the centre of the slab thus an increase in the stresses is observed in this part in the diagram. However, it is seen that with Mohr-coulomb model compressive stresses are smaller because no distinct cracks can be propagated at all. In addition, it can be seen in this Figure 84 that by using tension piles the compressive stresses at the bottom in mid-span is around half of the uniaxial compressive strength of the jet grouting compared to the analysis without piles (see Figure 61b), which failed at 11m excavation.

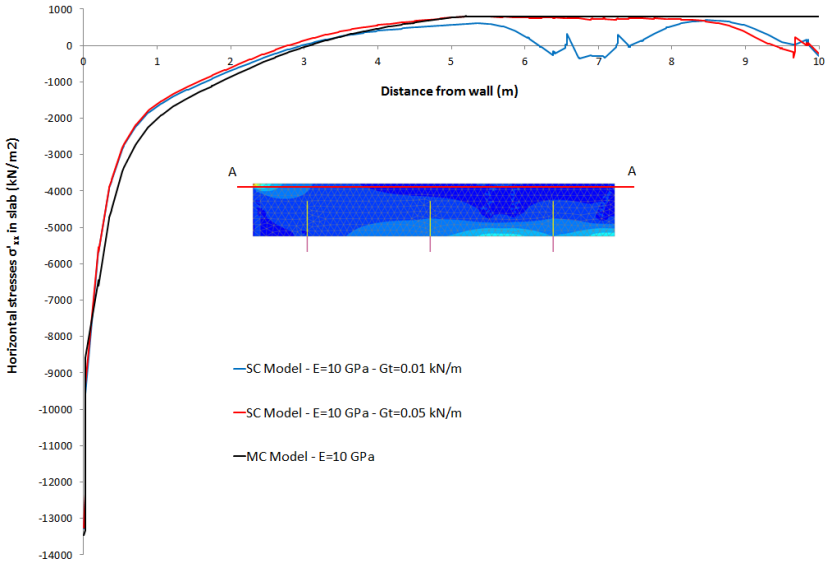

Fig. 82: Plot of horizontal stress σ'_{xx} on top of the slab (11m excavation)

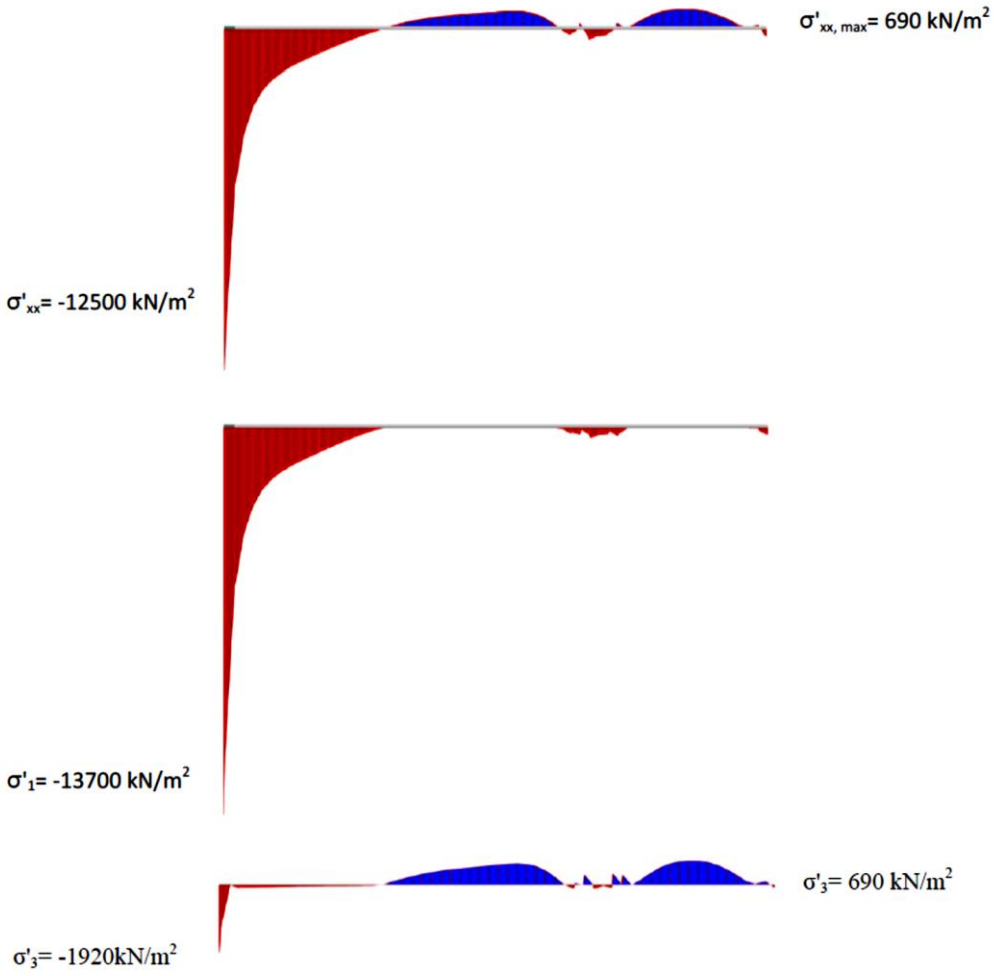

Fig. 83: Plot of horizontal stress σ'_{xx}, principal stresses σ'_1, σ'_3 in slab - E=10GPa, G_t=0.01 kN/m

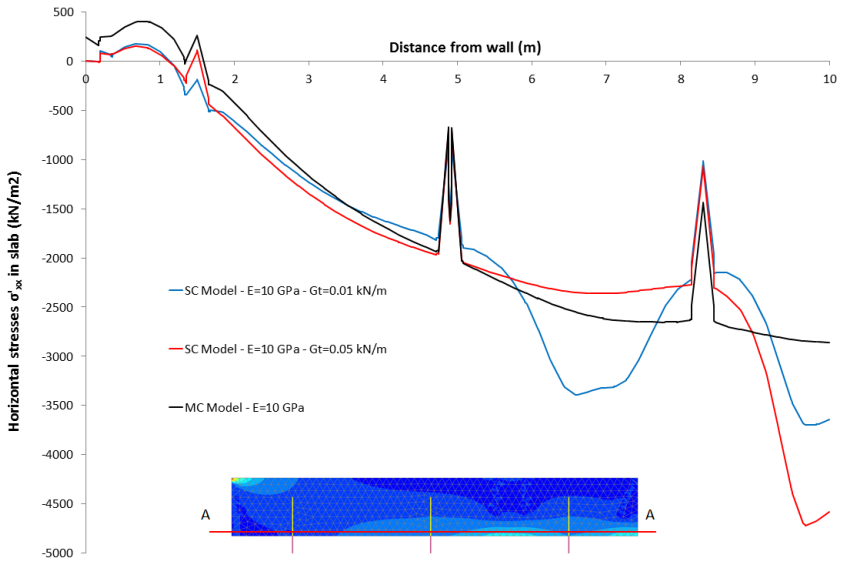

Fig. 84: Plot of horizontal stress σ'_{xx} at the bottom of slab (11m excavation)

Plotting the H_c parameter ($0<Hc<1$) for the analysis with E=10GPa and G_t=0.01 kN/m showed a small area near the wall showed a maximum H_c value equal to 1.57 which is in the softening zone but not at residual level (Figure 85).

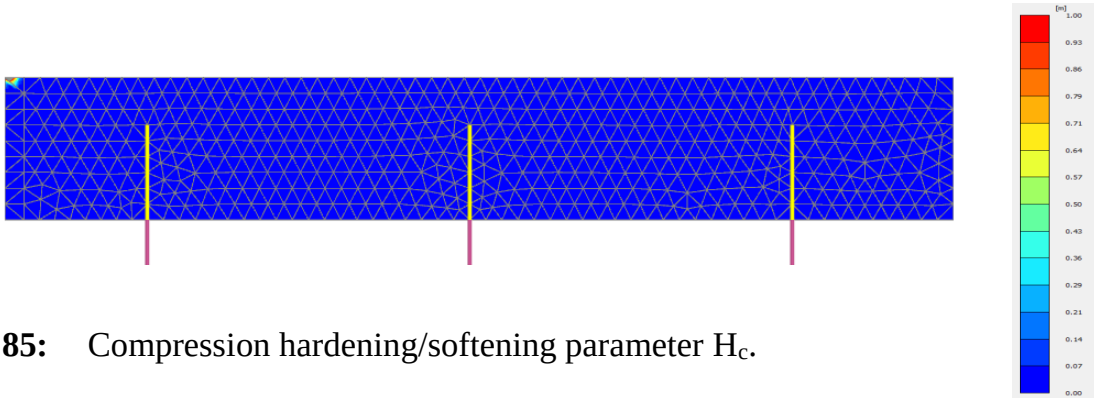

Fig. 85: Compression hardening/softening parameter H_c.

The embedded piles axial forces have been examined at the end of excavation for different calculations and various parameters. The pile force can be checked against the maximum allowable tension load, the bearing capacity of the single pile and the pile group capacity. The minimum value is accepted.

According to FHWA (2005), the maximum allowable tension load for uncased length of micro piles is equal to:

$P_{t\text{-allowable}}=0.55F_y\text{-bar}\times A_{bar}$ → P=735 kN

Where the yield stress of GEWI steel bar is 680 MPa and the bar diameter is 50mm.

Bearing capacity of the tension pile is given:

N= pile weight + shaft resistance → N=800kN

Based on the procedure for evaluating the pile-group uplift capacity in cohesionless soils FHWA (2005), the bearing capacity of each single pile was estimated roughly around 650kN. Therefore, the value of 650kN is accepted for the maximum axial force in the piles.

Figure 86 presents the axial forces in the piles for three different analysis using the shotcrete model and the Mohr-Coulomb criterion. As it is seen, the highest forces are imposed in the central pile (i.e. pile 3 in Figure 86) where the maximum slab deformation takes place. The axial forces in piles are the same for different fracture energy values (0.01 and 0.05 kN/m). The axial force in the central pile (pile 3) where the slab is modelled by Mohr-Coulomb criterion is smaller because in this analysis no cracks can develop in the mid-span and tensile stresses remain at 800kPa through one-third of the slab thickness. Therefore, the pile vertical displacement and consequently the relative displacement between pile and soil are smaller (Figure 87).

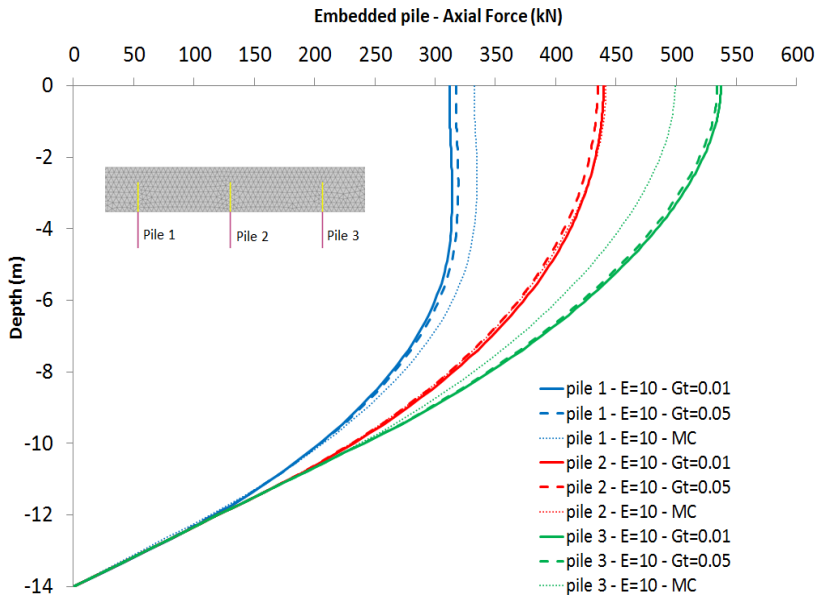

Fig. 86: Axial forces in embedded piles

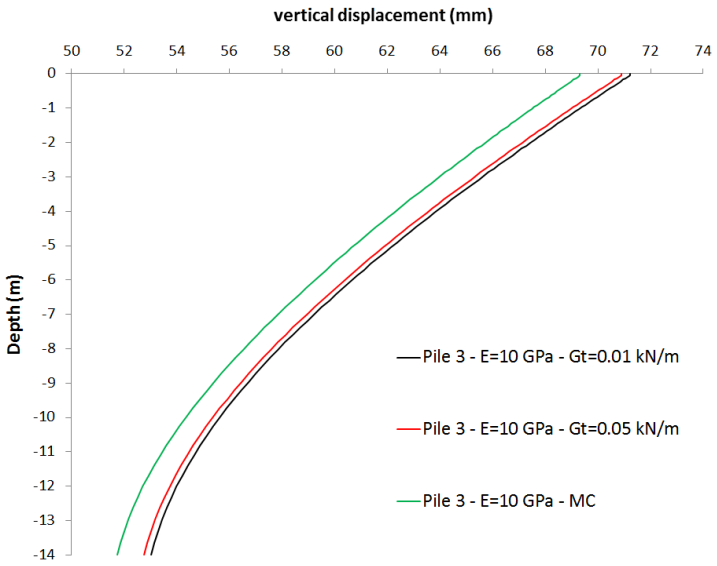

Fig. 87: Central embedded pile vertical displacement (pile 3)

4.1.4.2 Arched slab (Influence of slab geometry)

All analyses presented so far are with tension piles in place. As construction of these tension piles is a significant cost factor it is investigated whether or not a different geometry of the jet grout slab, namely in form of a staggered arch, would be a feasible alternative. The individual sections have a thickness of 2 m, i.e. the overlap at the boundary of the sections is 1.5m (Figure 88). The numerical analysis shows that it is indeed possible to achieve equilibrium with this system.

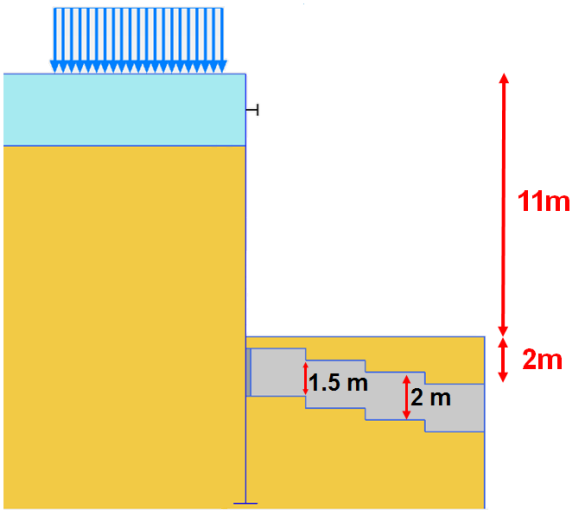

Fig. 88: Geometry of the arched slab

The crack patterns obtained by these calculations follow the Figures 89 and 90. In the analysis using G_t=0.01 kN/m cracks develop not only at the boundary of the sections but also near the wall. However, assuming a fracture energy of G_t is 0.05 kN/m, i.e. assuming a more ductile behaviour, reduces cracks significantly, and a crack only developed near the wall.

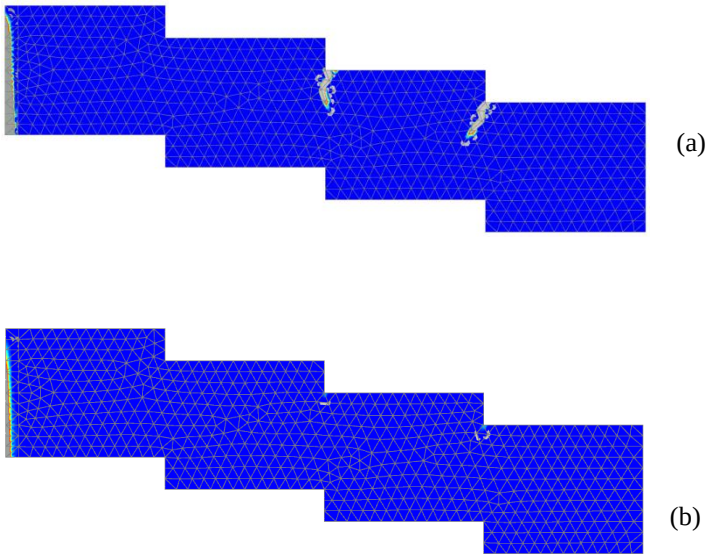

Fig. 89: Crack location in slab with 10GPa Stiffness. a) Gt=0.01 kN/m b) Gt=0.05 kN/m

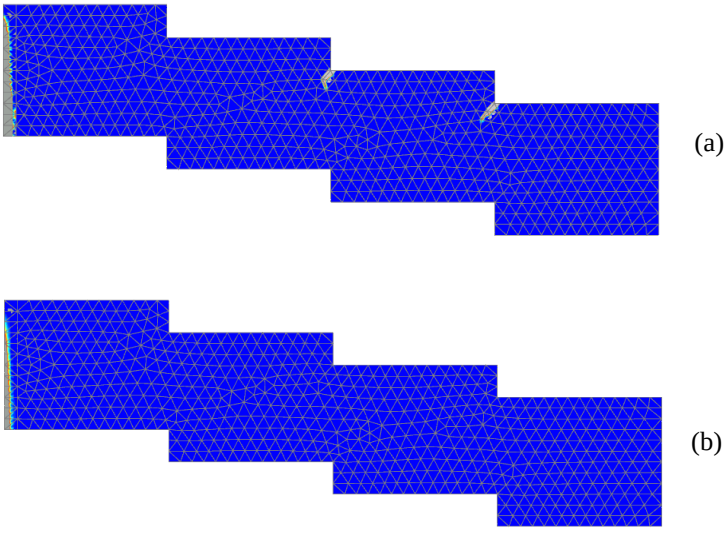

Fig. 90: Crack location in slab with 5GPa Stiffness. a) Gt=0.01 kN/m b) Gt=0.05 kN/m

The contour plot of σ_1 shows a very small part near the wall similar to the previous calculations in which stresses exceeded the peak compressive strength (Figure 91). Due to confining effect, peak strength has been increased in this zone. Figure 92 depict the horizontal stresses and normal forces near the wall and at the middle where a crack developed.

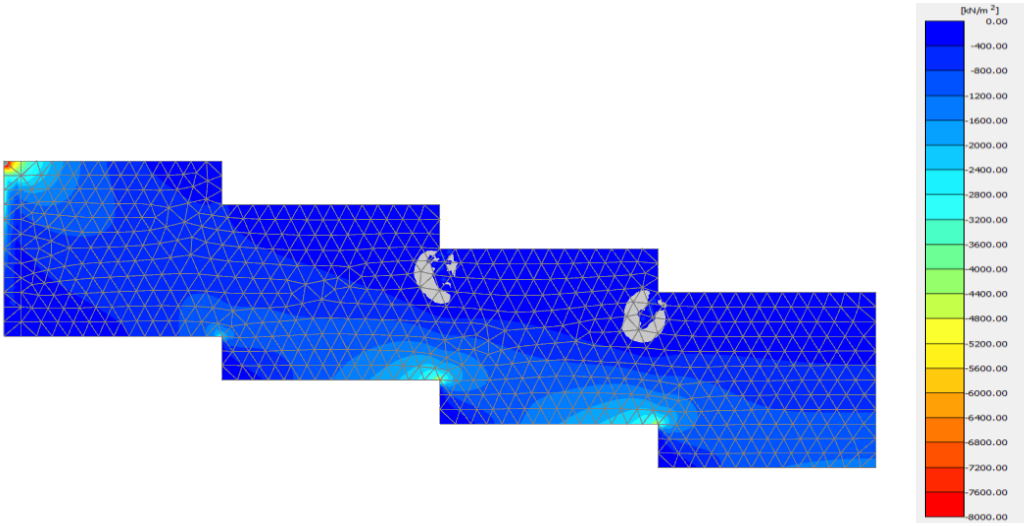

Fig. 91: Contour plot of principle stresses σ_1 in slab with 10GPa Stiffness and Gt=0.01 kN/m

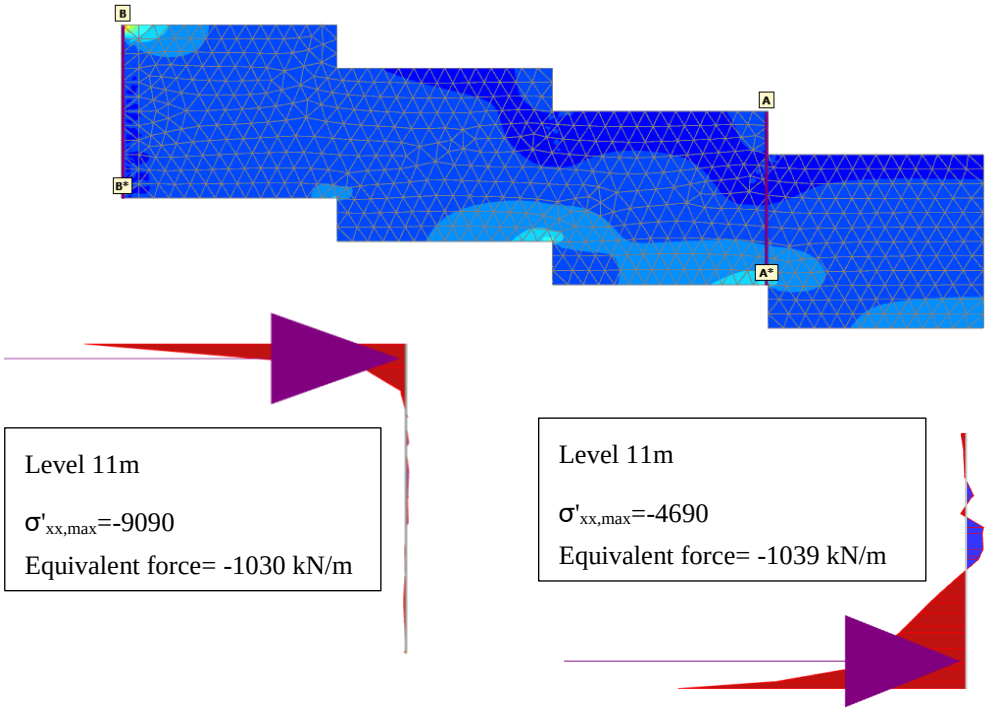

Fig. 92: Normal forces in slab – E=10GPa and Gt=0.01 kN/m

4.2 Deep excavation supported by row of deep soil mixing columns

4.2.1 Introduction

Deep soil mixing techniques with cement or lime-cement columns has been widely used since 40 years to reduce settlement and to improve stability of road embankments. In addition, this technique can be used to reinforce retaining structures (Rutherford et al. 2007). A newly developed method is to install a row or block of columns on the passive side in an interaction to sheet pile wall, which increase the passive resistance and act as improvement of the excavation bottom and foundation of the construction (Ignat et al. 2015).

A case study from Ignat et al. (2015) is used in this section, applying the new constitutive model to show the possible crack patterns and the orientation of cracks in intersected groups of columns. Therefore, the influence of various material parameters for the columns is investigated for a special case where the spacing between rows of columns is 1.5m. Furthermore, the obtained results are compared with the conditions where the Mohr-Coulomb criterion with tension cut-off limit is applied for the columns in order to highlight the different stress distribution.

4.2.2 Model description and material parameter

Figure 93 shows the 3D model with one row of columns. The model consists of 1m dry crust and 10.5m soft clay. A sheet pile wall with the height of 7m together with a steel wire anchor and a whaler beam support the excavation. A distributed load of 40kPa is applied on the surface adjacent to the sheet pile wall. The columns have the diameter of 60cm and are intersected with centre to centre distance of 50cm (i.e. 10cm overlap). The final shape of the supporting columns has a width and height of 7m. In order to decrease of the number of element and difficulties of mesh generation in overlapping zones an octagonal shape of columns has been chosen. The ground water table is one meter below the surface and excavation is performed up to the level of -4m. The construction stages include the installation of sheet pile wall, ground water lowering, 2m excavation and installation of columns, supporting beam and anchor (Pre-stressing force of 300kN), excavation up to level of -4m and loading. Since the excavation process and the loading were assumed to be exerted rapidly, the calculations were performed as an undrained effective stress analysis. The material parameters of the soil and undrained strength parameters are presented in Table 12. In the Plaxis the drainage type “undrained B” enables the modelling undrained behaviour using effective parameters for stiffness and undrained strength

parameters. Although this type of analysis for undrained behaviour is in general not recommended, it is performed here for the sake of simplicity and being compatible with the parameters presented in (Ignat et al. 2015). The sheet pile wall and the beam are PU12 type and HEB300 type respectively. The detail of material parameters of structural elements are the same as Ignat et al. (2015).

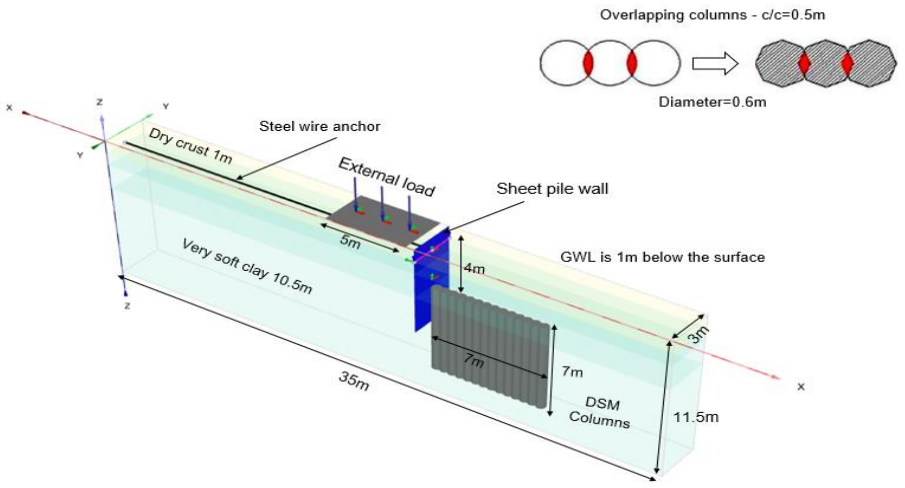

Fig. 93: 3D model of excavation supported by intersected columns with 1.5m spacing of rows of columns is (modified after Ignat et al. 2015)

Tab. 12: Material parameters of the soil layers.

soil layer	model	drainage	uint weight (kN/m^3)	E (kN/m^2)	ν (-)	S_u (kN/m^2)	K_0 (-)	$R_{int.}$ (-)
Crust	MC	undrained B	18	8000	0.33	40	1	0.5
Clay	MC	undrained B	16.5	250 S_u	0.33	10+1.5z	0.5	0.6

Two types of columns with different material parameters are used in this study to show the influence of the parameters on the softening behaviour of columns. The material parameters of columns type 1 refer to typical dry deep mixing lime-cement-treated clay and the second type is more common for cement-stabilized clay (Table 13).

Tab. 13: Material parameters of the columns for different analysis.

Columns	E (kPa)	f_c (kPa)	F_t (kPa)	ν (-)	$\varepsilon_{cp,28d}$ (%)	G_c (kN/m)	$f_{tu,n}$	$G_{t,28}$ (kN/m)	φ_{max} (°)
type1	20e3	200	10	0.3	0.01	0.1	0	10+1.5z	26
type2	350e3	1000	200	0.2	0.05	0.5	0	40	30

4.2.3 Results

The calculation without columns fails when applying the load of 40kN/m^2, but when columns are installed, no failure occurs. Figure 94 shows the deviatoric shear strains at the end of excavation that presents the initiation of failure zone in the soil and columns. A slip surface is generated under the sheet pile and develops through the columns and also the deviatoric shear strains develop in the zone below the columns. Results of the analysis using columns type1 (lower strength material) shows compression softening in the columns. Figure 95 shows the contour plot of compression hardening/softening parameter $0<H_c<1$ at the end of excavation. Where $H_c=1$ represents the zones that reached the maximum value of compressive strength and H_c higher than one represents the areas in the softening or the residual level.

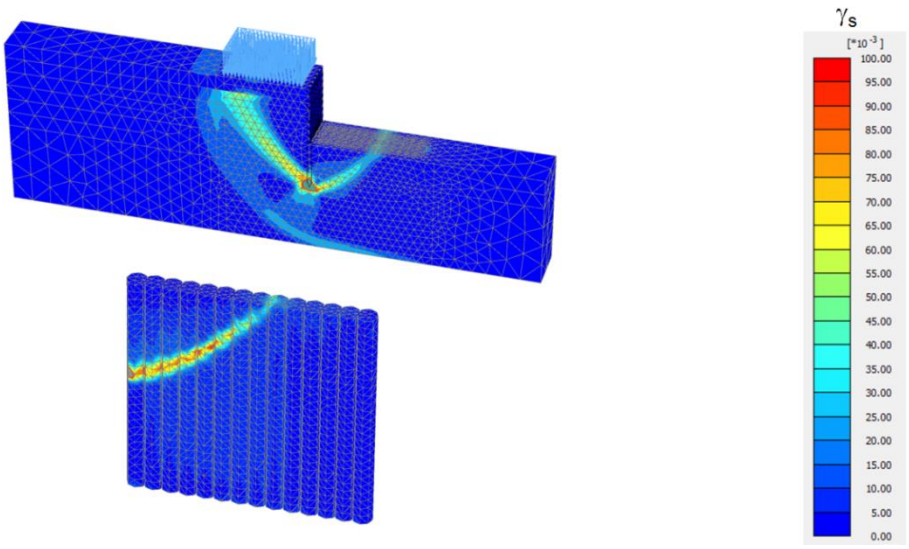

Fig. 94: Deviatoric shear strains at the end of excavation (-4m)

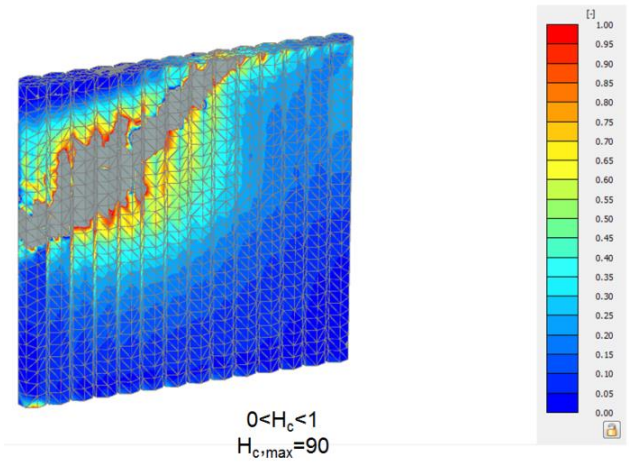

Fig. 95: Contour plot of hardening parameter H_c

To compare the stress distribution in the columns, the Mohr-Coulomb criterion has been applied to the columns. Figure 96 compares the obtained plastic points in the columns by employing the shotcrete model and MC model. The localization of plastic failure points can be clearly observed when the shotcrete model is applied while no distinct failure plane can be seen by MC model.

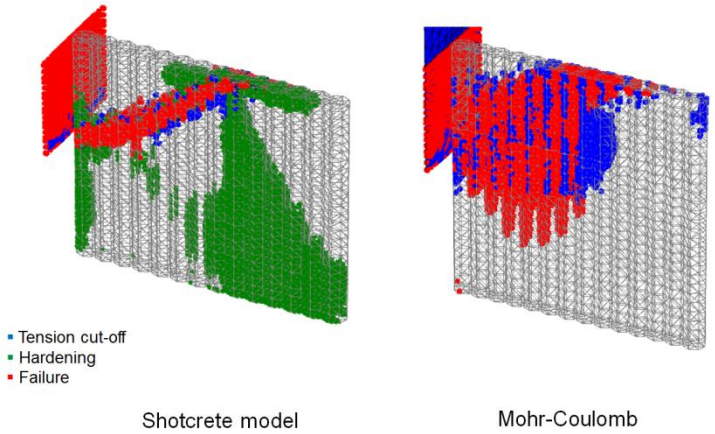

Fig. 96: Plastic points in the columns resulted from shotcrete model and MC model

In the following, stiffer columns (type 2) were used in the passive side. Figure 97 presents the developing of the deviatoric shear strain in the soil and columns together with the plastic points in the model. When stiffer columns (type2) are used, the direction of development of the deviatoric shear strains in the columns is different compared to the analysis with material type1.

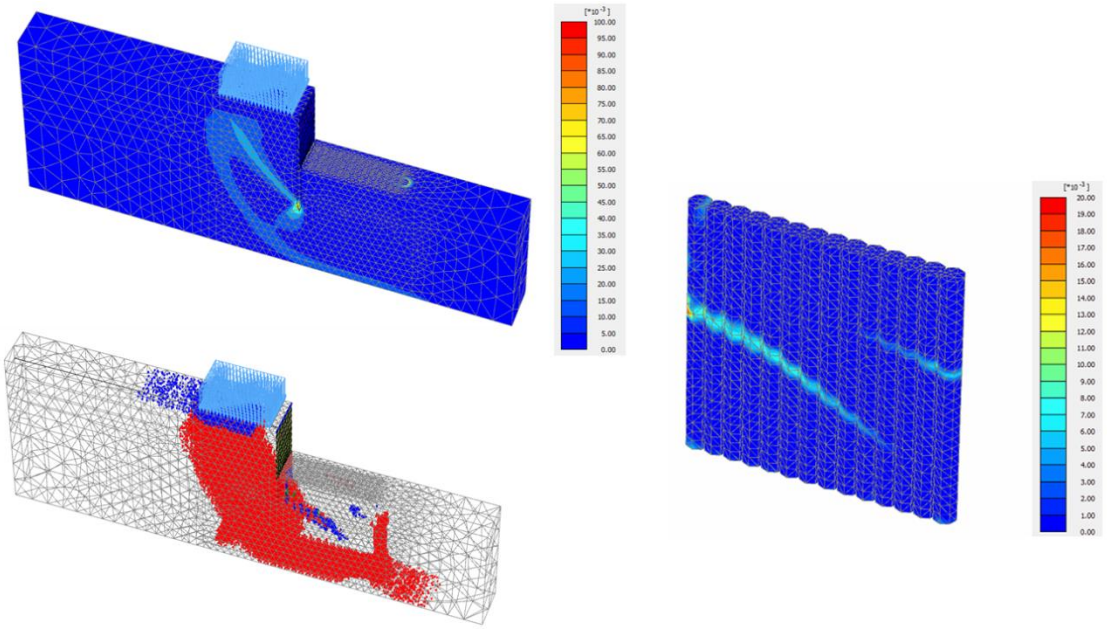

Fig. 97: Deviatoric shear strain in soil and columns and plastic points

Tension softening occurs when stiffer columns are utilized. The location of the tensile cracks and their orientation can be shown in Figure 98 by plotting the tension softening parameter H_t in the range of 0 to 1.

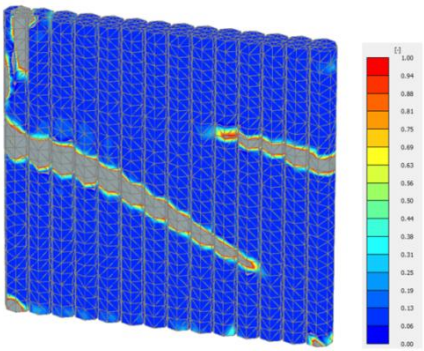

Fig. 98: The location and orientation of the tensile cracks ($0<H_t<1$)

The stress distribution in the columns is compared by applying the MC model to the columns. Figure 99 shows the distribution of principle stresses σ_3 in the columns where only tensile stresses are shown ($0<\sigma_3<100$). In addition, the corresponding plastic points are presented which prove that significantly different stress distribution is produced in the columns depending on the model employed.

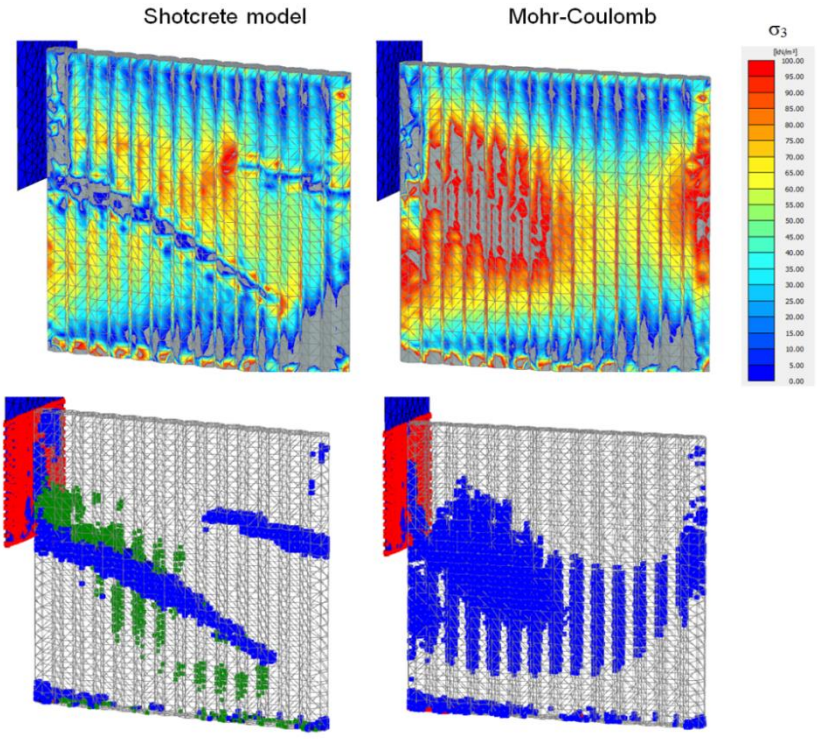

Fig. 99: Comparison of principal stresses and tension cut-off points

4.3 Summary and conclusion

Two different geotechnical problems were studied to show the applicability of a newly developed constitutive model for describing the mechanical behaviour of cemented materials. The first case was a deep excavation involving a jet-grout slab below an 11m excavation which was subjected to uplift pressure and where additional tension piles were required. The influence of the various modelling assumptions such as fracture energy, constitutive model and slab's geometry were investigated. Different results such as stress distribution, bending moment in the slab were compared to the condition where a simple elastic-perfectly plastic material model was employed for modelling the behaviour of the slab. The location of the tensile cracks and various crack patterns regarding to the fracture energy assumption were highlighted. Although no direct comparison with measurements is possible, it can be postulated that qualitatively realistic crack patterns are obtained. In addition, it could be shown that for a special geometry of slab the tension piles could be omitted.

The second example was a deep excavation supported by rows of overlapping deep mixed columns which were installed on the passive side of the excavation in an interaction to sheet pile wall. The influence of different material stiffness and strength on the results was investigated. Results revealed that the behaviour of the columns was different at the end of excavation depending on the material types. When the lower strength material was used in the analysis, compression softening occurred in the columns while with the stiffer material, tensile cracks developed in the columns. The location and orientation of the cracks could also be defined with the new constitutive model. Besides, in order to compare the obtained results and to emphasise on the ability of the new model to present the realistic stress distribution in the brittle columns, some analyses were performed by applying the Mohr-Coulomb criterion for the columns. When the new model was employed, a remarkably different stress distribution and consequently different zone of plastic points/failure points were obtained. However, when a brittle material is modelled with the elastic-perfectly plastic criterion, neither a distinct tensile crack nor its location and orientation can be highlighted. When the Mohr-Coulomb strength criterion was used with tension cut-off limit for the brittle cement-based material, a large area with plastic tension cut-off points were observed in the overlapping columns while with the shotcrete model a localization of the plastic tension cut-off points was obtained.

5 Methods of performing ground response analysis

One of the main goals of this thesis is to investigate the influence of ground improvement methods such as jet-grouting columns on the ground response of deposits. This chapter gives an overview of the importance of ground response analysis and briefly describes some methods of site response analysis. In addition, some expressions that will be used for the purpose of this thesis are explained. Finally, some considerations that must be taken into account when performing dynamic finite element analysis using Plaxis 2D/3D are discussed.

5.1 Site response analysis

Many earthquake events all over the world have demonstrated the effect of local site conditions on magnifying the earthquake load that acts at the bedrock level, and consequently affect the surface structures. This subject has been studied many years ago by Seed et al. (1976), who provided some considerations (e.g. the influence of local site on response spectral they produce) in design methods and for seismic building codes. Therefore, in order to have a better and safer structural design, a careful study of the local site effect is of great importance. Site response analysis determines the response of a soil deposit due to an earthquake excitation. This analysis is used to predict ground surface motions and consequently can determine the response spectra. It evaluates the liquefaction potential in soil layers by calculating the induced dynamic stresses and strains. In addition, it can be used to determine the earthquake induced forces in surface structures or buried structures in soils.

The effect of an applied dynamic force or imposed deformation, transfer through the soil/rock medium in the form of waves. The response of a continuum can be evaluated by a simulation of propagation of the seismic waves. Generally, when an earthquake occurs, different types of seismic waves are produced:

- Body waves
    - Primary waves (P-waves, compressional waves or longitudinal waves)
    - Shear waves (S-waves, secondary waves or transverse waves)
        - SH wave (horizontal plane movement)
        - SV wave (vertical plane movement)
- Surface waves (travel along the earth’s surface)
    - Rayleigh wave (produced by interaction of P and SV waves)
    - Love wave (produced by interaction SH waves and soft surficial layer)

For linear elastic materials, the following relationships hold:

$$V_p = \sqrt{\frac{G(2-2\nu)}{\rho(1-2\nu)}} \tag{20}$$

$$V_s = \sqrt{\frac{G}{\rho}} \tag{21}$$

Where G is shear modulus and ν is the Poisson's ratio and ρ is the density of the material.

For a complete site response analyses, the rupture mechanism at the source of an earthquake, the wave transition through the earth to the bedrock level beneath a particular site and the influence of the soil type of the site should be considered. However, in practice, mechanism of fault rupture is complicated and the energy transmission between source and site is uncertain. Empirical methods together with seismic hazard analyses are therefore used to predict bedrock motions at the site.

5.2 Earthquake motion characterization

Before doing site response analysis and evaluate the effect of earthquakes at a particular sites, the ground motion has to be characterized. Each earthquake can be defined by the following features:

- Time history (displacement, velocity or acceleration versus time)
- Ground motion parameters
    - Amplitude (peak values, e.g. peak ground acceleration PGA)
    - Frequency content (predominant frequency f_p)
    - Duration (δt)

In order to provide more knowledge about the dominant frequency of an earthquake, one can use a Fourier amplitude spectrum, which is computed by means of the fast Fourier transformation (FFT) of the time-history. By using Fourier series, the motion can be described mathematically by summation of series of harmonic functions with different amplitudes, frequency and phase angle. Any periodic function can be written as:

$$u(t) = a_0 + \sum_{1}^{\infty} a_n \sin(\omega_n t + \phi_n) \tag{22}$$

Where a_0 is the mean value of u(t), a_n is the amplitude, ω_n represents the frequency and ϕ_n is the phase angle.

The Fourier amplitude spectrum shows how the amplitude of a motion is distributed in frequency ranges. This also means that the frequency content of a given accelerogram can be fully determined.

The concepts such as low and high amplitude, short and long duration, low and high frequency motion is shown in Figure 100.

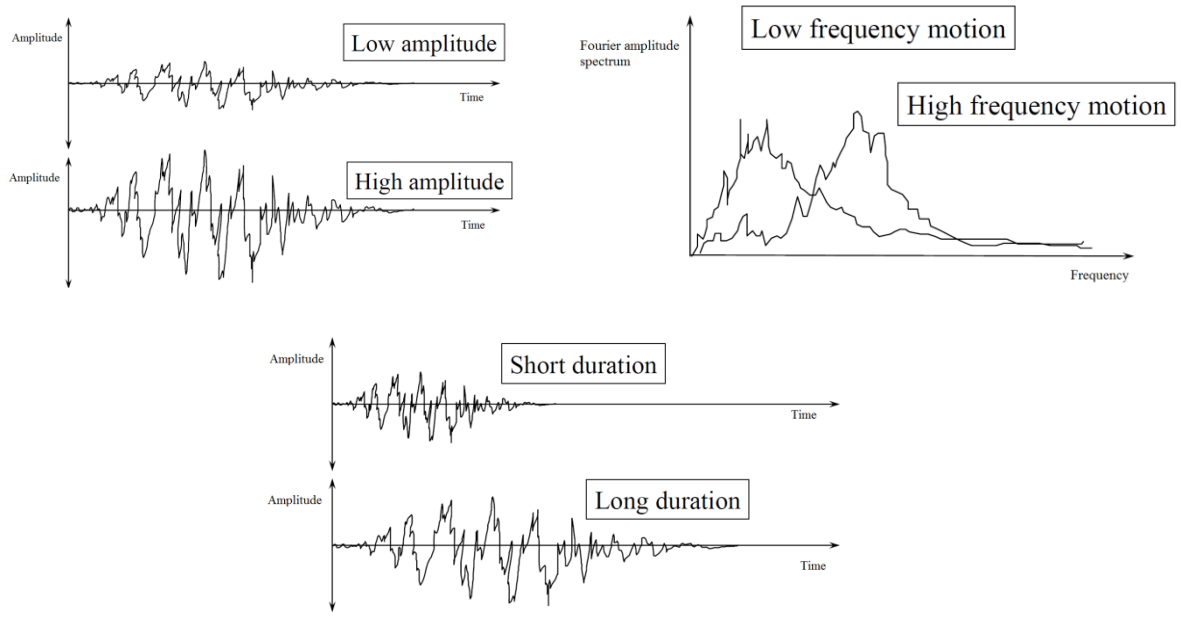

Fig. 100: Various ground motion conditions

5.3 Dynamic soil behaviour

Seismic surface motion is mainly governed by dynamic properties of soils which is determined by their cyclic non-linear behaviour. Dynamic behaviour of soils can be obtained in the field and in the laboratory via various standard test procedures which is categorized based on the level of shear strain they produce, defined as low strains limit (i.e. smaller than 10^{-5}) and high strain range (i.e. higher than 1%). For in-situ measurements usually geophysical tests are used which propagates seismic waves from a source through the soil at low strain level (10^{-5}) and interpret the arrival time at receivers. Soil behaviour in shear strain level equal to 10^{-2} becomes nonlinear and at shear strain level higher than 10^{-3} the

behaviour remains nonlinear and plastic deformations occur. Geophysical methods are only applicable for strain levels below 10e-4 and include seismic reflection and refraction, Cross-hole, Down-hole and Up-hole techniques, steady-state surface technique, Spectral analysis of surface waves, Suspension PS logging and Seismic Cone Penetration test SCPT (Luna & Jadi 2000).

In laboratory, the dynamic properties can be defined by resonant column tests; piezoelectric bender element and ultrasonic pulse tests at low-strain levels and the cyclic triaxial test, cyclic direct simple shear test, and cyclic torsional shear test are used in higher strain level (Woods 1991, Ali et al. 2013). The selection of the proper test method for a specific problem requires comprehensive knowledge and understating of the associated level of strain. Beside these tests, centrifuge and shaking table are also used to study the dynamic soil behaviour where cyclic loading exerted to small-scale models.

Important dynamic soil parameters are Shear wave velocity (V_{s0}), Maximum shear modulus (G_{max}), Shear modulus G_{sec} (varies with shear strain), damping ratio which is also changes with respect to shear strain and the Poisson's ratio. Accurate measure of these two parameters is necessary to solve geotechnical earthquake problems.

5.4 Cyclic stress-strain behaviour of soils

Soils exhibit non-linear and inelastic behaviour when subjected to dynamic loading. To solve geotechnical earthquake problems, simple and advanced models are available that can approximate the complex behaviour of soil. Use of each model requires knowledge about the limitations and assumptions and input parameters. Some of these models are discussed in the following.

5.4.1 Equivalent linear representation

When a soil undergoes symmetric cyclic loading with constant amplitude, a hysteresis loop is produced in (τ-γ) plane. The surface and inclination of this loop is related to the strain amplitude. The larger shear strains produce a wider and flatter loop (Figure 101). The shape of the loop has proven that is not affected by loading rate and as the cycles have no longer constant amplitude the description of the behaviour becomes more complex (Pecker 2007).

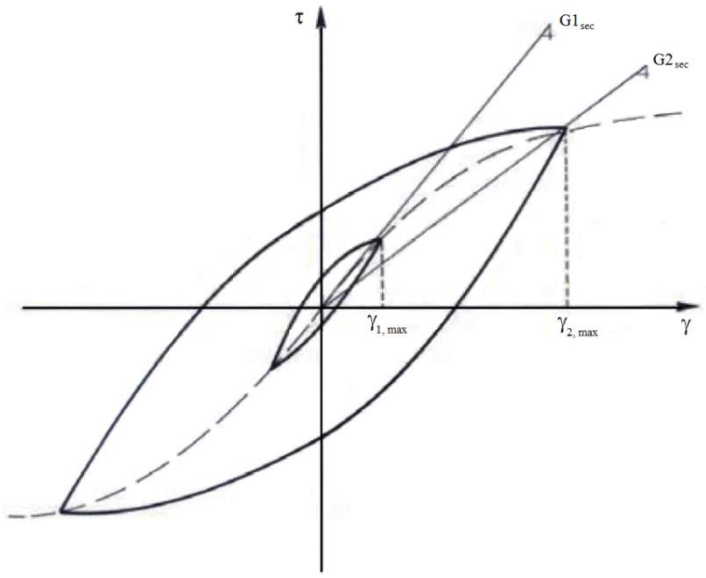

Fig. 101: Shear stress vs shear strain for constant amplitude cyclic loading (After Pecker 2007)

In order to describe the shape of this loop, two parameters namely shear modulus and damping is required. The shear modulus at strain levels can be described by G_{tan} (see Figure 102). The average shear modulus (G_{sec}) over one cycle of loading, i.e. the shear modulus corresponding to the tip of the loop is defined as:

$$G_{sec} = \frac{\tau_c}{\gamma_c} \tag{23}$$

where τ_c and γ_c are the shear stress and shear strain amplitudes in one hysteresis loop, respectively.

The width of the hysteresis loop indicates energy dissipation (Figure 102). Damping is often expressed as the damping ratio ξ and can be obtained from the hysteresis loop by dividing the area of the loop by a triangular zone defined by the secant shear modulus and the maximum strain (energy dissipated in one cycle by the peak energy during a cycle).

$$\xi = \frac{\Delta W}{4\pi W} = \frac{1}{2\pi}\frac{A_{loop}}{G_{sec}\gamma_c^2} \tag{24}$$

Where ΔW is the dissipated energy, W is the maximum strain energy, and A_{loop} the area of the hysteresis loop.

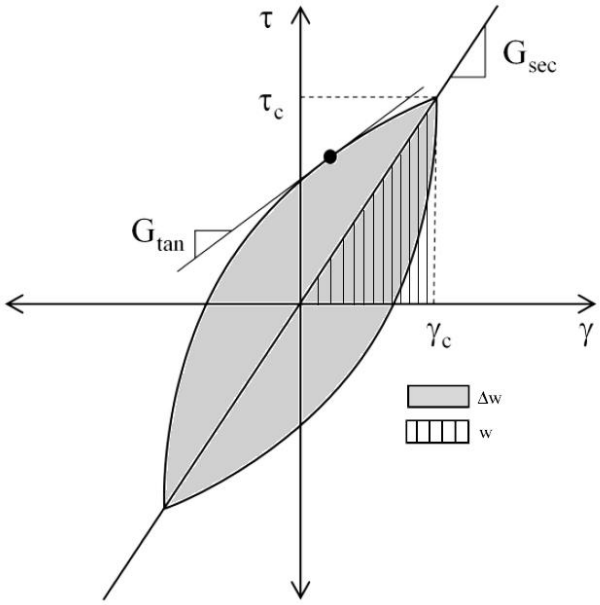

Fig. 102: Hysteresis loop-presenting secant and tangent modulus (After Kramer 1996)

5.4.1.1 Shear modulus degradation curves

Various types of loops will be created by change of strain amplitude during loading and the locus of the points corresponding to the tips of produced loop, shape the backbone curve. Secant shear modulus decreases as the shear strain increases. The maximum shear modulus is obtained at very low shear strains. Figure 103 presents the shear modulus reduction curve that is obtained by normalizing the secant shear modulus (G_{sec}) with the maximum shear modulus (G_{max}).

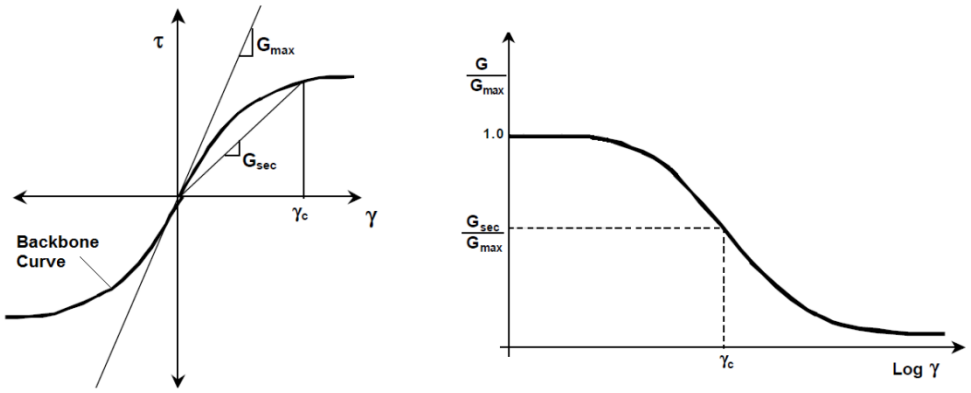

Fig. 103: Backbone curve (left); shear modulus reduction curve (right) (Kramer 1996)

Many factors affect the stiffness of soils, such as, plasticity index, relative density, mean principal effective stress, over-consolidation ratio, number of cycles and void ratio (Benz 2006). The maximum shear modulus can be calculated based on shear wave velocity measured by geophysical methods in the low strain range by means of the equation $G_{max}=\rho V_s^2$.

5.4.1.2 Damping ratio

The ability of a material to dissipate dynamic load or dampen the system is known as damping ratio. When the shear strains are increased, the soil body loses its stiffness and its damping effect is enhanced subsequently. This energy dissipation in soils can be caused by friction, plastic deformation or heat. The relationship of damping and shear strain is inversely compared to the shear modulus versus shear strains (Figure 104). Higher shear strains produce much more damping ability in soils.

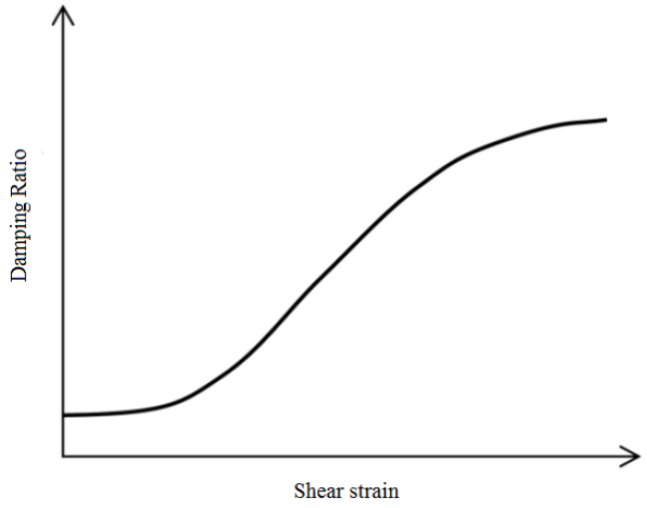

Fig. 104: Schematic variation of damping ratio with cyclic shear strain

5.4.2 Cyclic non-linear models

When soil undergoes large strain ranges during dynamic loads, significant changes occur in the soil skeleton, which induce irrecoverable volumetric and shear strains. On the other hand, increase in pore pressures may cause the effective stresses become equal to zero and liquefaction phenomenon may occurs. Increase in pore pressure can also decrease the soil stiffness even if liquefaction is not occurred. Therefore, proper non-linear models are required to

capture the non-linearity of saturated soil behaviour together with irrecoverable strains (Pecker 2007). Cyclic non-linear models follow the true stress-strain path and are able to capture the non-linear behaviour of the soil during cyclic loading. Generally, these models are characterized by a backbone curve and series of rules that governs the unloading-reloading and shear modulus degradation.

5.4.3 Advanced constitutive models

A number of advanced models to describe soil behaviour for general initial stress conditions, various stress paths, rotating principal axes, cyclic or monotonic loading, high or low strain levels and different drainage conditions are published in the literature.

However, it must be noticed that highly advanced models are rarely used in practice due to their difficulties for choosing the most appropriate model, high number of input parameters, correct measuring of input parameters and the high level of experience required for performing the dynamic analyses (Pecker 2007, Kramer 1996)

5.5 One-Dimensional Ground response analysis

As mentioned earlier site response analysis is performed by a simulation of propagation of seismic waves. Wave propagation can be described by the solution of the dynamic equation of motion combined with a stress strain behaviour of the material (i.e. constitutive model). Due to simplicity and providing reasonable results, the one-dimensional analysis is used more frequently in practice where soil shear strength is one of the most important factors. It has been well proven by researchers that the soil shear strength reduces during earthquakes due to non-linear behaviour. In one-dimensional analysis, it is assumed that the shear waves are propagating vertically through horizontal soil layers which are laterally extended to infinity. There are many codes available for performing 1D site response analysis such as SHAKE (Schnabel et al. 1972) and DEEPSOIL (Hashash & Park, 2001). The soil can be modelled in these codes based on linear viscoelastic (Kelvin-Voigt model), equivalent linear or non-linear model. A brief description of the various methods is given herein.

5.5.1 Linear method

One of the simple techniques that are used for ground response analysis is based on using transfer functions. Transfer functions can be used to express various response parameters such as displacement, velocity, acceleration, shear stresses and strains to bedrock acceleration (Kramer 1996). This method can be summarised as follows:

- A time history i.e. an earthquake record (acceleration-time diagram) at bedrock level is represented as a Fourier series using Fourier transform in the form of amplitude vs frequency instead of a function of a time.
- Each term in the Fourier series of the bedrock motion is then multiplied by the transfer function to produce the Fourier series of the ground surface motion.
- Finally, the Fourier series of the ground motion can then be translated to a function of time using inverse Fourier transform.

The transfer function shows how each frequency of bedrock motion is amplified, or de-amplified by the soil layers. It behaves as a filter that acts upon some input signal to produce an output signal.

It must be emphasised that the Fourier analysis in only applicable to linear systems because it is based on the principle of superposition. In this method, shear modulus and damping are required to be constant for each soil layers and therefore they must be correctly estimated.

Roesset (1970) proposed an analytical solution for a visco-elastic homogenous soil layer that lies on rigid bedrock. When the soil properties i.e. density (ρ) total unit weight (γ_{soil}), shear wave velocity at seismic level (V_s) and the corresponding damping ratio (D) are known the amplification function in terms of frequency (f) is given by:

$$A(f) = \frac{1}{\sqrt{\cos^2 F + (DF)^2}} = \frac{1}{\sqrt{\cos^2(2\pi \frac{H}{V_s} f) + (2\pi Df \frac{H}{V_s})^2}} \qquad (25)$$

Where F is the frequency factor and defined as:

$$F = \omega \frac{H}{V_s} = 2\pi f \frac{H}{V_s} \tag{26}$$

The n-th natural frequency of the homogeneous soil layer is given by:

$$f = \frac{\omega_n}{2\pi} \cong \frac{V_s}{4H}(2n-1) \tag{27}$$

In case of layered soil with N number of soil layer with the thickness of (h_i) and shear wave velocity of (v_i), the equivalent shear wave velocity ($V_{i,equiv.}$) can be defined as:

$$V_{i,equiv.} = \frac{\sum_1^N h_i}{\sum_1^N \frac{h_i}{v_i}} \tag{28}$$

More details about the linear approach and various transfer functions for homogeneous and layered soil on rigid or elastic bedrock conditions can be found in e.g. Kramer (1996) and Towhata (2008).

A visco-elastic soil is usually modelled as Kelvin-Voigt material. In this model, total resistance against shear deformations is given by an elastic and viscous component, i.e. spring and dashpot (Figure 105). The stress-strain relationship can be expressed with the following equation:

$$\tau = G\gamma + \eta \frac{\partial \gamma}{\partial t} \tag{29}$$

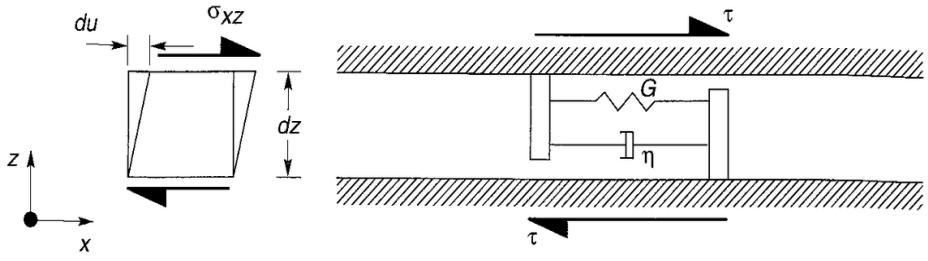

Fig. 105: A Kelvin-Voigt element subjected to horizontal shearing

Where $\tau=\sigma_{xz}$ is the shear stress, $\gamma=(\gamma = \partial u/\partial t)$ is the shear strain, $(\partial\gamma/\partial t)$ is the shear strain rate and η represents the viscosity of soil. In this way, the shear strain is the sum of an elastic part and a viscous part. In case of harmonic shear strain where $= \gamma_0 sin\omega t$, the shear stress is:

$$\tau = G\gamma_0 \sin\omega t + \omega\eta\gamma_0 \cos\omega t \tag{30}$$

The Equations 30 together with the equation $\gamma = \gamma_0 sin\omega t$ indicate that stress-strain loop shape is elliptical. The elastic energy dissipated is given by:

$$\Delta W = \int_{t_0}^{t_0+2\pi/\omega} \tau \frac{\partial\gamma}{\partial t} dt = \pi\eta\omega\gamma_0^2 \tag{31}$$

It can be observed that the dissipated energy is proportional to the frequency of the load. In contrast, real soil behaviour dissipates the energy hysteretically by grains slipping which means that the energy dissipation is independent of frequency. In Kelvin-Voigt model, damping ratio is related to stress-strain loop (Figure 106).

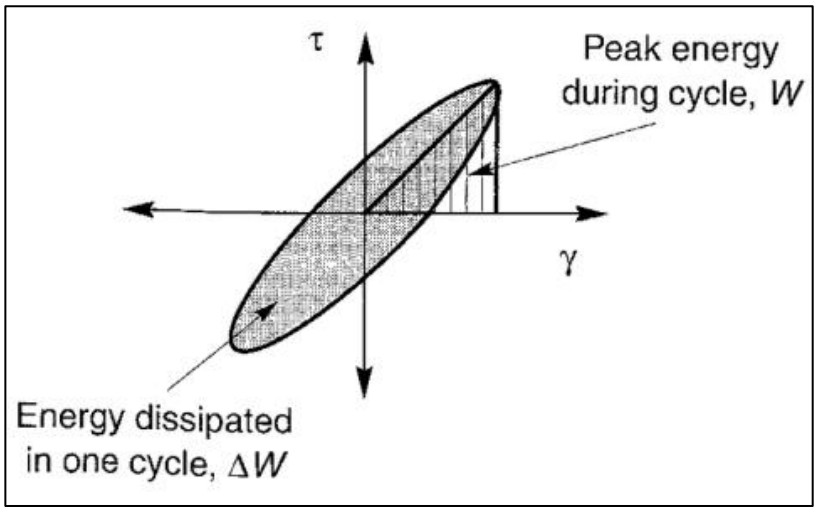

Fig. 106: Representation of damping ratio in Kelvin-Voight model (Krammer 1996)

The peak energy in the cycle is calculated by:

$$W = \frac{1}{2} G \gamma_0^2 \tag{32}$$

Therefore, the damping ratio is given by:

$$\xi = \frac{1}{4\pi} \frac{\Delta W}{W} = \frac{1}{4\pi} \frac{\pi \eta \omega \gamma_0^2}{\frac{1}{2} G \gamma_0^2} = \frac{\eta \omega}{2G} \tag{33}$$

In order to eliminate frequency dependence in Equation 33 an equivalent viscosity is introduced to ensure that the damping is frequency independent:

$$\eta = \frac{2G}{\omega} \xi \tag{34}$$

Considering a mass of very small Kelvin-Voigt elements, the one-dimensional equation of motion for a condition that shear waves are propagating vertically through the medium is expressed as:

$$\rho \frac{\partial^2 u}{dt^2} = \frac{\partial \sigma_{zx}}{\partial z} = \frac{\partial \tau}{\partial z} \tag{35}$$

By substituting Equation 29 in to Equation 35 the wave equation is:

$$\rho \frac{\partial^2 u}{dt^2} = G \frac{\partial^2 u}{\partial z^2} + \eta \frac{\partial^3 u}{\partial z^2 \partial t} \tag{36}$$

For harmonic waves, the displacement is:

$$u(z,t) = U(z)e^{i\omega t} \tag{37}$$

when the Equation 37 is substituted into Equation 36 it leads to:

$$(G + i\omega\eta)\frac{d^2U}{dz^2} = -\rho\omega^2 U \tag{38}$$

Where $(G + i\omega\eta)$ is called complex shear modulus G^* and by removing the frequency dependency, it is expressed as $G^*=G+2i\xi$.

G^* presents the complex valued secant modulus that must yield the same stiffness and damping properties as the real material. In the frequency domain analysis, it is recommended to use the frequency independent complex shear modulus which results in frequency independent damping (Hashash et al. 2015b).

5.5.2 Equivalent linear method

The equivalent linear model is considered as a modified version of the Kelvin-Voigt model. In one-dimensional analysis using equivalent linear method with an iterative procedure, the final seismic shear strain induced by the earthquake is calculated and the corresponding secant shear modulus and damping ratio in the soil layer(s) can be obtained from curves (i.e. shear modulus degradation curves and damping curves), available in the literature. First iteration generally starts using G_{max} and a small value of damping ratio which leads to a new shear strain level, then effective shear stain (γ_{eff}) is calculated and the corresponding secant shear modulus and damping ratio (G, D) are selected for the next iteration until compatibility is reached (Figure 107). Effective shear strain is calculated as a percentage of maximum shear strain (γ_{max}). The effective shear strain ratio (SSR) is related to the earthquake magnitude (M):

$$SSR = \frac{M-1}{10} \tag{39}$$

This value empirically varies between 50% and 70%. The default and recommended value in DEEPSOIL code is 0.65.

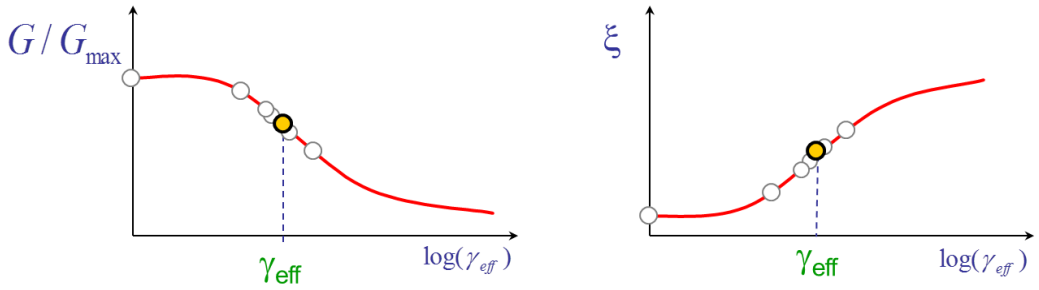

Fig. 107: Schematic iterative procedure applied in equivalent linear method

Beside the advantages and simplicity of this method there are also some weaknesses and limitations that must be taken into account when applying the equivalent linear method. The ground shaking level should not be higher than 0.4g or the peak shear strain should not exceed about 2% (Zheng et al. 2010). Based on the recommendation of Ishihara (1986), The Figure 108 presents the shear strain level in which the viscoelastic model and the equivalent linear methods of response analysis are valid.

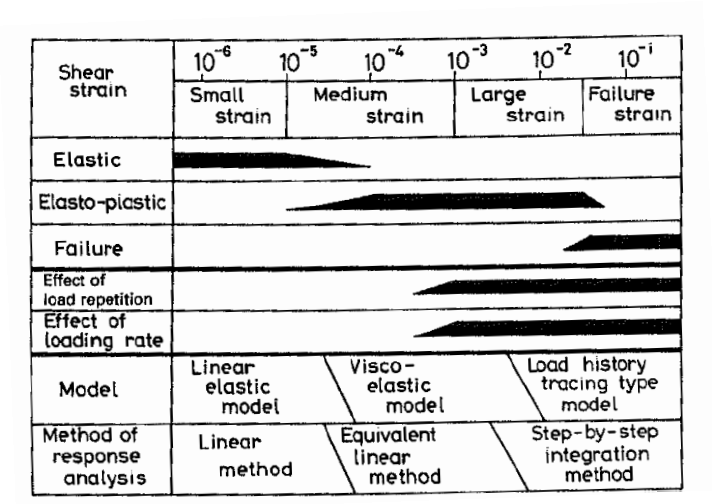

Fig. 108: Choose of suitable material model and method of analysis with respect to shear strain level (Ishihara 1986)

Although the equivalent linear method is an approximation compared to non-linear methods and despite all the weaknesses, this method has been widely applied as a simple and favourable approach for dynamic analysis of soil structure interaction (SSI) since most structural software can only deal with the equivalent linear method (Fatahi & Tabatabaiefar 2014).

5.5.3 Non-linear approach

This approach in ground response analysis is an alternative to the equivalent linear method for approximating real soil behaviour. This method applies direct numerical integration in time domain to simulate the soil behaviour. By integrating the equation of motion in small time steps, any type of material model can be incorporated. The nonlinear material behaviour is assumed to be incrementally linear, and at each time step the appropriate soil properties can be obtained from the stress-strain relationship of soil. With this approach, a more realistic behaviour of soil is captured. Non-linear approach is also capable to model the generation/dissipation of pore water pressure.

5.6 2D and 3D analysis

In order to perform ground response analysis to evaluate the local site effects, it is common to use one-dimensional analysis in practice. However, powerful 2D or 3D analyses are required in conditions where there are ground improvement elements or where soil-structure-interaction is studied. Furthermore, when buried and surface structures exist, and in the sites with complex geometry, the assumption of using 1D analysis by vertically propagating waves from bedrock to surface will not be valid anymore. For these cases, a dynamic finite element or finite difference method is required.

5.7 Calculation of ground response

As mentioned, there are two methods for evaluating the response of soil deposits to earthquake loading.

1- Frequency domain

2- Time domain

Frequency domain method applies a transfer function while time domain is based on numerical integrations. Table 14 compares some advantage and disadvantages of frequency and time domain solutions.

Tab. 14: Comparison between Frequency and time domain analysis

	Frequency domain	Time domain
Linear analysis	Yes	Yes
Non-Linear analysis	Equivalent linear shear modulus	Yes
Method of Analysis	1D (e.g. SHAKE, DEEPSOIL)	1D (e.g. DEEPSOIL) 2D and 3D (e.g. PLAXIS, FLAC)
Simplicity	Simple and few number of parameters	Advanced soil model with complex input parameters
Computational efforts	Low	High
Real soil behaviour	is not captured	is captured
Pore pressure generation/dissipation	No	Yes
Response analysis	Yes	Yes
Deformation evaluation	No	Yes
Damping	Viscous damping	Viscous and hysteretic

5.8 Amplification ratio

As mentioned earlier in this chapter, soil deposits can amplify (or de-amplify) the earthquake that act at the bedrock level (Figure 109). One of the useful expressions that can presents the amplification/de-amplification of bedrock motion by soil deposits at each frequency, is the amplification ratio. At the end of ground response analysis, the Fourier amplitude spectrum of the free surface motion is computed, on the other hand the Fourier amplitude spectrum of the given bedrock motion is known and therefore, the amplification ratio can be calculated as follows:

$$\text{Amplification ratio} = \frac{\text{Fourier amplitude at point B}}{\text{Fourier amplitude at point A}} \tag{40}$$

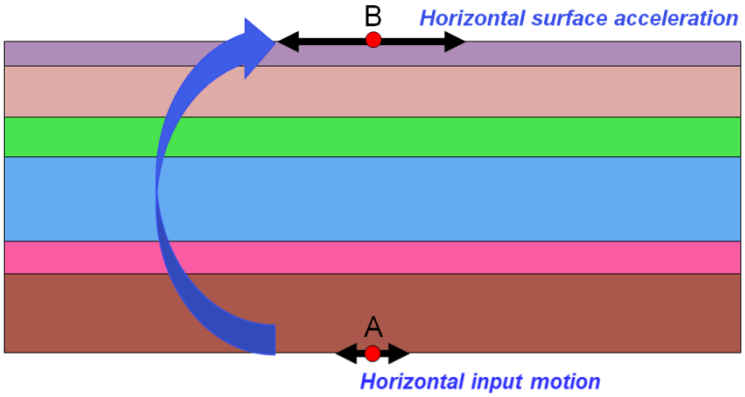

Fig. 109: Schematic representation of soil deposit behaviour under earthquake

Figure 110 presents two different type of amplification ratio of a homogeneous layer where a soft soil and a rock undergo a specific earthquake. It can be seen that the soft soil layer amplifies the lower frequencies and rock materials amplify the higher frequency ranges (the higher the stiffness, the larger the natural frequency). The values higher than unity represents amplification and the values lower than one indicates de-amplification. The amplification ratio takes higher values than unity at the natural frequencies of the deposit. The highest value occurs at the lowest natural frequency (so-called fundamental frequency) and the amplification ratio decreases by increasing frequency due to damping effect. Since real soils essentially dampen dynamic loads, the amplification ratio at the eigen frequencies cannot be infinite. If the damping ratio is set to zero, amplification ratio at each natural frequencies will be infinite which represents the resonance condition.

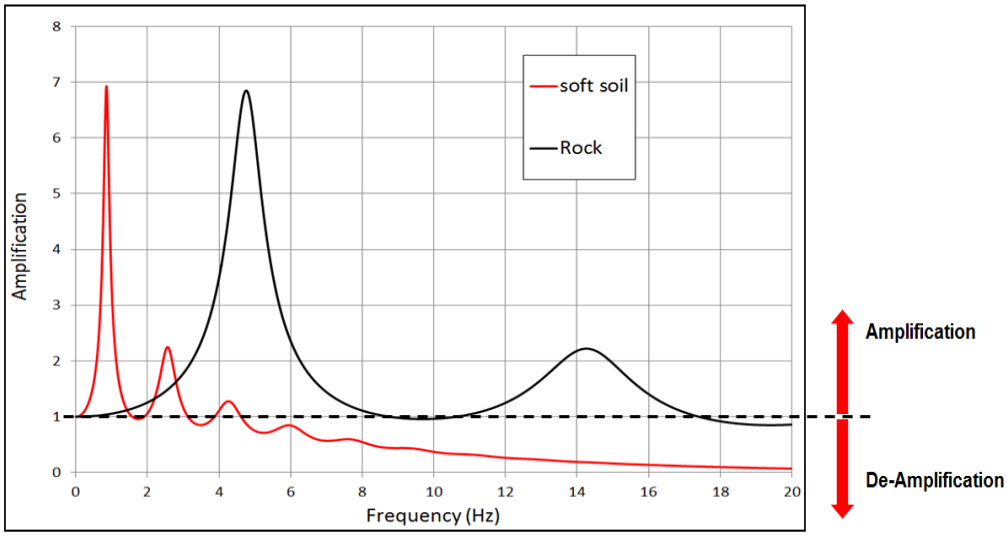

Fig. 110: Amplification ratio vs frequency for a soft soil and rock type materials

However, when ground improvement techniques such as jet-grout columns are used in a site to resist against earthquake, the ground response of the site may alter and therefore studying the amplification ratio's diagram can provide useful knowledge about the changes in natural frequencies and the rate of de-amplification or amplification at each frequency of the improved deposit.

5.9 Response to earthquake

For the design of earthquake-resistant structures, usually the entire time history of response may not be necessary and only the maximum response of a system to the motion is considered. In the field of earthquake engineering, there are two types of spectra available which are discussed herein.

5.9.1 Response spectrum

The response spectrum describe the maximum or steady state response (acceleration, velocity or displacement) of a series of single degree of freedom systems (SDOF) to a specific component of the base motion as a function of natural periods (T_n) and damping (ξ) of the system (Figure 111). The Response spectrum for actual ground motion can be quit irregular. A structure on the ground level is excited by its own inertial force caused by the acceleration of a motion at its base. A SDOF system is used to model surface structures in a simplest way with a mass concentrated on the top of the system, stiffness and damping (respect to the type of structure and its connections usually 5-20%).

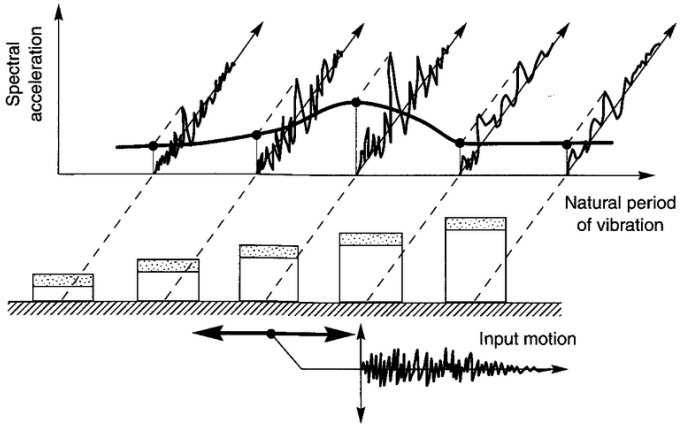

Fig. 111: Representation of the spectral acceleration (Kramer 1996)

The dynamic equation of the single degree of freedom structure motion is expressed by:

$$m_s\ddot{u} + c_s\dot{u} + k_s u = m_s\ddot{u}_g \tag{41}$$

Where m_s is the mass, c_s is the damping and k_s is the stiffness of the system and $\ddot{u}_g$ is the base acceleration. Dividing by "m_s" leads to:

$$\ddot{u} + 2\xi\omega_n\dot{u} + \omega_n^2 u = \ddot{u}_g \tag{42}$$

where, $c_s = 2m_s\xi\omega_n$, $k_s = m_s\omega_n^2$ and ω_n is the angular frequency

For a given base excitation the maximum response of the deformation *u(t)* depends only on the natural period and the damping. For a specific accelerogram the deformation, the velocity and the acceleration response of a single degree of structure can be determined. After calculation of u(t) using dynamic analysis the internal forces can be calculated based on the concept of the equivalent static forces F_s (See Figure 112):

$$F_s = k_s u(t) \tag{43}$$

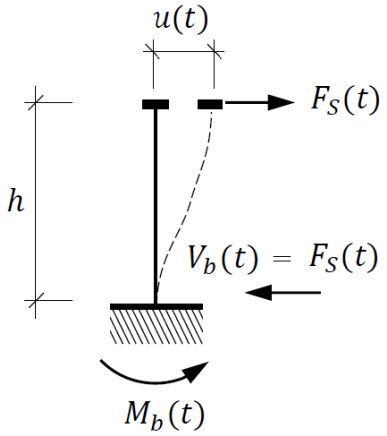

Fig. 112: Equivalent static force acting on SDOF systems

It is known that $k=m_s\omega_n^2$ then:

$$F_s = m_s\omega_n^2 u(t) = m_s A(t) \tag{44}$$

Where $A(t) = \omega_n^2 u(t)$ is called pseudo-acceleration.

If the peak deformation u_{s0} is available, the pseudo spectral velocity (*PSV*) and pseudo spectral acceleration (*PSA*) is related to each other as follow:

$$PSV = S_V = \omega_n u_{s0} \tag{45}$$

$$PSA = S_a = \omega_n^2 u_{s0} = \omega_n S_V \tag{46}$$

5.9.2 Design spectrum

The aim of defining a design spectrum is to design new structures or to evaluate the safety of existent structures against future earthquakes. The response spectrum is different for each specific earthquake, so it is impossible to predict such irregular response spectra for probable future earthquakes. Therefore, a design spectrum is required, which contains a set of smooth curves or straight lines. The design spectrum is obtained statistically from the response spectra of many different ground motions. Factors like magnitude of earthquake, distance from fault, rupture mechanisms, wave-travel-path geology and local site conditions can influence the design spectrum.

The design spectra can be found in the different national codes where usually pseudo acceleration for a defined structural damping (e.g. 5%) is given as a function of the natural period (T_n). In this thesis the spectra from EC8 are used. Within the scope of EN 1998, the earthquake motion at a given point on the surface is represented by an “elastic ground acceleration response spectrum”. Two types of spectra are known in EC8 that depend on the characteristics of the most significant earthquake contributing to the local hazard. Figure 113 only shows the elastic response spectra type I of high and moderate seismicity regions (M_S<5.5) for ground types A-E. The Equations of 47-50 describe the four distinct branches of the spectra for various ground conditions.

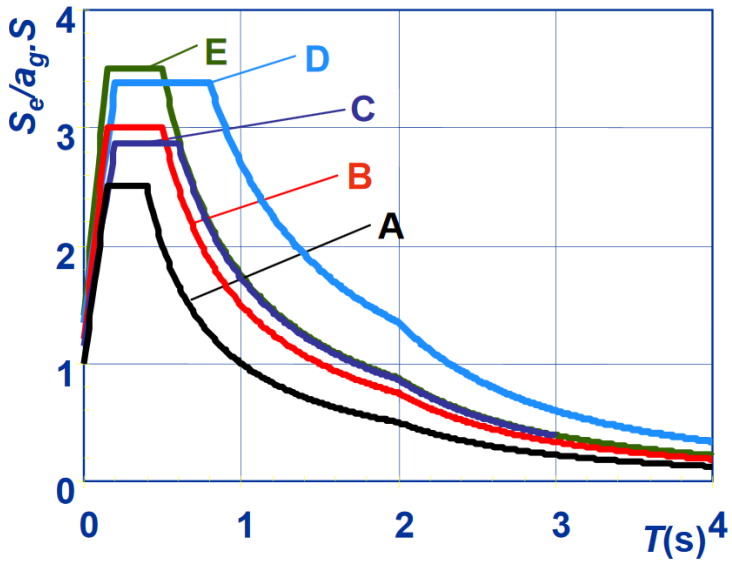

Fig. 113: Elastic response spectra type I for various ground type and 5% damping (CEN 2004)

For $0 \le T \le T_B$ $$S_e(T) = a_g.S.(1 + \frac{T}{T_B}.(\eta_d.2.5 - 1)) \quad (47)$$

For $T_B \le T \le T_c$ $$S_e(T) = a_g.S.\eta_d.2.5 \quad (48)$$

For $T_c \le T \le T_D$ $$S_e(T) = a_g.S.\eta_d.2.5(\frac{T_C}{T}) \quad (49)$$

For $T_D \le T \le 4$ $$S_e(T) = a_g.S.\eta_d.2.5(\frac{T_C T_D}{T^2}) \quad (50)$$

$$a_g = a_{gR}.\gamma_I \quad (51)$$

where S_e is the elastic response spectrum, T is the natural period of a linear SDOF system, S represents the soil factor and T_B,T_C,T_D are corner periods in the spectrum. The factor η_d is the damping correction (η_d is equal to one when ξ=5%). a_g and a_{gR} are the design and reference ground acceleration on type A ground respectively and γ_I is the importance factor of structures. It must be added that the design spectrum originates from an elastic response spectrum divided by the behaviour factor (q).

Table 15 presents the various ground types classification according to EC8 (CEN 2004). Where $V_{s0,30}$ is the average value of small strains shear waves velocity (at shear strain level of 10^{-5} or less) in the upper 30m of the soil column, N_{SPT} is the Standard Penetration Test blow-count and c_u is the undrained shear strength of the soil.

Tab. 15: Ground type according to EC8

Ground type	Description of stratigraphic profile	Parameters		
		$v_{s,30}$ (m/s)	N_{SPT} (blows/30cm)	c_u (kPa)
A	Rock or other rock-like geological formation, including at most 5 m of weaker material at the surface.	> 800	–	–
B	Deposits of very dense sand, gravel, or very stiff clay, at least several tens of metres in thickness, characterised by a gradual increase of mechanical properties with depth.	360 – 800	> 50	> 250
C	Deep deposits of dense or medium-dense sand, gravel or stiff clay with thickness from several tens to many hundreds of metres.	180 – 360	15 - 50	70 - 250
D	Deposits of loose-to-medium cohesionless soil (with or without some soft cohesive layers), or of predominantly soft-to-firm cohesive soil.	< 180	< 15	< 70
E	A soil profile consisting of a surface alluvium layer with v_s values of type C or D and thickness varying between about 5 m and 20 m, underlain by stiffer material with v_s > 800 m/s.			
S_1	Deposits consisting, or containing a layer at least 10 m thick, of soft clays/silts with a high plasticity index (PI > 40) and high water content	< 100 (indicative)	–	10 - 20
S_2	Deposits of liquefiable soils, of sensitive clays, or any other soil profile not included in types A – E or S_1			

5.10 Dynamic Finite element analysis with Plaxis

Some considerations must be taken into account when performing the dynamic analysis using finite element methods which is discussed in this section.

When a volume undergoes a dynamic load, the equation of its time-dependent movement can be expressed by:

$$M\ddot{u} + C\dot{u} + Ku = M\ddot{u}_g \tag{52}$$

Where, *M*, *C* and *K* are the Mass, the damping and the stiffness matrices of the whole system respectively and $M\ddot{u}_g = F$, which denotes the load vector.

The displacement (u), velocity ($\dot{u}$) and acceleration ($\ddot{u}$) can change with time. In PLAXIS all models can be used for dynamic analysis and the soil behaviour can be considered as drained and undrained. The matrix *M* is implemented as lumped matrix and it takes the soil, water and all the structures in to account. Similar to the static case when a soil is undrained the bulk stiffness of water is added to *K* matrix.

5.10.1 Time integration algorithm

The formulation of the time integration algorithm in the numerical implementation of dynamic problems is an important factor for the stability and accuracy of the calculations. In PLAXIS, the implicit time integration scheme of Newmark is used where the displacement and the velocity at the point in $t + \Delta t$ are given by:

$$u^{t+\Delta t} = u^t + \ddot{u}^t \Delta t + ((\frac{1}{2} - \alpha_N)\ddot{u}^t + \alpha_N \ddot{u}^{t+\Delta t})\Delta t^2 \tag{53}$$

$$\dot{u}^{t+\Delta t} = \dot{u}^t + ((1 - \beta_N)\ddot{u}^t + \beta_N \ddot{u}^{t+\Delta t})\Delta t \tag{54}$$

In these equations Δt is the time step and the coefficient α_N and β_N determine the accuracy of the numerical time integration which are discussed later.

5.10.2 Time steps

The dynamic time step used in the implicit time integration scheme plays an important role for the reliability and accuracy of the finite element analyses. The time step used in a dynamic calculation is equal to:

$$\Delta t = \frac{\delta t}{m.n} \tag{55}$$

Where δt is the duration of dynamic load (e.g. earthquake), m is the value of the max steps which is usually considered as the number of inputs in the earthquake record and n is the value of the number of sub steps. It is important to define a proper number of time steps in order to cover the input signal. A too large time step can give unreliable results. The time step can be automatically calculated in Plaxis regarding to material, mesh and number of data points in the input record. The correct time step ensures that that a wave during a single step does not move a distance larger than minimum dimension of an element (Brinkgreve et al. 2015b).

Critical time step for a single element is proposed by Pal (1998) as follows:

$$\Delta t_{critical} = \frac{l_e}{\alpha \sqrt{\frac{E(1-\nu)}{\rho(1+\nu)(1-2\nu)}} \sqrt{1+\frac{B^4}{4{S_{el.}}^2}-\frac{B^2}{2S_{el.}}[1+\frac{(1-2\nu)}{4}\frac{2S_{el.}}{B^2}]}} \tag{56}$$

Where B denotes the largest dimension of the finite element, $S_{el.}$ is the surface area of the element, α is a constant depending on element type (6-node or 15-node), l_e is the average element length and the ν is the Poisson's ratio. The first root term represents the compression wave velocity V_p.

5.10.3 Minimum element size

In order to ensure a correct wave transmission through a FE model, the element size should be less than approximately one-tenth or one-eighth of the shortest shear wave length considered in the analysis (Kontoe 2006):

$$l_{node} \leq \frac{\lambda_{\min}}{(8-10)} = \frac{V_s}{(8-10).f_{\max}} \tag{57}$$

Where l_{node} is the average node-to-node distance of the finite elements ($l_{node}=l_e/2$; for 6-node triangular element (2D) and 10-noded tetrahedral elements (3D)). λ_{min}

is the shortest wavelength, V_s is the minimum shear wave velocity at seismic level and f_{max} the maximum frequency of interest considered in the analysis.

5.10.4 Energy dissipation

The response of a finite element model is sensitive to several parameters that influence the source of energy dissipation in finite-element time-domain calculations (Visone et al. 2010). The amount of damping is determined by:

- Material damping
- Numerical damping
- Energy dissipation at boundaries

5.10.4.1 Material damping

Material damping includes viscous and hysteretic damping. Hysteretic damping is related to the area bounded by hysteretic stress-strain loops and is frequency independent. Hysteretic damping is a result of advanced constitutive models, but, for linear elastic materials hysteretic damping is zero. This problem can be solved numerically by assuming a visco-elastic soil element. In most dynamic FE codes such as Plaxis, this viscous damping is simulated according to the Rayleigh formulation as follows:

$$C = \alpha_R M + \beta_R K \tag{58}$$

In this formulation, the damping matrix C is proportional to the mass matrix M and stiffness matrix K. In contrast to hysteretic damping the viscous damping is frequency dependent. When the target damping ratios ξ_m and ξ_n are equal to D, the parameters α_R and β_R can be computed using two significant frequency intervals f_m and f_n based on Equation 59 (Park & Hashash 2004).

$$\begin{bmatrix} \xi_m \\ \xi_n \end{bmatrix} = \frac{1}{4\pi} \begin{bmatrix} \frac{1}{f_m} & f_m \\ \frac{1}{f_n} & f_n \end{bmatrix} \begin{Bmatrix} \alpha_R \\ \beta_R \end{Bmatrix} \tag{59}$$

5.10.4.2 Numerical damping

As mentioned in the section 5.10.1, the coefficients α_N and β_N determine the accuracy of the time integration. The typical values can be defined as: (Barrios et al. 2005)

- Linear acceleration scheme:
  α_N=0.167 and β_N=0.5 - conditionally stable

- Constant average acceleration
  α_N=0.25 and β_N=0.5 - unconditionally stable

- Fox-Goodwin method, fourth order accurate:
  α_N=0.083 and β_N=0.5 - conditionally stable

According to a modification of Hilber et al. (1997) the value of α_N and β_N can be expressed by a new numerical dissipation parameter γ_H which belongs to the range of 0-1/3:

$$\alpha_N = \frac{(1+\gamma_H)^2}{4} \tag{60}$$

$$\beta_N = \frac{1}{2} + \gamma_H \tag{61}$$

5.10.4.3 Boundary conditions

In dynamic finite element analysis, presence of standard fixities in boundary conditions (especially in the vertical model boundaries) causes the reflection of outward propagating waves. Therefore, artificial boundaries are used in dynamic analysis to reduce a very large required domain to a bounded analysed domain. Hence, to avoid any wave reflection, an increase in stresses on the boundaries of the minimized model resulted by dynamic loading has to be absorbed. Choice of boundary conditions depends on the type of problem (e.g. earthquake analysis or vibration of machinery), accuracy and stability of the boundary condition (Galavi et al. 2013). The position of the artificial boundary and its constraints must well reproduce the waves transmission outwards the analysed domain. The most common boundary conditions that are used for dynamic analysis are introduced herein.

In Plaxis 2D/3D for earthquake analysis, the input motion is exerted at the lower horizontal boundary (bottom of the model) via the line prescribed displacement. The input motion can be specified as a displacement, velocity or acceleration history.

Absorbing (Viscous) Boundary Condition (ABC)

The absorbing boundary, introduced by Lysmer & Kuhlmeyer (1969) is a wide spread procedure and also used in Plaxis. The increment of stress caused by dynamic loads is absorbed according to the following equations:

$$\sigma_n = -C_1 \rho V_P \frac{\partial u}{\partial t} + \sigma_n^0 \tag{62}$$

$$\tau = -C_2 \rho V_S \frac{\partial v}{\partial t} + \tau^0 \tag{63}$$

Where u and ν are the normal and tangential displacements, σ_n^0 and τ^0 are normal and tangential static stresses at the boundary respectively and $C_1$and C_2 are called relaxation factors. The behaviour of this type of boundary is perfect when the body waves cross the boundaries perpendicularly (i.e. $C_1=C_2=1$), but it can be also used in two-dimensional wave propagation where waves may not be perpendicular to the boundary.

Tied degree of freedom

During earthquake, usually left and right boundaries have almost the same displacements. Tied degrees of freedom were introduced by Zienkiewicz et al. (1988). The tied degree of freedom is only available for the lateral boundaries. In this model, nodes on the same elevation on the lateral sides of the finite element mesh are tied together such that they will undergo exactly the same displacements. This option works perfectly for modelling a one dimensional soil column to perform a site response analysis but it is unable to absorb the waves reflected from internal sources.

Free-field and compliant base boundaries (Earthquake boundaries)

The absorbent boundary was designed to absorb outgoing body waves. This type of boundary (i.e. ABC) is useful and can be used without modification when the source of vibration is inside the model (e.g. a generator on the ground level). Therefore, in case of earthquake or any excitation that comes from outside the model, the ABCs need to be extended and the model dimension increases.

A free-field boundary is a combination of tied degrees of freedom and an absorbing boundary. In a method described by Zienkiewicz et al. (1989) and Wolf (1988), the domain is reduced to the area of interest, which is called main domain, and the free-field motion is applied to the boundaries by means of free field elements (Figure 115). Within the free-field element the attached one-way viscous dashpots transfer the free field motion with an equivalent forces according to Equations 64 and 65 to the main domain but not vice versa (Figure 114). To absorb the waves reflected from internal structures or internal sources, viscous boundaries are considered at the lateral boundary of the main domain.

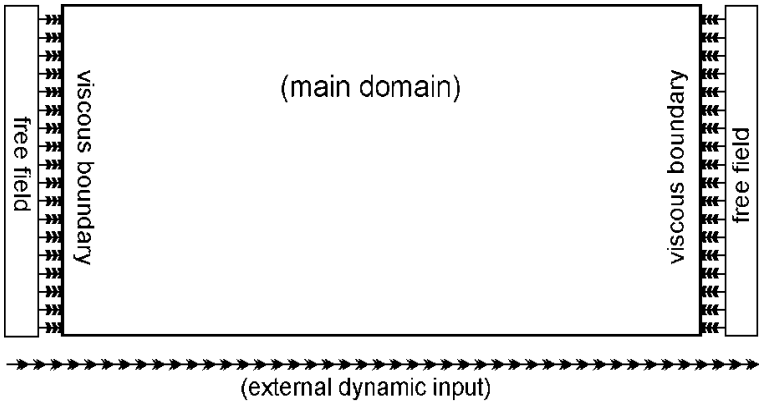

Fig. 114: Free-field boundary condition with rigid base-wave reflection at base (Galavi et al. 2013)

$$\sigma_n^m = -\rho V_P \left(\frac{\partial u^m}{\partial t} - \frac{\partial u^{ff}}{\partial t}\right) + \sigma_n^0 \tag{64}$$

$$\tau^m = -\rho V_S \left(\frac{\partial v^m}{\partial t} - \frac{\partial v^{ff}}{\partial t}\right) + \tau^0 \tag{65}$$

The terms “m” and “ff” represents the main domain and free-field domain.

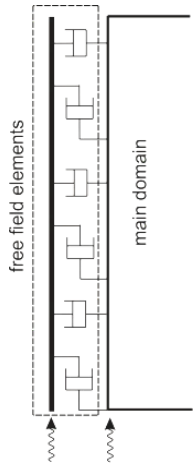

Fig. 115: Free-Field element (Galavi et al. 2013)

Free field elements can be also attached to the bottom of the main domain to form a compliant based boundary where no reflection at the base occurs (Figure 116) and it can be used to simulate the elastic bedrock condition.

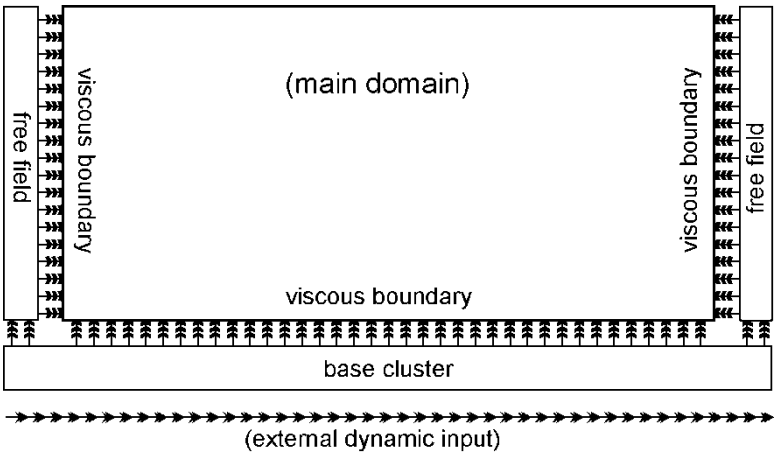

Fig. 116: Free field boundary condition with compliant base (Galavi et al. 2013)

Fixed base

The fixed base can be set up by selecting the “none” option from the Dynamic model conditions in combination with a line prescribed displacement. The fixed base is a fully reflective boundary. In this case the PLAXIS expects the input of the so called within motion (i.e. the sum of upward and downward travelling waves) for a fixed base.

5.11 Summary and further study

In this chapter, the various methods of performing ground response analysis in addition to the required considerations for the dynamic finite element analyses were discussed. In the following chapters and specifically in chapter 7, it will be attempted to study how the ground improvement methods such as jet-grouting/deep soil mixing influence the ground response of soil deposits.

Since one-dimensional analysis with equivalent linear approach is computationally convenient and gives reasonable results, it will be used as a basis for the numerical 2D/3D ground response analyses of unimproved deposits and then the behaviour of the improved deposits will be studied accordingly. To perform one-dimensional analyses for the unimproved soils the Deepsoil V6 (Hashash et al. 2015a) will be utilized. The diagrams of the amplification ratio together with the response spectra of the improved deposits will be investigated and a comparison is done with the EC8 elastic response spectra Type I, to highlight the variation in the spectrum and site classifications due to ground improvement.

In the following dynamic finite element analyses, the soils will be modelled as a visco-elastic material and consequently the damping can be simulated via Rayleigh formulation. The model boundary at the base is considered as a rigid condition i.e. fixed base boundary conditions and the influence of the viscous boundary condition and the free-field boundary condition will be discussed. For the numerical time integration, the constant average acceleration is chosen where the Newmark's method is unconditionally stable.

6 Preliminary dynamic analyses

6.1 Behaviour of jet-grout columns under earthquake loading

6.1.1 Model description

In this section, in some preliminary dynamic analyses, the behaviour of jet-grouting columns as soil improvement elements against earthquake is investigated using a simple 2D model. The model was taken from Floroiu & Schweiger (2013) and slightly modified for the purpose of this study. The soil layer is composed of a 30m cohesive layer that is underlaid by a rigid bedrock and viscoelastic soil behaviour is assumed (Figure 117). The cohesive layer is homogeneous over depth with average shear wave velocity ($V_{s,30}$=150 m/s), and fit to soil class D (CEN 2004). The considered soil improvement is 10 jet-grouting columns, which are modelled by the new constitutive model (Shotcrete Model). Diameter and depth of all columns are 80cm and 15m respectively, with spacing equal to 1.8m. The 2D model was created in Plaxis 2D (Brinkgreve et. al 2014) where only viscous boundary conditions were available.

The main purpose of current study is investigation of the effect of some input parameters of the new shotcrete model applied for describing the behaviour of the jet-grouting columns such as fracture energy, stiffness in addition to Rayleigh damping parameters, and also the width of the FE model on the columns behaviour and crack patterns under a specific earthquake.

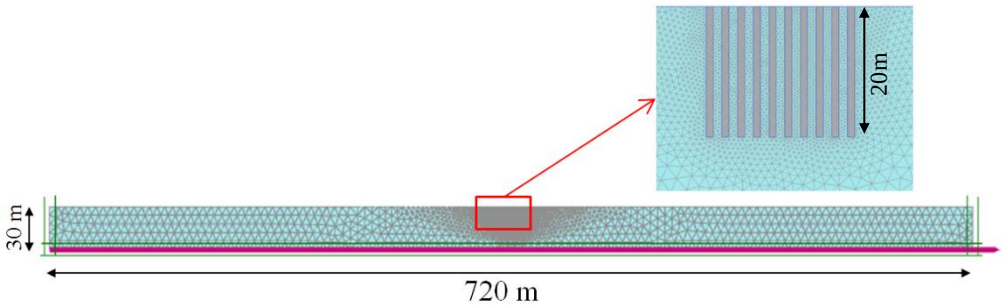

Fig. 117: The geometry of the FE model

The horizontal acceleration-time history recorded during the 1989 Loma Prieta U.S.A. (PEER 2011) earthquake was used as input signal at rigid bedrock level. The signal has a total length of 40.00s with a time step of 0.02s and dominant f_p= 2.68 (Figure 118).

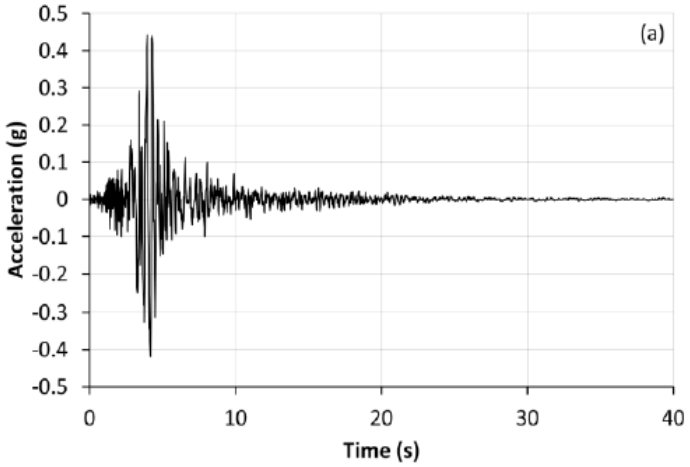

Fig. 118: Acceleration-time history Loma Prieta 1989

The finite element meshes are composed of 6-noded triangular elements. The average element size/length is roughly 1.1m. The input accelerogram was applied with constant amplitude throughout the model base in x direction. Absorbent (viscous) boundaries were used on both sides of the model, which together with the relatively large model width aim to better replicate far-field conditions. In this respect, both relaxation coefficients of the absorbent boundaries were considered equal to unity C_1=C_2=1. The implicit time integration scheme of Newmark was used with coefficients α=0.25 and β=0.5 as for the average acceleration method. The adopted material parameters of the soil body are according to the procedure described by Floroiu & Schweiger (2013) and are shown in Table 16. The damping ratio in the soil body according to average effective shear strain level in the soil layer (1E-3) was considered 10% based on proposed damping ratio's curves by Vucetic and Dobry (1991).

Tab. 16: Material parameter of the viscoelastic soil layer

Soil	Unit	Value
γ_{soil}	[kN/m^3]	19
E	[kN/m^2]	60E3
G_{sec}	[kN/m^2]	21.43E3
ν	[--]	0.4
Damping	%	10

Material parameters of the jet grouting columns are presented in Table 17. The stiffness has been chosen to reflect the extreme condition. For jet grouting columns, the effect of different damping ratios in range of 0.5-5% has been utilized regardless to shear strain level inside the columns and in order to check the influence of this value on crack patterns. It must be noted that

time dependency of stiffness and strength was switched off in these analyses.

Tab. 17: Material parameter of jet grouting columns

Jet grouting	Unit	Value
$\gamma_{col.}$	[kN/m^3]	19
E_{28}	[kPa]	5E6 and 10E6
ν	[--]	0.2
$f_{c,28}$	[kPa]	7500
$f_{t,28}$	[kPa]	750
$G_{t,28}$	[kN/m]	0.01 and 0.05

The first, second and third eigen frequencies of the unimproved soil column, based on the Equation 27, are f_1=0.88Hz, f_2=2.65Hz (i.e. $T_1=1/f_1$=0.37sec & $T_2=1/f_2$=1.14sec). The amplification function was checked against an analytical solution, the 1D frequency domain solution from Deepsoil (Hashash et. al 2015a) and the Plaxis 2D time domain FE solution. The results confirmed using the selected model (width of 720m) for the next stage analyses. The Rayleigh damping parameters were calculated based on the first and second eigen frequencies (Figure 119). As it can be seen results of the smaller FE model (240m width) does not coincide with the other calculations, the reason being most probably the influence of wave reflection at the boundaries. The latter will be discussed later in the section 6.1.4.

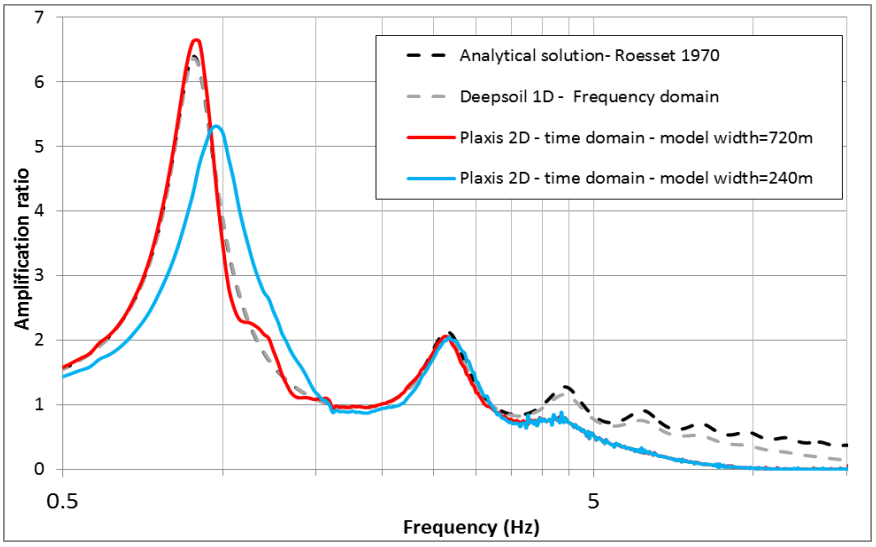

Fig. 119: Comparison of the amplification functions of unimproved soil with analytical solution and FE model with different width.

6.1.2 Influence of damping ratio of the columns

Results of the calculations showed that with constant material parameter for jet grouting columns (E=10GPa and G_t=0.01kN/m), by increasing the damping ratio in the range of 0.5%-5% the behaviour of the columns becomes more ductile, softening is less severe and the crack pattern will change (Figure 120). Introducing artificial viscous damping to the columns can postpone the softening phase and subsequently affect their behaviour.

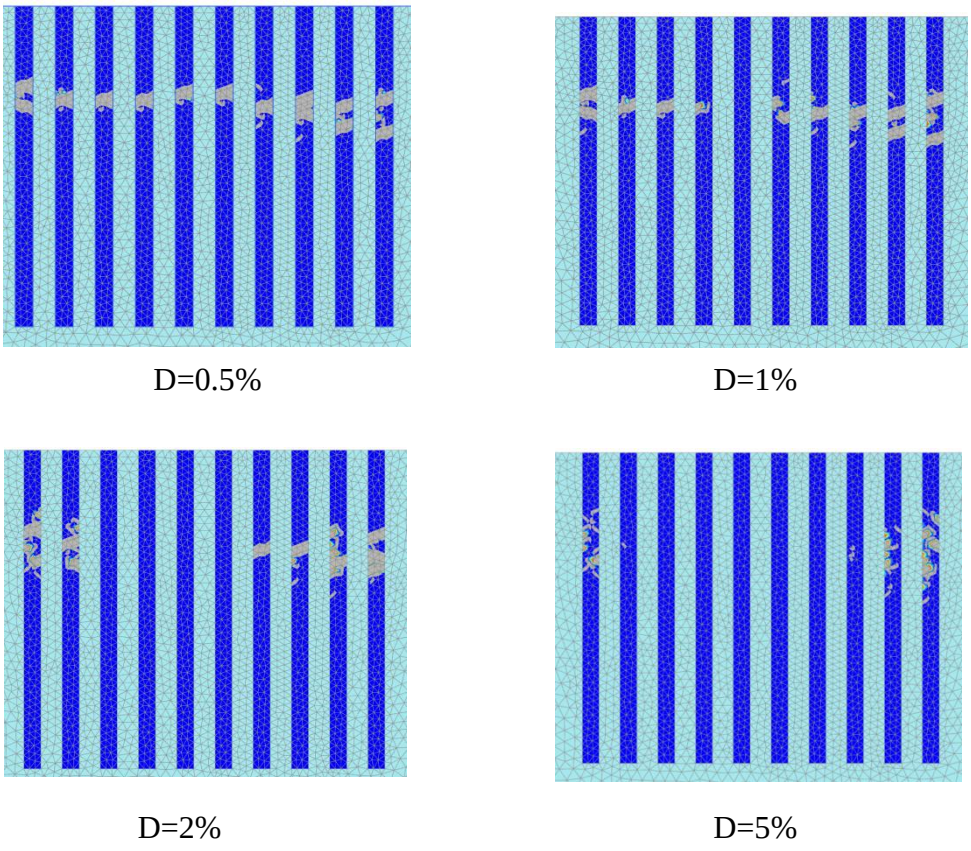

Fig. 120: Crack locations with different damping ratio for the columns E=10 GPa and Gt=0.01 kN/m

6.1.3 Influence of the stiffness and fracture energy

In another calculation, the fracture energy was increased to 0.05 kN/m with a damping ratio of 1% for the columns. Although tensile stress limit in the columns is reached, softening is not severe and equilibrium can be established with no cracks propagating inside the columns (Figure 121). Also by decreasing the stiffness of the jet grouting material to 5GPa and keeping the fracture energy

equal to 0.01kN/m no softening occurs, columns are elastic and the maximum tensile strength is not reached (Figure 122).

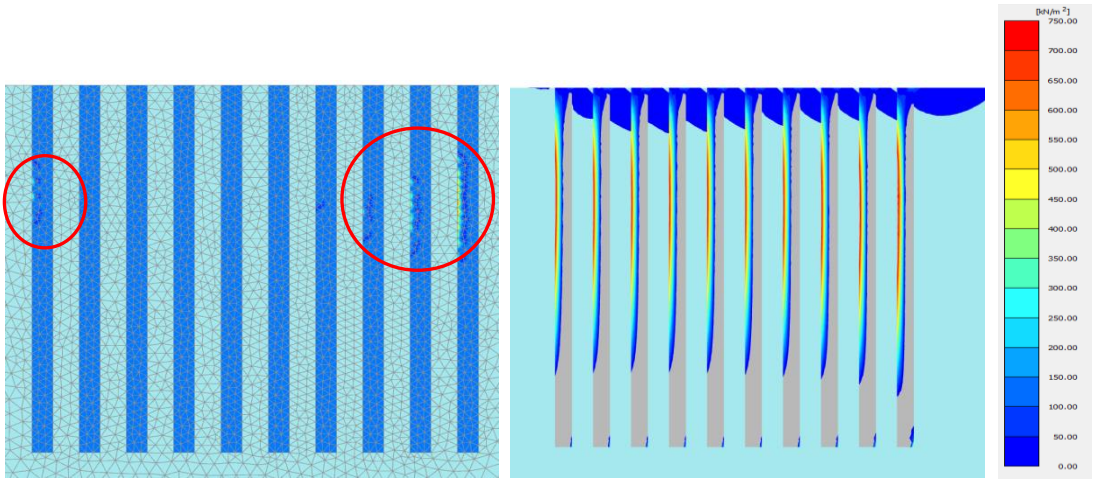

E=10GPa, G_t=0.05 kN/m, D=1%

Fig. 121: Crack locations (left) Principle stress (σ_3) distribution where only tensile stresses are shown (right)

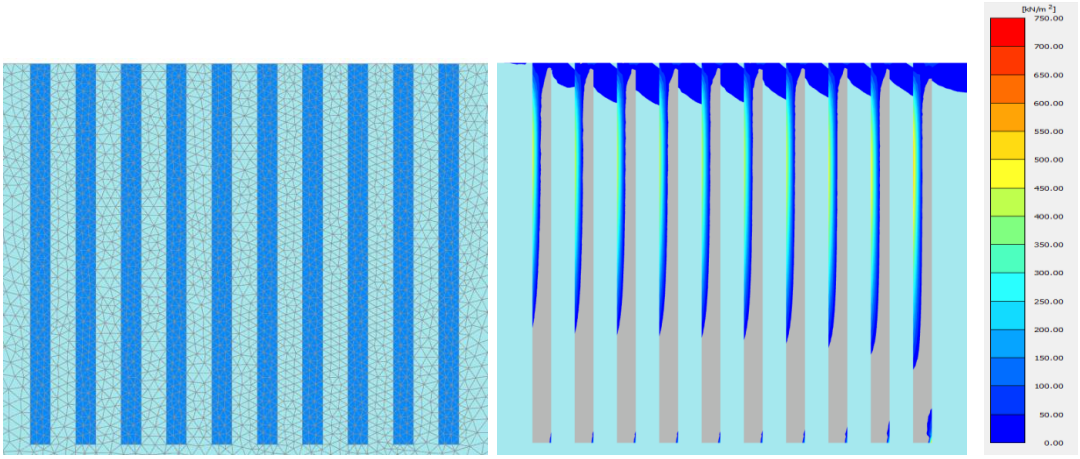

E=5GPa, G_t=0.01 kN/m, D=1%

Fig. 122: Crack in the columns (left) Principle stress (σ_3) distribution where only tensile stresses are shown (right)

6.1.4 Influence of the main domain width

The model width was reduced to 240m to assess the effect of the model width on the behaviour of the columns and crack patterns (Figure 123). The choice of the FE domain width is governed by minimizing the effect of the boundary conditions on the response zone. Trials should be performed with different widths to specify the optimum geometry in which the effect on the response spectrum or amplification ratio is negligible (Dey 2011). Result of the analysis revealed that with equal material properties and 1% damping ratio for the

columns in both FE models different crack patterns are obtained (Figure 124). Moreover, the amplification function of this model is different as was shown in the Figure 119.

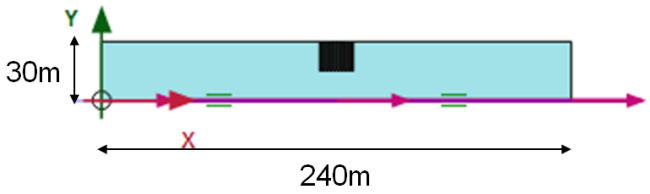

Fig. 123: FE model with 240m width

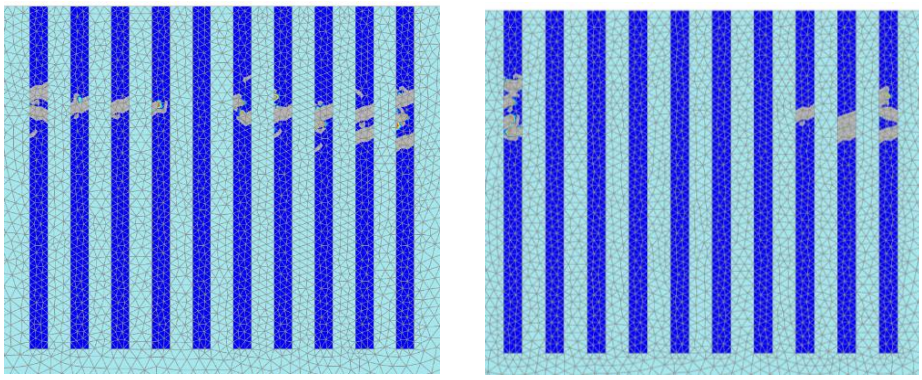

D=1% - model width 720m D=1% model width=240m

Fig. 124: Crack pattern in different domain's width.

Decreasing the model width changes the response of the model. For instance, it can be observed in Figure 125 that the horizontal displacements of a point in the middle of the model and on the surface are smaller for the model with 240m width. Thus for further studies the 720m wide model is used.

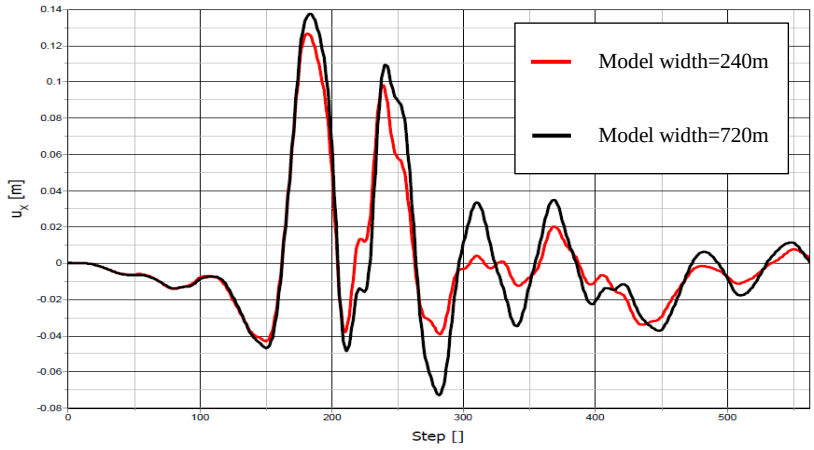

Fig. 125: Comparison of the horizontal displacements in both FE models.

6.2 Evaluation of shotcrete model in dynamic analysis

As mentioned in chapter two the shotcrete model was not developed for dynamic and cyclic loading. Crack opening and closure is not modelled correctly with this model, therefore only initiation of cracks can be modelled.

In this section, a simple calculation with only one jet-grout column (see Figure 126) is used to show the weakness of the model in dynamic loading. The main goal is to replace the crack with a softer cluster (reduced stiffness), therefore the columns is discretised in to small parts in the zone of cracking that makes it possible to select the cracked areas and replace the them with different material properties. The model features, soil and columns parameters are the same as in previous calculations.

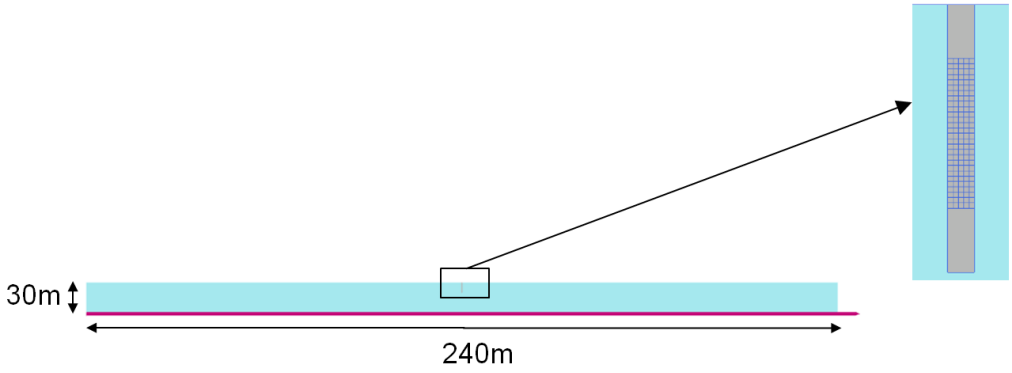

Fig. 126: Analysed model with one column

For decreasing the calculation time only a part of the Loma Prieta earthquake record, (the first 10 seconds) which contains the highest amplitude and has the most effect on the results and cracks of the columns was used as shown in Figure 127.

.

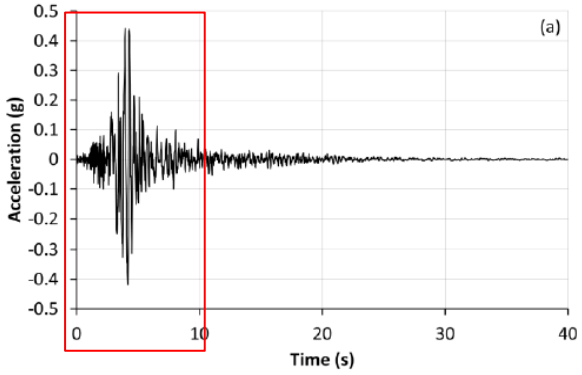

Fig. 127: New time history used for analysis.

First, the behaviour of the model without any changes is investigated. Calculation ends after 500 steps and in Figure 128 the deformation of the columns and corresponding crack propagations in some specific calculation steps are shown. At the end of analysis four full cracks occurs in the columns and this behaviour seems to be unrealistic because when a first full crack occurs a hinge is created and propagation of other full cracks across the columns is probably not realistic.

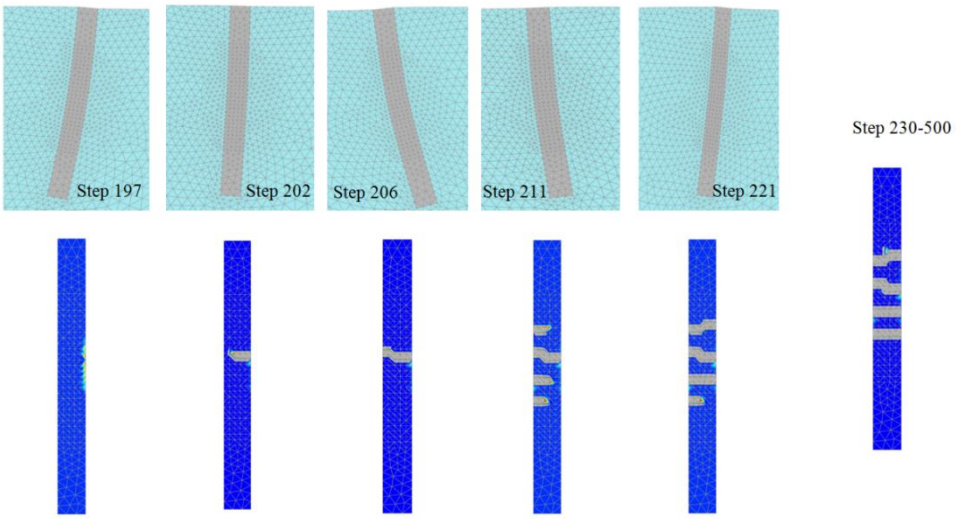

Fig. 128: Deformations and cracks propagation in the column.

In the next calculation, a softer cluster is assigned after a creation of first full crack across the column. Two different stiffness values are considered for the cluster equal to 0.5GPa and 2GPa. The earthquake data file is broken to two parts as follow:

1. Between 0 - 4.14sec. when a first full crack is created (i.e. steps 0-206)
2. From 4.14 - 10sec., (i.e. steps 207-500) where the softer cluster is added (Figure 129).

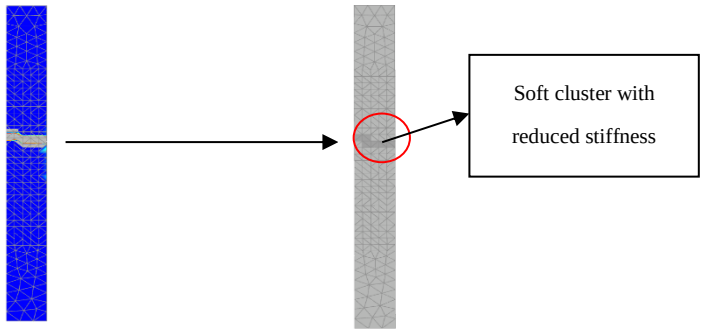

Fig. 129: Substitute the crack with a soft cluster.

Figure 130 indicates the influence of a soft cluster in this simple model. After creation of a full crack and replacement by a softer cluster, no new cracks develop which can represent a behaviour that is more realistic. The distribution of tensile stresses in the column at step 209 (i.e. three steps after the creation of first full crack see Figure 128) for two different conditions can be seen in Figure 131. Without the soft cluster, the maximum tensile strength was reached in a zone above and below the first full crack and therefore additional cracks developed in the column, while in other analysis using a soft cluster the maximum tensile strength is not at the vicinity of the first full crack. Applying a higher value of stiffness (equal to 2GPa) to the cluster showed the same results as the analysis with 0.5MPa stiffness.

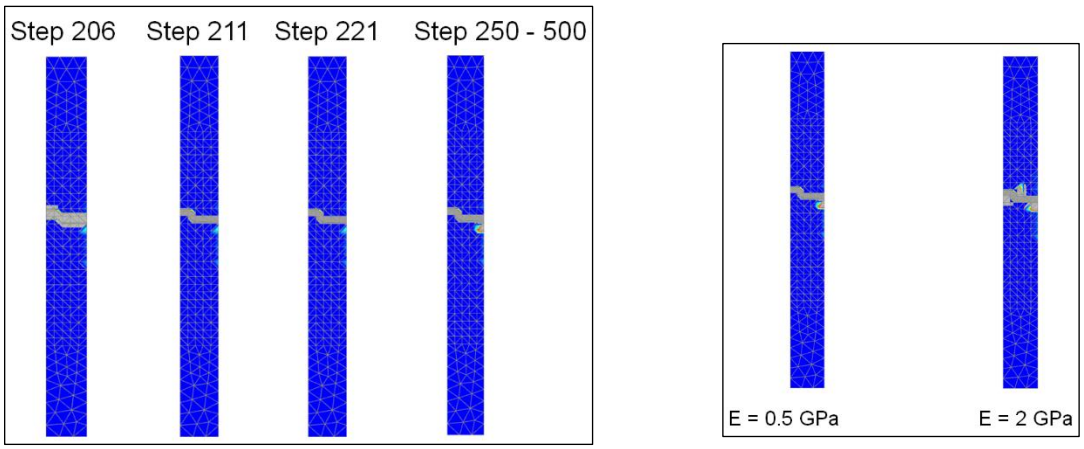

Fig. 130: Crack pattern: a) E=0.5GPa; b) at the end of calculation with two different cluster stiffness.

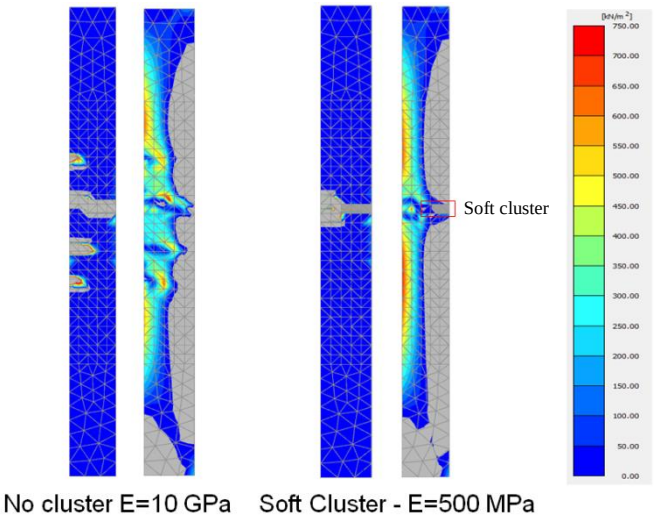

Fig. 131: Principle stress σ_3 distribution in step 209.

6.3 Summary and conclusion

A simple model was used to investigate the effect of jet-grout columns on ground response of a homogenous soil layer and the shotcrete model was employed to describe the behaviour of the jet-grouting columns. The influence of some input parameters of the model such as stiffness, fracture energy in tension together with the influence of Rayleigh damping parameters on the crack pattern was investigated. It was observed that very brittle behaviour i.e. higher stiffness (10GPa) value and the lower fracture energy (0.01 kN/m) could lead to crack propagation in all the columns while using more ductile material (i.e. 5GPa stiffness) even with the lowest fracture energy eliminated all the cracks. In addition, it was observed that introducing artificial viscous damping to the columns could affect the crack patterns. An increase in the damping ratio of the jet-grouting columns may postpone the softening process and therefore a proper and realistic damping ratio for the material has to be applied. Besides, the influence of the model width and the viscous boundary condition was shown on the amplification ratio and the obtained crack patterns. Incorrect choice of model's width may lead to inaccurate ground response.

It was mentioned in the second chapter that the shotcrete model has not been intended to be used for dynamic analysis and the crack opening/closing is not correctly modelled. The behaviour of the model in dynamic analyses was also investigated in this chapter with a simple example where only one column was assumed under earthquake loading. When the first full crack occurred in the middle of the column, actually a hinge was created, and the occurrence of subsequent cracks above and below the first full seemed to be unrealistic. The column was discretised into smaller parts in the zone of cracking which facilitated the substitution of first full crack with a soft cluster which might represents the behaviour of the crack more realistically. It was observed that a different crack pattern is obtained with this method and no further full cracks developed after the creation of the first one. It could be concluded that, with the shotcrete model only the initiation of cracks can be reliably assessed.

7 Ground response of improved soil deposits

7.1 Introduction

Soil improvement techniques are primarily employed in order to improve bearing capacity and reduce settlements of foundations on soft soils under static loading. However, ground improvement techniques such as soil-cement mixing or jet grout columns also will change the response of soft soil layers subjected to earthquake loading. Thus, the seismic response of these structures may be changed by the improvement methods. Ground response analysis is widely used to evaluate the influence of soil layers on amplification of earthquake loads. These analyses commonly are applied to unimproved soils using one dimensional wave propagation theory with little computational effort, but in order the provide a better insight into the dynamic behaviour of the soil-foundation-structure or the effect of different soil improvement techniques on ground response, more complex analyses are needed. In recent years much effort has gone into studying the seismic soil-pile-structure interaction or to investigate the behaviour of pile groups and pile-raft foundation under earthquake loading (e.g. Kumar et al. 2016, Ladhane & Sawant 2015, Hokmabadi et al. 2014, Isam et al. 2012, Hora 2011, Maheshwari & Sarkar 2011, Alsaleh & Shahrour 2009), but the effect of ground improvement has not been studied extensively. Floroiu (2016) investigated the effect of stone column-like and pile-like soil improvement on the ground response of a homogeneous clayey deposit employing 3D finite element analyses. These results showed that soil improvement changes the eigen frequencies and amplification ratio of the natural soil layer which can increase or decrease the seismic load on the surface structures. Pitilakis et al. (2011) reported the effect of soil reinforcement using stone columns and sand-rubber mixture columns on the seismic response of a single degree of freedom system (SDOF) and emphasized that regarding the seismic response of the structures the effects of the soil improvement are not always favourable. The authors also concluded that soil reinforcement due to the interaction between the structure and the non-linear soil behaviour may have serious impacts on the design values, which cannot be taken into account by seismic code design spectra. Durgunoglu et al. (2004) showed by analysing a case study from the 1999 Kocaeli earthquake that ground treatment by means of jet grout columns can effectively mitigate earthquake related damages. In a similar study Martin & Olgun (2007), using non-linear 3D dynamic analysis, found that jet-grout-treated zones suffered no settlement and ground damages compared to unimproved areas. However, these columns did not significantly reduce the seismic shear stresses and strains and consequently the excess pore pressure in the soil mass and therefore the effectiveness of the columns may have been more related to the vertical support against earthquake-induced settlements. Olgun & Martin (2010) suggested that

stiff ground reinforcement like soil-mix or jet-grouting in form of lattice-shape structures has a high potential to reduce the intensity of earthquake beneath structures, but these beneficial impacts, which could lead to significant cost saving in many conditions, are not considered in the international building code (IBC) for defining site classifications and design motion. Rayamajhi et al. (2014) using three-dimensional linear elastic finite element analysis presented the effect of discrete column reinforcement on the shear stress reduction in liquefiable soils along with the investigation of tensile crack development. By a parametric study they could show that an increase in shear modulus ratio (i.e. the ratio of shear modulus of the column to shear modulus of the soil $G_r=G_{column}/G_{soil}$) will increase the tensile stresses development in the discrete columns, whereas an increase in replacement ratio ($A_r=\text{Area}_{column}/\text{Area}_{total}$) decreases the potential of tensile crack occurrence slightly.

The focus of the current study is to investigate the effect of earthquake-resistant elements such as jet-grouting columns or soil-cement grids on the ground response of homogeneous and layered deposits during an earthquake. A series of numerical calculations are performed by means of the finite element method to investigate the impact of the soil improvement on the ground response, where the influence of various widths, depth and shapes of the soil improvement methods are investigated. The second goal is defining possible crack zones in the unreinforced columns during the earthquake by applying the new shotcrete constitutive model. In addition, the effect of so-called lattice-shaped improvement on the ground response is investigated.

7.2 Homogeneous soil layer

In this part, with a simple example the effect of improvement width and improvement depth on the ground response of a homogeneous cohesive layer is investigated. In addition, the application of new dynamic boundary condition in PLAXIS 2D (Brinkgreve et. al 2014), so-called free-field boundary conditions, to reduce the model length is investigated.

7.2.1 Model description

The model consists of a 20m cohesive layer employing a viscoelastic soil behaviour underlaid by rigid bedrock (The shear wave velocity of the rigid bedrock is considered to be V_{s0} > 800m/s at shear strains less than or equal to 10^{-5}, i.e. small strains). The unit weight of soil γ_{soil}=19kN/m^3, friction angle φ'=23°, earth pressure coefficient at rest K_0=0.6, small-strain shear wave velocity V_{s0}=150m/s are assumed to be constant over depth and consequently shear

modulus G_0 is also constant over depth. The cohesive layer fits to soil class D (CEN 2004). The soil improvement composes of jet-grouting columns, which are modelled by the new Shotcrete constitutive model. The input earthquake motion is applied at the base of the model with fixed based boundary. All soil layers are modelled using the equivalent linear method with linear viscoelastic behaviour and no ground water table is considered.

7.2.2 Input motion

The acceleration-time history recorded during the 1989 Loma Prieta U.S.A. earthquake (Pacific Earthquake Engineering Research Center (PEER) 2011) is used as seismic input signal at bedrock level. Duration of earthquake was set to 20s with a time step of 0.02sec and peak acceleration is 0.44g (Figure 132). Using Fourier transform, each time domain function can be translated to a frequency domain and make it possible to study the amplitude of the signal at each frequency. This transformation has been done using SeismoSignal V5.1 (Antonio & Pihno, 2012) which indicates that the dominant frequency of the earthquake is f_p=2.68Hz (Figure 132).

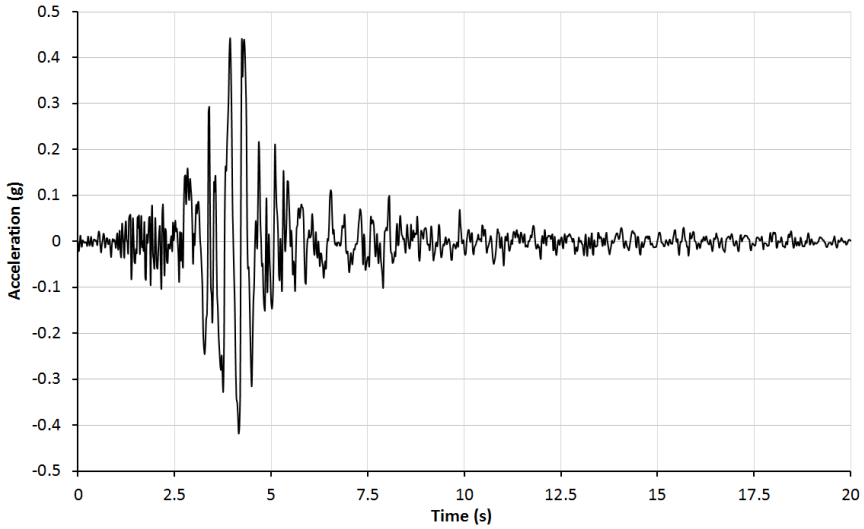

Fig. 132: Acceleration-time history Loma Prieta 1989

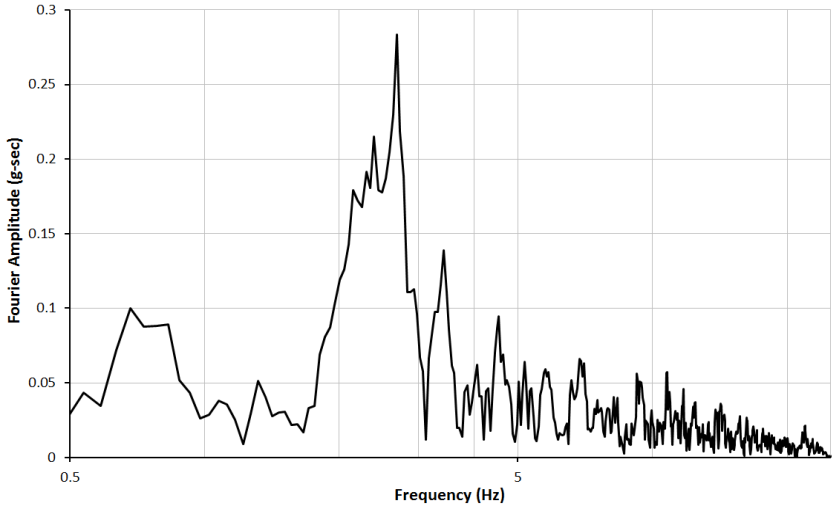

Fig. 133: Fourier amplitude spectrum of the motion

7.2.3 Model description

The reference model is 3D, in which a rectangular shape of the column grid was assumed (Figure 134). Diameter and center-to-center spacing of the columns are 80cm and 180cm respectively, and the 3D model's thickness is 1.8 meter. The replacement ratio (A_r) i.e. the area of the soil improvement divided by the area of the whole block is 16%. The soil improvement width considered is 25m, 50m and 100m respectively, and also the column depth is varied (10m, 15m and 20m).

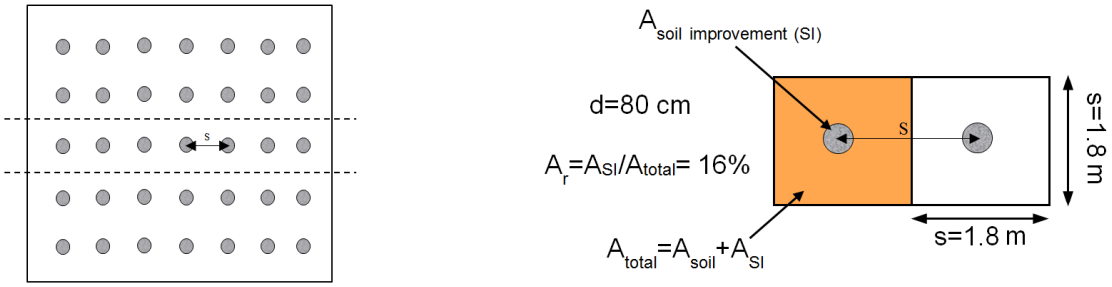

Fig. 134: Schematic representation of jet-grout columns arrangement (square grid) and selected region for numerical analyses

Figure 135 shows the geometry of the Plaxis 3D (Brinkgreve et al. 2013) model. The finite element meshes in 3D is 10-noded tetrahedral elements. In Plaxis 3D only viscous boundary conditions were available for the lateral boundaries of the main domain and therefore the model width was set to 720m via trial and error. in order to simulate the far field motion. The dynamic input is applied via

prescribed displacements throughout the model's base in x direction. Both relaxation coefficients of the absorbent boundaries are considered as $C_1=C_2=1$ which means that waves travelling perpendicular to the boundary are completely absorbed. Lysmer & Kuhlmeyer (1969) have shown that the efficiency of the viscous boundary is optimized when C_1 and C_2 are equal to unity. The standard setting of the Newmark scheme with $\alpha=0.25$ and $\beta=0.5$ is utilized. In order to ensure a correct wave transmission through a FE model, the element was selected one-eighth of the shortest shear wavelength according to Equation 57. The shear wave velocity V_s is equal to 106m/s and the f_{max} was chosen 20Hz. The average element size in the finite element models was l_e=0.8m, which is smaller than the minimum required value of 1.06m.

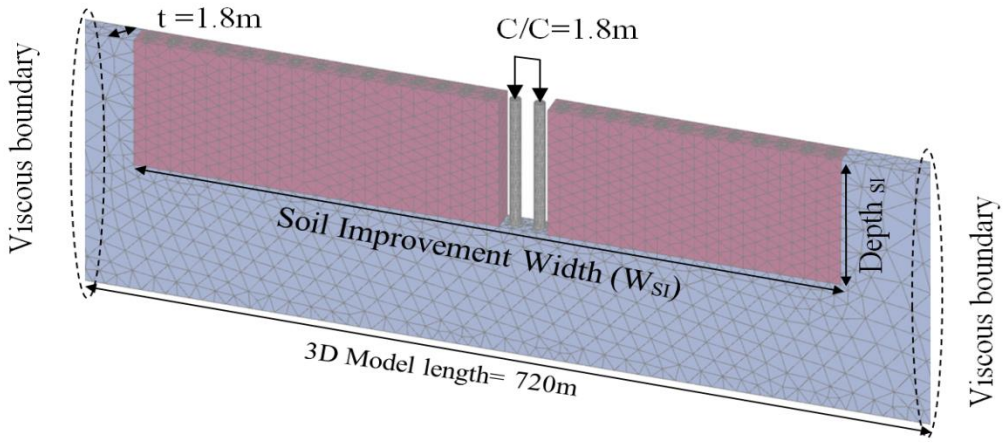

Fig. 135: Geometry of the 3D model

7.2.4 Material parameters of the soil

A viscoelastic model is used for the soil layer in the analyses with PLAXIS 2D/3D. In order to obtain the soil parameters for the numerical time domain analysis, a one-dimensional equivalent linear method can be used as a benchmark (Amorosi et al. 2010). It is assumed that the shear strain level obtained from 1D equivalent linear method with linear viscoelastic soil model is comparable with 2D/3D analyses applying the same material behaviour. For simplification, a constant shear modulus was considered over depth. In the equivalent linear method with an iterative procedure, the final seismic shear strain induced by the earthquake is estimated and the corresponding shear modulus and damping ratio within layer can be obtained from curves, available in the literature for the different type of soils. For the purpose of this study the mean values of proposed curves from Vucetic & Dobry (1991) for cohesive soils (30<PI<50) has been

chosen. DEEPSOIL is also able to perform these iterative analyses where normalized shear modulus degradation and damping ratio curves can be introduced directly into the program. Figures 136 and 137 present the average effective shear strain level over the soil layer ($\gamma_{eff.}$=0.0038*0.65=0.0025) and its corresponding shear modulus and damping ratio at the end of analysis using the DEEPSOIL V6 (Hashash et.al 2015a). Table 18 presents the obtained soil parameters for Plaxis.

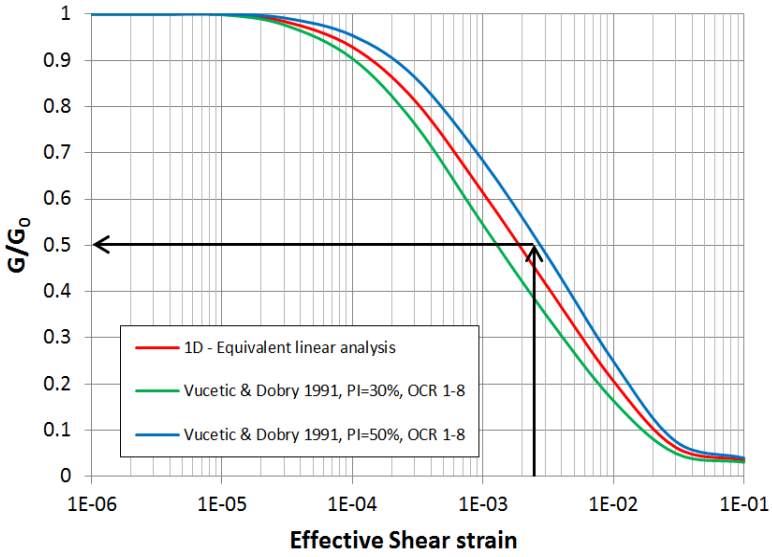

Fig. 136: Shear modulus variation with shear strain for cohesive soils (Vucetic & dobery 1991)

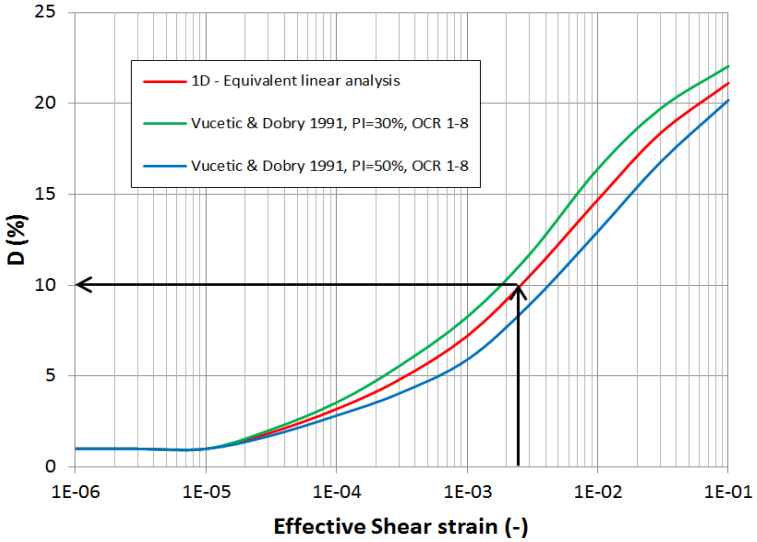

Fig. 137: Damping ratio variation with shear strain for cohesive soils (Vucetic & Dobery 1991)

Tab. 18: Soil parameters applied in Plaxis

Material	G_0 (MPa)	ν (-)	γ_{unsat} (kN/m^3)	G/G_0 (-)	G (MPa)	V_s (m/s)	E (MPa)	D (%)
Unimproved soil	43.6	0.4	19	0.5	21.8	106	61	10

As mentioned earlier in Chapter 5, beside the possible limitations of the 1D equivalent linear method, it can be used as a target solution for a time domain 2D/3D finite element analyses where a linear visco-elastic material model is applied. In time-domain analysis, generally there are two sources of damping include viscous damping and hysteretic damping. Viscous damping is frequency dependent in contrast to hysteretic damping which is frequency independent and related to the material constitutive model. In the following calculations, elastic soil material is considered and therefore hysteretic damping is ignored. Therefore, the selection of the proper target damping ratio and frequency range required by the Rayleigh damping function is important as they can have a decisive role on FE results (Amorosi et al. 2010).

The DeepSoil frequency domain solution (i.e. 1D equivalent linear method) uses frequency independent viscous damping whereas in time domain solution the frequency dependent Rayleigh damping formulation is used (Hashash et al. 2015b). In order to obtain a good match between the linear time-domain and the frequency-domain solutions, it is suggested to identify the two frequencies through an iterative procedure (Kwok et al. 2007, Hashash et al. 2015b). Viscous damping is added in the time domain analyses by Rayleigh formulation. When damping ratios ξ_m and ξ_n are equal, the parameters α_R and β_R can be computed using two significant frequency intervals f_m and f_n and according to the Equation 59.

7.2.5 Verification of the Free-Field boundary condition for the 2D analysis

In Plaxis 2D (Brinkgreve et al. 2015a) a so-called free-field boundary condition is available and therefore the width of FE model can be reduced significantly compared to the condition where a viscous boundary is used. Therefore, an improvement scenario with 50m improvement width and three different depth of penetration for columns are used to investigate the amplification ratio's curves resulted from the 3D analyses with 720m applying the viscous boundary condition and the equivalent 2D model applying the free-field condition. In order

to compare the results of 3D and 2D analyses some modifications to parameters and geometry of the improvement area have to be made. The spacing and dimension of the improvement elements are selected so that the improved 2D and 3D block as shown in Figure 138 have similar stiffness, weighted over the total moment of inertia of the block, and similar density and damping both weighted over the volume of soil improvement bodies (Floroiu & Schweiger 2014). Table 19 presents the selected dimension of 3D and 2D blocks and Equations 66-68 show the relationships applied.

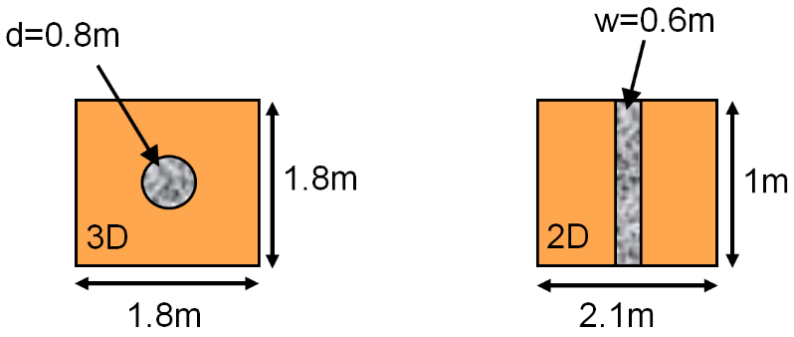

Fig. 138: 3D and 2D block properties

$$\gamma_{equivalent} = \frac{\gamma^{SI} \times A^{SI} + \gamma^{Soil} \times A^{Soil}}{A^{SI} + A^{Soil}} \tag{66}$$

$$D_{equivalent} = \frac{D^{SI} \times A^{SI} + D^{Soil} \times A^{Soil}}{A^{SI} + A^{Soil}} \tag{67}$$

$$E_{equivalent} = \frac{E^{SI} \times I^{SI} + E^{Soil} \times I^{Soil}}{I^{SI} + I^{Soil}} \tag{68}$$

Tab. 19: Soil improvement scenarios in 2D and 3D

Model	A	A_{SI}	A_{soil}	I	I_{SI}	I_{soil}	$E_{equiv.}$	$D_{equiv.}$	$\gamma_{equiv.}$
	[m^2]	[m^2]	[m^2]	[m^4]	[m^4]	[m^4]	[10^3 kPa]	[%]	[kN/m^3]
3D	3.24	0.503	3.273	0.875	0.0201	0.805	114.76	8.91	19
2D	2.1	0.6	1.5	0.772	0.018	0.754	114.75	8.91	19

*The material parameters used for calculations will be explained in the next section.

The width of the 2D model after several trial and errors has been selected to 360m as shown in Figure 139. The finite element meshes in 2D consists of 6-noded triangular elements and the average element size is l_e=0.8m.

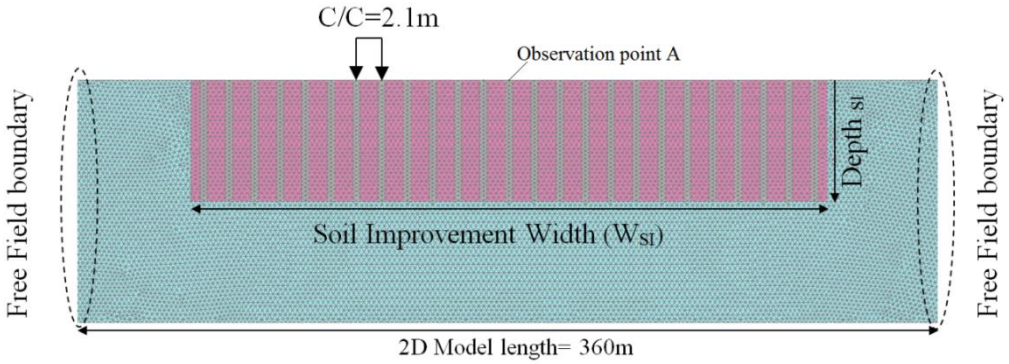

Fig. 139: Geometry of the equivalent 2D model with free-field boundary condition (soil improvement is 50 m)

Figure 140 presents the amplification ratio's curves for the point (A) on the surface and in the middle of the 3D model and its equivalent 2D model. It can be observed that for each depth of penetration the results of 2D analyses are similar to the 3D analyses. This proves that using free-field boundary condition and the modification to the soil parameters and the geometry in 2D model can provide similar results compared to the reference 3D model where viscous boundary were used. Both model length and computation time is decreased in 2D analysis, therefore, for the next calculations only 2D models are used.

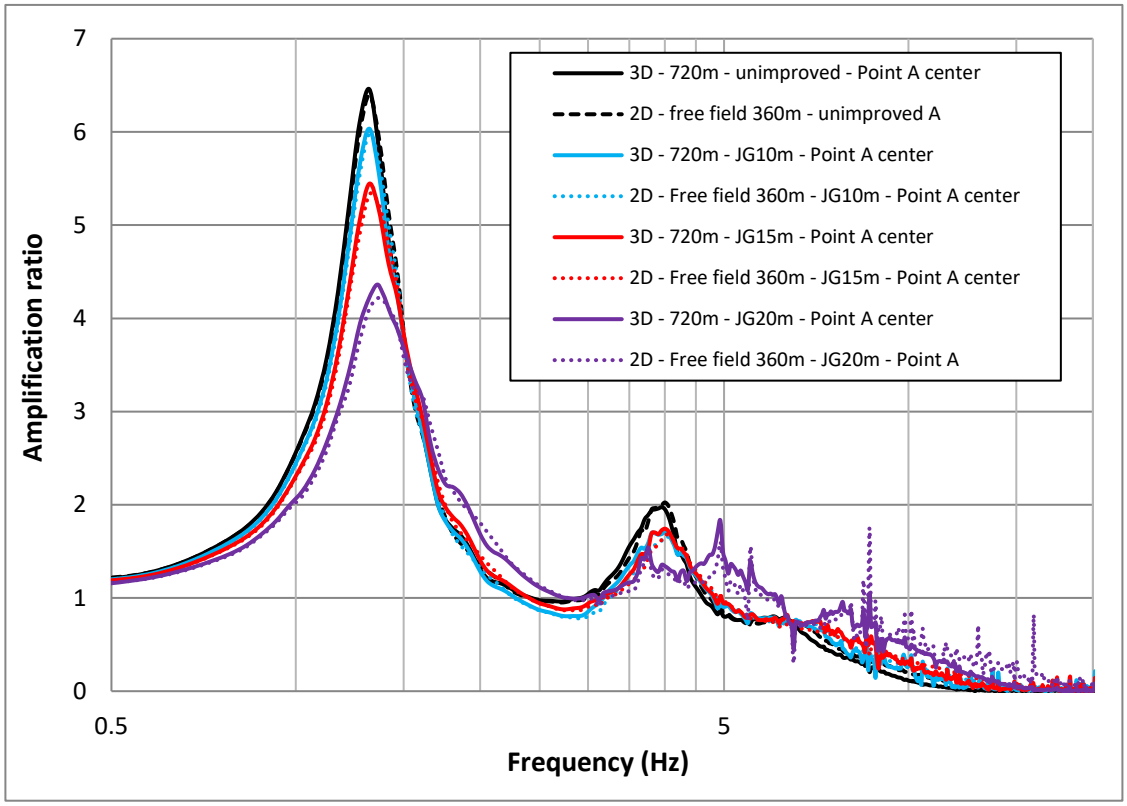

Fig. 140: Amplification ratio of the 3D model and equivalent 2D model – 50m soil improvement

7.2.6 Results

The first and second eigen frequencies of the unimproved homogeneous soil layer, based on Equation 27 are f_1=1.33Hz, f_2=3.99 Hz. Rayleigh damping parameters are calculated based f_1, f_2 and ξ=10%. The amplification ratio's curves of the 2D and 3D analyses are compared with the analytical solution proposed by Roesset (1970) and the 1D frequency and time domain from Deepsoil (Figure 141). In addition, in Figure 142 the spectral acceleration curves of the unimproved soil are presented for different analyses. These results will be used as a basis for further comparison with the results of the improved soil.

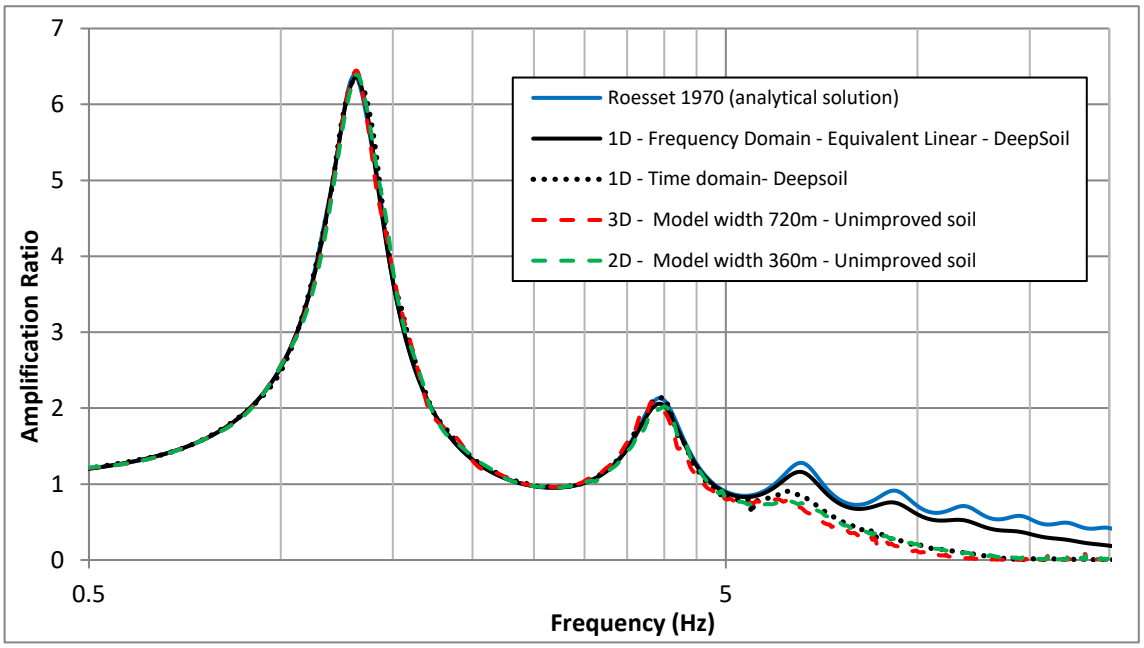

Fig. 141: Comparison of the amplification ratios - 1D frequency domain and Plaxis 2D/3D time domain

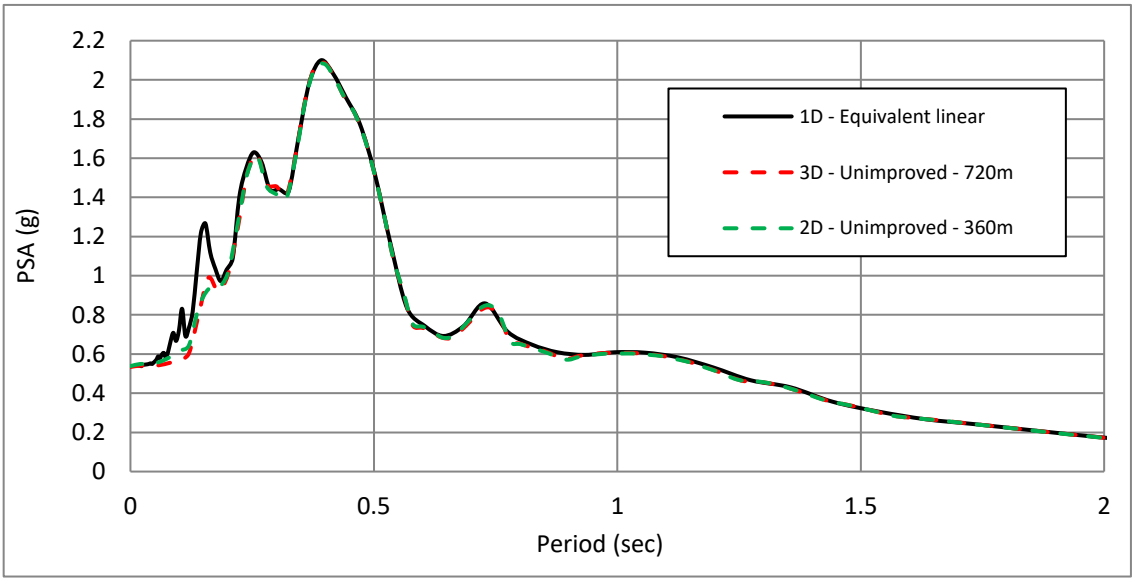

Fig. 142: Comparison of the Pseudo spectral acceleration - 1D frequency domain and Plaxis 2D/3D time domain

The influence of different soil improvement width and columns penetrations is discussed in the following. Material parameters of the jet grouting have been presented in Table 20. The time dependency of stiffness and strength was switched off. Maximum shear strain at seismic levels in the columns was around 1.2E-4. Figure 143 shows the shear strains at different levels inside the central column in the analysis of 50m improvement and 20m column penetration. The corresponding damping ratio according to results of Pantazopoulos et al. (2012)

and Delfosse-Ribay et al. (2004), (diagrams of Figures 51 and 52) was chosen 3%.

Tab. 20: Material parameters of jet grouting columns

Parameter	E	ν	F_c	F_t	G_t
	[kN/m²]	-	[kN/m²]	[kN/m²]	[kN/m]
values	2.4E6	0.22	8000	800	0.01

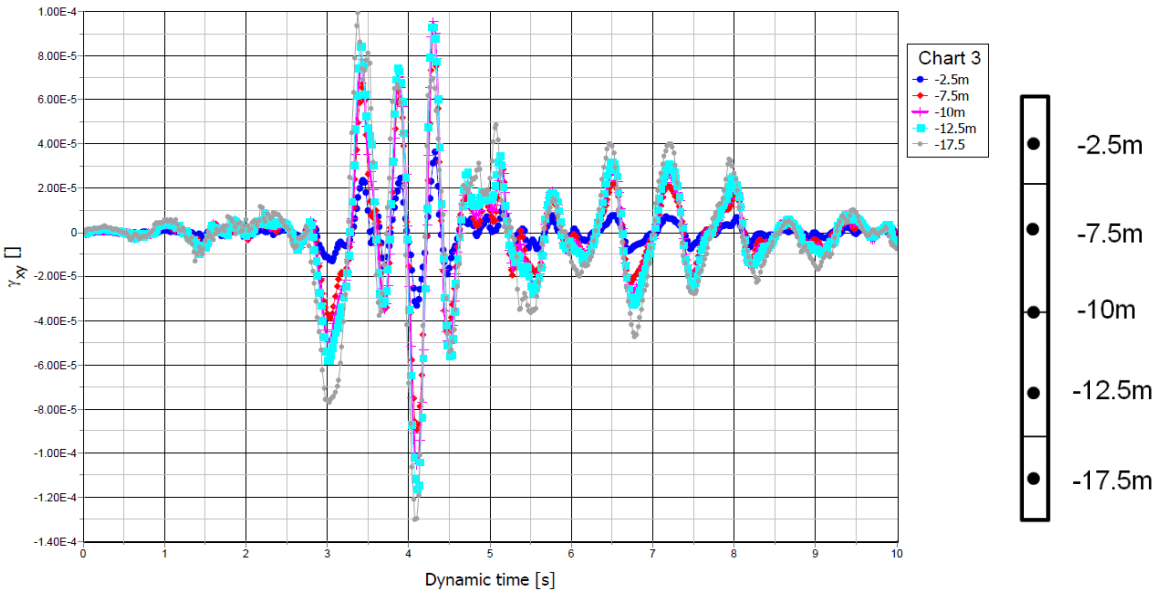

Fig. 143: Shear strain in central jet grouting column in the center of the model. Different points inside the columns

Table 21 shows the material parameters for the improved area in 2D. In further analyses, the required f_1 and f_2 of improved soil for calculation of Rayleigh coefficients has been chosen according to the results of the amplification ratio because the f_1 and f_2 may change due to soil improvement.

Tab. 21: 2D modified parameters for soil improvement area

3D	γ_{unsat}	E	D	2D	γ_{unsat}	E	D
	kN/m³	kN/m²	%		kN/m³	kN/m²	%
soil body	19	61000	10	soil body	19	61	10
Improved soil area	-	-	-	Improved soil area	19	60.2	11.28
jet grouting	19	2.4E6	3	jet grouting	19	2.4E6	3

Figure 144 shows the influence of the soil improvement in which the columns depth is kept 10m and the width of improvement varies in range of 25m, 50m and 100m. All these curves belong to an observation point on the surface of the centre of the model. As it can be observed, there is a small decrease of amplification ratio near the first eigen frequency with all three widths. At the second eigen frequency there is small decrease with 25m and 50m while using 100m improvement gives higher reduction and a shift of the second eigen frequency which means that the system is stiffer. By increasing the column depth to 15m again there is not so much decrease in the first eigen frequency but a small shift of f_1 with 100m improvement. Near f_2, a small shift of the second eigen frequency with 50m improvement and higher shift around 13% with 100m improvement can be seen (Figure 145). However, when the columns are installed in the whole layer a higher decrease of amplification ratio in f_1 can be observed and it can be concluded that in the previous analysis the first eigen frequency dictates with the unimproved part of soil below the columns and therefore the smaller decrease can be observed. Near f_2 with 25m improvement there is no shift but with 50m and 100 meter there is shift of the second eigen frequency around 25%. In addition, the amplification ratio increased near f_2 with these improvements. For 20m penetration, it is observed that in higher frequencies the curves are not smooth. This behaviour is caused by the occurrence of the cracks at the bottom of the columns where the earthquake load is exerted, and the columns are connected to the model's base. It can be seen when the columns are modelled with elastic behaviour or when the columns do not penetrate into the whole layer (e.g. JG depth=19.9m) the curves become smooth (Figure 146).

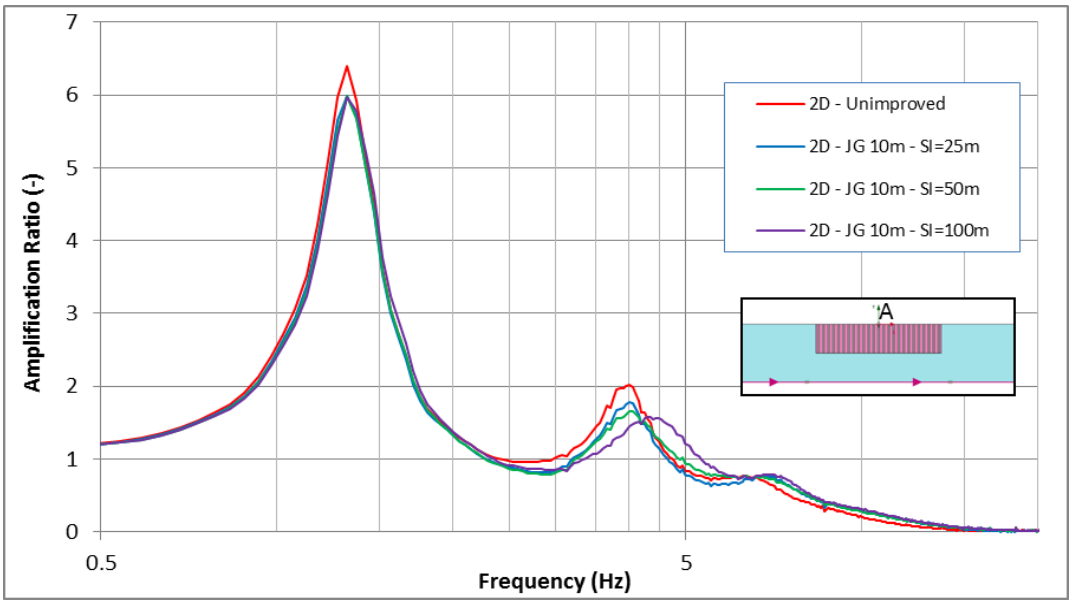

Fig. 144: Amplification ratio – columns depth 10m and soil improvement width 25m, 50m and 100m

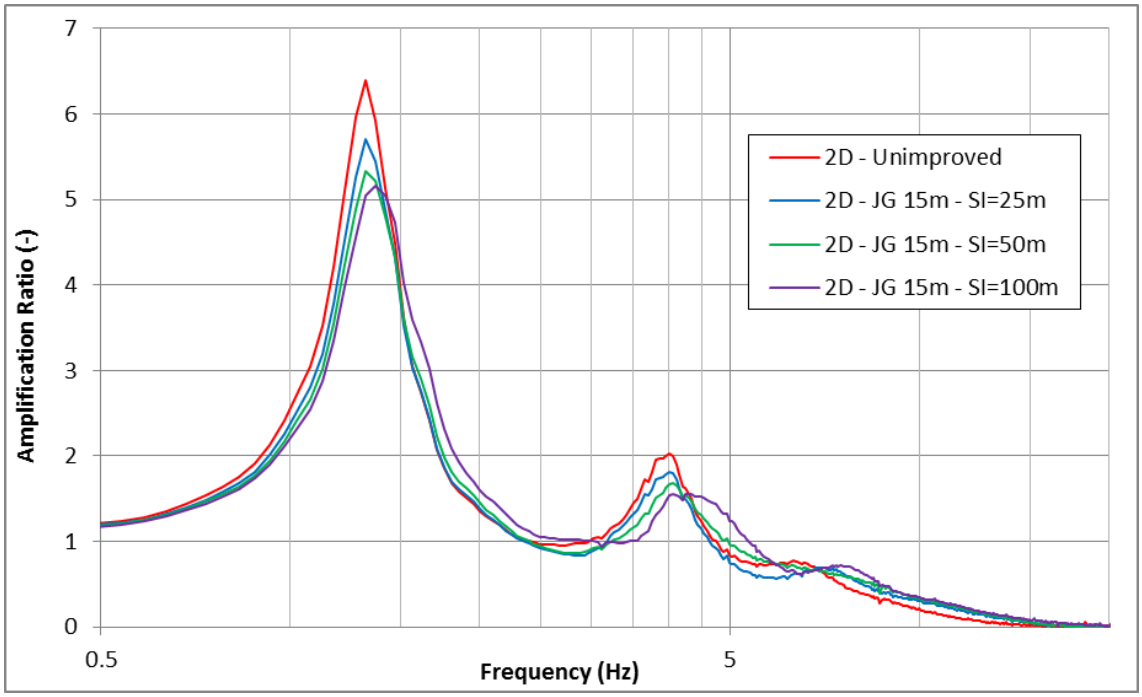

Fig. 145: Amplification ratio – columns depth 15m and soil improvement width 25m, 50m and 100m

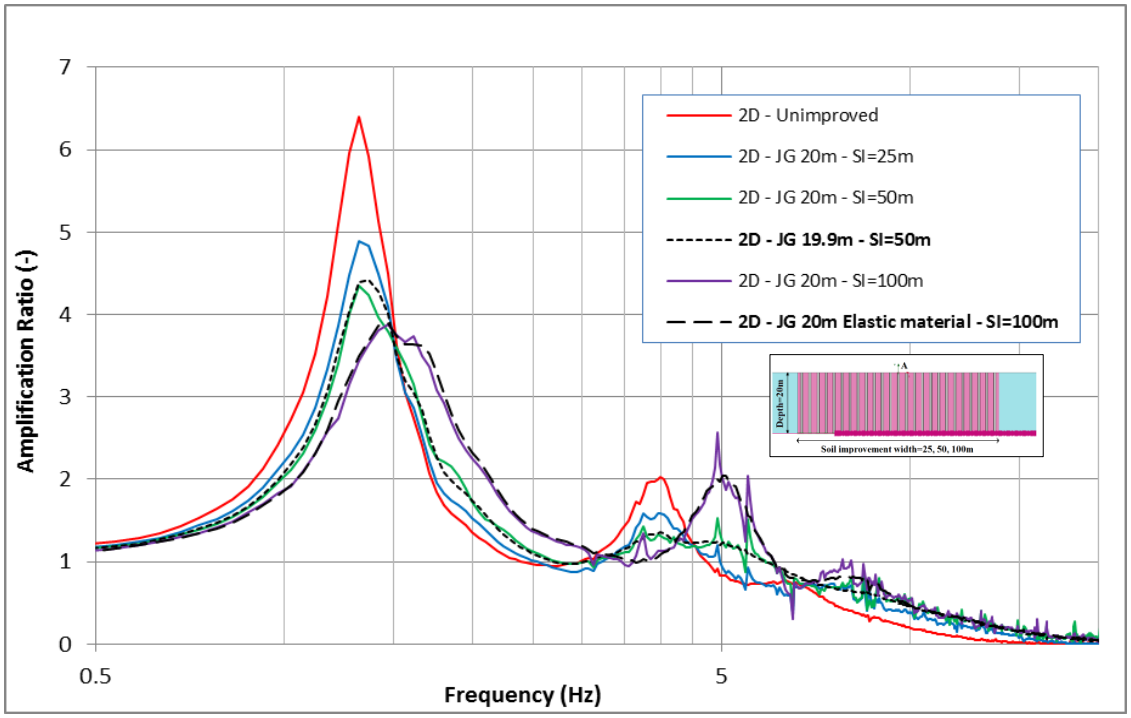

Fig. 146: Amplification ratio – columns depth 20m and soil improvement width 25m, 50m and 100m

The effect of soil improvement can be discussed using spectrum acceleration curves. Response spectrum shows the maximum acceleration of a single degree of freedom (SDOF) structure. Thus, if the natural period of a structure/system is available then the peak response can be estimated by selecting the value from the ground response spectrum. As an example, Figure 147 presents the response spectrum of the 50m soil improvement with 20m column's depth. It can be seen that in the range of 0.6-1.4sec (which can be considered roughly equal to the period of 6-story to 14-story building) the acceleration decreased by the soil improvement. However, in range of 0.2-0.6sec by increasing the depth of penetration, maximum acceleration increases where 20m columns show higher amplitude in comparison with the unimproved soil.

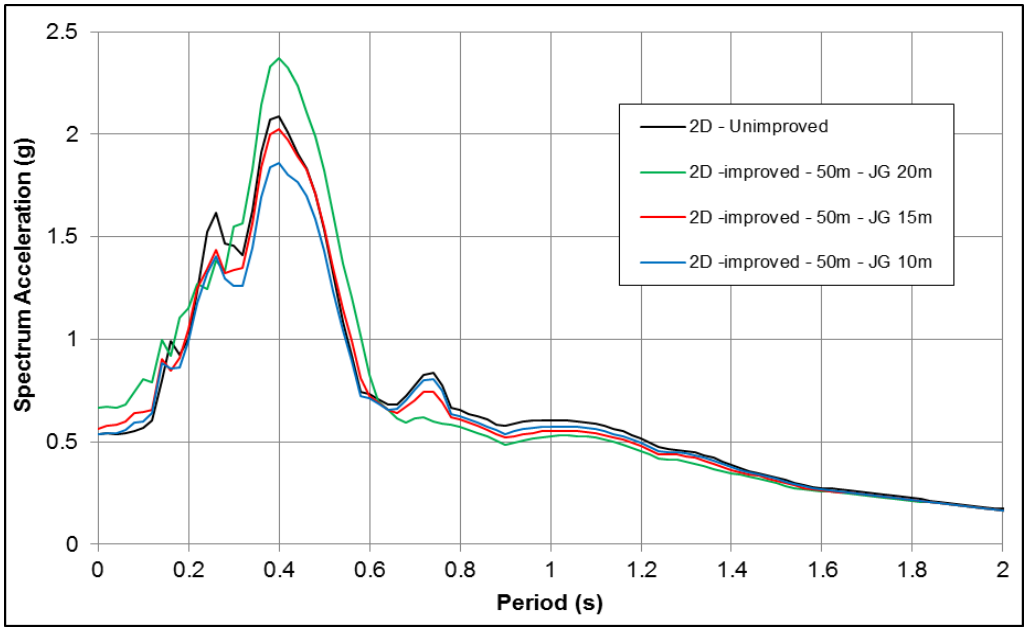

Fig. 147: Spectrum acceleration of unimproved soil and improved soil

By plotting the crack locations, it can be shown that, in the analysis with full penetration, all the cracks occurred at the bottom of the columns where the maximum shear stresses are induced by the motion. But with 10m and 15m depth of penetration no cracks developed (Figure 148).

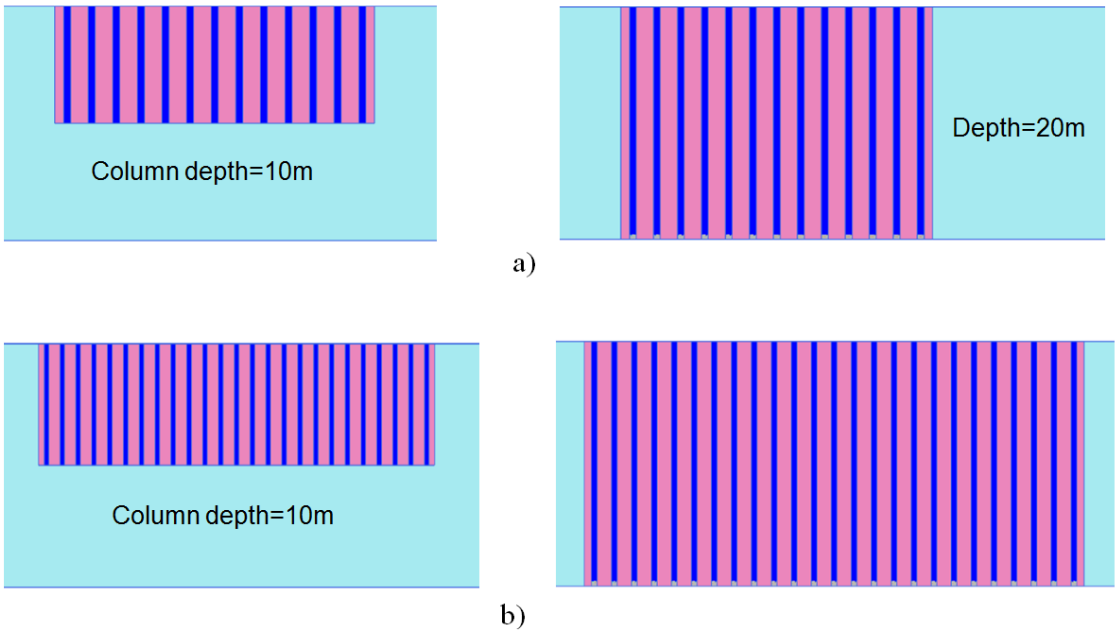

Fig. 148: Crack locations: a) 25 soil improvement; b) 50m soil improvement

7.3 Layered soil deposits

7.3.1 Ground conditions

The 20m layered soil profile consists of a 10m loose sand layer which is overlaid and underlaid by a 5m dense sand layers (Figure 149). Rigid bedrock condition is considered at the base where the shear wave velocity of the rock is assumed to be higher than 800m/s at shear strains of about 10^{-4} % similar to ground type A based on EC8 (CEN-EN 1998-1, 2004). The unit weight of 18kN/m^3 is assigned to all soils. Earth pressure coefficients at rest (K_0) for loose sand and dense sand are assumed as 0.44 and 0.33 respectively. The values of shear modulus (V_s) are assumed to be constant over depth for each layer. Small strain shear modulus ($G_{max}=\rho V_{s0}^2$) of the loose sand and dense sand layer are then equal to 54MPa and 187.5MPa respectively, which means that the dense layer is roughly 3.5 times stiffer than the loose layer.

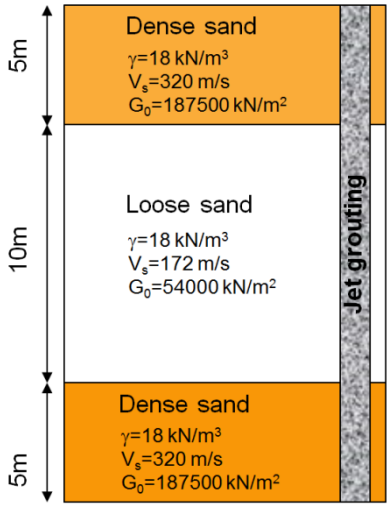

Fig. 149: Soil profile representing layered soil condition

7.3.2 Finite element model

Similar to the previous example the reference model is 3D, in which a rectangular shape of the column grid was assumed (Figure 145). Diameter and center-to-center spacing of the columns are 80cm and 180cm respectively, and the 3D model's thickness is 1.8 meter. The replacement ratio (A_r) is 16%. The soil improvement width considered is 25m, 50m and 100m respectively, and the column depth is varied (10m, 15m and 20m).

The acceleration-time history recorded during the 1989 Loma Prieta U.S.A. earthquake is also used in these analyses.

Figures 150 and 151 show the geometry of the 3D and equivalent 2D Plaxis models. The dynamic input is applied via prescribed displacements throughout the model's base in x direction. Both relaxation coefficients of the absorbent boundaries are considered as $C_1=C_2=1$. The standard setting of the Newmark scheme with $\alpha=0.25$ and $\beta=0.5$ is utilized.

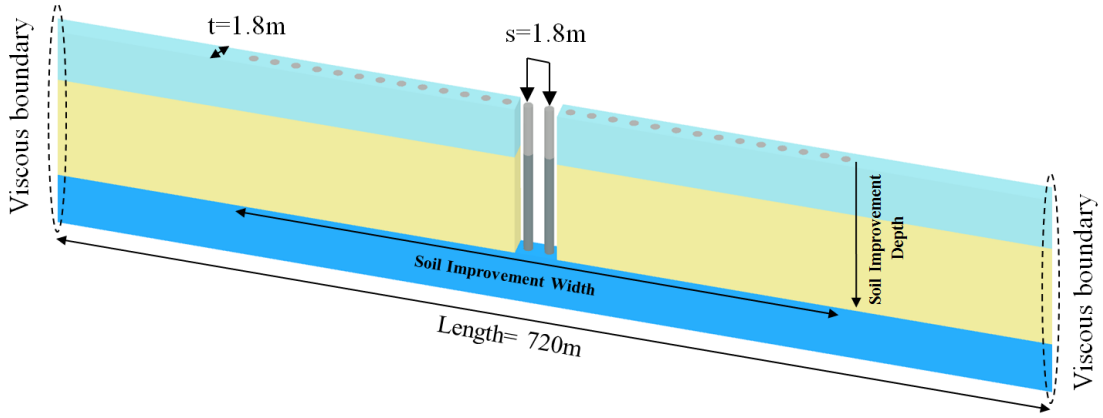

Fig. 150: Geometry of the 3D model for layered soil

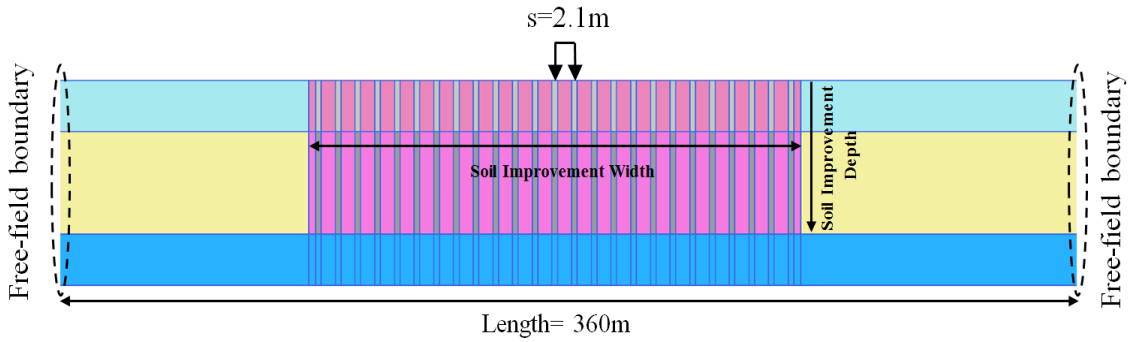

Fig. 151: Geometry of the equivalent 2D mode for layered soil

In order to compare the results of 3D and 2D analysis modifications to parameters and geometry of the improvement area have to be made for all soil layers similar to homogeneous layer (see Figure 138).

Tab. 22: Properties of 3D and 2D blocks

Model	A	A_{SI}*	A_{Soil}	I_{Total}	I_{SI}	I_{Soil}
	(m^2)	(m^2)	(m^2)	(m^4)	(m^4)	(m^4)
3D	3.24	0.503	3.273	0.875	0.0201	0.805
2D	2.1	0.6	1.5	0.772	0.018	0.754

*SI= Soil improvement

7.3.3 Material parameters of the soil layers

In this example, also a linear viscoelastic soil model has been considered in dynamic analyses. In order to obtain the soil parameters for the numerical analysis, one-dimensional method with the equivalent linear approach is used as a benchmark. A constant small-strain shear modulus over depth was considered for the soil layers. It is accepted that using a various shear modulus with depth is more reasonable and realistic, but for simplification reasons in FEM calculations to obtain the soil layer parameters, it was decided to use constant shear modulus over depth. If the value of the constant G_0 is chosen reasonably then the results of the ground response are comparable with the condition where variable stiffness is used. In the DEEPSOIL code, the entire soil deposit was modelled and the material properties of each layer include the density and the small-strain shear modulus (or the small-strain shear wave velocity) was given and the earthquake record was applied at the bottom of the model with rigid half-space condition. Via the equivalent linear method, and according to the obtained effective shear strain for each layer, the secant shear modulus and the damping ratio are defined by applying the proposed curves for sandy soils by Seed & Idriss (1970). Figures 152 and 153 present the average effective shear strain level over each layer and its corresponding shear modulus and damping ratio at the end of analysis using the DEEPSOIL code.

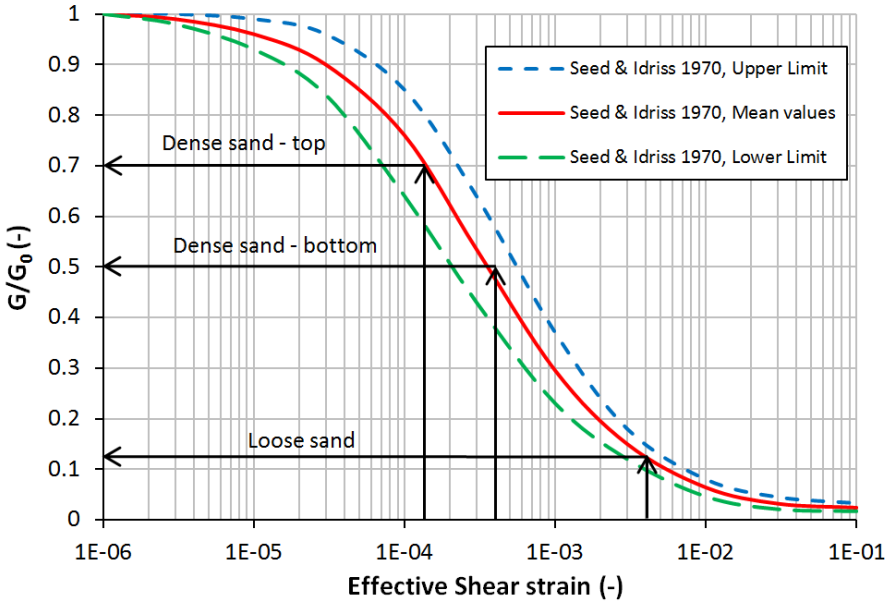

Fig. 152: Shear modulus reduction (G/G_0) with shear strain for sandy soils

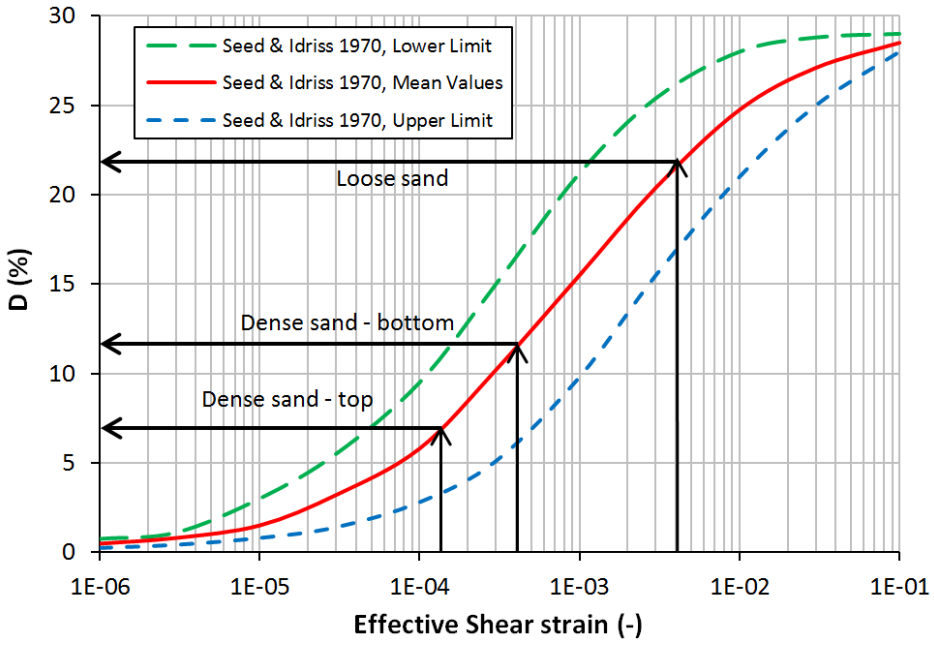

Fig. 153: Variation of damping ratio (D) with shear strain for sandy soils

Table 23 shows the soil parameters resulting from calculations of the equivalent linear method which were used for defining linear viscoelastic soil parameters. The maximum shear strain level calculated in the unimproved loose sand layer was around 7E-3. Based on the recommendations of Ishihara (1996), shear strain levels between 1E-3 and around 1E-2 are still acceptable for viscoelastic models and the equivalent linear method.

Tab. 23: Material parameters of the soil layers

Material	G_0	γ_{unsat}	G/G_0	G	E	D
	(kN/m^2)	(kN/m^3)	(-)	(kN/m^2)	(kN/m^2)	(%)
Dense sand (top)	187500	18	0.7	132000	369600	7
Loose sand	54000	18	0.135	7500	21000	22
Dense sand (bottom)	187500	18	0.5	94000	263200	12

The minimum element size according to Equation 57 is considered one-eighth of the shortest wavelength. The minimum shear wave velocity at seismic level was 65 m/s and the maximum frequency f_{max} of interest in this study is equal to 20Hz.

The average element size in the finite element models was l_e=0.55m which is smaller than the minimum 0.8m.

For the considered layered soil profile, the first and second eigen frequencies are 1.05Hz and 3.35Hz respectively. To match the linear time domain analysis with equivalent linear result in this interval, by trial and error, the target frequencies f_m and f_n required for the calculation of Rayleigh formulation have been chosen as 1.72Hz and 5Hz respectively. Figure 154 shows the result of the amplification ratio for a point on the surface at the center of the 2D and 3D unimproved soil model in addition to the result of 1D frequency domain resulting from DEEPSOIL. The average effective shear strain level resulted from 2D/3D analysis in first, second and third layer were 1.4E-4, 3.9E-3 and 4E-4 respectively. These values are comparable with those obtained from 1D equivalent linear method.

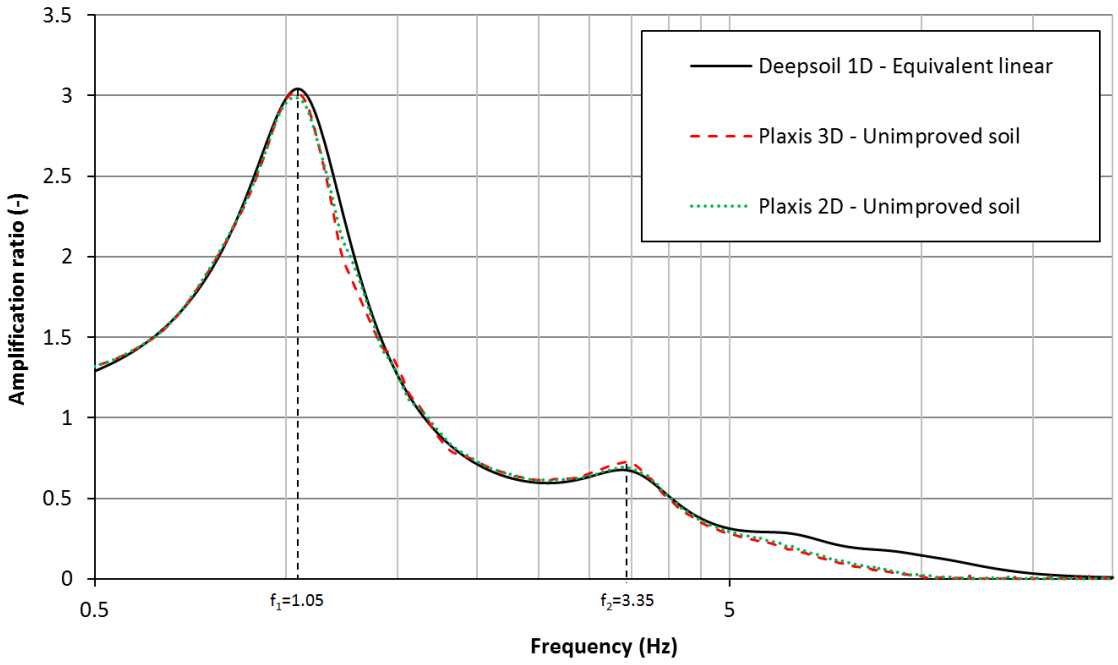

Fig. 154: Amplification ratio of the unimproved soil

7.3.4 Material properties of the columns

Table 24 shows the material parameters used for the jet grout columns. The Young's modulus of jet-grouting materials in sandy soils can be based on the uniaxial compressive strength, usually in the range of $300q_u$ -$1000q_u$, where q_u is the uniaxial compressive strength (van der Stoel 2001). Here the stiffness value used for the analysis is equal to $300q_u$. The fracture energy values in tension are

in general small and for the purpose of current study, this value was chosen as 10N/m representing brittle behaviour. The tensile strength was estimated about 10% of the uniaxial compressive strength according to DIN 4093: 2012-8. The time dependency of stiffness and strength has been switched-off in the following analyses.

Tab. 24: Material parameters of the jet grout columns

Parameter	γ	E	ν	F_c	F_t	G_t
	(kN/m^3)	(kN/m^2)	(-)	(kN/m^2)	(kN/m^2)	(kN/m)
values	18	2.4E6	0.2	8000	800	0.01

Following Delfosse-Ribay et al. (2004) and Kitazume & Terashi (2013) the damping ratio of the jet grout columns according to the maximum seismic shear strain inside the columns in the upper, middle and lower layer were chosen as 2%, 4% and 3% respectively. Rayleigh damping parameters of the jet grout columns have been also calculated based on the first and second eigen frequency of the improved system.

7.3.5 Results and discussion

In the following analyses, according to the previously mentioned assumptions in section 7.2.5 and Equations 66-68 the 2D models are modified based on the 3D model. Table 25 shows the modified parameters which are used for the soils between the columns inside the improvement zone.

Tab. 25: 2D modified parameters for improved soil between columns

Soil layer	γ_{soil}	E_{soil}	D_{soil}
	(kN/m^3)	(kPa)	(%)
2D-top	18	361400	7.9
2D-middle	18	20200	25.9
2D-bottom	18	262500	14.2

Figure 155 shows results in which the soil improvement width is 50m and the depth of the jet grout (JG) columns is 20m, both for the 2D and 3D model. It

follows that results are in a good agreement and therefore only 2D results will be discussed in the following.

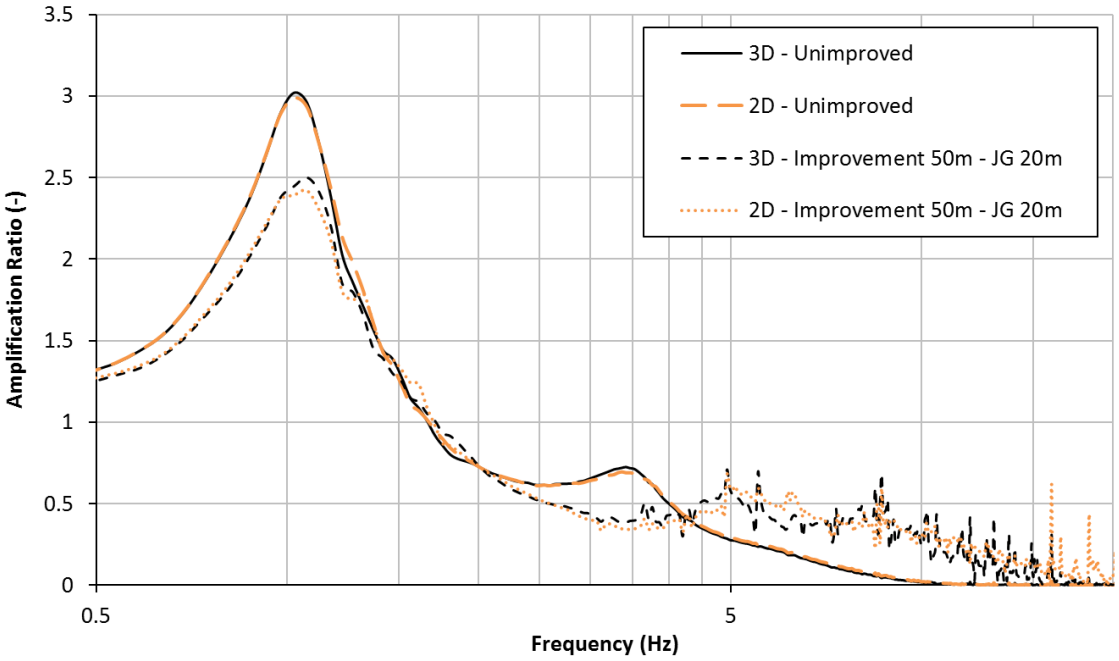

Fig. 155: Comparison of 3D and 2D improved soil results

Evaluating the amplification ratio at the central point on the ground surface, when the column depth is 10m and soil improvement width changes from 25m to 50m and 100m it is observed that the decrease in amplification ratio is very small at the first eigen frequency and the second eigen frequency of the soil deposit is de-amplified (Figure 156). The soil improvement is not efficient, as the columns did not penetrate the loose layer. By increasing the column depth to 20m (i.e. entire layer), there is a larger decrease of amplification ratio at f_1 and this reduction increases by utilizing a wider soil improvement width, also a small shift of first eigen frequency is observed (Figure 157). It is observed that the second eigen frequency (f_2) of the improved soil is shifted to higher values and its corresponding amplification ratio increases when a wider improvement width is used (Figure 157). Figure 158 proves that there is not so much difference between 20m (see Figure 157) and 15m penetration and it is also shown that when the columns are only installed in the loose sand layer the behaviour is similar to 15m penetration as could be expected. It is noted that the average shear strain level in the soils between the columns does not change significantly as compared to the unimproved soil. However, further parametric studies would be required before these findings could be generalized for other conditions.

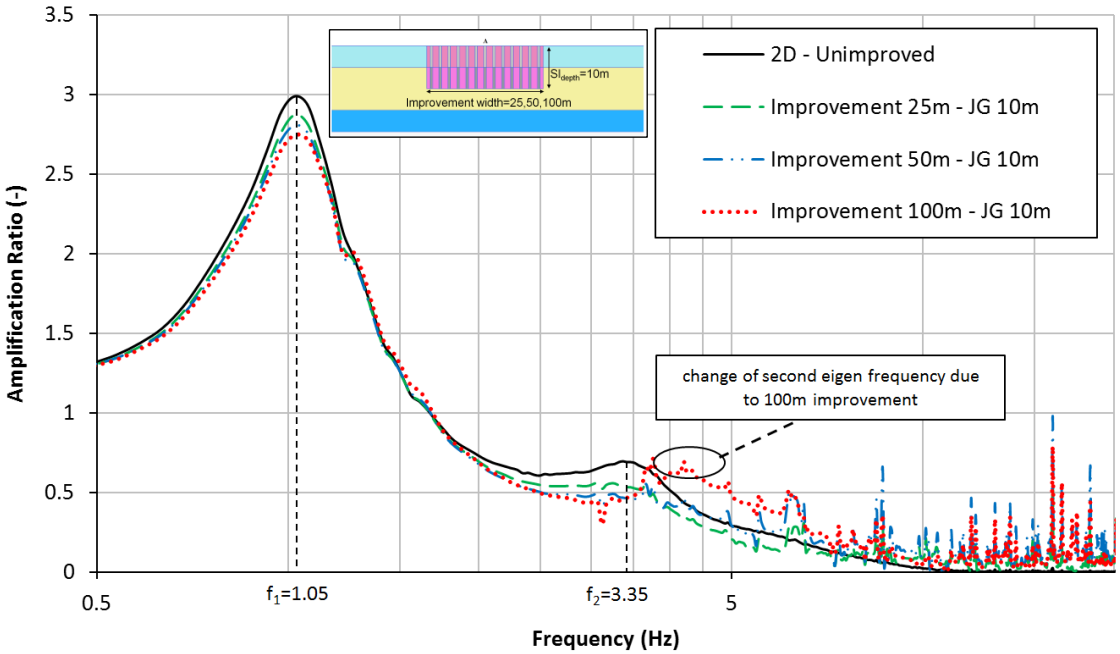

Fig. 156: Amplification ratio – columns depth 10m and soil improvement width 25m, 50m and 100m

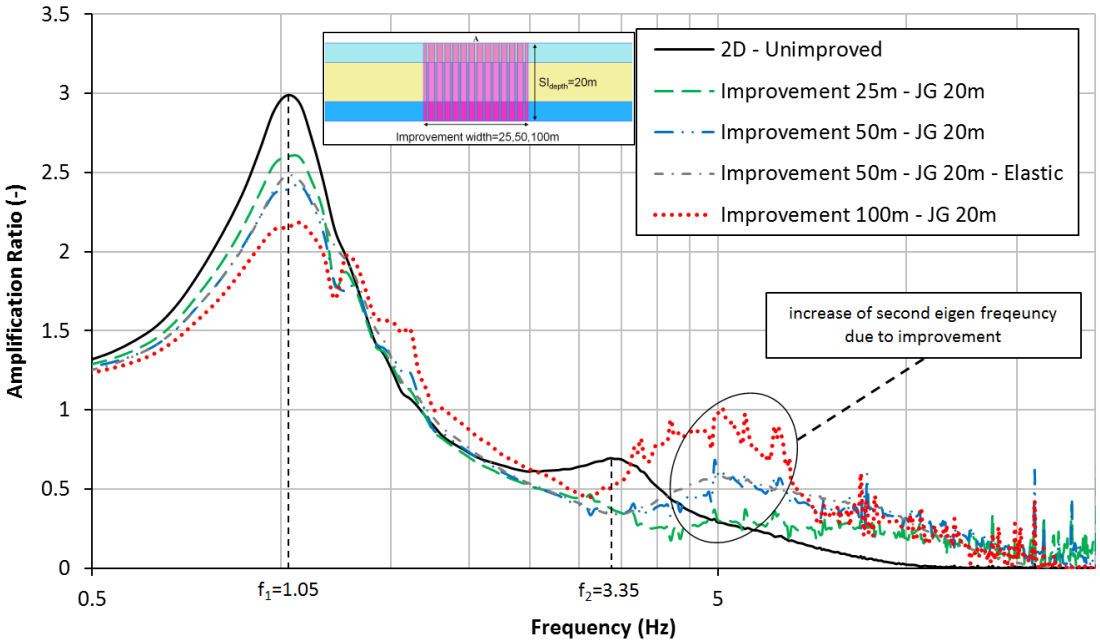

Fig. 157: Amplification ratio – columns depth 20m and soil improvement width 25m, 50m and 100m

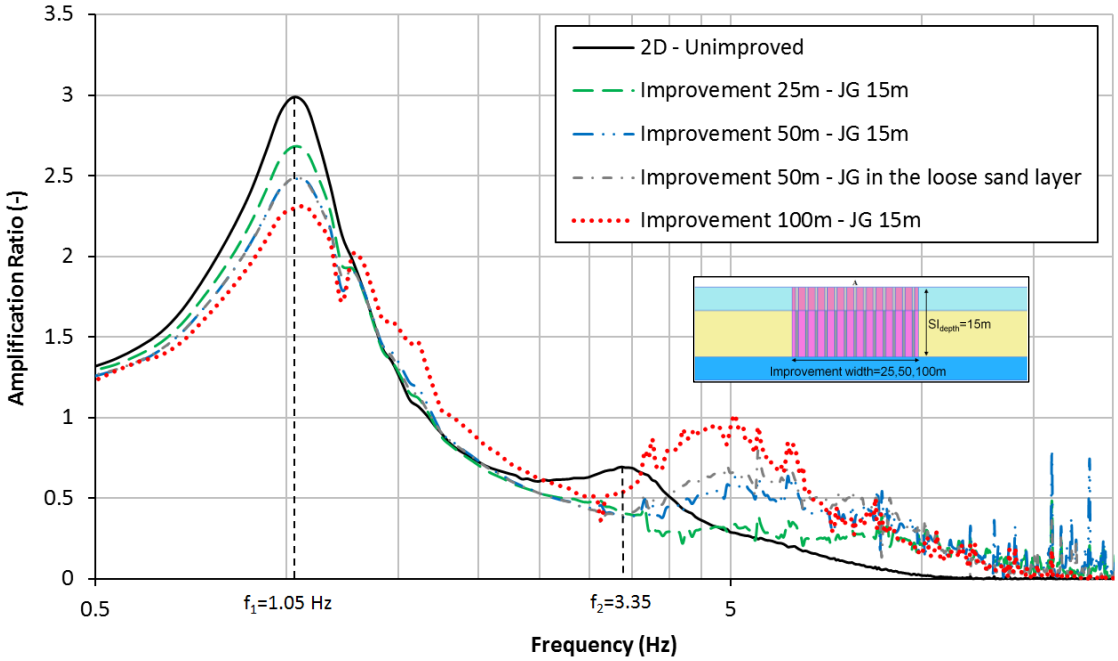

Fig. 158: Amplification ratio – columns depth 15m and soil improvement width 25m, 50m and 100m

Figures 159 and 160 depict examples of possible crack zones. It is observed that the cracks develop at the boundary of the dense and loose layer where the maximum shear stresses occurs; also cracks occur at the base level when full penetration is implemented. As mentioned previously it is emphasized that the shotcrete model cannot capture the real behaviour of the cracks in unloading/reloading. Crack closure is too stiff and therefore realistic initiation of crack patterns may be obtained, but post-cracking behaviour will not be modelled realistically.

Additionally it was tried to investigate the effect of the column's dimension on the amplification reduction. The diameter was increased to 1.2m (i.e. A_r= 35%) but the other properties of the columns are kept constant. Figure 172 shows the influence of the higher replacement ratio on the amplification ratio for 50m improvement width and 20m penetration. It can be shown that for the replacement ratio of 35%, the reduction in the amplification ratio at f_1 is even higher than the 100m improvement where A_r=16%. It also shifts the second eigen frequency towards 8 Hz. Similar to previous analyses in the high frequency zone the amplification ratio's curve is not smooth which is related to the crack occurrence in the columns.

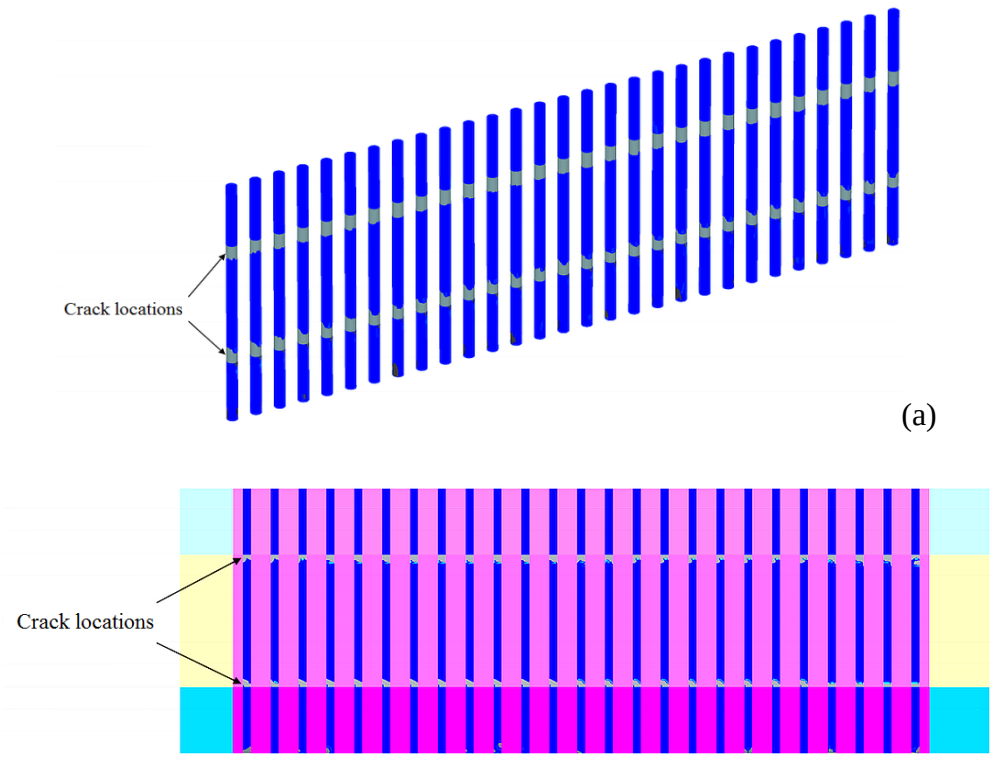

Fig. 159: Crack locations for 50m improvement and 20m column depth: (a) 3D model; (b) equivalent 2D model

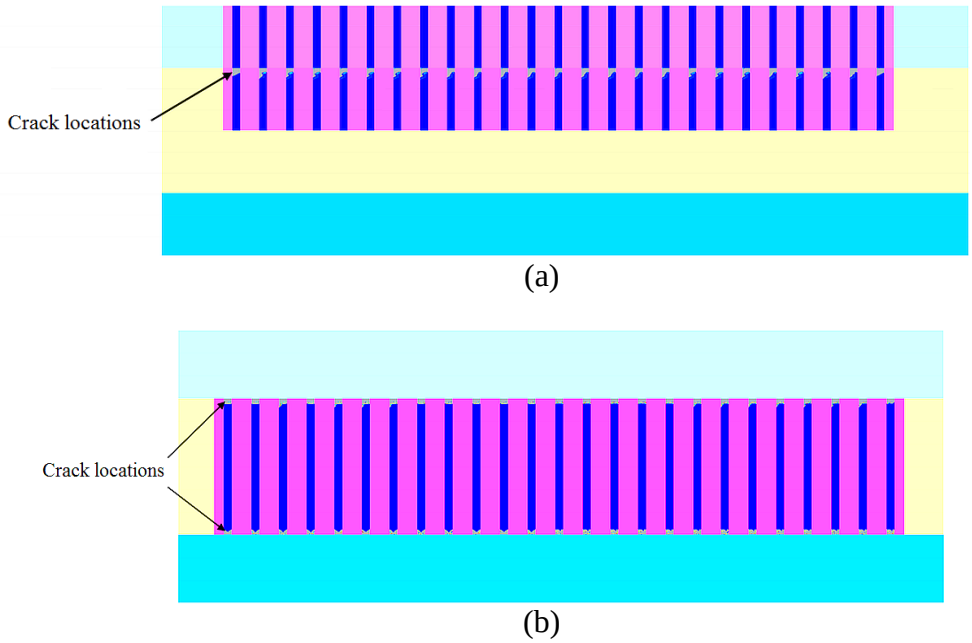

Fig. 160: Crack locations for 50m improvement: (a) column depth 10m; (b) columns in the middle layer

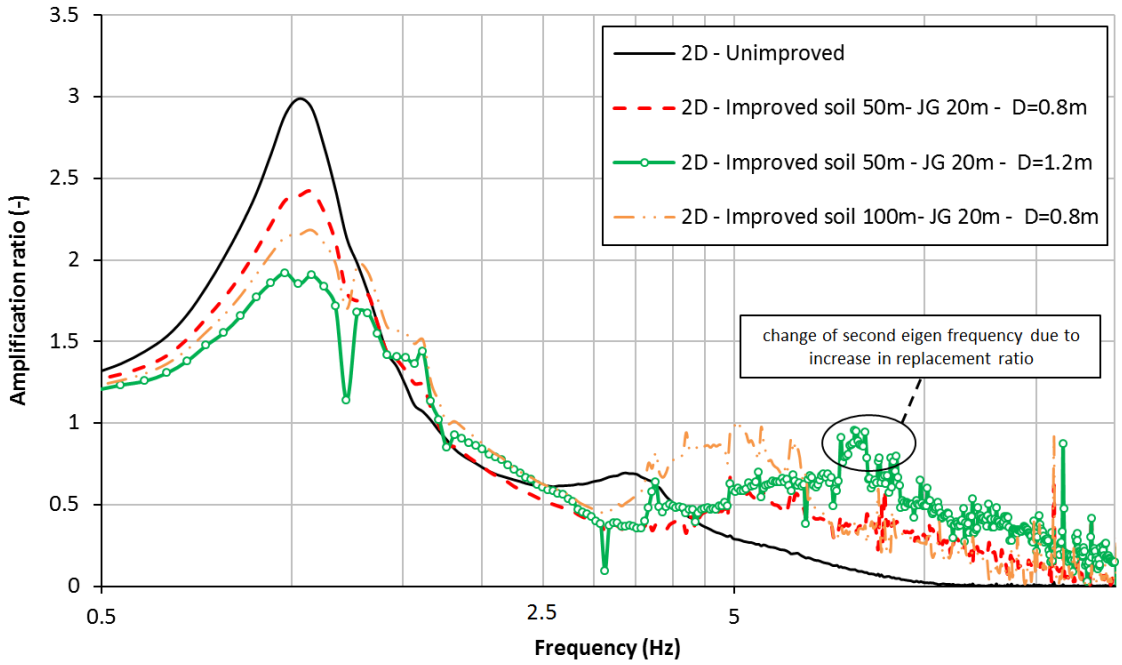

Fig. 161: Amplification ratio – influence of the column's diameter

Considering the spectral acceleration for the conditions with 20m column's depth and various improvements width and replacement ratio, it follows that in general the improved soil can decrease the structure's acceleration compared to unimproved soil (Figure 162). But, in the range of T=0.2sec the structural acceleration is increased compared to the unimproved soil by increasing the soil improvement width and also the replacement ratio. At the periods of 0.37sec (i.e. the frequency of 2.68 Hz, which is equal to the dominant frequency of the earthquake), the acceleration reduction rate compared to the unimproved soil is small when the width of soil improvement is 100m, or the replacement ratio is 35% because the stiffness of the system increases. To provide a better insight to the periods of T=0.2 and 0.37sec (i.e. f=1/T=5Hz and f=2.68Hz) it can be referred to Figures 158 and 161 where a higher amplification ratio at 5Hz and roughly identical amplification ratios at 2.68Hz compared to unimproved soil were obtained. The influence of higher replacement ratio and wider improvement width are more significant in the range of 0.6sec-1sec. At the period equal to zero which presents the ground level acceleration it is also clear that the maximum ground acceleration is attenuated by soil improvement.

In addition, it is attempted to compare the results with the proposed elastic response spectra type I from EC8 (CEN-EN 1998-1, 2004). These spectra are plotted using 5% damping and they are scaled by applying a design ground acceleration a_g. Where a_{gR} and γ_I have been chosen as 0.35g and 1.2 respectively and therefore a_g=0.42g. For instance it can be observed that in low periods due to a 25m or 50m improvement and 20m column's penetration, the maximum

spectral acceleration of unimproved soil which was located between soil classes D and C has been shifted to soil class A. In the range of higher periods (e.g. T=0.9 Sec) the improved soil class also shifts toward site class A.

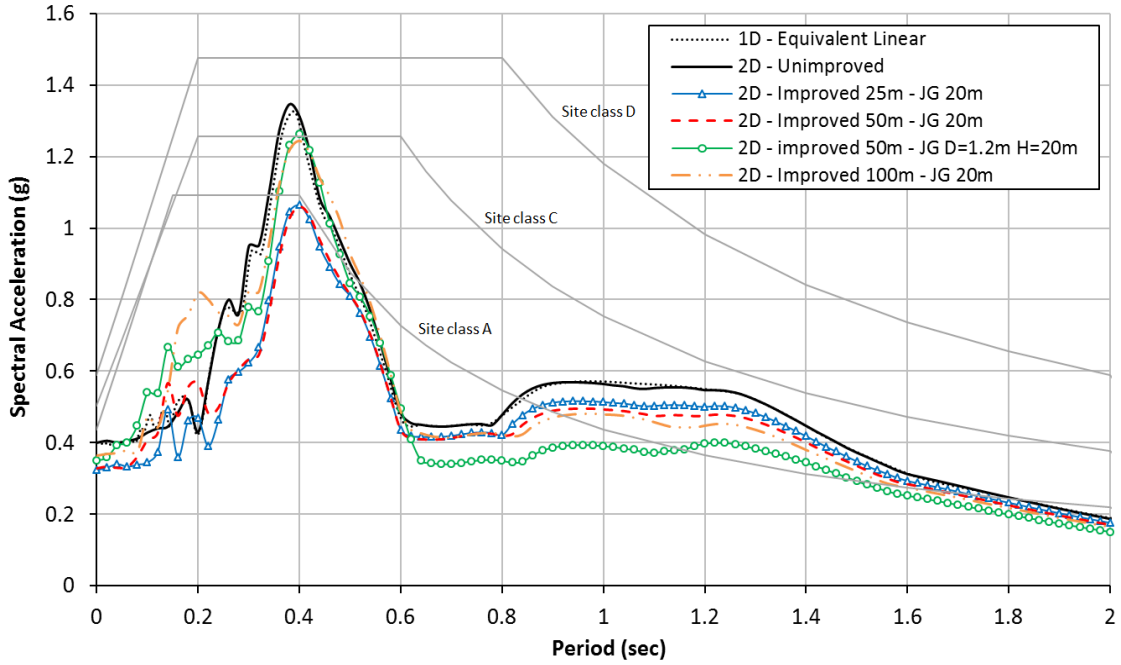

Fig. 162: Response spectra for unimproved and improved soil

7.4 Influence of a different earthquakes

In this section, two different excitations are applied to the base of a layered soil deposit in order to provide more details about the behaviour of the improved deposit using jet-grouting columns under different earthquakes which have various characteristics. Figures 163, shows the acceleration time history of the Northridge01-century city and its Fourier amplitude spectrum. The motion was scaled to maximum horizontal acceleration of 0.35g. The dominant frequency of the motion is 1.67 Hz. The second motion is Loma Prieta which has been introduced earlier in Section 7.2.2 (See Figures 132 and 133).

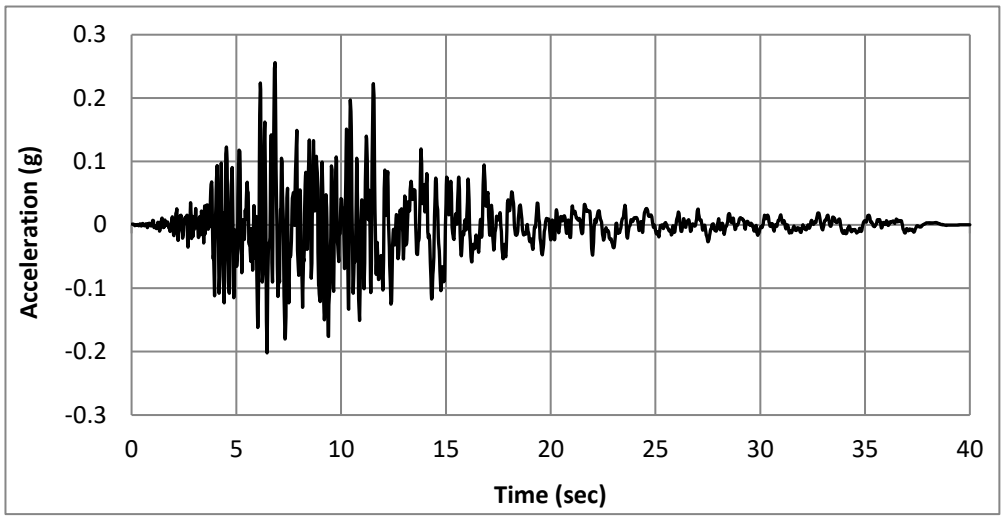

(a)

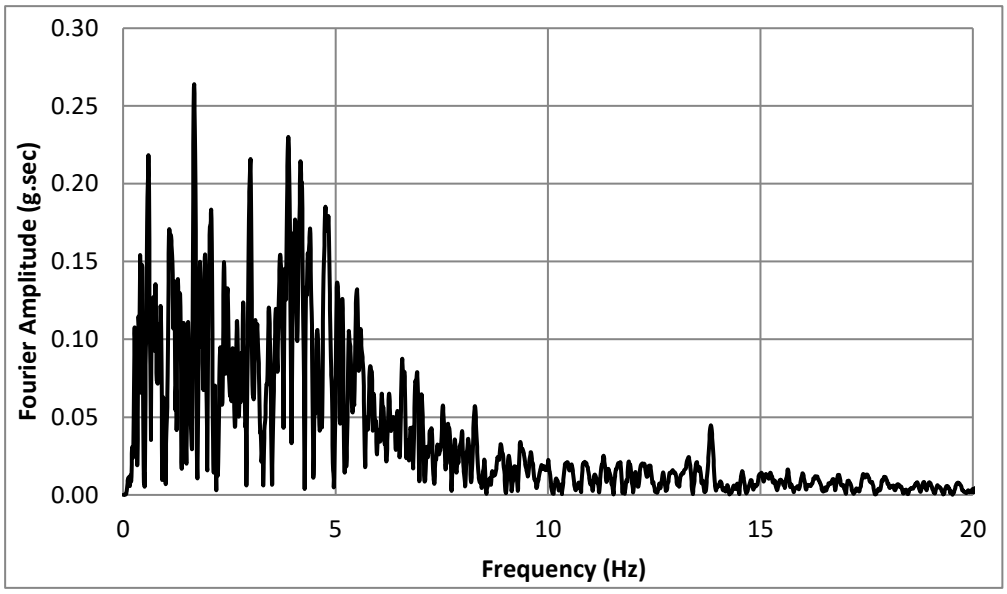

(b)

Fig. 163: Northridge01-century earthquake; a) Acceleration time - b) Fourier amplitude spectrum

7.4.1 Unimproved soil

7.4.1.1 Material parameters of the soil layers

Different material properties have been assigned to the layered soil deposit compared to the previous example (Figure 164). The base of the model is considered as a rigid bedrock condition. The unit weight of soil layers are 19kN/m^3 and 18kN/m^3 for dense sand and loose sand respectively. The Friction angle of dense sand considered as 40° and for loose sand is 32°. The Coefficient

of earth pressure at rest (K_0) is 0.357 and 0.47 for dense and loose layer respectively.

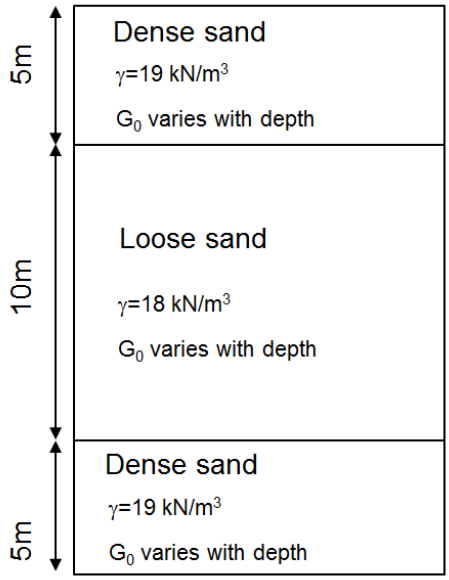

Fig. 164: layared soil condition

The small strain shear modulus changes with depth. The profile of small strain shear modulus was calculated according to the equations 69 & 70, suggested by Chaudhary et al. (2004) and Hoque & Tatsouka (2004) for dense and loose sand respectively:

$$G_0 = 84 \times \frac{(2.17-e)^2}{1+e})(\frac{p'}{p_{ref}})^{0.5} \quad (69)$$

$$G_0 = 71 \times \frac{(2.17-e)^2}{1+e})(\frac{p'}{p_{ref}})^{0.41} \quad (70)$$

Where e is the void ratio and is set to 0.55 and 0.75 for dense and loose sand respectively, p' is the mean effective stress in kPa, p_{ref} is the reference pressure which is equal to 100kPa. Figure 165 depicts the variation of small strain shear modulus and small-strain shear wave velocity with depth for the soil layers.

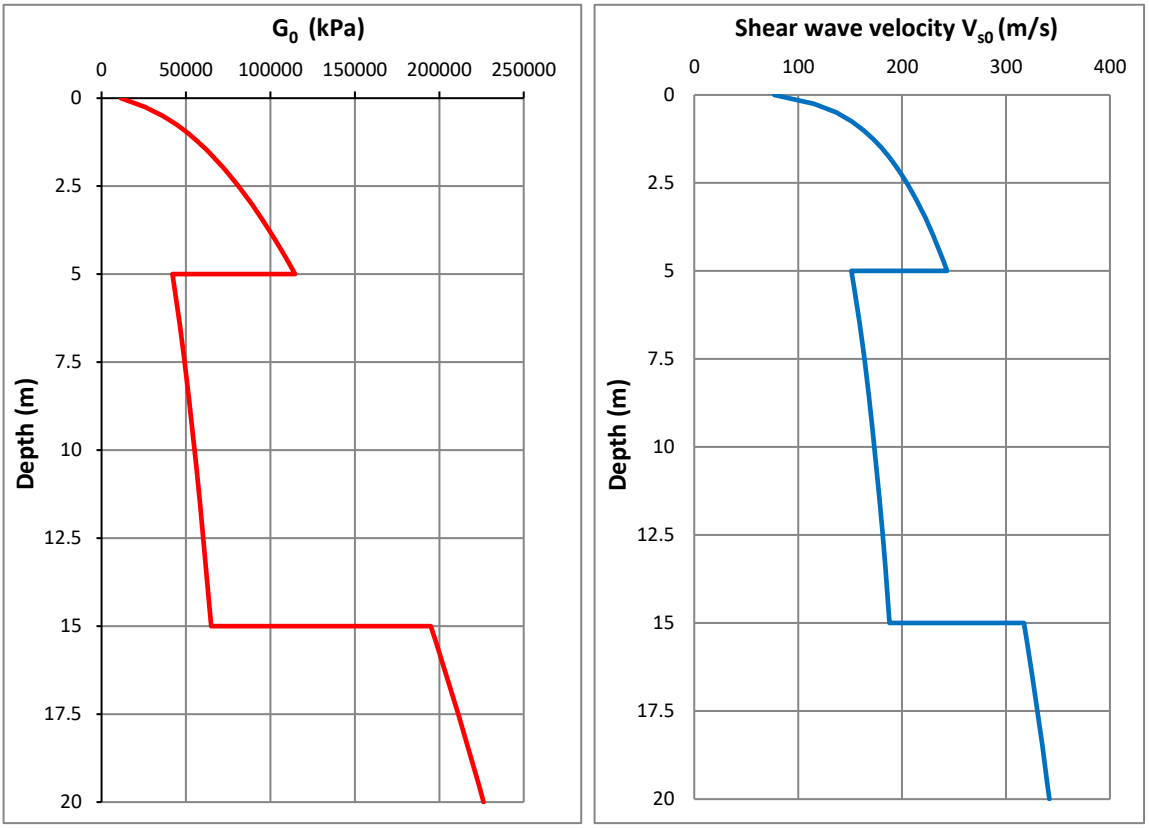

Fig. 165: Variation of small strain shear modulus (G_0 in kPa) with depth (left) Variation of corresponding shear wave velocity with depth (right)

Similar to the previous examples, the one-dimensional frequency domain method with equivalent linear approach is used as a target for time domain analyses. In order to capture the nonlinear distribution of the soil shear modulus with depth, the soil layers are discretised to 25 layers and in each sublayers a constant shear modulus is assumed according to Figure 166. For performing the equivalent linear analysis with DEEPSOIL the mean curves of shear modulus reduction and damping ratio reported by Seed and Idriss (1970) are used.

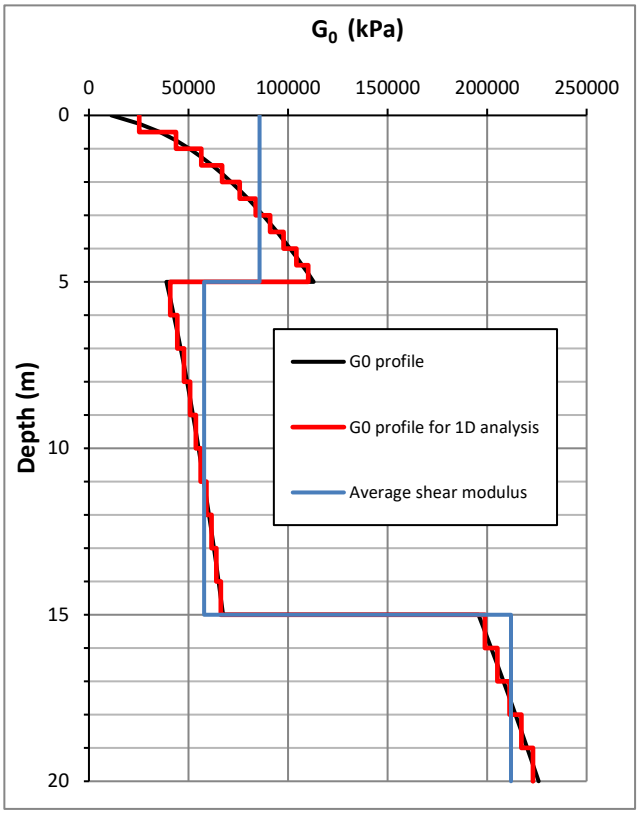

Fig. 166: Profile of G_0 applied in 1D-equivalent linear method and the average shear modulus in each layer

The effective shear strain (which is assumed to be 65% of the maximum shear strain) in each small layer, is shown in Figure 167. It can be seen that the shear strain distribution over top dense sand layer, loos sand and lower dense sand layer confirm the use of average effective shear strain over each soil layer which leads to a constant shear modulus and damping ratio over depth. Table 26 presents the material parameter which will be used in the numerical 3D analysis. Figures 168 and 169 show the amplification ratio and spectral acceleration curves, resulting from 1D equivalent linear method and the 3D time domain analyses for the unimproved soil where a constant shear modulus and damping ratio for dense and loose sand layers were used. These results are in good agreement and therefore the amplification ratio's curves and the spectral acceleration of the 3D unimproved deposit are used for further comparisons with the improved deposit.

The first and second eigen frequency of the system are 1.07 and 3.4 Hz respectively, which were used to calculate the Rayleigh damping parameters of the unimproved soil. The other numerical considerations such as minimum element size and time stepping and numerical integration obey the previously mentioned criteria in Chapter 5.

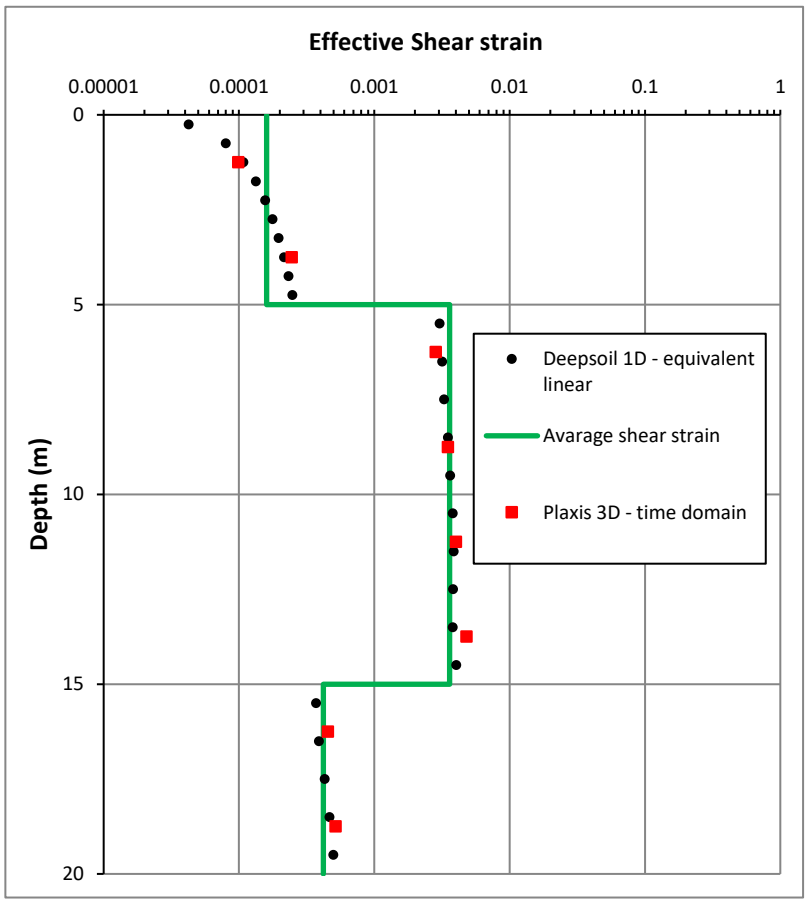

Fig. 167: Effective shear strain distribution over depth resulting from DEEPSOIL (1D) and PLAXIS 3D

Tab. 26: Material parameters used in Plaxis 3D

Material	$G_{0,ave}$	ν	K_0	γ_{unsat}	G/G_0	G	D
	(kN/m^2)	(-)	(-)	(kN/m^3)	(-)	(kN/m^2)	(%)
Dense sand (top)	85700	0.26	0.357	19	0.7	60000	7
Loose sand	57800	0.32	0.47	18	0.14	8150	21
Dense sand (bottom)	212000	0.26	0.357	19	0.44	94000	12

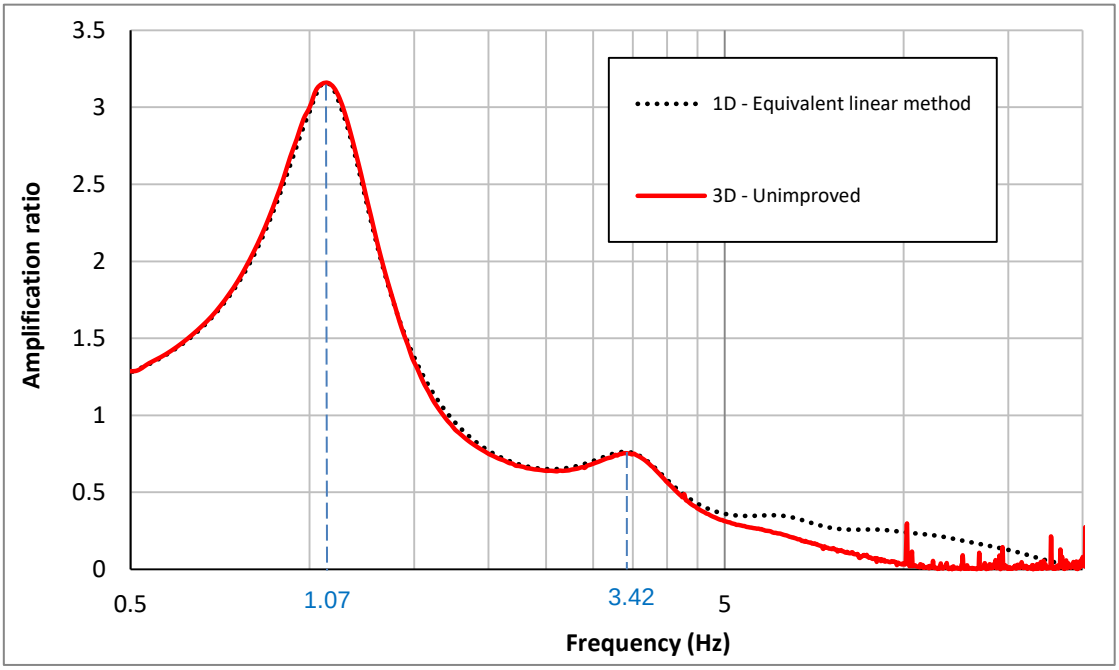

Fig. 168: Amplification ratio – resulted from 1D equivalent linear analysis and Plaxis 3D for unimproved soil deposit

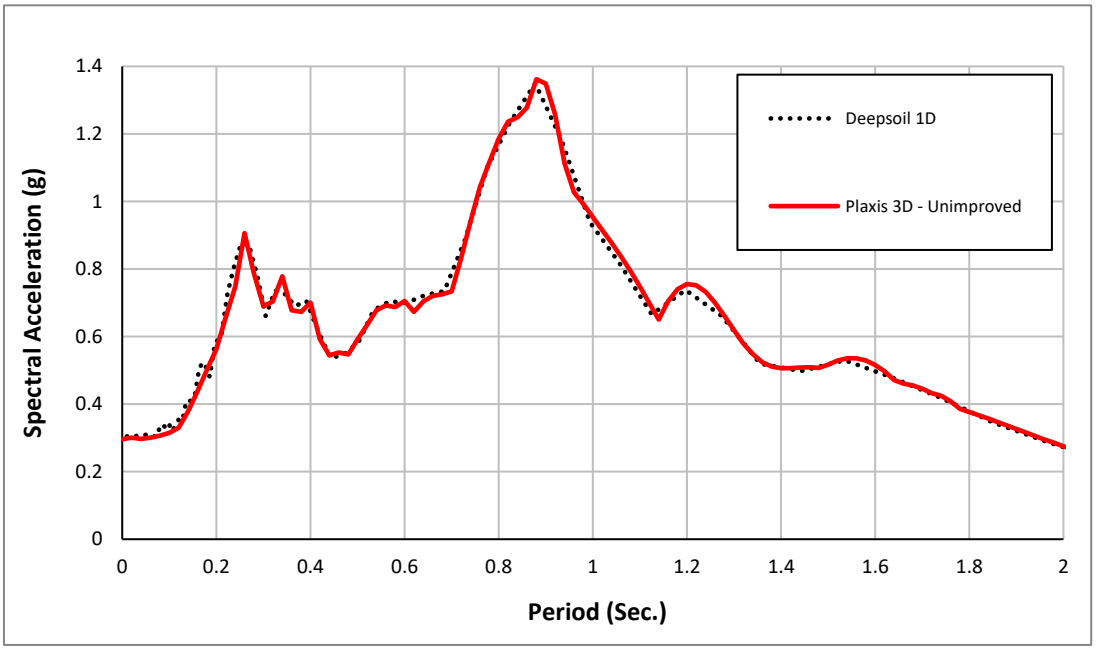

Fig. 169: Spectral acceleration resulted from 1D equivalent linear analysis and Plaxis 3D for unimproved soil deposit

7.4.2 Improved soil deposit

In this section, it is attempted to investigate the effect of single columns using PLAXIS 3D (Brinkgreve et al. 2015) in which free-field boundary conditions are

available (this feature was not available in the previous PLAXIS3D versions) and therefore the length of the model can be chosen equal to 360m. The arrangement of the columns and their spacing are the same as in Figure 134. The diameter of the columns are considered 80cm and 120cm and only one improvement scenario is considered with an improvement width of 50m where jet-grouting columns penetrate 19m in the soil layers (to avoid cracking at the bottom of the columns they did not penetrate the entire layer). The material parameters of the jet-grout columns are the same as in Table 24.

Results of numerical calculation are presented in Figure 170 where the amplification ratio is presented for a point located on the surface and middle of the model. It can be seen that when the columns with the diameter of 80cm are used, the amplification ratio at the first eigen frequency is decreased less compared to the condition where wider columns (i.e. d=120cm) are utilized. The first eigen frequency is increasing slightly with the improvement but, the second eigen frequency shifted to a higher value when wider columns are used with a larger increase in the amplification ratio. Figure 171 depicts the influence of improvement on the spectral acceleration curves. It can be observed that the wider columns can decreased the structural acceleration considerably in the period range of 0.8-1.4 sec.

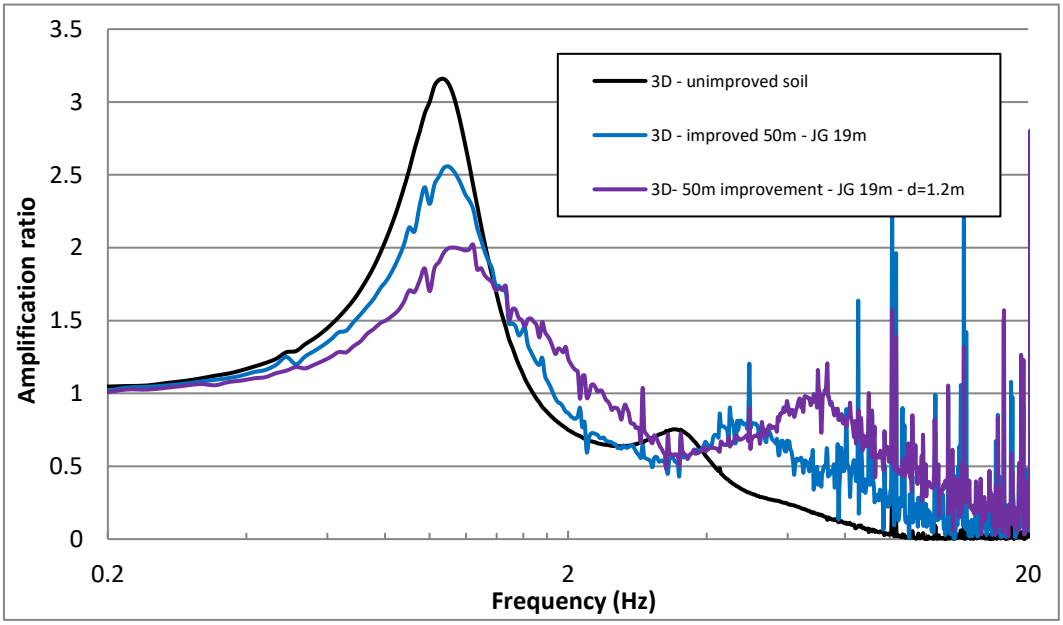

Fig. 170: Amplification ratio - Various improvement scenarios

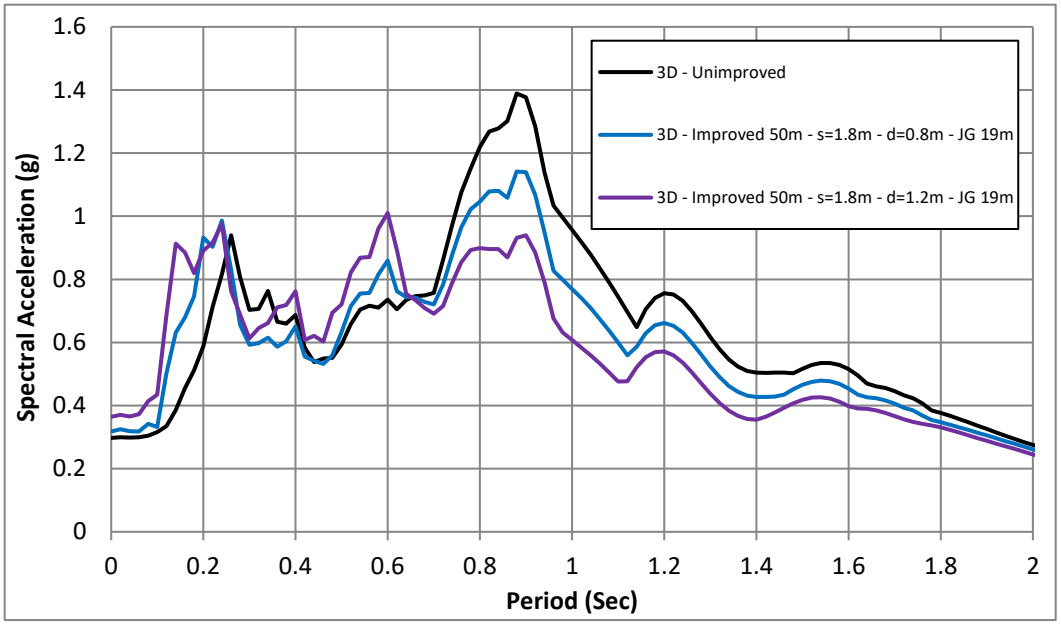

Fig. 171: Spectral acceleration - Various improvement scenarios

In order to provide more details about the effect of different earthquakes which have various properties (e.g. frequency content and peak acceleration), the Loma Prieta earthquake (see Figures 132 and 133) is also applied to the current layered soil model and the material parameter of the soil layers are defined through the same procedure described in section 7.4.1. Figure 172 indicates the response spectra of the unimproved deposit resulting from both earthquake motion in addition to the results of one improvement scenario where the width of improvement is 50m and the depth of the columns are 19m. Although not all the conditions are equal (e.g. peak acceleration), it can be useful to highlight the point that various earthquakes have to be examined with probabilistic analysis to provide unique design spectra for improved deposits like unimproved soils. It can be seen that the specific layered deposit being studied amplifies the long period SDOF structures (0.8-1 sec) when Northridge01-century city earthquake is used while it amplified the low period structures (ca. 4sec) when Loma Prieta earthquake was used. In addition, the effect of soil improvement by means of the stiff columns on changing the site classifications based on the EC8 elastic response spectra can be observed. The elastic response spectra of EC8 has been scaled by applying the a_g=0.4.

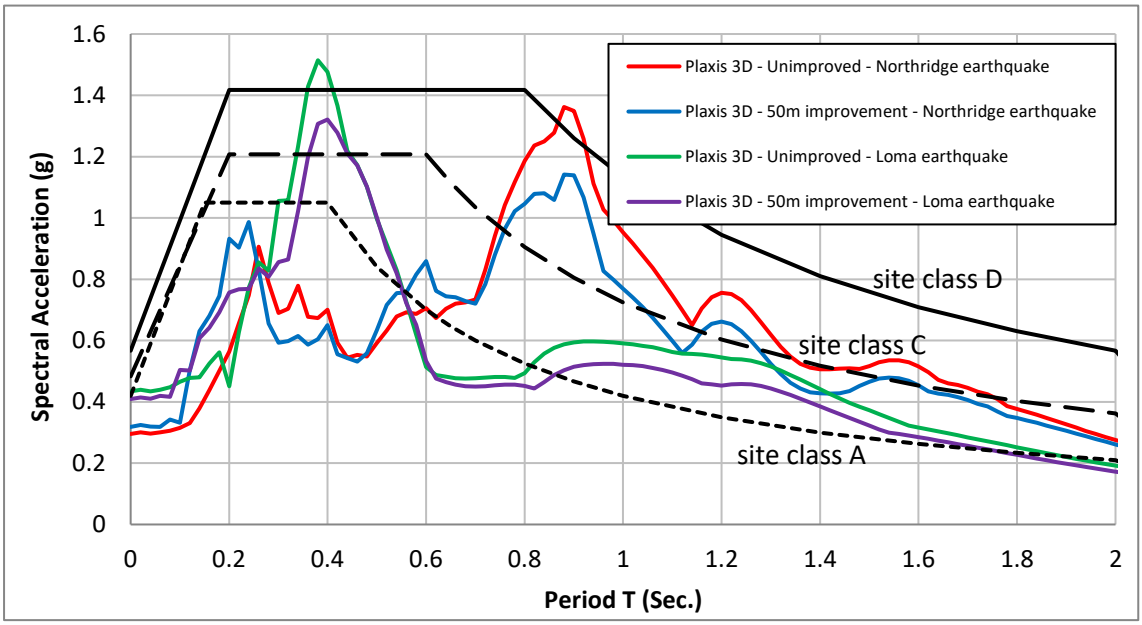

Fig. 172: Spectral acceleration of unimproved and improved soil deposit resulted by from two different earthquakes

7.5 Influence of overlapping jet-grouting columns against single columns

In all the previous analyses the effect of single jet-grouting columns were examined. In the further calculation, it is aimed to investigate the effect of different type of improvement in which the jet-grouting columns are overlapped during the installation to form a double-columns or series of overlapped columns to form a wall (Figure 173). The diameter of the columns is 80cm and the overlapping zone is 20cm. The material parameters of the jet-grout columns are the same as in Table 25. Although the arrangement of these selected type of improvements are asymmetrical in plan and may not be applicable in practice, but it is worthwhile to highlight how such improvement influence the system frequencies compared to the single columns.

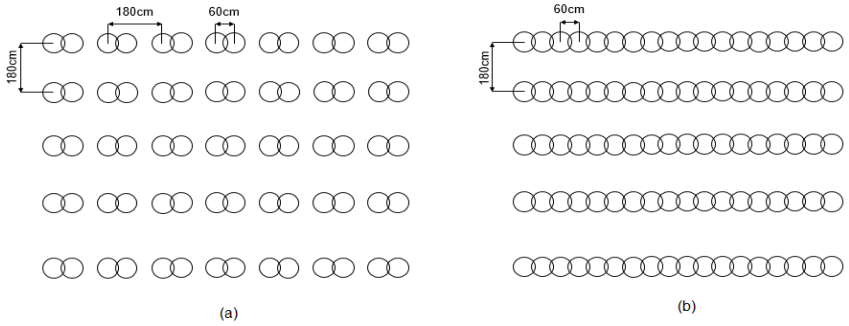

Fig. 173: Schematic representation of overlapping columns arrangement; a) double columns, b) wall

The layered soil condition, the earthquake motion (i.e. the Northridge01-Century city), the boundary conditions and the material parameters of the soils and the columns are the same as presented in Section 7.4.1. Figure 174 shows the geometry of the 3D model. The width off the improvement zone which is studied in these analyses, is 50m and the overlapping columns penetrates 19 m in the deposit.

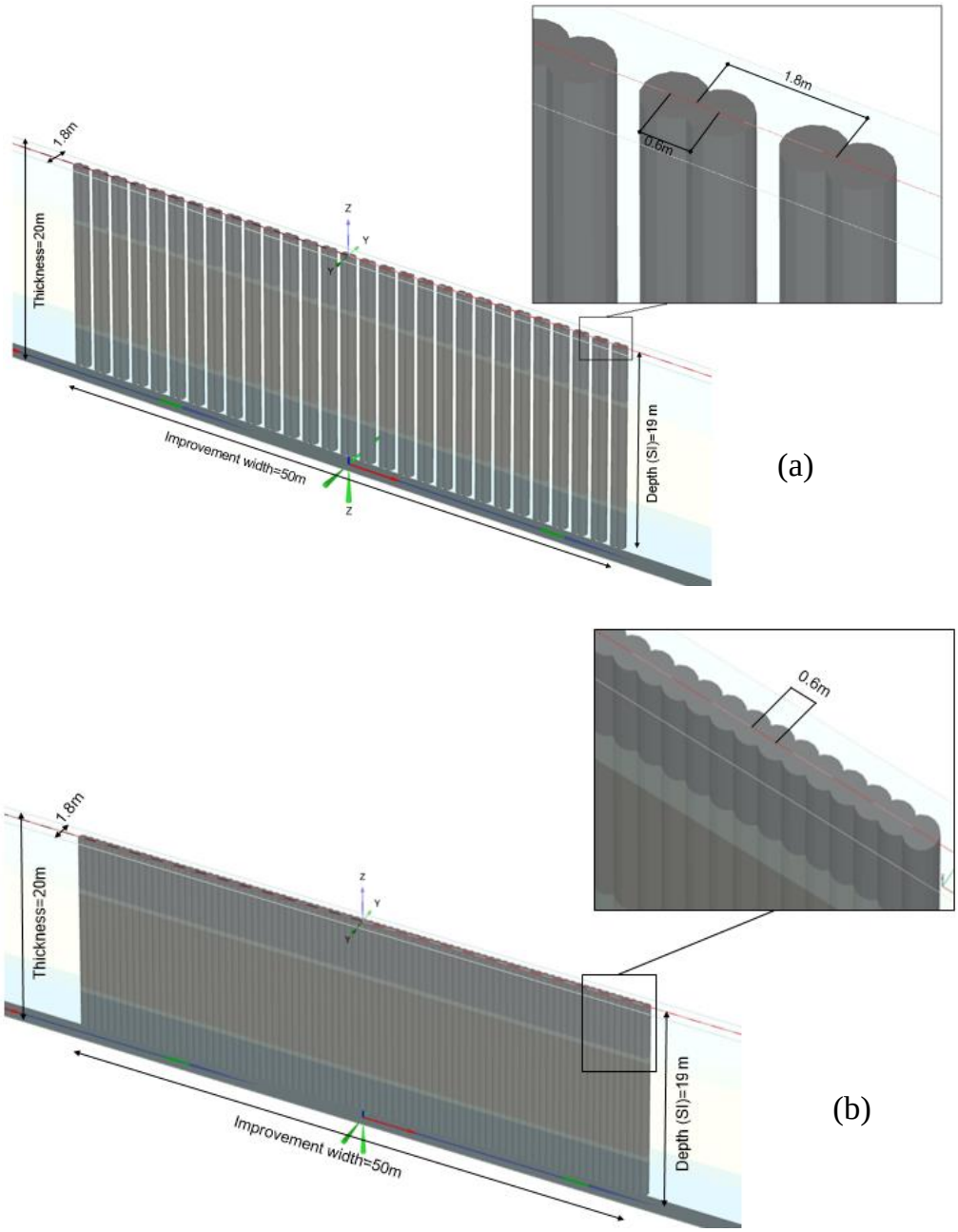

Fig. 174: Geometry of the 3D models; a) Double columns, b) wall

7.5.1 Results

Results of the numerical calculation are presented in Figure 175 where the amplification ratio is presented for a point located on the surface and middle of the model. It can be seen that where a wall is used, the system becomes so much stiffer that the first eigen frequency of the system shifts to the value of ca. 4.7Hz and the second eigen frequency shifts to ca. 13.5Hz and higher amplification ratio compared to unimproved soil is observed on that frequency level. When the double columns and single columns with the diameter of 120cm are used the first eigen frequency is increasing slightly but, the second eigen frequency shifted to a higher value with an increase in its amplification ratio. At the first natural frequency, the system of double overlapping columns decreases the amplification ratios higher compared to single columns with 80cm and 120cm due to increase in its replacement ratio.

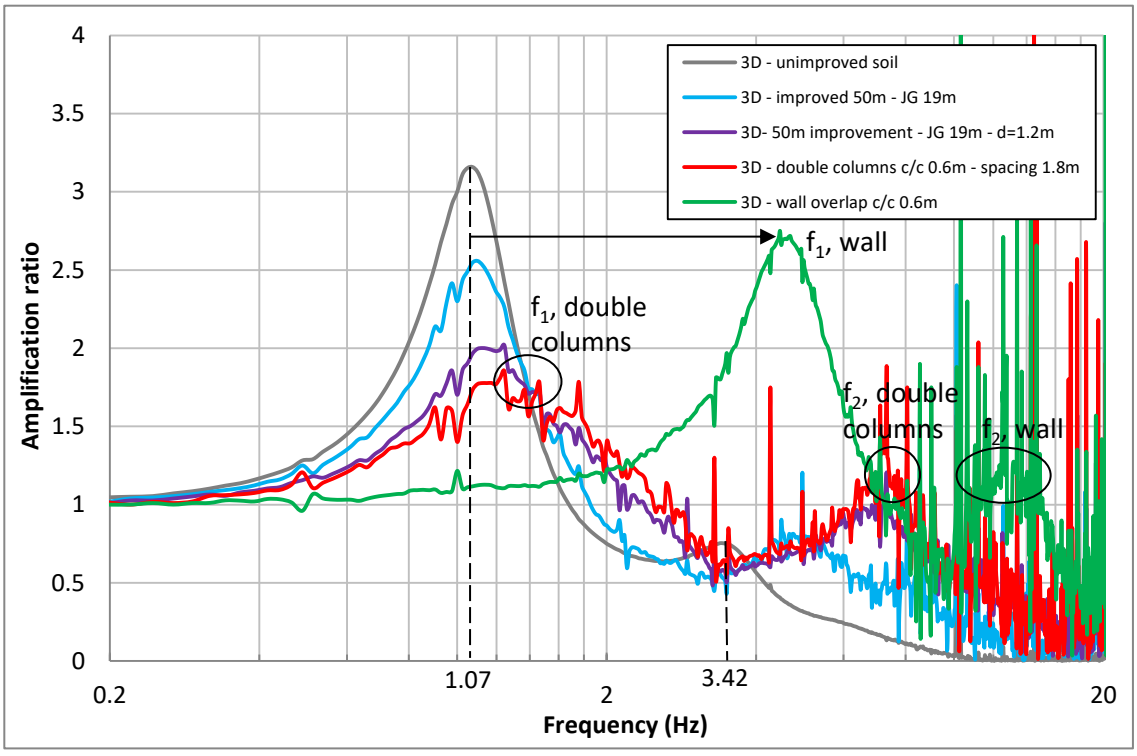

Fig. 175: Amplification ratio – Various improvement scenario

The change of natural frequency of the system and amplification ratio of the soil deposit can be reflected in spectral acceleration. Figure 176 depicts the influence of improvement in different range of periods. The elastic response spectra of EC8 (Type I) has been scaled by applying a_g=0.42g. It can be observed that when a wall improvement is used the behaviour in periods higher than 0.6sec is coincide with the ground type A, but this type of improvement considerably increase the

spectral acceleration in range of 0.2-0.3sec (i.e. frequency range of 3.5-5 Hz). However, in reality maybe this type of improvement is not used to improve the foundation of such structures with low natural period. For other improvement scenarios also it can be seen that the site classification in range of high periods (>0.6 sec) shifted from ground type D towards ground type A.

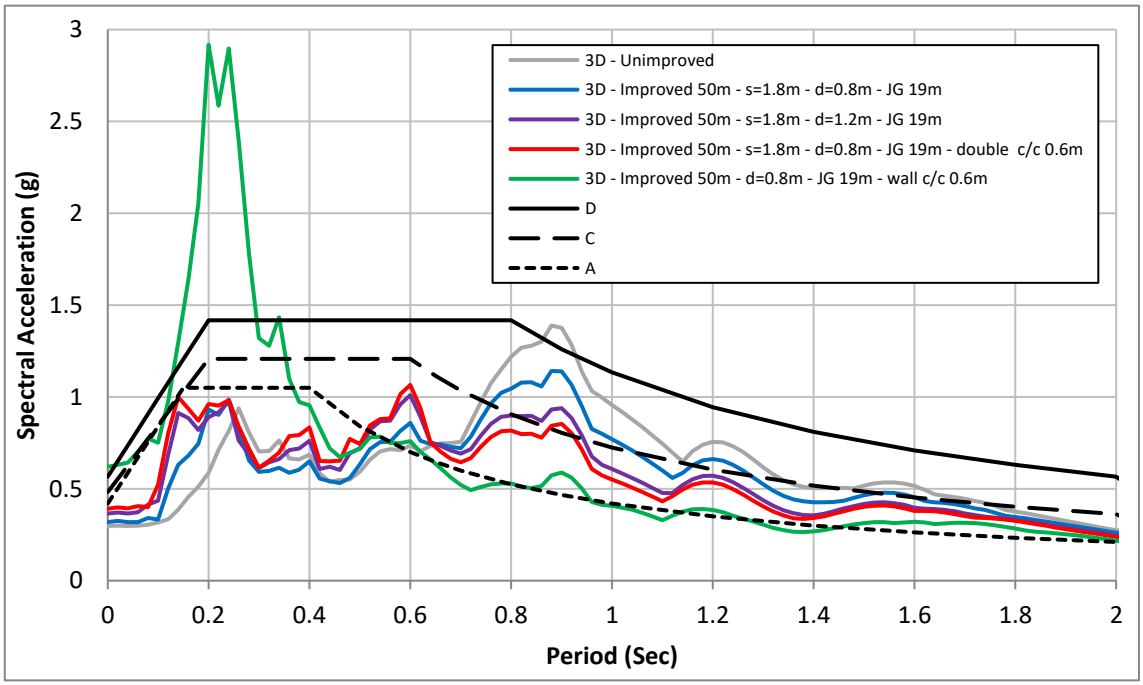

Fig. 176: Spectral acceleration – Various improvement scenarios

The crack location in the columns is shown in Figure 177. As it is seen when a wall-shaped improvement is used to resist against earthquake, full horizontal-cracks only propagate in the lower part of some lateral columns near the boundary of the loose sand and lower dense sand layer, but not in the central columns. In addition, the cracks propagate vertically inside the overlapping zone of the lateral columns and slightly in the central parts (see Figure 177a). In other scenarios, where there is spacing between columns like in the double-column system or in the single-column systems in Section 7.4.2, cracks are observed in all the columns parallel to the motion's direction and at the boundary of the loose layer and dense layers (See Figure 177 b and c and d).

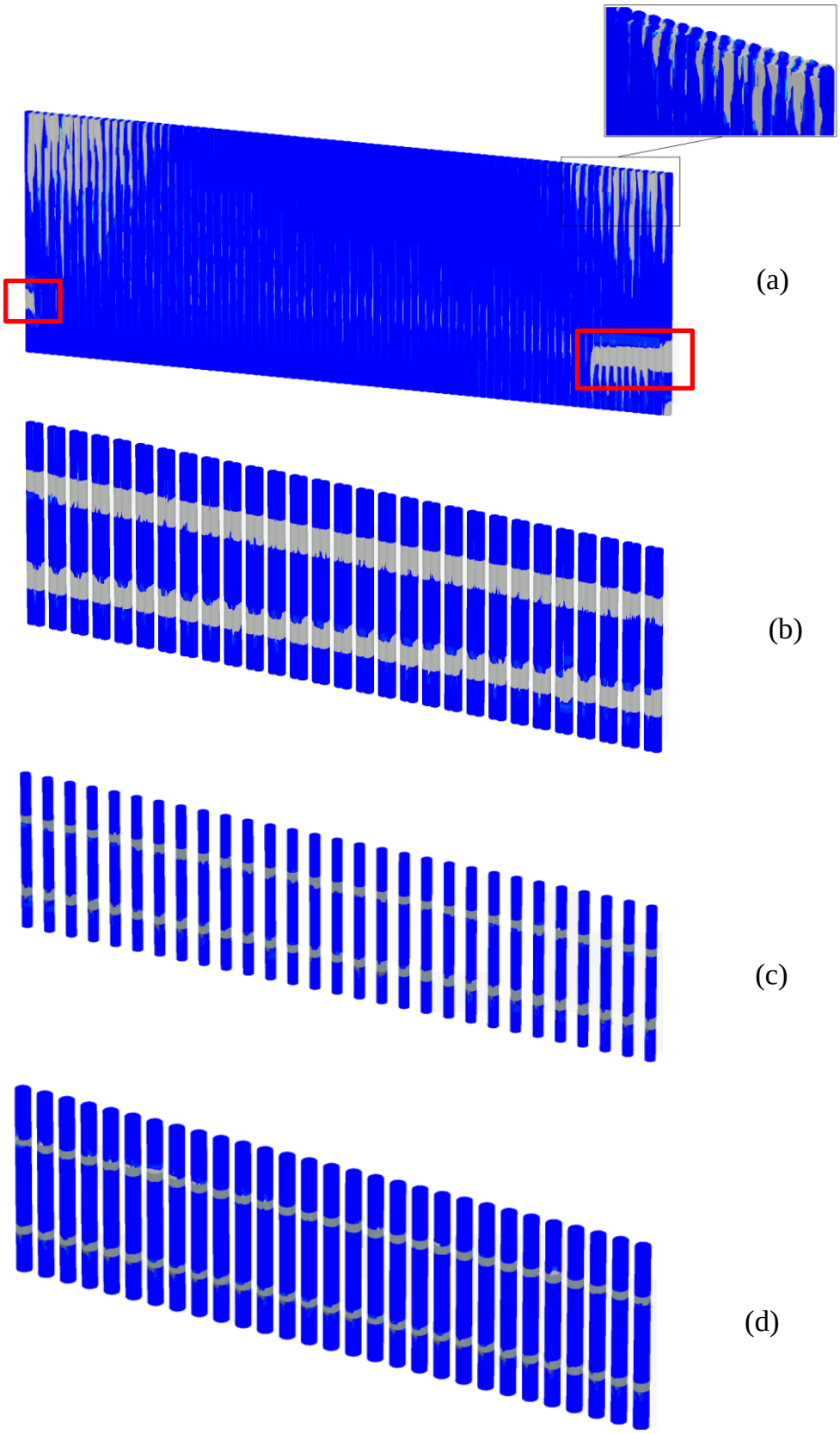

Fig. 177: Crack location in various systems; a) wall b)double columns c) single-columns A_r=16%, d) single columns A_r=35%

7.6 Influence of Lattice-shaped improvement on ground response of a layered soil

7.6.1 Introduction

The deep soil mixing method has been widely adopted to reinforce foundations such as port and harbour facilities and recently latticed-shaped type improved ground has also been applied for the purpose of liquefaction remediation where cement-treated columns are intersected to from a grid or any arbitrary shape of improvement (Takahashi et al. 2006, Takahashi et al. 2013). It is well known that a grid pattern of soil-cement walls behaves like a confined shear box, which can provide additional shear stiffness and strength for loose sand deposits to mitigate liquefaction (Nguyen et al. 2013). During an earthquake the latticed-shaped improvement is subjected to inertial forces of the soil mass within the soil grid's walls and also the dynamic earth pressures exerted from the unimproved soil outside of the panels which can cause large tensile and shear stresses (Khosravi et al. 2015). Various numerical and experimental studies have been carried out to investigate the influence of soil-mix grids on reducing the seismic shear strains, pore pressure generation and seismic ground response, also defining the failure zones of the grids is of interest. Olgun & Martin (2010) showed the performance of a soil-mix panel reinforced ground to reduce the ground motion using the software DYNAFLOW and their results suggest that lower seismic motions and more favorable NEHRP/IBC site class may be obtained using such improvement, which can lead to significant cost saving. Using the code OpenSeesPL Nguyen et al. (2013) attempted to provide a basis for a first-order estimate of the potential for tensile cracking in DSM walls. Namikawa et al. (2007) introduced an elasto-plastic model for defining the failure zones of DSM grids which was applied in the Dynamic Effective Stress Analysis Code and published the effect of lattice-shaped improvement for reducing the shear strains, excess pore water pressure and liquefaction mitigation. Bradley et al. (2013) using 3D seismic effective stress analysis discussed the effect of various geometry of the lattice-shaped soil improvement on the seismic response of a liquefiable soil deposit. A series of centrifuge model tests were conducted by Takahashi et al. (2006) to investigate the effect of grid spacing on liquefaction prevention and proposed a guideline using the ratio of grid spacing to depth. Khosravi et al. (2015) reported the effect of soil-cement grids on surface acceleration of a soft clay deposit and also defined the cracks location during an earthquake via dynamic centrifuge tests.

The focus of the following study is first to investigate the influence of the grid type of improvement as an alternative to reduce the seismic load on surface structures. As the construction cost of DSM/Jet-grouted walls is relatively higher, compared to other conventional improvement methods, therefore decreasing the volume of the cement-treated zones and defining the optimum geometry could be

beneficial. The second goal is defining the possible locations of earthquake-induced cracks in the lattice-shaped improvement by applying the new constitutive model. The obtained zones of cracking are also compared with the available case study in order to show how the new developed model is able to predict the correct location of cracks initiation. Series of numerical calculations are performed by means of the final element method where different geometry of soil improvement (i.e. various replacement ratios) with different material model and parameters are used to provide better insight into behaviour of this type of ground improvement.

7.6.2 Model description:

It must be emphasize that the goal of the current study is investigating the efficiency of the latticed-shaped ground improvement on seismic load reduction and liquefaction problem is not within the scope of this study. The soil stratification, the geometry of the soil improvement and the material parameters of soil-mixed panels have been chosen from Namikawa et al. (2007). But the soil constitutive model and the boundary conditions in dynamic analyses have been changed. A linear viscoelastic soil model is applied to soil layers and no water table is considered. The soil layers and the assumed parameters in this research are shown in Table 27.

Tab. 27: Soil layer parameters

Depth	**Soil type**	**ν (-)**	**γ_{soil} (kN/m^3)**	**G_0 (kN/m^2)**
0-2m	Thin layer of sand	0.33	18	40000
2-8m	Loose sand	0.33	19	45000
8-11m	Clay	0.33	16	80000
11-14m	Gravel	0.33	20	115000

Two types of lattice-shaped improvements are generally used in practice, the fixed-type improvement and the floating-type. In this study a fixed-type lattice-shaped improvement is examined where the soil improvement penetrate the entire loose layer and is fixed to the clayey stratum (unliquefiable) at its base. The thickness of the DSM wall is 80cm and two different cement-treated walls with the spacing of 4m i.e. the replacement ratio of A_r=36% and spacing of 8m

with A_r=19% have been studied (Figure 178). Half of the grids are modelled and they are installed in the entire loose sand layer penetrating 0.6m into the clay deposit. In the current study the model has been created in Plaxis 3D (Brinkgreve et al. 2013), applying viscous boundaries at the sides and a rigid boundary at the base (Figure 179). The input motion is applied at the base of the model in x direction.

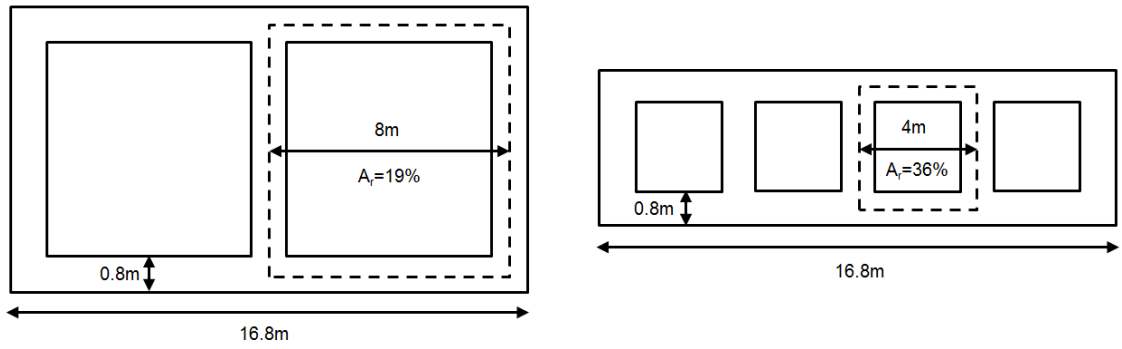

Fig. 178: Plan view of the panel, 80cm thickness and two different centre to centre spacing 4m and 8m

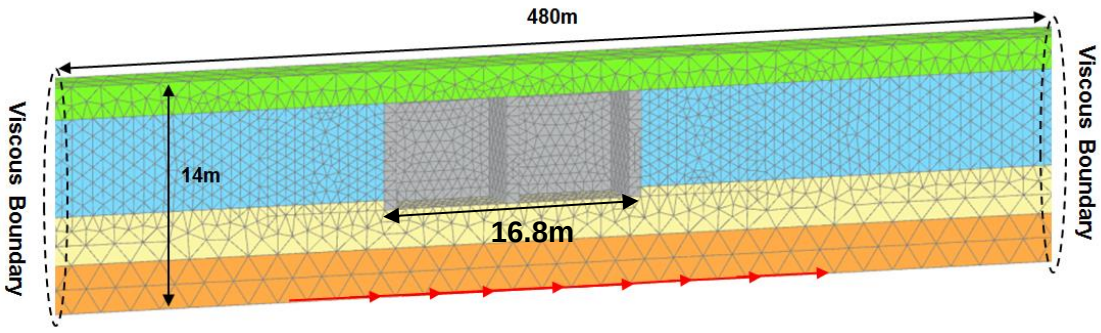

Fig. 179: Model geometry in Plaxis 3D

7.6.3 Input motion

The acceleration-time history recorded at Kobe JMA station 1995 is used as seismic input signal at bedrock level. Duration of the motion is 20sec with a time step of 0.02sec and the acceleration-time history has been scaled such that the peak horizontal acceleration is equal to 0.25g (see Figure 180) in order to obtain approximately the same maximum surface acceleration compared to the results of Namikawa et al. (2007). The maximum earthquake amplitudes are between the frequency range of 1-3Hz and the dominant frequency is 2.89Hz (Figure 181).

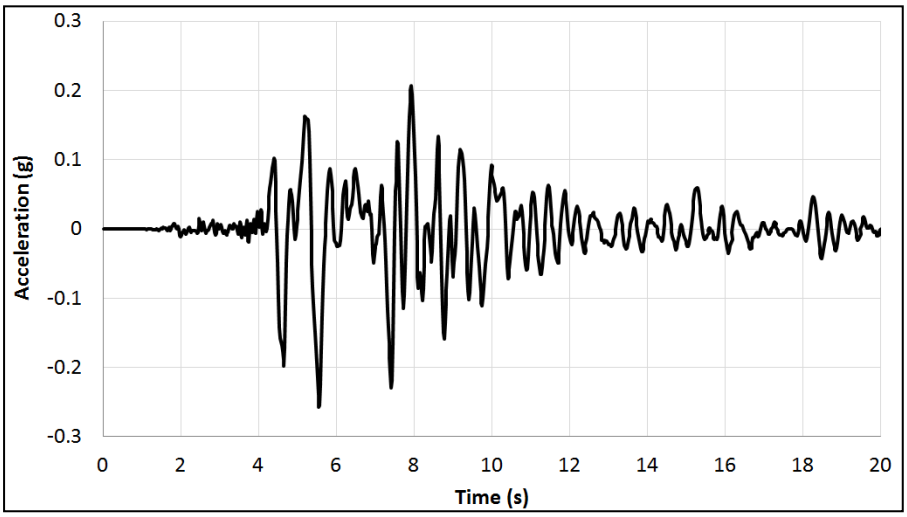

Fig. 180: Acceleration-time history of input motion, Kobe 1995

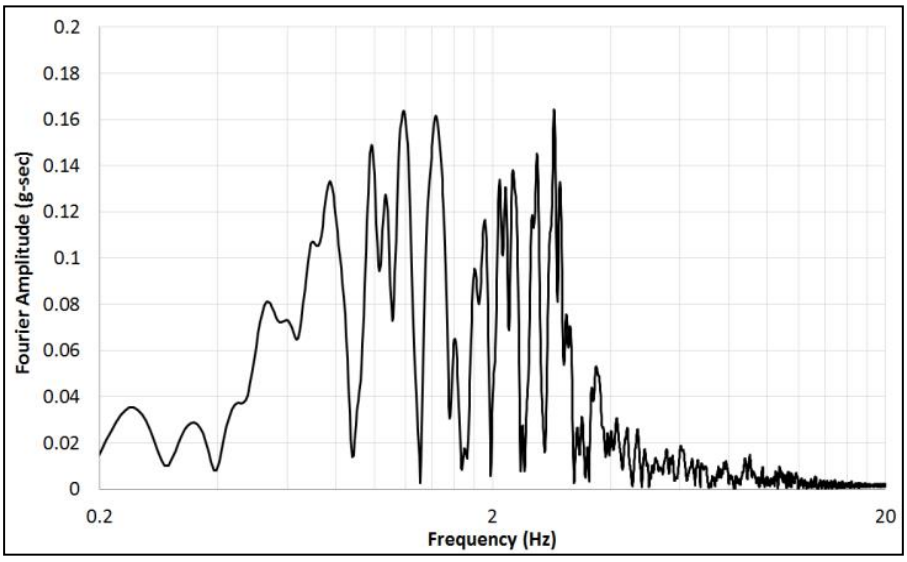

Fig. 181: Fourier amplitude of the input motion

7.6.4 Material parameter of the soil

A linear viscoelastic soil model is considered for the soil layers. In order to obtain the soil parameter for the numerical analysis again one-dimensional equivalent linear method is used as a benchmark. A constant small-strain shear modulus over depth was considered for the soil layers. Applying the equivalent linear method, the final seismic shear strain induced by the earthquake was estimated and the corresponding shear modulus and damping ratio within each

layer were obtained from mean curves for sandy layer proposed by Seed & Idriss (1970) and Vucetic & Dobry (1991) and clay respectively (Figure 182).

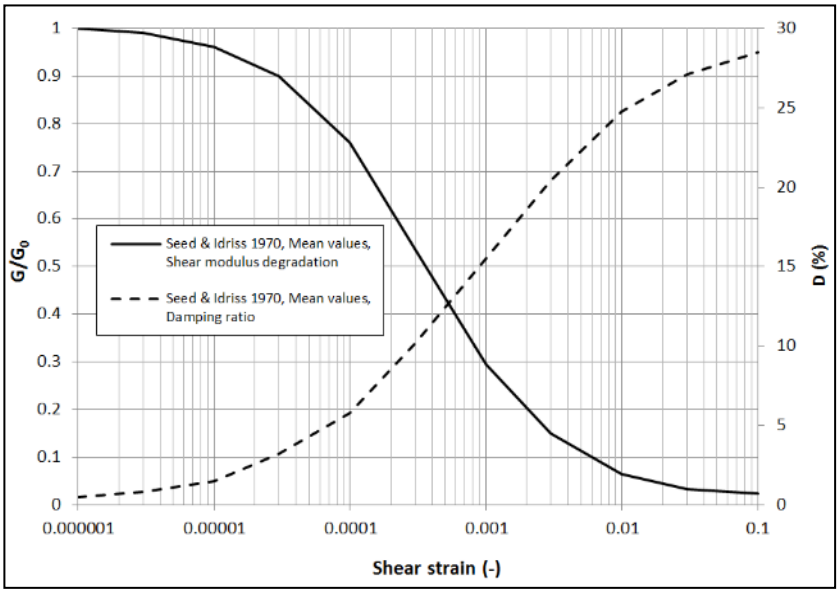

(a)

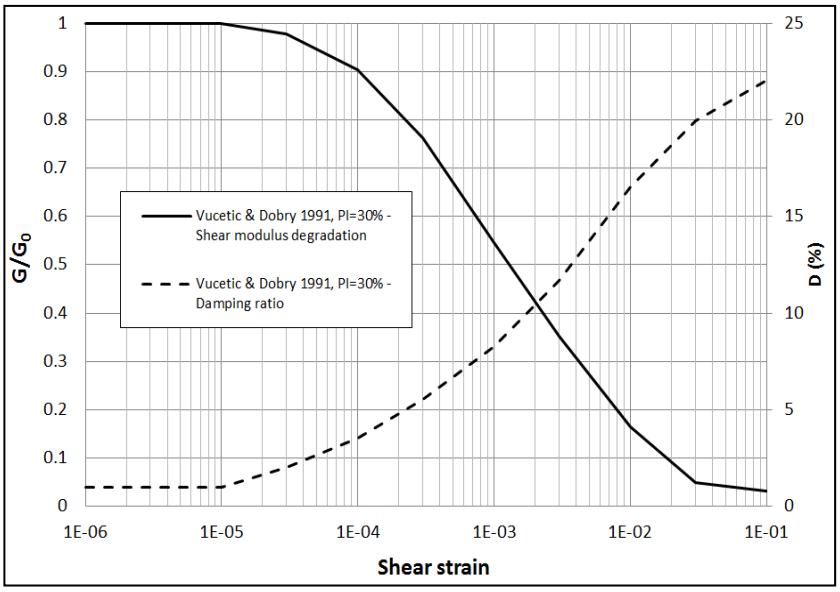

(b)

Fig. 182: Shear modulus degradation and damping ratio versus shear strain: a) Seed & Idriss (1970); b)Vucetic & Dobry (1991)

Table 29 presents the material parameters of the soil layers which are used with the linear viscoelastic soil model in Plaxis 3D.

Tab. 28: Material properties of the soil in Plaxis 3D

Material	G_0 kN/m^2	ν -	γ_{soil} kN/m^3	G/G_0 -	G kN/m^2	E kN/m^2	D %
Loose sand top	40E3	0.33	18	0.63	25.2 E3	67 E3	8
Liquefiable sand	45E3	0.33	19	0.13	5.9 E3	15.7 E3	22
Clay	80 E3	0.33	17	0.57	45.71 E3	121.3 E3	7.5
Gravel	115 E3	0.33	20	0.27	30.75 E3	80.3 E3	16

In order to obtain a good match between the linear time-domain and the frequency-domain solution, through an iterative procedure, f_n and f_m for calculation of Rayleigh damping were chosen as 2 and 4.8 Hz respectively. Figures 189 and 190 show the DEEPSOIL 1D frequency-domain results and the PLAXIS 3D time domain results in terms of amplification ratio's curves and response spectra and they are in good agreement. It must be mentioned that the minimum element length has been considered according to Equation 57 with the maximum frequency of interest 20Hz and the dynamic time step was set to be selected by the PLAXIS automatically.

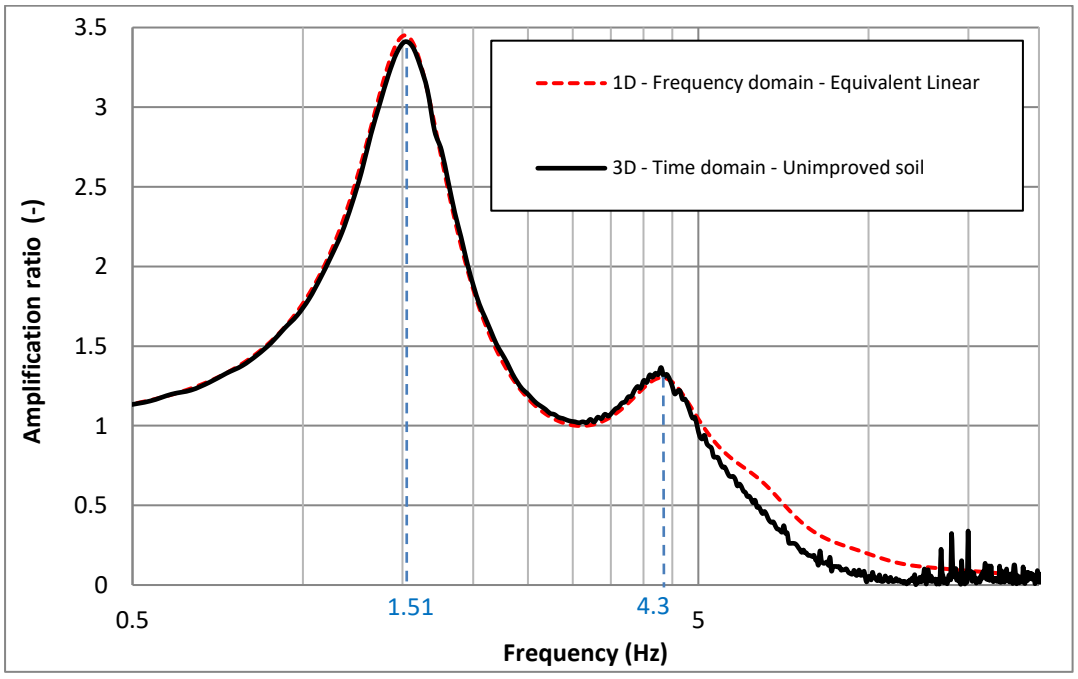

Fig. 183: Amplification ratio of unimproved soil

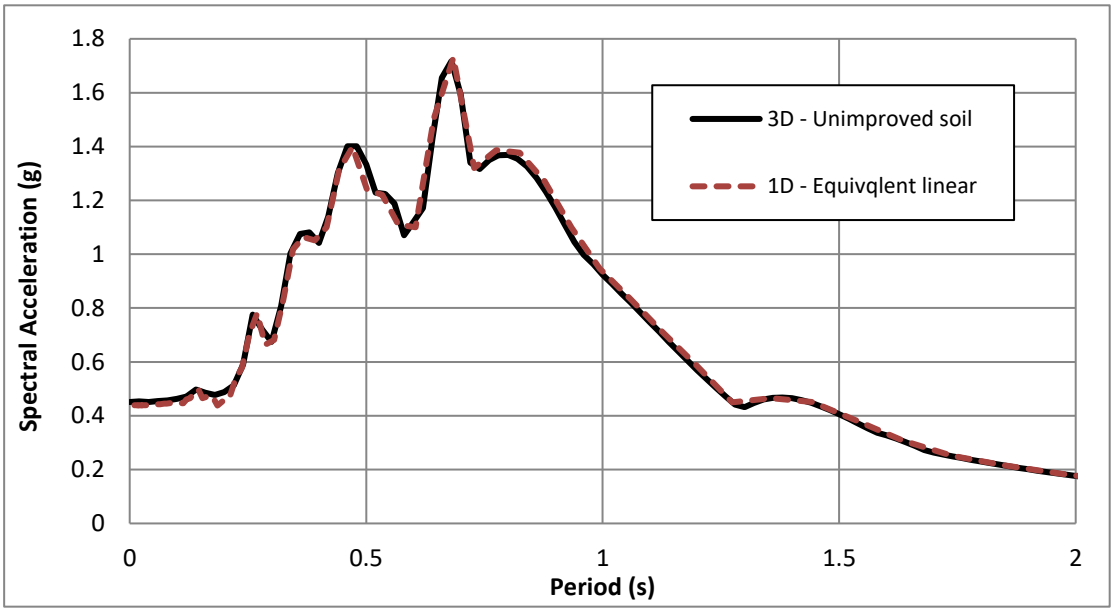

Fig. 184: Spectral acceleration – Unimproved soil

7.6.5 Material parameters of the soil improvement

For the purpose of this study, the material parameters of the soil improvement were chosen the same as adopted in Namikawa et al. (2007). Two different analyses have been done using 4m and 8m spacing with an uniaxial compressive strength of 2MPa and a tensile strength of 500kPa. The other analysis uses 8m spacing with higher stiffness and uniaxial compressive strength. Table 30 presents the two set of utilized material parameter in this analysis.

Following Kitazume & Terashi (2013) the damping ratio of the soil improvement according to the seismic shear strain inside the elements were chosen equal to 4%. Rayleigh damping parameters of the jet grouting columns have been also calculated based on the eigen frequencies of the system (f_1 and f_2).

Tab. 29: Material parameters of DSM grids

Analysis type (grid spacing)	γ_{unsat} (kN/m^3)	ν (-)	E_{28} (kPa)	$F_{c,28}$ (kPa)	F_t (kPa)	$G_{t,28}$ (kN/m)
(1) 4m and 8m	19	0.17	3.5E6	2000	500	0.015
(2) 8m	19	0.17	8.75E6	5000	1000	0.0375

7.6.6 Results

By checking the amplification ratio for a point on the surface in the centre of the model, the efficiency of this latticed-shape improvement, can be evaluated (Figure 185). DSM panels decrease the shear strains amplitude in the soils that are located between the grids. Therefore, based on average effective shear strain in the soils in between the grids, with trial and error, new modified values of shear modulus and damping ratio have been applied, representing the behaviour of the soil inside the grids more realistically (see Figure 188). Considerable reduction of the first eigen frequency is observed, but at the second eigen frequency there is no reduction and the amplitudes are damped afterwards. In addition, an increase (ca. 6%) and shift of first eigen frequency can be observed but, the width of the soil improvement (i.e. 16.8m) is not so much to have an influence on the second eigen frequency. The different shape of amplification ratio's curves compared to the condition where stiff columns were used can be caused by the special shape of the DSM grids. This behaviour of the improved soil can be also explained by comparing the Fourier amplitude spectrum of a surface motion for unimproved and improved systems (Figure 186). In the range of 0.5-2.2Hz the amplitude of the improved system is lower compared to unimproved one but in range of 2.2-4.3Hz the improved system produced higher amplitude.

It can be seen in Figure 185 that the improvement with 4m grids spacing reduces the amplification ratio at the first eigen frequency slightly more than the improvement with 8m grids spacing. In addition, it is seen that when the material parameters of the soil improvement with 8m spacing is set to type 2 i.e. a higher stiffness, uniaxial compressive strength and fracture energy (see Table 29) it does not affect the amplification ratio's curve considerably at least at the first eigen frequency (the green curve in Figure 185). This means that varying the replacement ratio has more influence on the results when the material parameters are the same. In the frequency range greater than 5 Hz, very jagged and erratic results are observed in Figure 185, which are mainly caused by the cracking in the improvement elements. By using a linear elastic material model for describing the DSM grids behaviour it can be shown that a smoother curve is obtained (Figure 187).

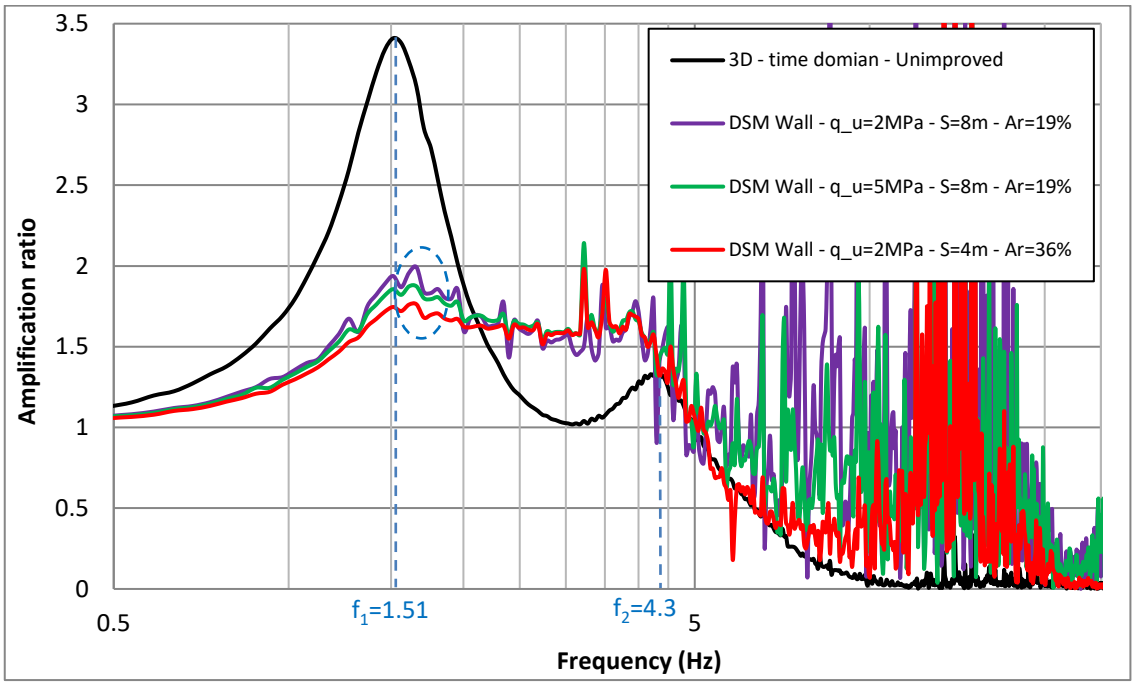

Fig. 185: Amplification ratio for unimproved soil and improved soil with different grids

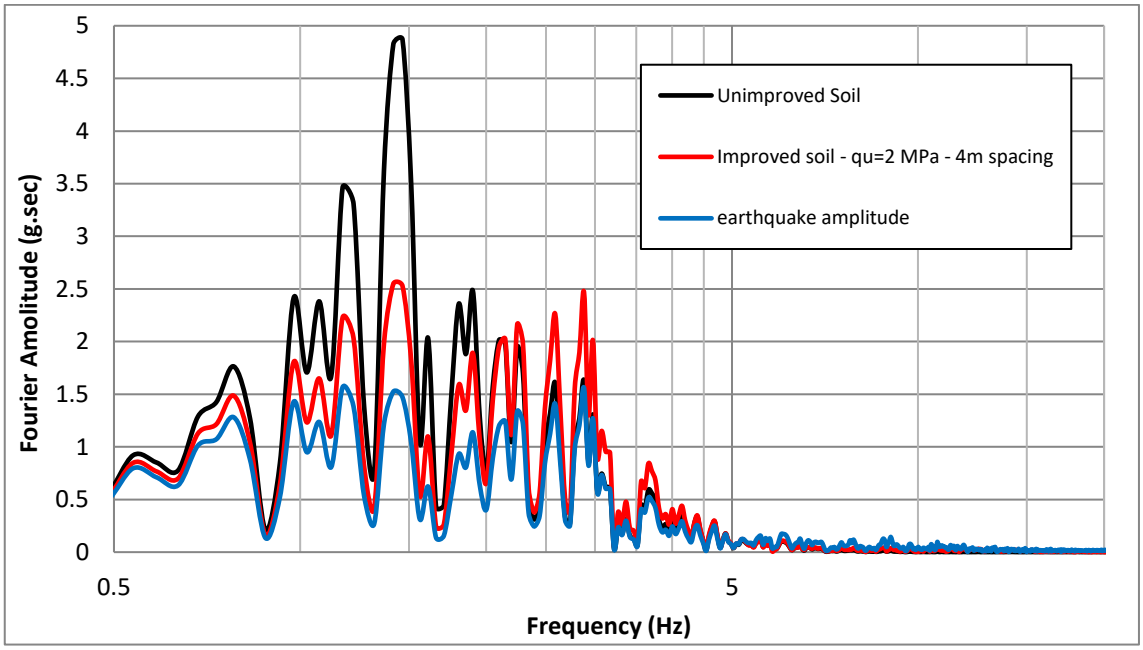

Fig. 186: Fourier amplitude vs frequency curves for unimproved and improved soil

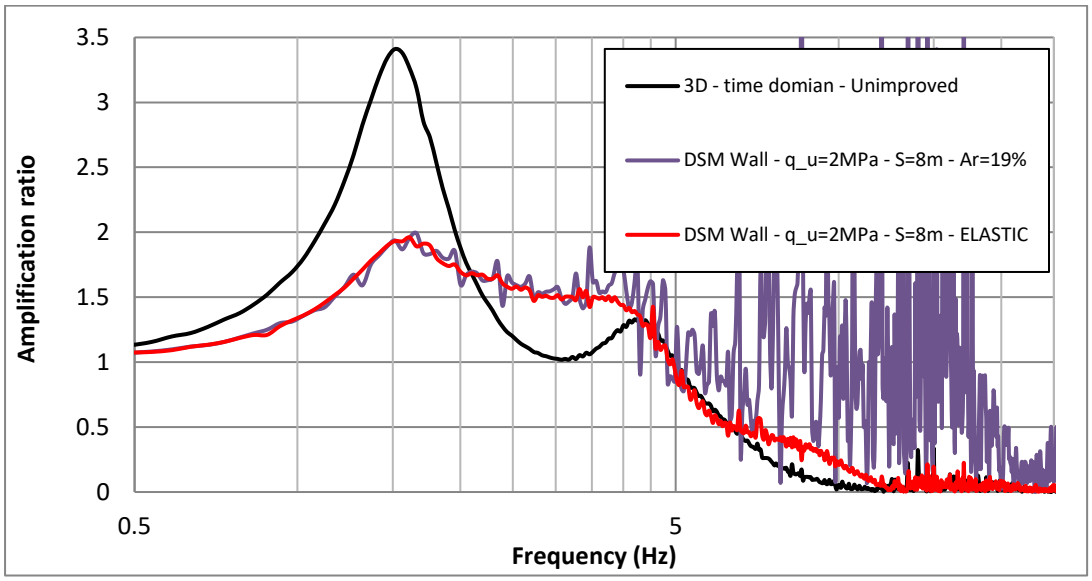

Fig. 187: Amplification ratio – Comparison between elastic panels and panels modelled by shotcrete model

As mentioned earlier, due to lattice-shaped improvement the shear strain amplitude in the soils that are located in between the grids is decreased. The effect of two different panel's geometry in decreasing the shear strain in improved zone can be seen in Figure 188.

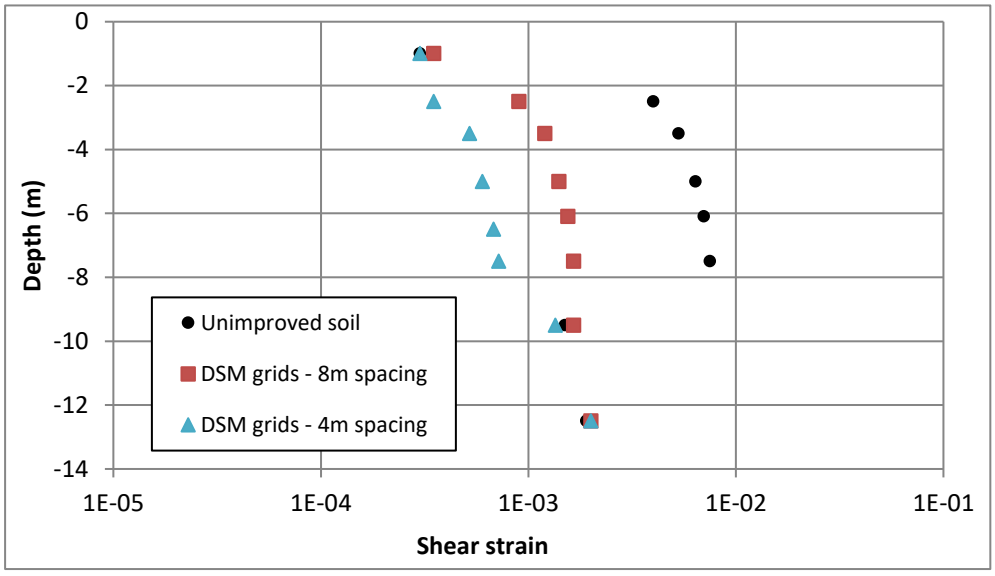

Fig. 188: Maximum shear strain in unimproved soil and various improvement scenarios

The same conclusion can be obtained by investigating the curves of the spectral acceleration for improved and unimproved depoist (Figure 189). It can be seen that in the range of 0.44-1.4 sec (or frequency of 0.7-2.3 Hz), maximum acceleration has been reduced by soil improvement and reduction with 4m spacing is slightly higher in the range of 0.5-0.9sec.

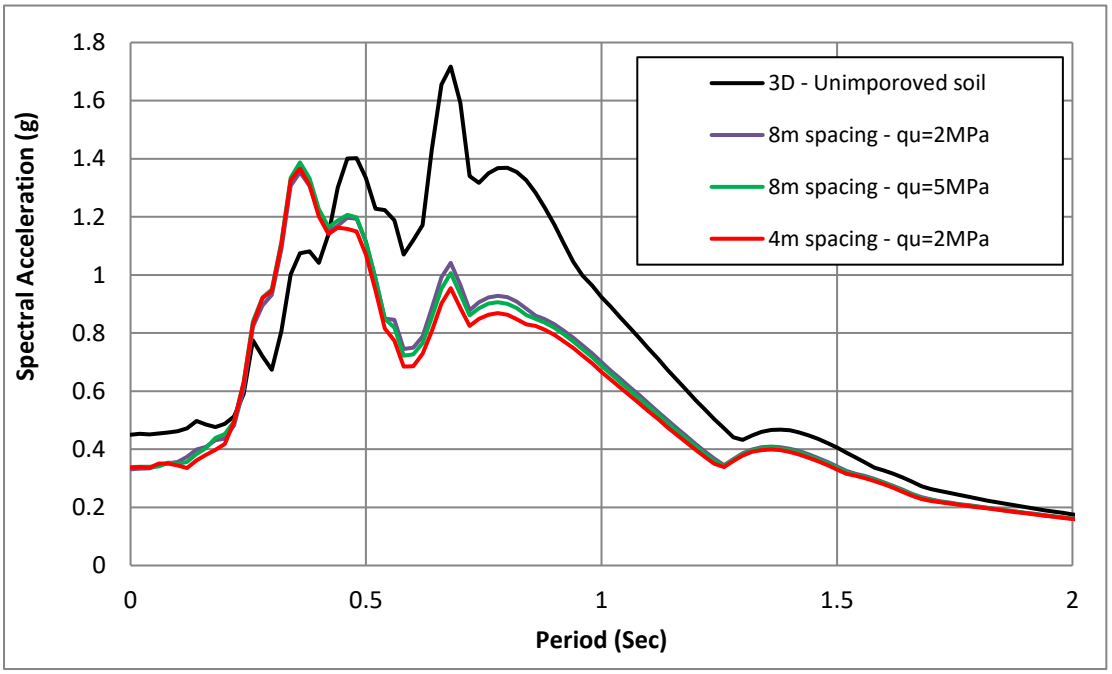

Fig. 189: Spectrum Acceleration for unimproved soil and lattice-shaped soil improvement

Figure 190 shows the crack location in the grids at the end of calculation, i.e. after 20sec. It can be seen that by using the 4m grid's spacing the cracks in the central part of the grids are reduced, while with 8m spacing the failure zone is wider, and occurs at the corners of the grid which penetrates through the entire grid's wall. In another analysis with 8m grid's spacing and the material parameter type 2, it is seen that the failure zones are reduced and the cracks do not propagate the entire grid's wall. It is also observed that the obtained crack patterns are similar to the reported results of Namikawa et al. (2007) and Khosravi et al. (2015). Cracking was seen at the connections between panels and perpendicular to the direction of motion and propagated along the entire depth of panels. It must be noticed that the obtained results are not exactly the same as Namikawa 2007 because there are some different assumptions in the boundary conditions, soil constitutive model, input motion and presence of ground water table.

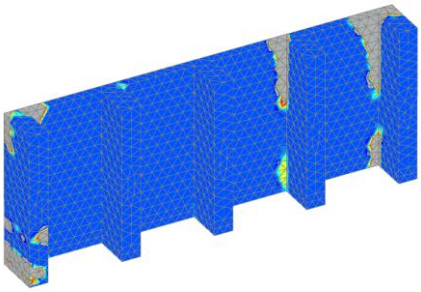

(a) Plaxis model – 4m spacing (1) - E=3.5 GPa

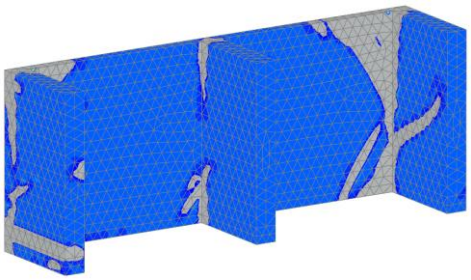

(b) Plaxis model – 8m spacing (1) – E=3.5 GPa

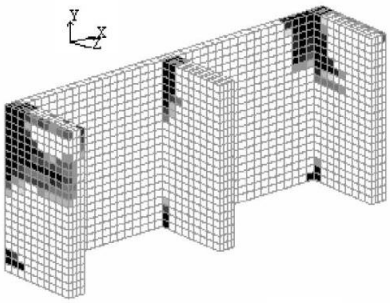

Failure zone in the panles after 20s (Namikawa et al. 2007)

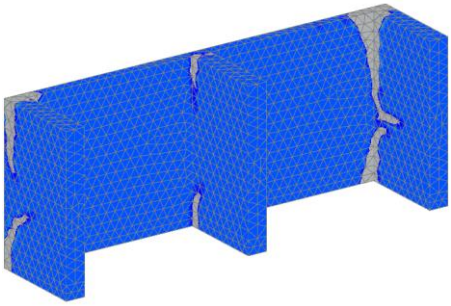

(c) Plaxis model – 8m spacing (2) – E=8.75 GPa

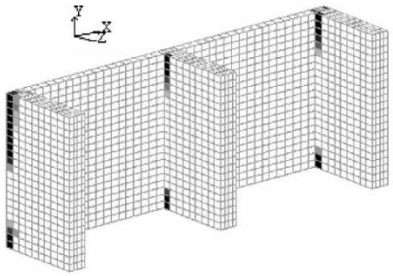

Failure zone in the panles after 20s (Namikawa et al. 2007)

Fig. 190: Comparison of the crack locations with results of Namikawa 2007; a) 4m, analysis (1); b) 8m, analysis (1); c) 8m, analysis (2)

In additional calculations, the influence of improvement by means of the single columns is compared with the lattice-shaped improvement. The geometry of the 3D model is shown in Figure 191 where the width of improved zone by the columns was considered equal to the width of lattice-shaped improvement (i.e. 16.8 m). Two replacement ratios for the column are used as 19% and 37% (i.e. the columns diameter of 80cm and 110cm) which are the same as the replacement ratios of the panels (see Figure 178).

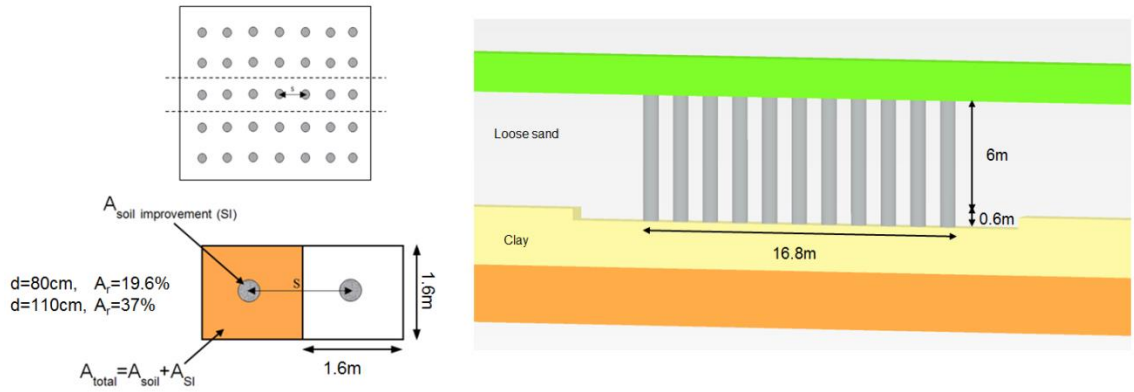

Fig. 191: The geometry of the improvement scenario by means of the single columns

The results are shown in Figure 192 where the reduction of amplification ratio at first eigen frequency is higher when a latticed-shaped is utilized but near second eigen frequency roughly similar amplification ratio were obtained. In between the frequency range of 2.2-4.3 Hz, the lattice-shaped improvement generates higher amplification ratio compared to single columns improvement.

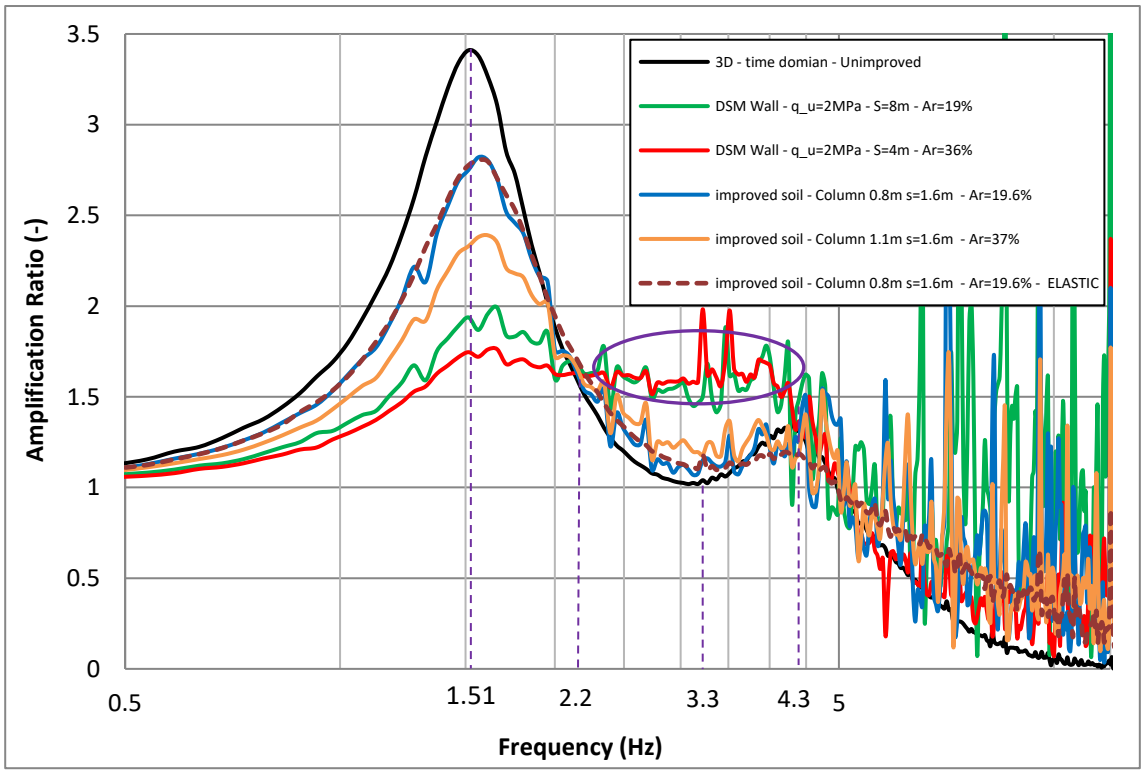

Fig. 192: comparison between columns improvement and lattice-shaped improvement

The curves are very jagged and erratic especially in the frequencies greater than 5Hz, which is related to the cracking in the columns and applying a linear elastic material model, produce smoother curve. Figure 193 presents the crack zones in the columns. Cracks occurred on the top of the columns and also at the lower level in the boundary of the loose sand layer and stiff clay.

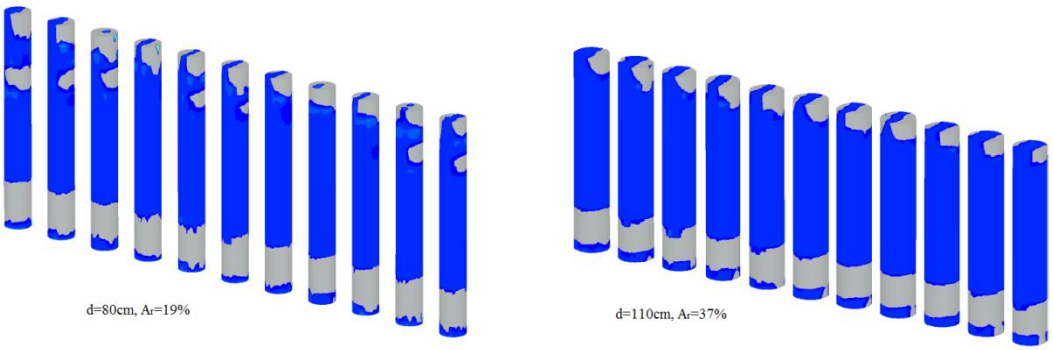

Fig. 193: Crack locations in the columns with different replacement ratio

In order to find out the reason for a higher de-amplification obtained by the panel one can compare the level of seismic shear strain level in the soil in between the columns and panels. Figure 194 shows that the improvement by columns cannot change the shear strain (between columns) significantly, while as seen, the panels caused a large reduction in the soil as they act as a box.

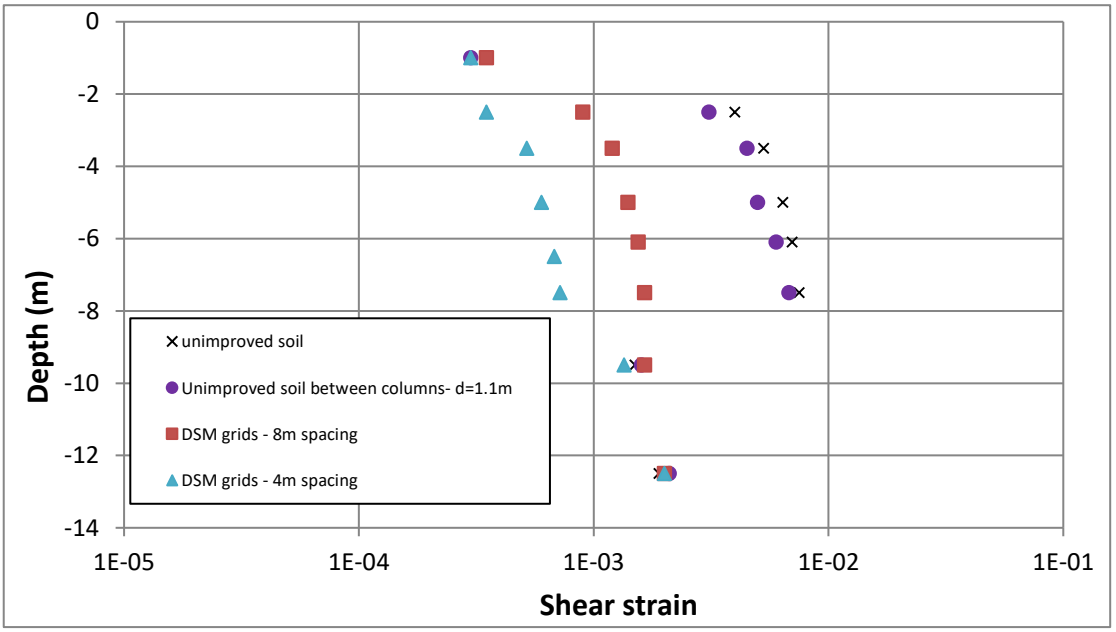

Fig. 194: Shear strain is soil in between the columns and panels

The different behaviour of the two improvement systems can be presented also using the response spectra (Figure 195). Lattice-shaped improvement highly decreases the spectral acceleration in the period range 0.5-1.1 sec compared to the improvement by means of the single columns. In range of 0.3sec, the DSM grids increase the spectral acceleration which was also seen in the amplification ratio's curve in the frequency range of 3.3Hz (see Figure 192). Moreover, it is observed that the lattice-shaped improvement can effectively alter the EC8 elastic response spectra from type D to the types C or even A.

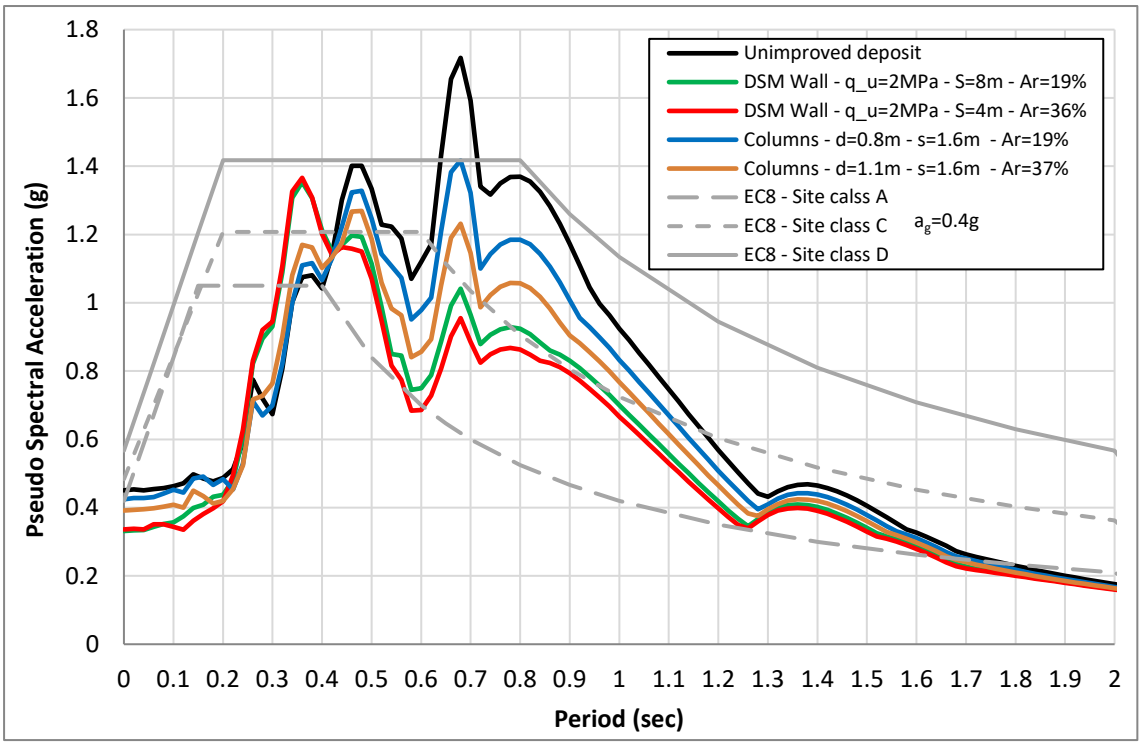

Fig. 195: Comparison of response spectra resulted from column and grid improvement

7.7 Summary and conclusion

Effect of ground improvement by means of jet-grout columns on the ground response of a homogeneous soil and layered soil deposit with a specific geometry and material parameters were investigated. A linear visco-elastic model was assigned to the soil layers and the advanced constitutive model, which allows for initiation of cracks, was applied for modelling the mechanical behaviour of the columns. One-dimensional equivalent linear method was utilized for defining the material parameters of the soil layers. A series of numerical calculations were performed employing the finite element method to investigate the impact of jet-grouting columns on ground response of a homogeneous and layered soil deposit,

where influence of various width and depth of improvement in addition to different replacement ratios was checked. It could be shown that the natural frequencies of the improved soil layer changed, which reflects the influence of the stiff columns embedded in the soil layer. Results also proved that using wider improvement width and higher replacement ratio have a significant effect on the amplification ratio as expected. Soil improvement by means of stiff elements have the potential to decrease, but also may increase the seismic load on surface structures. Comparing the results of spectral acceleration with the proposed design spectra of Eurocode 8 also showed that the site classification could be altered by ground improvement. The application of lattice-shaped improvement in the reduction of seismic load has been presented. In contrast to the single columns improvement the latticed-shaped improvement has the ability to decrease the earthquake-induced shear strain amplitude in the soils in between the panels. Results also depicted that one feasible alternative to reduce the seismic loads on the surface structures constructed on soft deposits, can be the use of a lattice-shaped improvement, or increasing the replacement ratio by using wider columns or overlapping columns. However, more analyses with various earthquakes are required to obtain general conclusions and also to define specific design spectra for improved deposits which is not discussed in the codes and guidelines. In addition, it was shown that the new advanced model adopted for modelling the behaviour of the jet-grouting columns or the lattice-shaped improvement is capable in identifying the possible zone of cracks initiations.

8 Evaluation of influence of concrete slab above stiff columns

8.1.1 Introduction

All previous examples were done in a condition where no foundation slab was considered and also without assuming a real surface structure and its influence on the results. This section aims to provide more information about the presence and role of a concrete slab above the stiff columns and the soil-structure-interaction on ground response. The effect of slab parameters (e.g. stiffness and damping ratio) and slab geometry have been separately investigated. In addition, in case of supported slabs, the effect of the connection of columns and slab on the amplification function is studied.

Deep soil mixing columns are applicable in the foundation of road bridges, heavily loaded footings and have recently been used to support wind turbine foundations. The columns can be unreinforced or reinforced. For the unreinforced condition, usually a transition layer above the columns is considered (Topolnicki & Soltys 2012). In the following analysis, both conditions were examined.

8.1.2 Influence of unsupported slab

First of all, the effect of an unsupported slab on the amplification function was investigated and compared with unimproved soil. The model and soil parameter are the same as in Section 7.2.

8.1.2.1 Damping ratio of slab

When the slab undergoes seismic loading, it amplifies the earthquake slightly more than an unimproved soil. Figure 200 shows that the first and second eigen frequencies are amplified compared to unimproved soil. This can be caused by the smaller damping ratio and higher unit weight of the slab compared to the natural soil. A damping ratio equal to 1% has been assumed for the slab in the first calculation. Damping ratio of the reinforced concrete can vary from 0.05%-5% (Adams & Askenazi 1999).

In another calculation, a damping ratio of 5% was assumed for the slab. In this situation, the behaviour of amplification ratio’s curve does not change

considerably and just a very small reduction at the first and second eigen frequency has been observed (Figure 196).

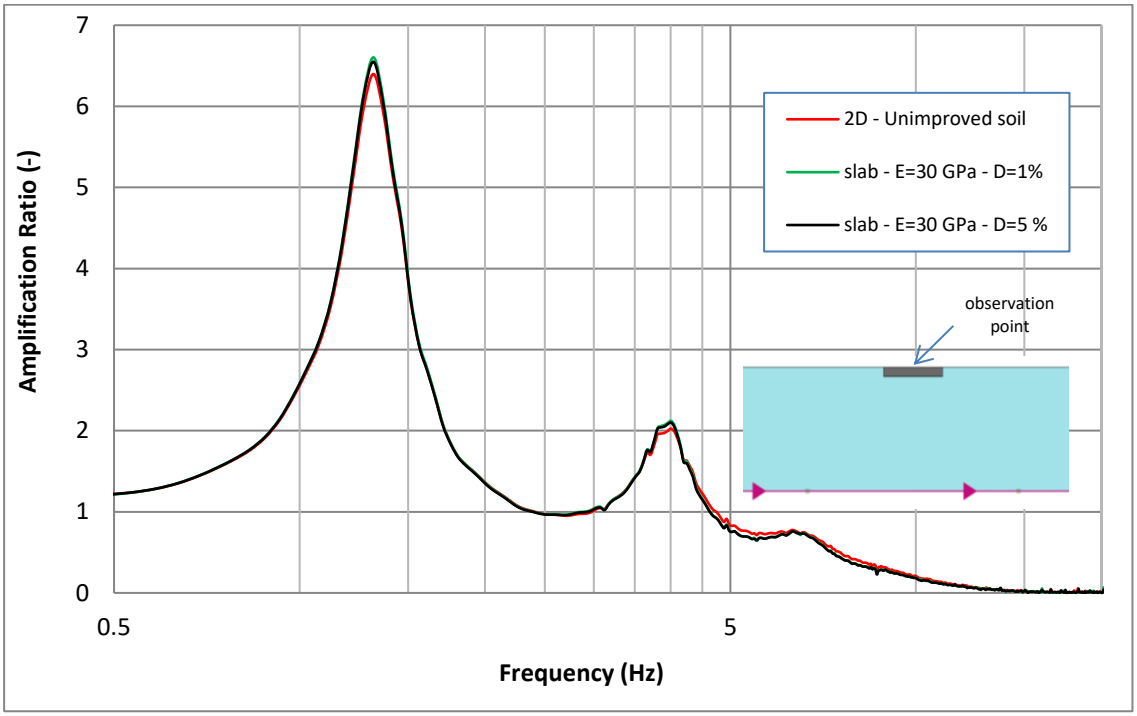

Fig. 196: Amplification ratio; effect of slab damping ratio

8.1.2.2 Slab stiffness

In addition, the influence of slab stiffness on the amplification ratio's curves is investigated. Figure 197 shows that changes in slab stiffness do not change the results, and all amplification ratio's curves derived from different analysis are coincident. It should be noted that a damping ratio of 1% was considered for all three calculations.

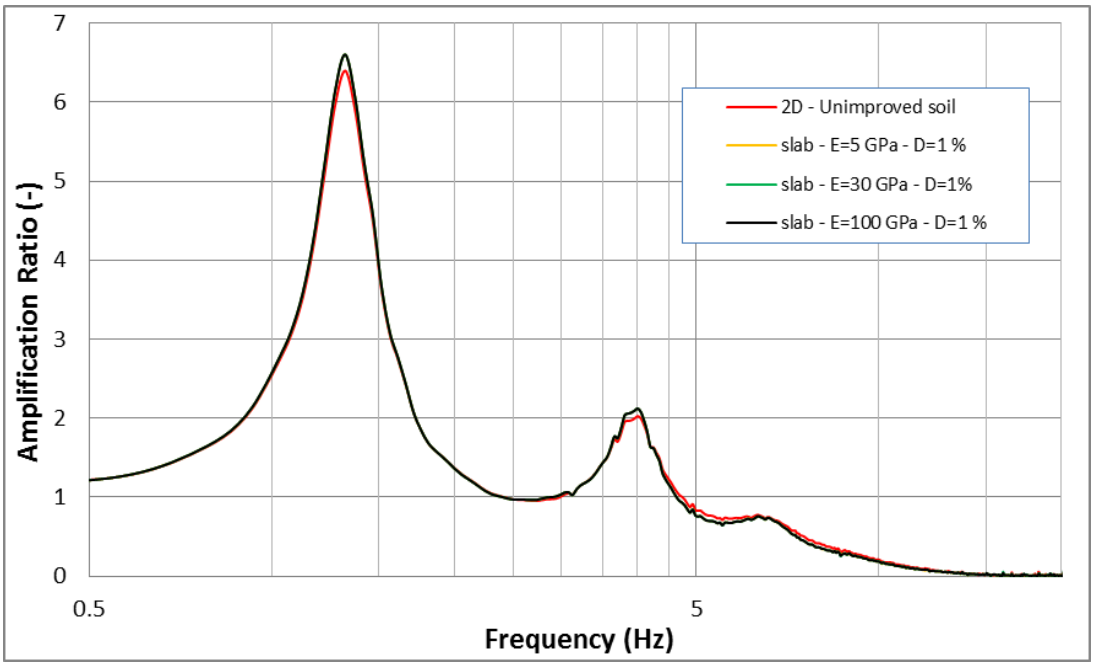

Fig. 197: Amplification ratio; Effect of slab stiffness

8.1.2.3 Slab geometry

Figures 198 and 199 indicate the influence of slab geometry on the ground response. The thickness and the width of the slab were varied. Slab thickness varies from 0.5m to 3.5m with constant width of 16m. In further calculations, the width of the slab altered from 8m to 64m while the thickness is kept constant and equal to 1.8m.

Figure 198 presents that at the vicinity of the first eigen frequency by increasing the slab thickness, the amplification ratio is increasing. This is caused by increasing the area of smaller damping ratio when higher thickness is used. It should be emphasized that unimproved soil below the slab dictates the model's first eigen frequency and keeps it unchanged (Floroiu & Schweiger 2015). At the second eigen frequency, by increasing the thickness of the slab a higher reduction of the amplification ratio is observed, as could be expected.

In Figure 199, it can be seen that a wider slab width amplifies the first eigen frequency. The amplification ratio at the second eigen frequency is higher compared to the unimproved soil, but by increasing the width of the slab, the amplification ratio is decreased slightly. As mentioned before, the second eigen frequency can be more affected by increase in the thickness of slab. These results showed that changes of geometry and damping ratio play a more dominant role than stiffness variation on the slab's effect on the amplification ratio.

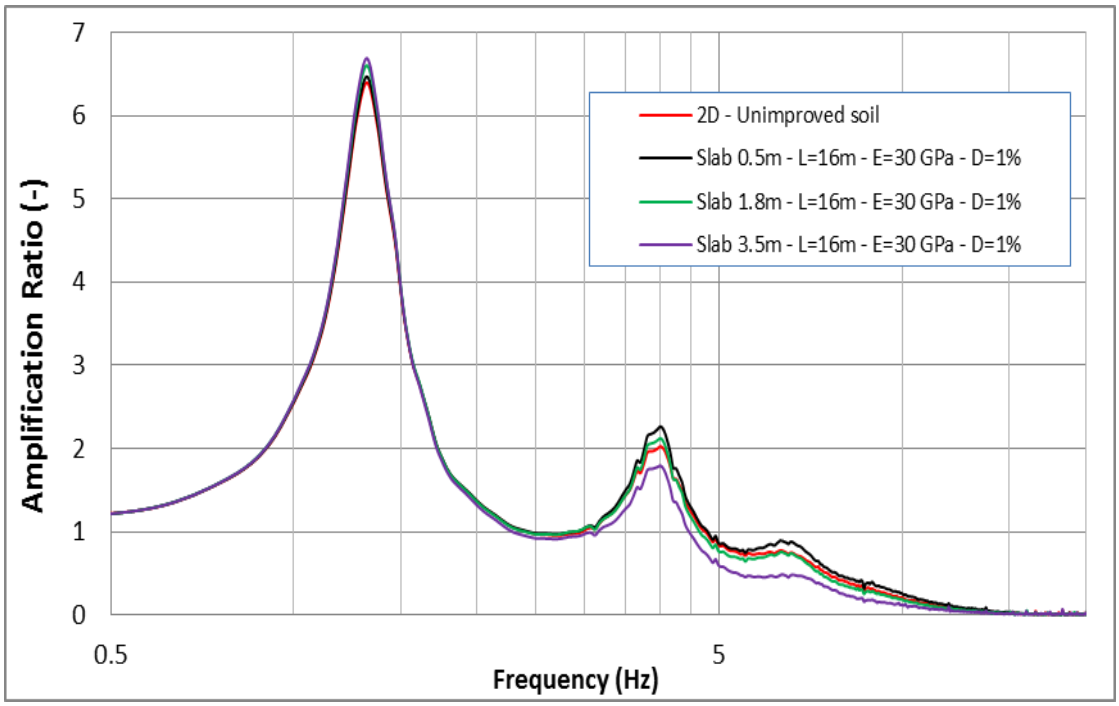

Fig. 198: Amplification ratio; Effect of slab thickness

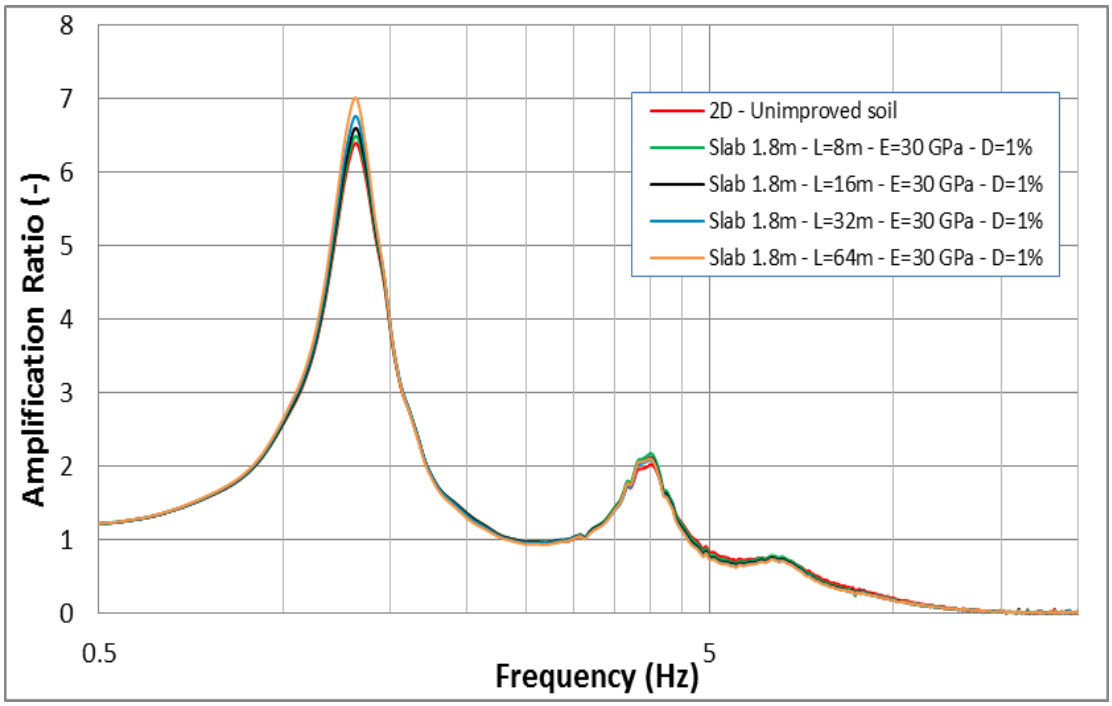

Fig. 199: Amplification ratio; effect of slab width

8.1.3 Supported slab

8.1.3.1 Geometry of the models

In case of supported slabs, diameter and center-to-center spacing of the columns are 80cm and 125cm respectively, the replacement ratio (A_r) is 32%. The width of the foundation is 16.8m, and the depth of columns varies from 10m to 20. Figures 200 and 201 show the geometry of the Plaxis 2D model for homogeneous and layered soil deposits.

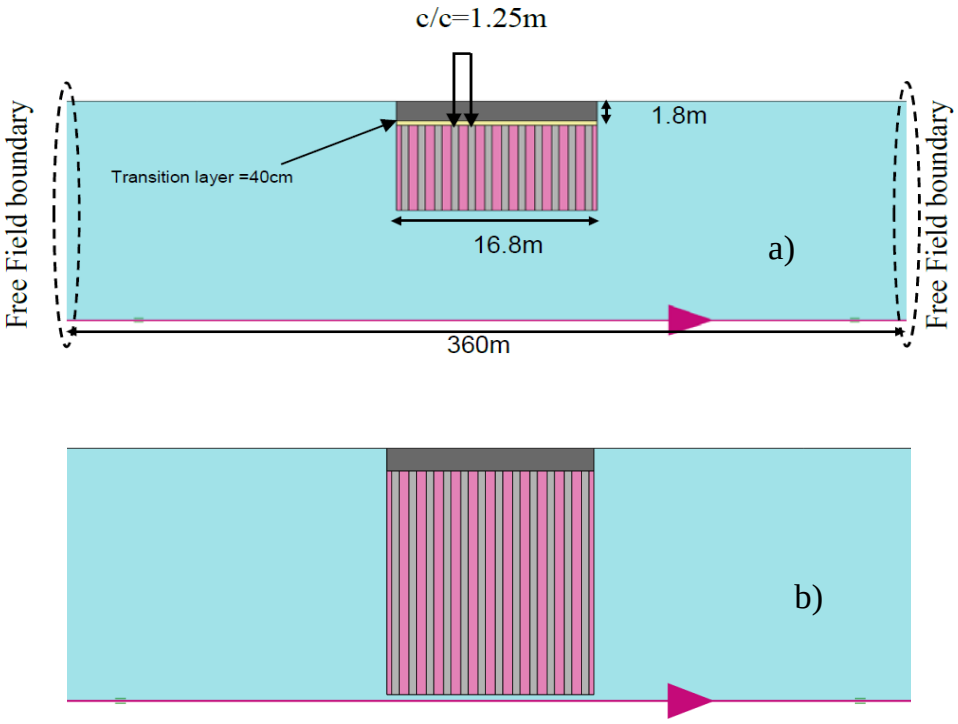

Fig. 200: Geometry of the 2D model homogeneous layer a) with transition layer and b) without transition layer i.e. connected columns to slab

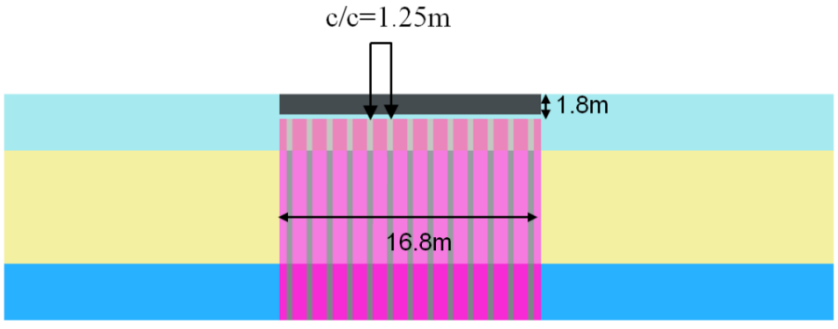

Fig. 201: Geometry of the 2D model layered deposit

8.1.3.2 Material parameters of the columns and slab

The material properties of soil deposits are the same as used in Sections 7.2 and 7.3 for the homogenous and layered soil deposits respectively. The soil improvement composes of deep soil mixing columns, which are modelled by the constitutive model for shotcrete, and the slab was modelled as a linear elastic material. Tables 30 and 31 show the material parameters of columns and slab.

Tab. 30: Material properties of the columns

DSM properties	γ_{col} (kN/m^3)	E (kN/m^2)	ν (-)	f_c (kN/m^2)	f_t (kN/m^2)	G_t (kN/m)
values	19	875E3	0.2	2500	250	0.01

Tab. 31: Material properties of slab

slab properties	γ_{slab} (kN/m^3)	E (kN/m^2)	ν (-)	D (%)
values	24	30 E6	0.2	1

8.1.3.3 Results

Figure 202 shows the amplification ratio in homogeneous soil where the columns penetrate to 10m and 19.5m, and the slab stiffness changes from 10GPa to 100GPa with 1% damping ratio. In these cases, columns are not connected and there is a 40cm transition layer above columns. It can be seen that slab stiffness does not have any considerable influence on the results and all the curves are almost coinciding. In addition, the difference between the slab supported by 19.5m deep columns and the condition of improvement without slab (i.e. columns start from ground level and penetrate 19.5 m) has been presented. It can be seen that at the first eigen frequency the amplification ratio is higher compared to the condition without slab. This is again caused by the smaller damping ratio of the slab compared to the natural soil. At the second eigen frequency the amplification ratio from 19.5m columns improvement is higher than the condition with 10m penetration. In these cases where the columns penetrate 19.5m, the system are stiffer and the second and the third eigen frequency are slightly increased. Figure 203 indicates that there is not a clear difference in the amplification curves in case of connected columns to the slab. In this situation, columns are reinforced with steel profiles (e.g. IPE) and to

consider this effect in the analysis, tensile fracture energy in the columns has been increased to 0.3kN/m in the model.

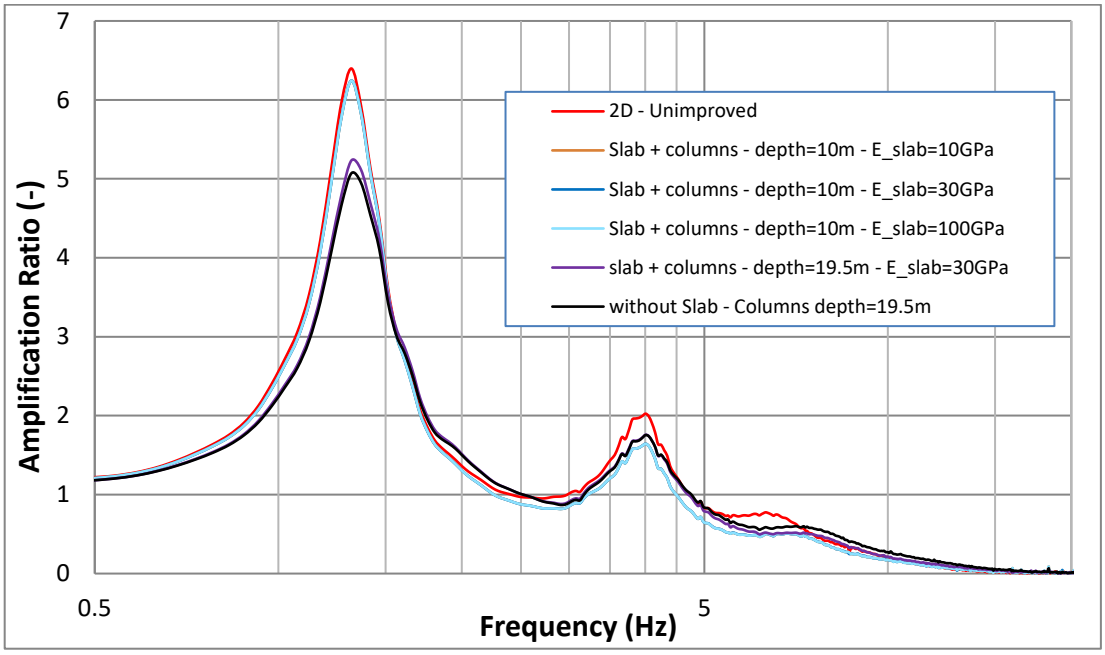

Fig. 202: Amplification ratio, slab supported by columns-columns are not connected

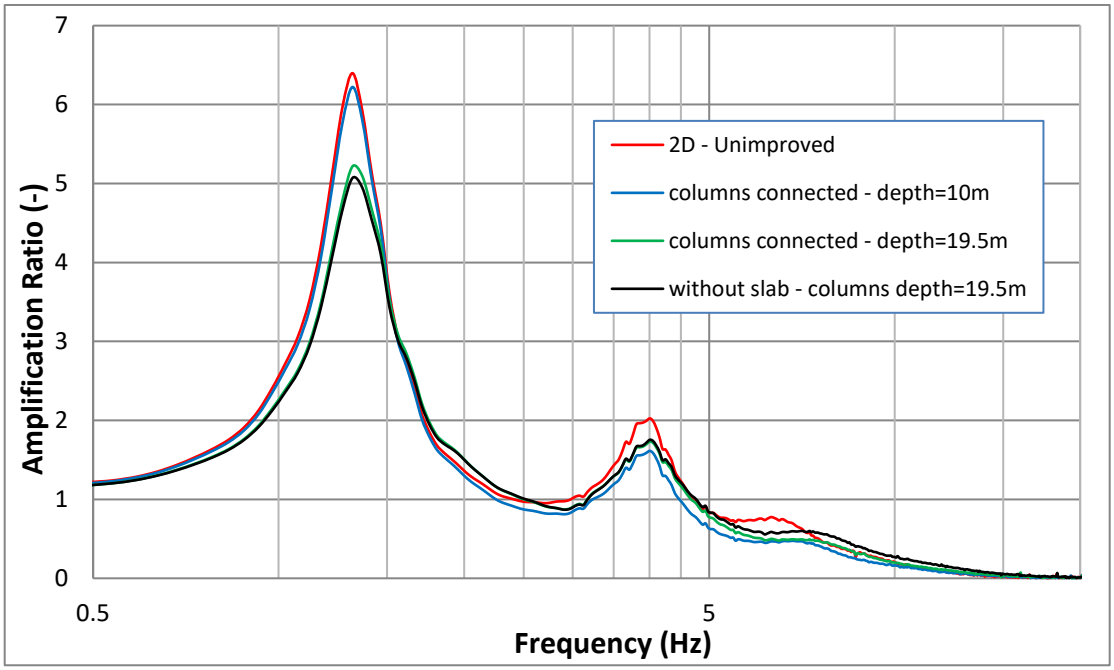

Fig. 203: Amplification ratio, slab supported by columns-columns are connected

The same behaviour has been observed in the case of improved layered soil (Figure 204). In these analyses, when the columns are not connected to the slab and penetrate the whole layer, it is observed that variation of the slab stiffness does not have any considerable influence on the amplification ratio's curves. In the case of improvement by columns without a slab, a higher decrease of amplification ratio is observed at the first eigen frequency, because the slab was replaced by soil and columns that have higher damping ratio. In addition, the effect of connected columns to the slab has been checked and the results compared. Reinforcing elements i.e. steel profiles were not modelled and to simulate the reinforced columns, just the fracture energy has been increased to 0.3kN/m i.e. columns are more ductile and cracks do not propagate immediately after reaching the peak tensile strength. The behaviour of amplification ratio is roughly equal to the condition where columns are not connected to the slab (i.e. with a transition layer). One reason for such behaviour might be that the reinforcing elements that connect the columns and slab as an integrated system were not considered.

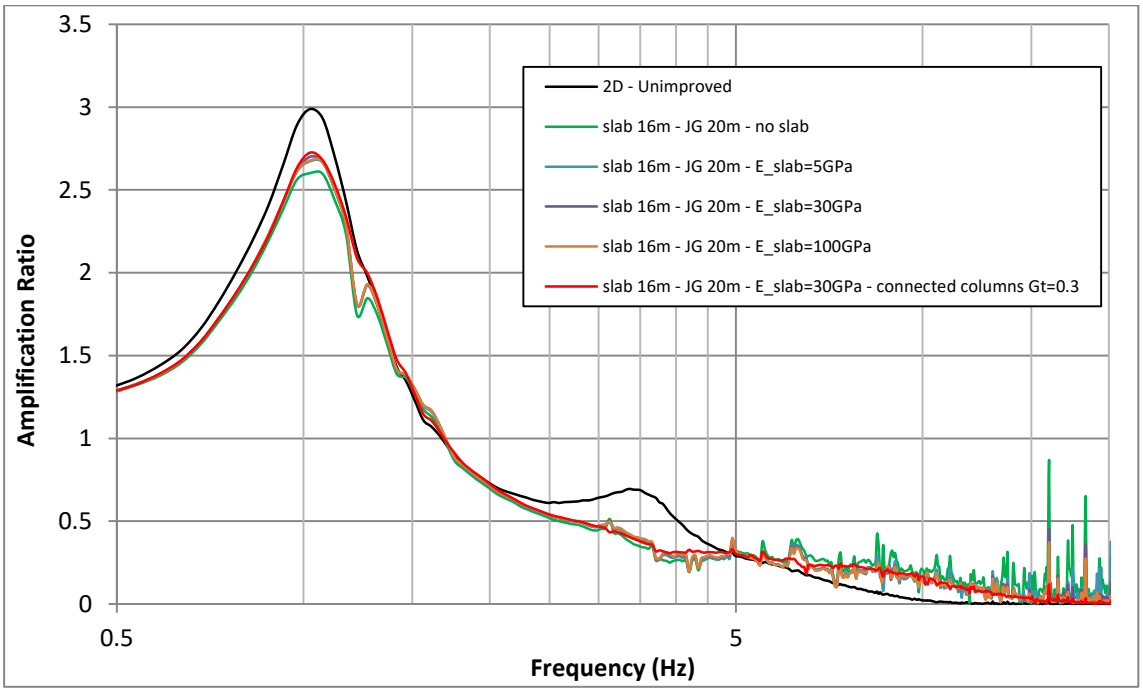

Fig. 204: Amplification ratio of improved layered soil

Figure 205 depicts the failure zones in columns in the two above-mentioned conditions. It can be seen that when the columns are connected to the slab and assumed to be reinforced (i.e. use of higher tensile fracture energy in the model), cracks do not propagate in the columns. The values of the softening parameter H_t in the shotcrete model is between $0<H_t<1$ which indicates that softening is less

severe and residual level has not been reached. But in the case of unreinforced columns, H_t is higher than 1 which means that residual level is reached and cracks can develop inside the columns.

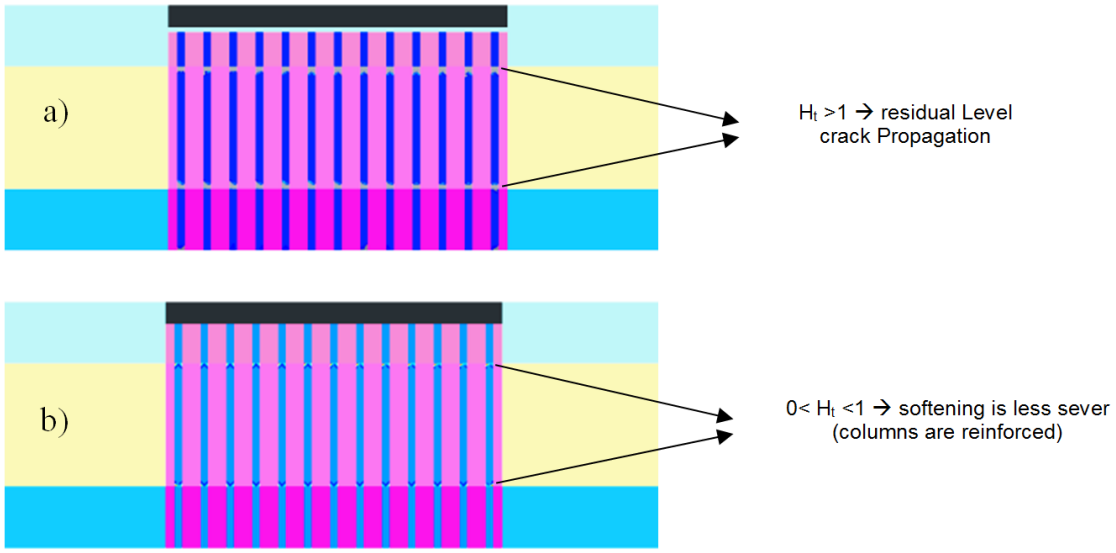

Fig. 205: Crack propagation in the columns; a) transition layer, b) columns connected to the slab and reinforced

8.2 Effect of presence of surface Structure on soil amplification ratio

When a structure (e.g. a building or a bridge) is located on the ground, the effect of the structure on the soil deposit amplification depends on some factors such as the frequency content of the structure. Soil structure interaction (SSI) can be described as the effects that the vibrating structure, the foundation and the ground can have on each other. These mutual effects can change the vibrational characteristics of each of the above-mentioned elements (Torabi and Reyhani 2014). Generally, two dominant mechanisms have been reported for SSI in the literature: Kinematic loading and inertial loading. (Torabi and Reyhani 2014, Kampitsis et al. 2013).

In this part a preliminary study about the effect of the surface structure on the soil amplification ratio under the conditions following condition has been considered, (Figure 206):

a) Only a slab, b) 3-story building, c) 15-story building

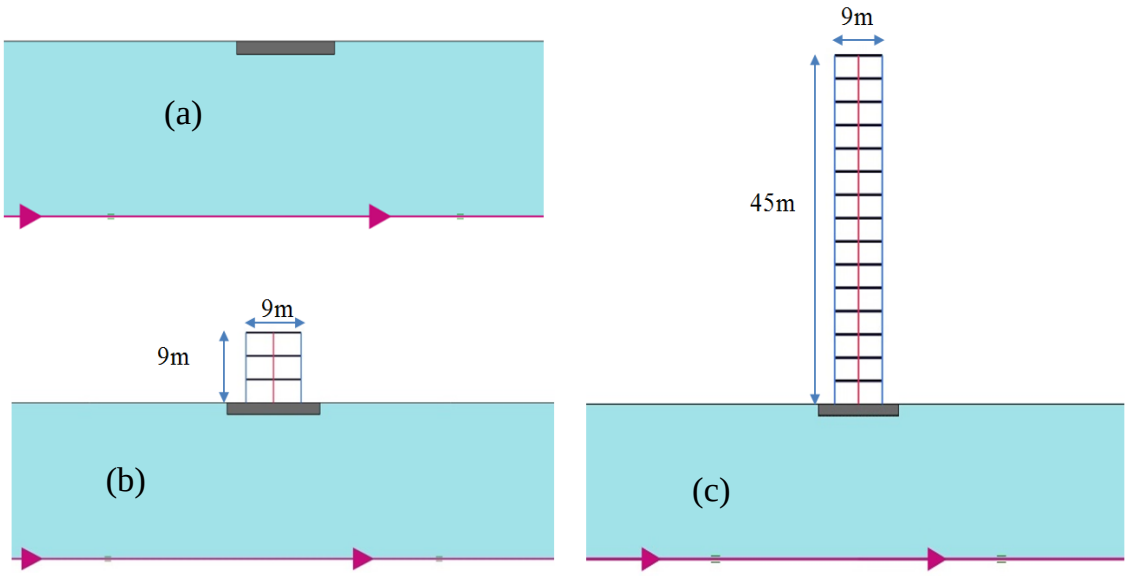

Fig. 206: Different surface structures: a) only ta slab; b) 3-story building; c) 15-story building

The building is modelled using plate elements which represent the walls of the building, floors and the central columns. The material properties of the plates have been presented in Table 32. The physical damping in the building is modelled using Rayleigh damping by the assumption of damping ratio of 5% and using the fundamental first and second frequencies of the buildings. The periods/frequencies of the buildings was obtained from the Modal analysis by using the approximate approach for the buildings that have uniform mass and stiffness at each floor. The fundamental period of the 3 and 15 story buildings were obtained 0.46 and 2.02 seconds, respectively.

Tab. 32: Material properties of the buildings

Parameter	unit	Walls and Floors	columns
Material type	-	Elastic-Isotropic	Elastic-Isotropic
Normal stiffness (EA)	kN/m	9E6	840 E3
Flexural rigidity (EI)	kN/m^2/m	6.75E4	6300
Weight (w)	kN/m/m	10	5
Rayleigh damping (α)	-	0.32	0.32
Rayleigh damping (β)	-	5.7 E-3	5.7 E-3

The homogeneous soil and earthquake is the same as in previous calculations. The observation point is on the center of the model on the surface. Four different amplification ratios have been compared in this analysis; a) Condition with only a slab, b) 3-story building supported by 1.8m slab, c) 15-story building and d) unimproved soil, supported by 1.8m slab. It should be noted that in order to study only the effect of the buildings on the amplification ratio, all of the conditions including the slab thickness was considered the same for both 3-story and 15-story building (i.e. slab thickness equal to 1.8m), although this is unrealistic.

Figure 207, presents the amplification ratio of the above-mentioned conditions. As it is observed, the three-story building amplifies the first eigen frequency higher than the unimproved soil. In addition, the first eigen frequency has been changed and decreased to smaller values. The second eigen frequency is not changed in this case. However, the 15story building indicates different behaviour and decreases the amplification ratio at first eigen frequency. This may be caused by the higher inertial effect of the higher building.

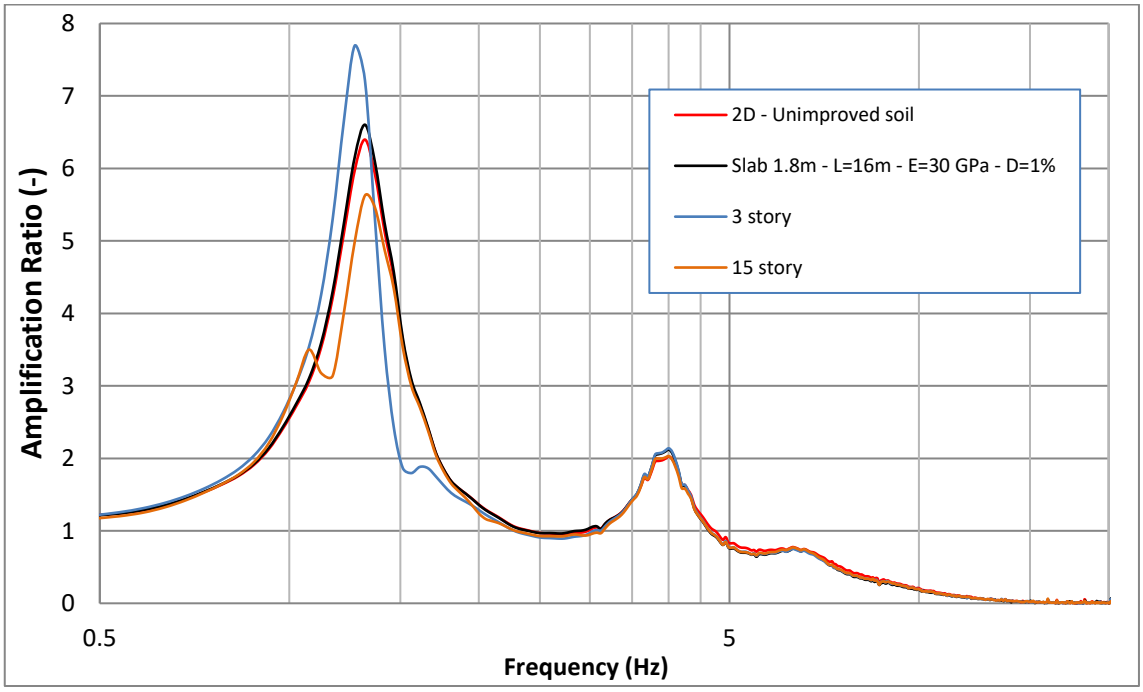

Fig. 207: Amplification ratio – Presence of surface structures

Figure 208 shows the maximum acceleration on the top of the both modelled buildings. It follows that the maximum acceleration of the 3-story building is higher compared to the 15-story building.

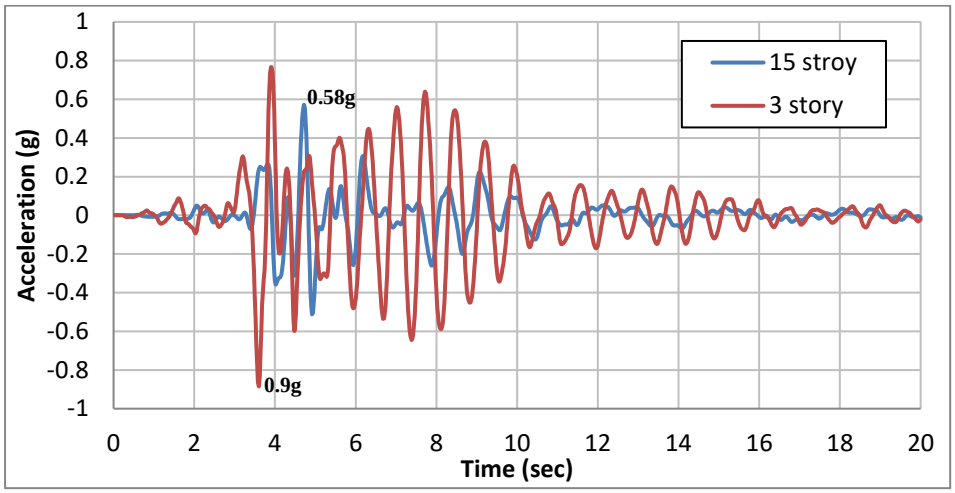

Fig. 208: Maximum acceleration recorded on top of the buildings

In order to provide more information about the seismic behaviour of the surface structures above this specific soil deposit and under the aforementioned earthquake, it could be beneficial to verify the spectral acceleration diagram from the calculation where only a slab has been used (i.e. case b without any structure on the surface). Spectral acceleration presents the maximum acceleration of various single degree of freedom structures (SDOF). It can be seen in Figure 209 that in the period range of 0.35-0.5sec the highest acceleration has been obtained whereas in range of 2 seconds the acceleration is decreased. This can also reveals why the maximum acceleration of the 3-story building was greater compared to the 15-story building. However, further studies are required with various building models, soil conditions and earthquakes in order to draw conclusions that are more general.

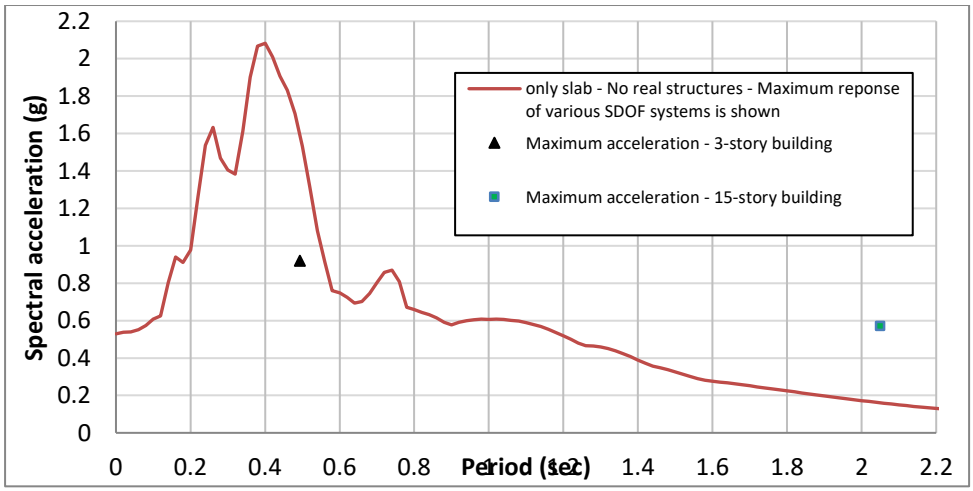

Fig. 209: Spectral acceleration from the analysis where only a slab is considered

8.3 Summary

The influence of concrete slab above the DSM columns has been investigated. It could be observed that in the case of unsupported slab the damping ratio and the thickness of the slab has the main influence on the amplification ratio's curve. For the supported slab with DSM columns, two different scenarios were considered including a) unreinforced columns, which are not connected directly to the slab and therefore a thin transition layer were used between the columns and the concrete slab, and b) reinforced columns which are connected to the slab. It was observed that the amplification ratio's curves are almost similar in both cases. One reason for this behaviour could be that the reinforcing elements that connect the columns and slab together as an integrated system were not modelled and only the fracture energy of the columns was increased to simulate the reinforcing effect. The effect of presence of surface structure on the ground response was also investigated. A 3-story and 15-story buildings with a foundation located on a soft clayey deposit were considered under the Loma Prieta earthquake. The higher acceleration obtained at the top of the 3-story building compared to the 15-story. It was observed that modelling the real soil-foundation-structure interaction instead of assuming, a SDOF system could be beneficial to obtain reasonable estimation about the maximum acceleration of the surface structures by considering the soil-foundation-structure interactions. However, this findings need to be confirmed by further detailed studies.

9 Conclusion and further research

9.1 Conclusion

In this thesis, a new constitutive model originally developed for modelling the mechanical behaviour of shotcrete has been introduced and applied to model the behaviour of the cement-based materials used as ground improvement methods such as jet grouting or deep soil mixing. The main advantages of this constitutive model can be summarised as: a) Most important features of cement-based materials can be captured include time dependency of stiffness and strength, hardening/softening in compression and tension and creep behaviour. b) The input parameters of the model can be calibrated via back-calculation of the laboratory test results such as the uniaxial compression, triaxial test, three point bending test and creep test. c) Providing continuum model for studying the behaviour of ground improvement techniques. One of the shortcomings of the shotcrete model is that only the initiation of cracks can be defined correctly with this model in dynamic analysis.

In this thesis, two different types of numerical calculations namely static and dynamic analyses were performed by means of the finite element method to investigate the application of this new constitutive model in the field of ground improvement.

The new model was applied to simulate the behaviour of a jet-grout slab, constructed below the base of a deep excavation to provide resistance against uplift pressure. Emphasis was put on the behaviour after reaching the tensile strength of the material. It could be shown that significantly different results with respect to the stress distribution in the slab are obtained as compared to modelling the behaviour of the slab with a simple Mohr-Coulomb failure criterion with tension cut-off limit. The influence of different assumptions such as the value chosen for fracture energy has been addressed. It could be shown that with a different slab geometry (curved slab) the tension piles could be eliminated. In addition, the compression-softening zone on top of the jet-grout panel near the wall could be identified. In another example, it was aimed to show the capability of the model to define possible crack locations and their orientation in rows of overlapping deep mixed columns acting as a method of improvement on the passive side of the excavation in an interaction to the sheet pile wall. Various types of material properties were investigated and the obtained results were compared to the condition where columns were modelled with Mohr-Coulomb criterion to highlight the differences in stress distributions and the obtained failure zones.

Jet-grout columns were utilized as earthquake-resistant elements in a homogenous soil layer where the new shotcrete model was employed to describe

the behaviour of the columns. The influence of some input parameters of the model such as stiffness, fracture energy in tension together with the influence of Rayleigh damping parameters on the crack pattern was investigated. It was seen that high stiffness and the low fracture energy led to crack propagation in all the columns while using a more ductile material (i.e. 5GPa stiffness) even with the lowest fracture energy eliminated all the cracks. In addition, it was observed that introducing artificial viscous damping to the columns could affect the crack patterns. It was shown that the choice of a correct model width is important and can affect the amplification ratio's curve and incorrect crack patterns may be obtained. A simple example was used to investigate the behaviour of the model in dynamic analyses where only one jet-grouting column was considered. It is emphasized that with the shotcrete model in its present formulation, only the initiation of cracks could be reliably assessed because an opening closure mechanism for cracks applicable in dynamic analysis , is not yet implemented.

The effect of jet grouting columns on ground response in layered soil was checked by a series of numerical calculations employing the finite element method, where influence of various soil improvement width and columns depth was checked. It could be shown that stiff columns embedded in the soil layer could change the natural frequencies of the improved soil layer. Results also proved that using wider improvement width and higher replacement ratio has a significant effect on the reduction of amplification ratio. Soil improvement by means of the jet grouting columns can decrease, but also may increase the seismic load on surface structures. Comparing the results of spectral acceleration with the proposed curves from EC8 also showed that the site classification could be altered by soil improvement. Knowledge of this reduction may be beneficial from structural point of view and may lead to significant cost saving due to use of lower seismic design acceleration. On the other hand, the results showed that an alternative to reduce the seismic loads on long period structures constructed on soft deposits can be the use of a lattice-shaped improvement that can decrease the earthquake-induced shear strain in the soils in between the panels, or increasing the replacement ratio by using wider columns or overlapping columns. However, more analyses with various earthquakes are required to obtain general conclusions and also define unique design spectra for improved deposits. In addition, it was shown that the model adopted for the improvement elements is capable in identifying possible zone of cracks initiation, which could be a useful information for designers to optimize the dimensions of such brittle elements, or even decide to reinforce them.

Finally, the influence of concrete slab above the DSM columns has been presented. The damping ratio and the thickness of the slab have the main influence on the amplification ratio's curve when the slab is not supported by the DSM columns. In addition, no significant difference were observed in the amplification ratio's curves of the supported slab in both cases of connected

columns to the slab and discrete columns with a thin transition layer. On the other hand, it was shown that modelling the real structure on the surface could be beneficial to have a correct estimation about the maximum acceleration of a structure during an earthquake, since the soil-foundation-structure interaction may change the behaviour of the amplification ratio's curve. However, these findings require to be confirmed by further studies.

9.2 Further research

In the following recommendations for further research on constitutive modelling, ground improvement and seismic analyses is presented:

- Optimisation of the shotcrete model for applying in dynamic analysis by considering change of stiffness with shear strain for cement-based material.

- Improving the shotcrete model to simulate realistic crack opening and closure.
- Evaluate the crack locations obtained from numerical simulations with real measurements.

- Using more earthquake records in connection with probabilistic hazard analysis in order to propose design spectra for improved deposits.

- Consider realistic bedrock condition by assuming elastic bedrock condition in response analyses

10 Bibliography

Adams, V & Askenazi, A. (1999)
Building Better Products with Finite Element Analysis , OnWord Press, Santa Fe, N.M.

Alsaleh, H & Shahrour, I. (2009)
Influence of plasticityontheseismicsoil–micropiles–structureinteraction, Soil Dynamics and Earthquake Engineering 29 (2009) 574– 578

Ali, H., Mahbaz, S.B., Cascante, G. & Garbinsky, M. (2013)
Low strain measurement of shear modulus with resonant column and bender element tests-Frequency effects. In Proceedings of the GeoMontreal 2013: Geoscience for Sustainability, Montreal, QC, Canada.

Amorosi, A., Boldini, D. & Gaetano, E. (2010)
Parametric study on seismic ground response by finite element modelling, Computers and Geotechnics, 37(4), 515-528.

Antoniou, S., Pihno, R. (2013)
SeismoSignal, Version 5.1, Seismosoft srl.

Arroyo, M., Ciantia, M., Castellanza, R., Gens, A. & Nova, R. (2012)
Simulation of cement-improved clay structures with a bonded elasto-plastic model:A practical approach.Computers and Geotechnics, 45: 140–150.

Axtell P.J., Stark, T.D. (2008)
Increase in Shear Modulus by Soil Mix and Jet Grout, Journal of deep foundation institute." Deep Found. Inst. J., 2(1), 11–22.

Barrios, D. B., Angelo, E., & Gonc¸alves, E. (2005)
Finite element shot peening simulation, Analysis and comparison with experimental results,'' ECOM 2005, VIII Congreso Argentino de Meca`nica Computacional, Larreteguy, A., Ed., vol. XXIV, Buenos Aires, Argentina, Noviembre.

Barros, J.A.O. & Figueiras, J.A., (1999)
Flextural behaviour of SFRC: Testing and Modeling, Journal of Materials in civil engineering,erring 11, No. 4., ASCE, paper No. 15853.

Bell, A.L. & Burke, G.K. (1992)
The compressive strength of ground treated using triple system jet grouting, Proceedings of the conference of grouting in the ground, organized by the institution of civil engineers, Edited by Dr. A. L. Bell., London.

Benz, T. (2006)
Small-strain stiffness of soil and its numerical consequences. PhD Thesis. Stuttgart University, Stuttgart, Germany.

Borchert, K.-M., Henke, S. & Richter, T. (2013)
Die Düsenstrahlsohle als horizontales Aussteifungselement. In Proceedings Workshop Bemessen mit NumerischenMethoden (Grabe, editor), Hamburg Harburg, 24.–25.9.2013, 198–220.

Bradley, B.A., Araki, K., Ishii, T. & Saitoh, K. (2013)
Effect of latticed-shaped ground improvement geometry on seismic response of liquefiable soil deposits via 3-D seismic effective stress analysis, Soil and dynamics and earthquake engineering 48 (2013) 35-47.

Brinkgreve, R.B.J., Engin, E. and Swolfs, W.M. (2013)
Plaxis 3D, Version 2013, Plaxis bv.

Brinkgreve, R.B.J., Engin, E. and Swolfs, W.M. (2014)
PLAXIS 2D, AE, 2014, Plaxis bv.

Brinkgreve, R.B.J., Engin, E. and Swolfs, W.M. (2015a)
PLAXIS 2D, AE, 2015, Plaxis bv.

Brinkgreve, R.B.J., Engin, E. and Swolfs, W.M. (2015b)
PLAXIS 2D, AE, Reference, Scientific and Dynamic Manuals, Lisse, Balkema.

Brinkgreve, R.B.J., Engin, E. and Swolfs, W.M. (2015c)
Plaxis 3D, Version 2015, Plaxis bv.

Bruce, D.A., Cadden, A.W. & Sabatini, P.J. (2005)
Practical Advice for Foundation Design – Micropiles for Structural Support, Geo-Frontiers Congress 2005, January 24-26, 2005, Austin, Texas, United States.

Bzowka, J. (2009)
Współpraca kolumn wykonywanych techniką iniekcji strumieniowejz podłożem gruntowym (Interaction of jet grouting columns with subsoil). Monograph, Gliwice, Poland: Silesian University of Technology Publishers 244 p [in Polish].

CEB-FIP model code (1990).
Design code – comite Euro-international du Beton. London: Thomas Telford.

CEN 1998-1, (2004)
Design of structures for earthquake resistance – Part 1: General rules, seismic actions and rules for buildings." Eurocode 8, European Committee for Standardization, Brussels, Belgium.

Chen, B. & Liu, J. (2004)
Effect of aggregate on the fracture behavior of high strength concrete, Journal of Construction and Building Materials 18 (2004) 585–590.

Cifuentes, H., Alcalde, M. & Medina, E., (2013)
Comparison of the size-independent fracture energy of concrete obtained by two test methods, 8th international conference on fracture mechanics of concrete and concrete structures, Teldo, Spain.

Coulter, S. & Martin, C.D. (2006)
Single fluid jet-grout strength and deformation properties, Tunnelling and Underground Space Technology 21, 690–695.

Croce, P. & Flora, A. (1998)
Effects of jet grouting in pyroclastic soils. Rivista Italiana di Geotecnica 2: pp. 5–14.

Croce, P., Flora, A. & Modoni, G. (2014)
Jet Grouting Technology, design and Control, Taylor & Francis Group, Boca Raton, FL, USA. 278 pp.

Delfosse-Ribay, E., Djeran-Maigre, I., Cabrillac, R. & Gouvenot, D. (2004)
Shear modulus and damping raio of grouted sand." Soil dynamics and earthquake engineering, Vol. 24(6), 461-471.

Dey, A. (2011)
Calibration of a PLAXIS Finite Element Dynamic Model: Effect of Domain Width and Meshing Schemes." Third Indian Young Geotechnical Engineers Conference (3IYGEC), New Delhi, India.

DIN 4093:2012-08
Design of ground improvement: Jet grouting, deep mixing, or grouting." Standard of the Deutsches Institut für Normung, 2012 ed.: Dusseldorf, Germany: 17 p.

Durgunoglu, H.T., Chinchelli, M., Ikiz, S., Emrem, C., Hurley, T. & Catalbas, F. (2004)
Soil improvement with Jet-grout columns: a case study from the 1999 kocaeli earthquake." Proc. of 5th international conference on case histories in geotechnical engineering, New York, NY, Paper No. 26.

EN 14487-1 (2006)
Sprayed concrete - Part 1: Definitions, specifications and conformity. European Committee for Standardization.

Fang, Y. S., Kuo, L. Y. & Wang, D. R. (2004)
Properties of soilcrete stabilized with jet grouting. Proceedings of the 14th International Offshore and Polar Engineering Conference, Toulon, France, May 23–28, 2004: pp. 696–702.

Fang, Y, Liao, J., & Lin, T. (1994a)
Mechanical properties of jet grouted soilcrete, Quarterly Journal of Engineering Geology, 27, 257-265.

Fang, Y., Liao, J., & Sze, S. (1994b)
An empirical strength criterion for jet grouted soilcrete, Engineering Geology 37: 285-293.

Fatahi, B. & Tabatabaiefar, S. (2014)
Fully Nonlinear versus Equivalent Linear Computation Method for Seismic Analysis of Midrise Buildings on Soft Soils." Int. J. Geomech., 10.1061/(ASCE)GM.1943-5622.0000354, 04014016.

FHWA. (2005)
Micropile design and construction, FHWA-NHI-05-039, Federal Highway Administration, U.S., Department of transportation, Washington, DC.

Floroiu, L.G. & Schweiger, H.F., (2013)
Influence of soil improvement techniques on soil behaviour and consequences for earthquake design, VEESD, 28-30 August 2013, Vienna, Austria.

Floroiu, L.G. & Schweiger, H.F. (2014)
Influence of vibro stone columns on ground response. Second European conference on earthquake engineering and seismology, Istanbul, Turkey, Paper No. 1305.

Floroiu, L.G. & Schweiger, H.F. (2015)
Parametric study of the seismic ground response of a linear visco-elastic soil layer improved by stone columns or pile-like elements. Geotechnik, 38 (2015), Heft 4: 304-315.

Floroiu, L.G. (2016)
A contribution to seismic ground response of improved foundation soil. PhD Thesis, Graz University of Technology, Institue for soil mechanics and foundation engineering, Graz, Austria.

Galavi, V., Petalas A. & Brinkgreve, R.B.J. (2013)
Finite element modelling of seismic liquefaction in soils. Geotechnical engineering journal of the SEAGS and AGSSEA, 44 (3): 55–64.

Gens, A.&Nova, R. (1993)
Conceptual base for a constitutive model for bonded soils and weak rocks. In Proceedings of the international symposium on Geotechnical engineering of hard soils-soft rocks, Athens, 485–494.

Hashash Y.M.A., Park D. (2001)
Non-linear one-dimensional seismic ground motion propagation in the Mississippi embayment, Eng. Geol., 62: 185–206.

Hashash, Y.M.A, Groholski, D.R., Phillips, C.A., Park, D. & Musgrove, M. (2015a)
DEEPSOIL, Version 6, University of Illinois at Urbana-Champaign.

Hashash, Y.M.A, Groholski, D.R., Phillips, C.A., Park, D. & Musgrove, M. (2015b)
DEEPSOIL, version 6. User's Manual and Tutorial, 116 pp.

Hashhash Y.M.A. & Waterman, (2010)
Advanced course on computational geotechnics, dynamics day, 18-20 march, Schiphol, Netherlands.

Hilber, H. M., Hughes, T. J. R., & Taylor, R. L. (1997)
Improved numerical dissipation for time integration algorithms in Structural dynamics, Earthquake Engineering and Structural Dynamics, 5, 283–292.

Hokmabadi, A., Fatahi, B., & Samali, B. (2014)
Physical Modeling of Seismic Soil-Pile-Structure Interaction for Buildings on Soft Soils." Int. J. Geomech., 10.1061/(ASCE)GM.1943-5622.0000396, 04014046.

Hoque. E. & Tatsuoka, F. (2004)
Measurement of quasi-elastic stiffness parameter of dense Toyoura sand in hollow cylinder apparatus and triaxial apparatus with bender element, Geotechnical testing journal, (1):1-13.

Hora, M.S. (2011)
Nonlinear interaction analysis of tall building frame-layered soil system subjected to seismic loading Proceedings 13th international conference of the international association for computer methods and advances in geomechanics, IACMAG 2011, pp 800-816.

Horpibulsuk, S., Liu, M.D., Liyanapathirana, D.S. & Suebsuk, J (2010)
Behaviour of cemented clay simulated via the theoretical framework of the Structured Cam Clay model. Computers and Geotechnics, 37: 1–9.

Ignat, R., Baker, S., Larsson, S. & Liedberg, S. (2015)
Two-and three-dimensional analyses of excavation support with rows of dry deep mixing columns, Computers and geotechnics 66, 16-30.

Isam, S., Hassan, A., & Mhamed, S. (2012)
3D elastoplastic analysis of the seismic performance of inclined micropiles, Computer and Geotechnichs 39 (2012), 1-7.

Ishihara, K. (1996)
Soil behaviour in earthquake geotechnics, Department of civil engineering science university of Tokyo, Oxford University press. New York, N. Y., 360pp.

JCI (Japan concrete institute) -S-001. (2003)
Method of test for fracture energy of concrete by use of notched beam;

Kampitsis, A.E., Sapountzakis, E.J., Giannakos, S.K. & Gerolymos, N.A. (2013)
Seismic soil–pile–structure kinematic and inertial interaction—A new beam approach, soil dynamics and earthquake engineering, 55(2013)211–224.

Karihaloo, B. (2003)
Failure of concrete, comprehensive structural integrity (2), edited by I.Milne, R.O. Ritchie and B.Karihaloo, Perfamon, Oxford, 477-548

Karihaloo, B. L., Abdalla, H. M. & Imjai, T. (2003)
A simple method for determining the true specific fracture energy of concrete, Magazine of Concrete Research, 55, No. 5, 471-481

Kosravi, M, Tamura, S., Boulanger, R.W, Wilson, D.W., Olgun, C.G., Rayamajhi, D. & Wang. Y. (2015)
Dynamic centrifuge test of soft clay reinforced by soil-cement grids, IFCEE conference 2015, March 17–21, San Antonio, Texas, http://dx.doi.org/10.1061/9780784479087.218

Kitazume, M. & Terashi, M. (2013)
The deep mixing method, Taylor & Francis Group, London, UK, 405pp.

Kontoe, S. (2006)
Development of time integration schemes and advanced boundary conditions for dynamic geotechnical analysis, Ph.D. thesis, Imperial College of Science, Technology and Medicine, London, U.K.

Kramer, S.L. (1996)
Geotechnical Earthquake Engineering, Prentice-Hall, Inc., Upper Saddle River, New Jersey, 653pp.

Kudella, P., Mayer, P.M., Möller, G. (2003)
Testing and modelling the ductility of buried jetgrout structures. Int. Symp. On Geotechnical Measurements and Modelling, Karlsruhe. Ed. O. Natau, E. Fecker, E. Pimentel, Balkema/Swets & Zeitlinger, S. 467-474

Kumar, A., Choudhury, D., and Katzenbach, R. (2016)
Effect of Earthquake on Combined Pile–Raft Foundation, Int. J. Geomech. , 10.1061/(ASCE)GM.1943-5622.0000637 , 04016013.

Kwok, A.O.L., Stewart, J.P., Hashash, Y.M.A., Matasovic, N., Pyke, R., Wang, Z., et al. (2007)

Use of exact solutions of wave propagation problems to guide implementation of nonlinear seismic ground response analysis procedures, J. Geotech Geoenviron Eng, 133(11), 1385-98.

Ladhane, K. and Sawant, V. (2015)

Effect of Pile Group Configurations on Nonlinear Dynamic Response, Int. J. Geomech., 10.1061/(ASCE)GM.1943-5622.0000476, 04015013.

Lysmer, J. and Kuhlemeyer, R. L. (1969)

Finite dynamic model for infinite media, Journal of Engineering and Mechanical Division ASCE 95, EM4, 859–877.

Luna, R. & Jadi, H. (2000)

Determination of dynamic soil properties using geophysical methods, Proceeding of the first international conference on the application of geophysical and NDT methodologies to transportation facilities and infrastructures, St. Louis, MO. Paper No. 3-1.

Maher, M. H., Ro, K. S. & Welsh, J. P. (1994)

High strain dynamic modulus and damping of chemicallz grouted sand." Soil dynamic and earthquake engineering, Vol. 13(2), 131-138.

Maheshwari, B. & Sarkar, R. (2011)

Seismic Behavior of Soil-Pile-Structure Interaction in Liquefiable Soils: Parametric Study." Int. J. Geomech., 10.1061/(ASCE)GM.1943-5622.0000087, 335-347.

Martin, J.R. & Olgun, C.G. (2007)

Liquefaction mitigation using jet-grout columns – 1999 Kocaeli earthquake case history and nnumerical modeling." 4th international conference on earthquake geotechnical engineering, June 25-28, Greece, Paper No. 1273.

Nakamura, H. & Higai, T. (2001)

Compressive fracture energy and fracture zone length of concrete, modelling of inelastic behaviour of RC structures under seismic loads. ASCE 2001:471-478.

Namikawa, T. & Koseki, J. (2006)
Experimental determination of softening relations for cement-treated sand, Soils and foundation, Vol. 46, No. 4, 491-504.

Neville, A.M. (1997)
Properties of concrete, Essex Addison Wesley Longman Ltd. Publ, p.306.

Nguyen, T.V., Rayamajhi, D., Boulanger, R.W., Ashford, S.A., Lu, J., Elgamal, A. & Shao, L. (2013)
Design of DSM grids for liquefaction remediation, J. Geotech. Geoenviron. Eng. 2013.139:1923-1933.

Niina, A., Saitoh, S., Babasaki, R., Miyata, T. & Tanaka, K. (1981)
Engineering properties of improved soil obtained by stabilizing alluvial clay from various regions with cement slurry. Takenaka Technical Research Report. Vol. 25. pp. 1–21.

Nikbakhtan, B. & Ahangari, K. (2010)
Field study of the influence of various jet grouting parameters on soilcrete unconfioned compressive strength and its diameter, international journals of rock mechanics & mining science 47,685-689.

Nikbakhtan, B., Ahangari, K. & Rahmani, N. (2010)
Estimation of jet grouting parameters in shahriar dam, Iran, Mining science and technology 20,0472-0477.

Olgun, C.G., Martin J.R. (2010)
Seismic performance of soil-mix panel reinforced ground, Proc. of 5th international conference on recent advances in geotechnical earthquake engineering and soil dynamics, San Diego, California, USA, Paper No.: 5.47a.

Pacific Earthquake Engineering Research Center (PEER) (2011)
PEER Ground Motion Database, (http://peer.berkeley.edu/products/strong_ground_motion_db.html)

Pal, O. (1998)
Modelisation du comportement dynamique des ouvrages grace a des elements finis de haute precision, Thesis Luniversite Joseph Fourier – Grenoble I.

Pantazopoulos, I.A. & Atmatzidis D.K. (2012)
Dynamic properties of microfine cement grouted sands, Soil dynamics and earthquake engineering, Vol. 42, 17-31.

Park, D. & Hashash, Y. M. A. (2004).
Soil damping formulation in nonlinear time domain site response analysis, J. Earthquake Eng., 8(2), 249–274.

Pecker, A. (2007)
Soil behaviour under cyclic loading, advanced earthquake engineering analysis, Volume 494 of the series CISM international center for mechanical sciences, springer, pp 1-13.

Petersson, P.E., (1980)
Fracture energy of concrete: method of determination, Cement and concrete research, Vol. 10, pp. 78-89, Pergamon press, Ltd., USA.

Pitilakis, K., Trevlopoulos, k., Anastasiadis, A. & Senetakis, K. (2011)
Seismic response of structure on improved soil, Proceedings of the 8th international conference on structural dynamics, EURODYN, Leuvenm Belgium, 72-81

Pölling, R. (2000).
Eine praxisnahe, schädigungsorientierte Materialbeschreibung von Stahlbeton für Strukturanalysen.” Ph.D. thesis, Ruhr-Universität, Bochum.

Porbaha, A. (1998)
State of the art in deep mixing technology, part I. basic concepts and overview. Ground Improvement, Vol. 2, No. 2, 81-92.

Rayamajhi, D., Nguyen, T., Ashford, S., Boulanger, R., Lu, J., Elgamal, A., & Shao, L. (2013)
Numerical Study of Shear Stress Distribution for Discrete Columns in Liquefiable Soils, J. Geotech. Geoenviron. Eng., 10.1061/(ASCE)GT.1943-5606.0000970, 04013034.

Rutherford C.J., Biscontin G., Koutsoftas D., Briaud J.L. (2007)
Design Process of Deep Soil Mixed Walls for Excavation Support, International Journal of Geoengineering Case histories, Vol.1, Issue 2, p.56-72.

Roesset J.M. (1977)
Soil amplification of earthquakes. In: Desai CS, Christian JT, editors. Numerical Methods in Geotechnical Engineering. New York: McGraw-Hill, p. 639–82.

Schädlich, B., Schweiger, H.F. (2014a)
A new constitutive model for shotcrete, Proc. Numerical Methods in Geotechnical Engineering (Hicks, Brinkgreve & Rohe, eds), Taylor & Francis Group, London, 103-108.

Schädlich, B. & Schweiger, H.F. (2014b)
Shotcetemodel. Internal report: Implementation, validation and application of the shotcrete model. Computational Geotechnics group, Institute for soil mechanics and foundation engineering, Graz university of technology.

Schnabel P.B., Lysmer J., Seed H.B. (1972)
SHAKE: A computer program for earthquake response analysis of horizontally layered sites, Report No. CB/EERC-72/12, Earthquake Engineering Research Center, University of California, Berkeley, CA.

Schweiger, H.F., Sedighi, P., Henke, S. & Borchert, K.-M. (2014)
Numerical modelling of ground improvement techniques considering tension softening." 8th International Symposium on Geotechnical Aspects of Underground Construction in Soft Ground, Seoul, South Korea, 209 – 214.

Seed, H.B. & Idriss, I.M. (1970)
Soil moduli and damping factors for dynamic response analyses, Technical repot, College of Engineering University of California Berkeley, U.S.A., 41pp.

Seed, H.B., Ugas, C., & Lysmer, J. (1976)
Site dependent spectra for earthquake resistant design, *Bulletin of Seismological Society of America*, Vol. 66, 221-243.

Sluis, J., Besseling, F., Stuurwold, P. & Lengkeek, A. (2013)
Validation and application of the embedded pile row feature in PLAXIS 2D, Plaxis Bulletin, Autumn 2013.

Takahashi, H., Kitazume, M. & Ishibashi, S. (2006)
Effect of deep mixing wall spacing on liquefaction mitigation, Proceedings of the Sixth International Conference on Physical Modelling in Geotechnics, 6th ICPMG '06, Hong Kong, 4 – 6, Taylor & Francis Group plc, London, UK.,

Takahashi, H., Morikawa, Y., Iba, H., Fukada, H., Maruyama, K. & Takehana, K. (2013)
Experimental study on lattice-shaped cement treatment method for liquefaction countermeasure, Proceeding of the 18th International Conference on Soil Mechanics and Geotechnical Engineering, Paris,

Tariq, K.A. & Maki, T. (2014)
Mechanical behaviour of cement-treated sand, Journal of construction and building material, Vol. 58, 54-63.

Taylor. S.E., Rankin G.I.B. & Cleland, D.J. (2002)
Guide to compressive membrane action in concrete bridge deck, concrete bridge development group, queen's university of Belfast.

Terashi, M., Tanaka, H., Mitsumoto, T., Niidome, Y. & Honma, S. (1980)
Fundamental properties of lime and cement treated soils (2nd Report). *Report of the Port and Harbour Research Institute*. Vol. 19. No. 1. pp. 33–62 (in Japanese).

Topolnicki, M. (2004)
In situ soil mixing. Ground Improvement, New York, Spon Press, 331-428.

Topolnicki, M. & Soltys, G. (2012)
Novel application of wet deep soil mixing for foundation of modern wind turbines, proceedings oft he 4th International Conference on Grouting and Deep Mixing, New Orleans, USA, 2012.

Torabi, H. & Rayhani, M.T., (2014)
Three dimensional finite element modeling of seismic soil-structure interaction in soft soil. Computers and Geotechnis 60 (2014) 9 – 19

Towhata, I. (2008)
Geotechnical earthquake engineering, Springer-Verlag Berlin Heidelberg, 685 pp.

Trunk, B. & Wittmann, F. H. (1998)
Experimental investigation into the size dependence of fracture mechanics parameters. In Fracture mechanics of concrete structures. Proc. Third Int. Conf. of Fracture Mechanics of Concrete Structures (eds) H Mihashi, K Rokugo (D-Freiburg: Aedificatio Publ.) vol.3, pp. 1937–1948

Tsai, P. H. & Ni, S. H. (2011)
A Study on Dynamic Properties of Cement-Stabilized Soils, Advanced Materials Research, Vols. 243-249, 2050-2054.

Van der Stoel, A.E.C. (2001)
Grouting for pile foundation improvement, Ph.D. thesis, faculty of Civil engineering and geosciences." Delft university press, Netherlands.

Visone, C., Santucci, F., & Bilotta, E. (2010)
Comparative study on frequency and time domain analysis for seismic site response, EJGE, Vol 15., Bund. A

Vucetic, M. & Dobry, R. (1991)
Effect of soil plasticity on cyclic response. Journal of Geotechnical Engineering 117(1): 87-107.

Witasse, R. (2016)
Plaxis knowledge base: On the use of the shotcrete USDM for modelling concrete, Plaxis bv, the Netherlands.

Wittmann, F.H. (2002)
Crack formation and fracture energy of normal and high strength concrete." Sadhana, 27(4), 413–423.

Wolf, J.P. (1988)
Soil-structure Interaction Analysis in Time Domain, Prentice Hall.

Woods, R. D. (1991)
Field and Laboratory Determination of Soil Properties at Low and High Strains. International Conferences on Recent Advances in Geotechnical Earthquake Engineering and Soil Dynamics.Paper 9.

Xiao, H. W., & Lee, F. H. (2009)
Curing Time Effect on Behavior of Cement Treated Marine Clay, International Journal of Engineering and Applied Sciences 5:7

Yu, H.S. (1998)
CASM: a unified state parameter model for clay and sand. Int. J. Numer. Anal. Methods Geomechanics, 22: 621–653.

Zheng. W., Hashash, Y., Petersen, M. M. &Whittaker, A. S. (2010)
Site-specific response analysis in the new Madrid seismic zone, Fifth international conference on Recent advances in geotechnical earthquake engineering and soil dynamics and symposium in Honor of professor I.M. Idriss, San Diego, California, paper No. 3.01b.

Zienkiewicz, O.C., Bicanic, N., & Shen, F. Q. (1989)
Earthquake input definition and the transmitting boundary bonditions, Proceedings Advances in computational Nonlinear Mechanics I, pp. 109-138, Springer-Verlag, 1989